**Fünfundneunzigster Band
Volume 95**

Theoretical and Practical Aspects of High-Rate GNSS Geodetic Observations

Simon Häberling

2016

VORWORT

Zu Beginn der Entwicklung von GPS in den späten 70er und frühen 80er Jahren hätte niemand gedacht, welche Vielfalt von GNSS-Anwendungen in den darauffolgenden Jahrzehnten Realität werden würden. Die Global Navigation Satellite Systems (GNSS) werden heute oft in völlig unvorhergesehener Art und Weise eingesetzt. Neben der grossen Zahl an unterschiedlichen Signalen (Frequenzen und Modulationen), die in letzter Zeit dank der Weiterentwicklung der bestehenden und der Entwicklung neuer GNSS verfügbar geworden sind, sind auch in der Empfänger- und Antennentechnologie signifikante Fortschritte erzielt worden. Insbesondere werden heute mit GNSS-Empfängern (z.B. Javad) sehr hohe Messraten von bis zu 100 Hz erreicht. Eine Vielzahl von Anwendungen kann von solchen hohen GNSS-Aufzeichnungsraten profitieren, darunter die GNSS-Seismologie, d.h. die Messung der Bodenbewegungen während eines Erdbebens. Weitere Anwendungen umfassen die Überwachung von Gebäuden und Brücken, Maschinensteuerung und -führung, Flugzeuggravimetrie, hochdynamische Navigations- und Positionierungsaufgaben, Beobachtung hochfrequenter Szintillationen in der Ionosphäre, Frühwarn-systeme und die schnelle Reaktion auf Naturkatastrophen.

Trotz dieser interessanten und herausfordernden Aufgaben und der Tatsache, dass hohe Aufzeichnungsraten bereits in vielen Anwendungen zum Einsatz kommen, ist bisher sehr wenig Forschung betrieben worden, um die Leistungsfähigkeit aber auch die Unzulänglichkeiten von GNSS-Empfängern zu erfassen und zu beurteilen, die grosser Dynamik ausgesetzt sind und mit sehr hohen Aufzeichnungsraten arbeiten.

Genau diese Lücke versucht die Dissertation von Simon Häberling zu schliessen. Das Ziel der Dissertation war es, die Qualität aber auch die Grenzen von GNSS-Daten, die mit einer sehr hohen Aufzeichnungsrate erhoben wurden, im Detail zu verstehen. Mit unterschiedlichen Hilfsmittel (Null-Basislinien, kurze Basislinien und einem 1-dimensionalen Rütteltisch zur Erzeugung einer Vielfalt von Bewegungen) hat Simon Häberling systematisch das Rauschverhalten und die zeitlichen Korrelationen der GNSS-Beobachtungen sowie die zentrale Frage der Empfängerreaktion auf starke Dynamik für einen grossen Satz von unterschiedlichen, heute verfügbaren GNSS-Signaltypen untersucht. Er konnte eindrücklich zeigen, dass unter grosser Dynamik sehr grosse Fehler entstehen können und dass die Reaktion eines GNSS-Empfängers sehr stark von der eingestellten Bandbreite der Tracking-Loops abhängig ist. Die Doktorarbeit trägt in einer tiefgreifenden Art zur Charakterisierung der GNSS-Datenqualität bei hohen Aufzeichnungsraten bei. Dies ist von grosser Bedeutung, da in Zukunft immer mehr Anwendung GNSS-Daten mit sehr hohen Aufzeichnungsrate einsetzen werden.

Prof. Dr. M. Rothacher   **Prof. Dr. A. Geiger**
Institut für Geodäsie und Photogrammetrie   ETH Zürich
ETH Zürich   Präsident der SGK

PREFACE

A l'époque du développement du système GPS, entre la fin des années 70 et le début des années 80, personne n'avait imaginé la multitude d'applications qu'il engendrerait. En effet, aujourd'hui, les systèmes de navigation globale par satellites (GNSS) sont utilisés de façon souvent très inattendue. En plus développement continuel des systèmes GNSS, mettant à disposition des utilisateurs de nouveaux signaux de différentes fréquences et modulations, les récepteurs et des antennes ont également pu bénéficier d'avancées technologiques significatives. En particulier, certains récepteurs GNSS (par ex. Javad) sont capables d'atteindre des fréquences d'acquisition allant jusqu'à 100 Hz. De ce fait, nombreuses sont les applications qui peuvent bénéficier de ces avancées. Cela ouvre notamment la possibilité de mesurer précisément les mouvements du sol lors d'un séisme, en d'autre termes cela ouvre le champ de la séismologie par GNSS. D'autres champs d'applications peuvent également en bénéficier comme la surveillance de bâtiments et d'ouvrages d'art, le pilotage automatique de machines, l'observation des hautes fréquences de la scintillation de l'ionosphère, où encore, les systèmes déclencheurs d'alarmes en cas de catastrophes naturelles.

Bien que que l'utilisation de récepteurs GNSS à hautes fréquences soit déjà courante et qu'ils soient déjà souvent mis en œuvre en pratique, ils n'ont pas encore vraiment fait l'objet de recherches approfondies quant à leurs performances et à leurs défaillances lorsqu'ils sont soumis à de fortes contraintes dynamiques.

Ce sont ces aspects qui forment le corps de la dissertation de Simon Häberling. L'objectif de la dissertation était d'étudier en détail le comportement ainsi que la qualité des données GNSS à haute fréquence. Grâce à différentes expériences et méthodes (ligne de base nulle, ligne de base courte ainsi qu'une plateforme vibrante 1D permettant la réalisation d'une large gamme de mouvement) Simon Häberling a étudié de façon systématique le bruit de mesure, les corrélations temporelles des observations GNSS ainsi que les temps de latence engendrés par de grandes accélérations. Ceci, pour un grand nombre de signaux GNSS actuellement disponibles. En outre, il put montrer de façon impressionnante, que dans certaines conditions, de grandes erreurs de mesures peuvent survenir, et que le temps de latence dépend très fortement des largeurs des bandes passantes des boucles d'asservissement de suivi des signaux définies dans le récepteur. Ce travail de doctorat contribue de façon approfondie à la caractérisation de la qualité des mesures GNSS à hautes fréquences. Ceci revêt d'une importance toute particulière au vue de la mise en œuvre toujours plus fréquente de ce type d'acquisition.

La commission suisse de Géodésie (SGK) remercie l'auteur Simon Häberling pour cette contribution de valeur à la validation des mesures GNSS à hautes fréquences. Nos remerciements vont aussi à l'académie suisse des sciences naturelles pour avoir pris à sa charge les coûts d'impression du présent fascicule.

Prof. Dr. M. Rothacher   **Prof. Dr. A. Geiger**
Institut de Géodésie et Photogrammétrie   ETH Zürich
ETH Zürich   Président de la CGS

FOREWORD

Nobody would have expected in the beginning of the GPS developments that such a diversity and multitude of GNSS applications would become reality as we see it today. The GNSS systems are nowadays exploited in an unprecedented way. Besides the huge number of different signals (frequencies and modulations) that have lately become available due to the development of the various GNSS systems also significant improvements in receiver and antenna technology have taken place. Especially, trying to go to the limits of the GNSS technology, the increase in the achievable sampling of the receivers has now reached very high rates of up to 100 Hz (e.g., Javad receivers). Quite a large number of applications may benefit from such high-rate GNSS recordings, among them the new field of GNSS seismology, i.e., the measurement of ground motions during earthquakes. Other applications comprise structure monitoring (bridges, buildings, …), machine control and guidance, airborne gravimetry, highly dynamic navigation or positioning tasks, the observation of high-frequency scintillations in the ionosphere as well as natural hazard monitoring and early warning in general.

Despite of these interesting and challenging applications and the fact that high-rate GNSS data are already used for most of these applications, almost no research has been done so far in order to carefully and thoroughly assess the performance (and the deficiencies) of GNSS receivers under high dynamics using very high sampling rates.

This is where the Ph.D. thesis of Simon Häberling comes into play. Its goal was to study and understand the quality and also limitations of GNSS high-rate data in a detailed way. Using diverse experimental setups like zero-baselines, short baselines and a single-axis shake table (allowing the generation of a variety of motions), Simon Häberling systematically tested the noise level as well as the temporal correlation of GNSS observations and, most importantly, the receiver response during strong dynamics for a large set of different GNSS signal types as available nowadays from GPS, GLONASS and GALILEO. He showed that the errors under high dynamics may be very large and that the receiver response depends very much on the tracking loop bandwidths used by the GNSS receivers. The doctoral thesis contributes in a very thorough way to the validation of high-rate GNSS observations, a topic that is becoming more and more important and is relevant for a considerable and growing number of applications.

Prof. Dr. M. Rothacher **Prof. Dr. A. Geiger**
Institute for Geodesy and Photogrammetry ETH Zürich
ETH Zürich President of SGC

Abstract

The main goal of the thesis is the thorough investigation and quantification of GNSS observation errors in the frequency range above 1 Hz while going to the limit of the actual receiver technology with sampling rates up to 100 sps. The potential GNSS errors in this high-frequency band are mainly caused by receiver internal error sources. Due to theoretical considerations and empirical results derived from GNSS observations of almost all available carrier signals, the carrier jitter induced by thermal noise and the receiver frequency response produced by highly dynamic motions could be detected as the two most dominant disturbances affecting high-rate GNSS observations above 1 Hz.

The zero-baseline configuration (splitting the signal from one antenna to two receivers) allowed a detailed study of the carrier phase jitter and correlations between subsequent epochs dependent on different GNSS signal characteristics and baseband parameters. The size of the carrier phase jitter is directly determined by the carrier-to-noise density ratio at baseband and the corresponding loop bandwidth. Especially encrypted code sequences have a strong influence on the quality of the corresponding carrier phase component due to signal strength consuming decryption algorithms. The final consequences are a higher carrier jitter and a stronger frequency response due to the necessary PLL guiding by the strong loop signals such as GPS L1 derived from the C/A component. The impact of this higher carrier phase jitter plays a dominant role for the overall noise in the high-frequency spectrum while building the ionosphere-free linear combination. This has been demonstrated using a zero-baseline, but also a 10 m and 110 km baseline. The carrier phase jitter induced by thermal noise defines the noise level above 1 Hz. This high-frequency noise is therefore baseline independent. No significant differences between a baseline of 10 m and 110 km could be detected considering the signal spectrum between 0.01 Hz and 50 Hz.

For the determination and analysis of the GNSS errors caused by high-frequency motions an experimental setup has been established consisting of a single-axis shake table as motion generator and of a well-known ground-truth defined by inductive displacement transducers. The ground-truth was validated by a strong motion seismometer with a flat frequency response carried on the shake table. With an additional precise time synchronization between all the sensors, the experiment with a mounted GNSS antenna on the shake table enabled the determination of the GNSS receiver frequency response between 1 and 20 Hz. Using different receiver types and PLL bandwidths, the amplitudes even at 3 Hz can be overestimated by about 50%, above 10 Hz also an overestimation can be observed or a reduction by well over half of the amplitude. Not only the amplitude is affected, but also the signal phase with errors between 30 and 90 degrees. This demonstrates the importance of a detailed knowledge of the loop parameters for an assessment of the expected errors, but also for applying an inverse filter in order to correct the GNSS receiver frequency response based on a simple digital PLL model. These results are relevant for all applications with strong dynamics using high-rate GNSS, such as structural health monitoring, machine

guidance, navigation, and ionosphere scintillation studies.

Further, seismological implications and the potential contribution of high-rate GNSS to seismology has been evaluated. Based on a moderate synthetic earthquake expected for Switzerland generated on the shake table, the sensitivity of high-rate GPS to high-frequency seismic signals using a realistic baseline length could be tested. Additionally, the receiver response has been simulated for real earthquakes in order to demonstrate the displacement errors caused by the response.

Zusammenfassung

Das Hauptziel dieser Arbeit ist die genaue Untersuchung und Quantifizierung von Abweichungen in den GNSS-Beobachtungen im Frequenzbereich oberhalb von 1 Hz. Dabei soll die aktuellste Empfänger-Technologie mit einer Aufzeichnungsrate von bis zu 100 Messepochen pro Sekunde genutzt werden. Die möglichen Fehlereinflüsse in diesem hohen Frequenzbereich werden hauptsächlich durch Fehlerquellen im Empfänger selbst generiert. Aufgrund von theoretischen Untersuchungen und empirischen Resultaten aus GNSS Beobachtungen von fast allen zur Verfügung stehenden Trägersignalen, konnten das Phasenrauschen induziert durch thermisches Rauschen und die Empfänger-Frequenzantwort generiert durch hoch-dynamische Bewegungen als die zwei dominanten Fehlereinflüsse für hochfrequente GNSS-Beobachtungen über einem 1 Hz detektiert werden.

Die Konfiguration als Nullbasislinie, bei welcher das von der Antenne empfangene Signal zu zwei Empfängern geleitet wird, erlaubte eine detaillierte Untersuchung des Phasenrauschens und der Korrelationen zwischen aufeinander folgenden Messepochen in Abhängigkeit von verschiedenen GNSS Signal-Eigenschaften und Basisband-Parametern. Die Grösse des Phasenrauschens wird direkt von der Spektraldichte des Träger-Rausch-Verhältnisses und der entsprechenden Regelschleifen-Bandbreite bestimmt. Die Verschlüsselung der auf den Trägerwellen aufmodulierten Code-Sequenzen hat im speziellen durch Entschlüsselungs-Algorithmen einen starken Einfluss auf die Qualität der entsprechenden Komponente der Trägerphasen-Beobachtung und auf die Signalstärke. Die Konsequenzen sind ein höheres Phasenrauschen und eine stärkere Frequenzantwort aufgrund der nötigen Unterstützung des Leitkanals der Phasenregelschleife wie zum Beispiel der unverschlüsselten C/A-Code Signalkomponente auf GPS L1. Für das Bilden der ionosphären-freien Linearkombination spielt das erhöhte Phasenrauschen der verschlüsselten Signale eine entscheidende Rolle und bestimmt das Gesamtrauschen im hohen Frequenzbereich. Dies wurde nicht nur für den Fall der Nullbasislinie demonstriert, sondern auch für Basislinien mit einer Länge von 10 m und 110 km. Dabei definiert das durch thermisches Rauschen induzierte Phasenrauschen den Gesamtrauschpegel oberhalb von 1 Hz. Dieses hochfrequente Rauschen ist deshalb unabhängig von der Basislinie. Zusätzlich konnten keine Unterschiede zwischen einer 10 m und 110 km Basislinie im Frequenzbereich zwischen 0.01 Hz und 50 Hz festgestellt werden.

Die Bestimmung und Untersuchung von GNSS Beobachtungsfehlern während hochfrequenten und dynamischen Bewegungen wurde mit Hilfe eines Rütteltisches durchgeführt. Der Versuchsaufbau bestand hauptsächlich aus einem Bewegungsgenerator und einem sehr genau überwachten Bewegungsverlauf, welcher durch zwei induktive Wegaufnehmer garantiert wurde. Die Validierung der Wegaufnehmer wurde mit Hilfe eines Seismometers durchgeführt, welches auf dem Rütteltisch montiert wurde und eine flache Frequenzantwort aufweist. Durch die Bewegung der auf dem Rütteltisch befestigten GNSS Antenne und einer sehr genauen Zeitsynchronisation zwischen allen verwendeten Sensoren konnte die Frequenzantwort der GNSS Empfänger zwischen 1 Hz und 20 Hz empirisch bestimmt

werden. Für verschiedene Empfänger konnte gezeigt werden, dass die beobachteten Amplituden bei einer Bewegung von 3 Hz bis zu 50% überschätzt werden und oberhalb von 10 Hz sogar bis um die Hälfte reduziert werden. Neben der Amplitude weicht auch die Phasenlage der Bewegung zwischen 30 und 90 Grad von der Sollbewegung ab. Dies zeigt die Wichtigkeit auf, die Basisband-Parameter sehr genau zu kennen, um die zu erwartenden Abweichungen im hohen Frequenzbereich abschätzen zu können und um ein inverses Filter für die Korrektur dieser Fehler anbringen zu können. Sind die Parameter bekannt, reicht ein einfaches digitales PLL Modell für die Modellierung der Fehler und für die Anbringung der Korrekturfilter. Diese Resultate sind für alle Anwendungen relevant, welche auf der Aufzeichnung von hoch-dynamischen Bewegungen basieren, wie zum Beispiel die Überwachung von Bauwerken, Baumaschinensteuerung, Navigation und Untersuchungen der Ionosphärenszintillation.

Zusätzlich wurden die Auswirkung der genannten Fehlereinflüsse für hochfrequente GNSS Beobachtungen und der mögliche Beitrag für die Seismologie untersucht. Synthetische mit dem Rütteltisch generierte Erdbeben, welche in der Schweiz erwartet werden können, erlaubten die Bestimmung der Sensitivität von GNSS Beobachtungen mit hoher Aufzeichnungsrate unter realistischen Bedingungen und Basislinien-Konfigurationen. Weiter wurden mit Hilfe der bekannten Empfänger-Frequenzantwort Beobachtungen von tatsächlich stattgefundenen Events simuliert, was die zu erwartenden Messabweichungen der von Erdbeben verursachten Bodenverschiebungen demonstriert.

Contents

Abbreviations

ACF   Autocorrelation function
ADC   Analog-to-digital converter
AGC   Automatic gain control
AltBOC   Alternative binary offset carrier
AM   Amplitude modulation
ARP   Antenna reference point
AS   Antispoofing

BOC   Binary offset carrier
BPF   Bandpass filter
BPSK   Binary phase shift keying

CBOC   Composite binary offset carrier
CDMA   Code division multiple access
CDMU   Clock distribution and monitoring unit
CL   Civil long
CLL   Code-locked loop
CM   Civil moderate
CS   Commercial service
CW   Continuous wave

DAC   Data acquisition board
DC   Direct current
DCO   Digital controlled oscillator
DD   Double-difference
DLL   Delay-locked loop
DPLL   Digital phase-locked loop
DSSS   Direct sequence spread spectrum

EL   Early-minus-late

FDMA   Frequency division multiple access
FEC   Forward error correction
FLL   Frequency-locked loop
FM   Frequency modulation

GDOP   Geometric dilution of precision
GNSS   Global navigation satellite systems
GPS   Global positioning system

HOW   Hand-over-word

ICD	Interface control document
ID	Integrate and dump
IERS	International Earth Rotation and Reference Systems Service
IF	Intermediate frequency
IGS	International GNSS Service
ITU	International Telecommunication Union
KiK-net	Kiban-Kyoshin network
K-NET	Kyoshin network
LC	Linear combination
LF	Loop filter
LHCP	Left-hand circularly polarized
LNA	Low noise amplifier
LO	Local oscillator
LOS	Line of sight
LPF	Lowpass filter
NCO	Numerically controlled oscillator
NF	Noise figure
OEM	Original equipment manufacturer
OS	Open service
OCXO	Oven-compensated crystal oscillator
PAC	Phase-to-amplitude converter
PCV	Phase center variations
PD	Phase discriminator
PGA	Peak ground acceleration
PGD	Peak ground displacement
PGV	Peak ground velocity
PI	Proportional-integral
PLL	Phase-locked loop
PM	Phase modulation
PPS	Pulse-per-second
PRN	Pseudorandom noise
PRS	Public regulated service
PSD	Power spectral density
PSK	Phase shift keying
QPSK	Quadrature phase shift keying
RF	Radio frequency
RHCP	Right-hand circularly polarized
RNSS	Radionavigation Satellite Service
RTF	Receiver time frame
SAR	Search and rescue service
SD	Single-difference
SNR	Signal-to-noise ratio
SOL	Safety-of-life service

TCXO	Temperature-compensated crystal oscillator
TD	Triple-difference
TDM	Time division multiplexing
TDMA	Time division multiple access
TLM	Telemetry word
TMBOC	Time multiplexed binary offset carrier
TTL	Transistor-transistor logic
UHF	Ultra high frequency
UPM	Universal power module
VCO	Voltage controlled oscillator
VGA	Variable gain amplifier
ZD	Zero-difference

1 Introduction

1.1 Motivation

Due to considerable improvements in receiver and antenna technologies and the development of new processing algorithms, the Gobal Navigation Satellite Systems (GNSS) – comprising the Global Positioning System (GPS), supplemented by the Russian GLONASS, the European GALILEO and the Chinese BEIDOU – has become a tool of ever growing importance for Earth science research, the monitoring of natural hazards and for early warning systems. In particular, rapid earthquake (and tsunami) detection and quantification is a very active field of research today.

One such development is that it is now usual to sample GNSS data at 1 sample-per-second (sps), and it is possible to push the sampling up to 100 sps. These considerable improvements have the potential of measuring earthquake ground motions. Large and moderate earthquakes were successfully observed by permanent 1 sps GPS stations in the last decade. Beside significant global events moderate earthquakes have produced seismic displacements also observed by GPS. Events of $M > 6.0$ should be expected in Switzerland every 80 years (*Giardini et al.*, 2004) and have been identified as the natural hazard with the highest risk potential for Switzerland. For recording ground motions and displacements of such moderate earthquakes by GNSS, sites have to be installed within 100 km from the epicenter (*Clinton et al.*, 2007). Furthermore, the ability of GNSS to detect the surface waves depends not only on the earthquake magnitude and on the distance to the epicenter, but also on the mechanism of the earthquake (depth and fault structure). However, unless GNSS is combined with more sensitive seismic instruments, 1 sps is not sufficient if GNSS is to become a valuable tool for measuring dynamic seismic displacements. Therefore, this thesis will study GNSS observations with sampling rates up to 100 sps. Beside directly measuring the time-dependent surface displacement, GNSS has the crucial advantage that, unlike traditional seismometers and strong motion sensors, there is no expected saturation during extreme ground motions. GNSS can therefore make a significant improvement to the observation capabilities of dynamic surface movement during earthquakes at all scales, and will be complementary to ground motion measurements (from seismometers and accelerometers). The goal will be to investigate the limits of the measurement technique, even if it is possible that no significant seismic signal can be expected and measured at extremely high frequencies.

In addition to capturing earthquake ground motions, tsunamis, landslides and rock glaciers can benefit considerably from high-rate GNSS. Using the most recent GNSS receiver technology and studying the behavior of GNSS receivers up to a sampling rate of 100 sps is also of significance to the health monitoring of critical infrastructures such as nuclear power plants, high rise buildings, bridges and dams, but also to aero-gravimetry, navigation, machine guidance and to the growing field of sport applications.

However, if GNSS data is to be used at high sampling rates more detailed studies on high-rate GNSS receiver performances are required. The major GPS error sources in the frequency range between months and several seconds (e.g. ionosphere, troposphere, and multipath) have thoroughly been studied in the last decades. In contrast, the errors in the frequency range above 1 Hz (mainly receiver-induced errors) have not been studied in detail yet.

1.2 Tasks and Goals

This Ph.D. thesis is a part of the Swiss National Science Foundation (SNSF) project "High-Rate GNSS for Seismology" and was carried out in coordination with the Swiss Seismological Service. The main objective of this project is the thorough investigation of the contribution of GNSS seismology (measuring dynamic displacements with GNSS) to the characterization and quantification of earthquake parameters and, thus, to natural hazards monitoring and early warning systems. For the assessment an end-to-end simulator (E2E simulator) is developed, where each of the critical steps and all important aspects of the processing can be considered, evaluated and improved. Based on real and virtual earthquakes with specific characteristics, consistent seismograms and ground motions were numerically generated for station networks with different geometry and density. These waveforms were then used to 1) simulate GNSS observations with realistic error sources and to 2) steer and control the movement of the available shake table carrying a GNSS antenna. Measurements were recorded at a rate of up to 100 sps. The processing of these GNSS datasets delivered ground motions that can be compared with those originally generated, in order to assess the quality of the GNSS ground motion recovery. As the final step of the E2E simulation, the GNSS-derived ground motions are introduced into a joint inversion with the seismic data. In this way, the benefit we can expect from having GNSS data complementary to seismometers can be assessed, with an enhanced understanding of relative strengths and weaknesses of "GNSS seismometers". The simulation and research tasks for three researchers have been divided into two main sections. The seismological part includes the ground motion generation and final source inversion. The geodesy part is split into 1) the investigation of the GPS data retrieved from real earthquake events and detection algorithms based on real and simulated site networks, and into 2) this thesis, i. e., tests with high-rate GNSS receivers based on static antennas and shake table measurements for a theoretical and empirical quantification of deviations in high-frequency GNSS recordings. In addition to *Elósegui et al.* (2006), who published tests with a single-axis shake table and 1 sps GPS measurements, *Wang et al.* (2012) (published during this thesis) extended the investigations by a six-degree-of-freedom shake table and sampling rates up to 10 sps. However, both did not focus on the quantification of the GPS displacement deviations induced during highly dynamic motions which is one of the main focus of this thesis. The main tasks are described in the following.

Task 1: Data processing
The base for all further tasks of high-rate GNSS data analysis and experiments is a software enabling the processing of GNSS data up to 100 sps. For this purpose, the highly sophisticated Bernese GNSS software package has to be adapted to 100 sps because the standard version is only able to handle 1 sps data. The new Bernese version is then used

for the processing of all high-rate GPS measurements collected in the following research tasks.

Task 2: Static tests with high-rate GNSS receivers
In this task the performance of some high-end GNSS receivers (focused on the new Javad Sigma-G3TAJ receivers) are tested in a static mode. The receivers are able to collect observations for all GPS, GLONASS and GALILEO satellites in view with a sampling rate of 100 sps. This is a unique feature of this new receiver generation and permits the investigation of the highly dynamic processes taking place during an earthquake with an unprecedented temporal resolution for GNSS. Much attention is to be devoted to the statistical analysis of the observations to obtain information on the type of measurement noise and on the correlation between subsequent observations dependent on different receiver parameters. The static tests are carried out with different measurement configurations (zero-baselines, short and long baselines) and focusing on different GNSS signals with their specific characteristics.

Task 3: GNSS experiments with a single-axis shake table
This task includes the investigation of the behavior of high-rate GNSS measurements during highly dynamic motions. A small single-axis shake table from the Institute of Structural Engineering at ETH Zurich is used as motion generator. An accurate empirical determination of deviations in high-frequency GNSS recordings can only be achieved with a very accurately known ground-truth defined by inductive sensors. The establishing and validation of the ground-truth is a crucial part for the analysis and is complemented by a strong motion accelerometer mounted on the shake table. The known motion of the shake table forms the ground-truth for the motion of the GNSS antenna mounted on the table and allows the comparison of the GNSS results to assess the GNSS performance over a wide range of dynamic motions while going to the limit of the currently available receiver technology.

Task 4: High-rate GNSS measurements of earthquakes
The obtained knowledge and understanding about high-rate GNSS observations from the previous tasks is applied to seismic events. Simulated earthquake ground motions, but also real recordings build the base to assess the potential contribution and limitation of high-rate GPS measurements to seismic ground motion records.

1.3 Structure of the Thesis

According to the described tasks, the thesis is structured as follows:

Chapter 2 introduces the fundamental requirements for GNSS and the consequences on the signal structures with different modulation types.

Chapter 3 describes the architecture and basic functionalities of a common GNSS receiver. It is the goal to demonstrate how the natural measurements in a GNSS receiver are carried out. This fundamental understanding, also dependent on different signal characteristics described in Chapter 2, is crucial for the analysis and interpretation of the final high-rate GNSS observations.

Chapter 4 provides tools for a linear modeling of the carrier tracking functionalities in-

troduced in Chapter 3 and describes the most important tracking parameters. With the assistance of such tools pre-analyses of expected tracking errors are possible. In addition to the errors of the receiver system, the chain from the satellite to the retrieved measurements at the receiver and the final geodetic observation equations with all existing signal perturbations is completed.

Chapter 5 presents the results of the noise analysis for almost all available GNSS signals according to Task 2. Dependent on the different signal structures described in Chapter 2 and the corresponding tracking requirements, the different characteristics of the final GNSS observations, focusing on the frequency band above 1 Hz, are determined. This analysis is also expanded to large baseline lengths in order to demonstrate the behavior of the GNSS noise dependent on the baseline over a wide range of the frequency spectrum.

Chapter 6 describes the equipment and setup of the shake table experiments. Especially the establishing of a ground-truth and its validation with a strong motion sensor is a crucial part for the assessment of dynamic observations in Chapter 7. Additionally, short descriptions of the software package update (Task 1) and the standard processing strategies used are given.

Chapter 7 includes the assessment of dynamic high-rate GPS recordings dependent on different tracking parameters according to Task 3. Beside the empirical estimation of relative amplitude errors and phase shifts based on the motions generated by the shake table, a simple digital phase-locked loop model (based on Chapter 4) is introduced in order to enable a comparison between theoretically and practically determined GPS errors under dynamic stress.

Chapter 8 shows the results of high-rate GPS-derived seismic ground motions for an earthquake expected in Switzerland. The investigation is expanded to GPS receiver response simulations of real seismic events recorded in the near-field in order to quantify the limiting factors and a potential contribution of high-rate GPS observations.

Chapter 9 draws the conclusions of this thesis and provides an outlook.

2 GNSS Signal Structure

This chapter introduces and describes the different types of GNSS signals and their characteristics. The structure of the transmitted signals by the satellites directly determine the antenna and receiver architecture with their acquisition and tracking capabilities, and finally the performance and accuracy of positioning. The global positioning satellite systems (GNSS) have the main objective to enable a real-time positioning and navigation all over the globe with an accuracy of some meters. The required bandwidth for such an accurate navigation without ambiguity has to be large. A positioning accuracy of 3 m (10 ns) and a possible dissolving of the modulation component of 1–10% leads to a bandwidth of 1–10 MHz. The navigation has to be guaranteed under high dynamics (e. g. aircraft) which requires an omni-directional antenna. These two requirements demand a frequency in the radio frequency (RF) spectrum. The bandwidth is large compared to the frequency, but not too large with respect to the signal loss while traveling through space (*Spilker*, 1980). For the minimization of path delays induced by the dispersive ionosphere in this frequency band, at least two frequencies have to be allocated.

The concept of satellite and user clock timing while receiving the signal from one single satellite requires an extremely stable clock at the receiver. If the receiver knows the position of the satellite and both clocks are perfectly synchronized, the propagation delay can directly be measured and indicates that the receiver is located on a sphere surface around the satellite. After several observations over a longer time period while the satellite is transmitting the signals from different orbit positions, the receiver is able to calculate a 3D position. This concept does not conform to the objective that a real-time positioning should be assured allowing a certain user dynamic. Additionally, the GNSS user cannot be forced to carry an atomic clock. Therefore, the receiver has to track several satellite signals simultaneously in order to determine a receiver clock correction. This request of multiple access without large interferences demands sophisticated code modulations which are shortly described in the following sections. The positioning accuracy is strongly related to the number of available satellites and geometric distribution, called geometric dilution of precision (GDOP). For this purpose, the orbital planes for up to 30 satellites (global systems) are chosen in a way to guarantee a sufficient number of visible satellites over almost the whole globe all the time.

Even the satellite atomic clocks are affected by uncertainties such as internal drifts and relativistic frequency shifts. Several ground receivers have to collect the transmitted signals and estimate the satellite clock corrections. The clock corrections are sent to the satellites by an uplink and have to be provided to the users with other information such as ephemeris parameters, ionospheric delays, and health data. The so called navigation message has to be additionally modulated on the carrier to enable an accurate positioning in real-time.

In the course of the system developments and modernizations, signal modulations with specific advantages in multipath mitigation, with higher interference and jamming tolerance

while providing integrity information were considered especially for safety relevant applications. In addition to pseudorange measurements for navigation or time synchronization, the extended demand of GNSS in an extremely wide field of high-precision applications requires accurate Doppler shift measurements in order to reach an accuracy level of some millimeters.

2.1 Spread Spectrum and Modulation Types

For the compliance with the requirements stated above, some fundamental signaling schemes and their characteristics are introduced. There are several methods how a RF carrier and a data stream can be superimposed for the transmission and demodulation in the receiver afterwards. In general, three fundamental modulation techniques are distinguished, the amplitude modulation (AM), the frequency modulation (FM), and the phase modulation (PM). The implementation of an AM is quite simple, and the demodulation electronics only consist of few components. However, the AM is not very efficient to power usage and required bandwidth, additionally, it is very sensitive to noise which is amplitude based for the most part. In contrast, the FM shows a far better signal-to-noise characteristics over a wider bandwidth than AM and is not extremely sensitive against power variations, but requires much more complicated demodulators. These advantages against AM are the reasons for the extremely wide usage of FM in analog radio communication. In the analog domain the PM is closely linked to the FM in the way that a phase change is induced by a frequency change during a limited time. In addition to a higher spectral efficiency for data transmission compared to FM, the PM is often preferred for digital signals that can easily be modulated while switching between a finite number of phases with the phase shift keying (PSK) technique (*Couch II*, 2013).

2.1.1 Binary Phase Shift Keying (BPSK)

The most basic PSK modulation is the binary phase shift keying (BPSK) that modulates a single binary data stream $D(t)$ on an RF carrier. A binary data stream with symbols 1 or 0 can be represented as a train of k rectangular pulses $p(t)$

$$D(t) = \sum_k a_k \, p(t - kT_\mathrm{d}) \tag{2.1}$$

with the corresponding polar bit sequence a_k

$$a_k = \begin{cases} 1 & \text{for binary symbol 1} \\ -1 & \text{for binary symbol 0} \end{cases} \tag{2.2}$$

and the pulse

$$p(t) = \begin{cases} 1 & -\frac{T_\mathrm{d}}{2} \leq t < \frac{T_\mathrm{d}}{2} \\ 0 & \text{elsewhere.} \end{cases} \tag{2.3}$$

The BPSK signal $d(t)$ (for rectangular pulses often termed as BPSK-R) is accomplished by the product of the data stream $D(t)$, with constant bit values over the interval $T_\mathrm{d} = 1/R_\mathrm{d}$

defined by the data bit rate R_d [bps], and an unmodulated carrier wave $w(t)$ with an amplitude A and frequency f_0

$$d(t) = D(t)\,w(t) = D(t)A\cos(2\pi f_0 t). \tag{2.4}$$

The multiplication of the signals represented by polar coefficients ± 1 is equal to the modulo-2 sum of the binary values 1 and 0. The signal $D(t)$ is also considered as a baseband signal because it includes frequencies around 0 Hz. On the contrary, the carrier $d(t)$ with the modulation on its center frequency is a so-called bandpass signal (see Fig. 2.1). The bandpass bandwidth B_d is still narrow and extremely vulnerable against narrowband interferences. In addition, the regulations of the International Telecommunication Union (ITU) define a maximum flux density for each 4 kHz frequency band in order to prevent interferences with voice channels. However, the total power radiated by a GPS satellite can exceed the limit of -154 dBW/m^2 if the signal power is spread over a wider bandwidth (*Spilker*, 1996). The BPSK signal with its narrow bandwidth can be spread by a binary signal $c(t)$ with a random or pseudorandom sequence of ± 1 and a chip length T_c that is much smaller than T_d

$$s(t) = c(t)\,d(t) = A\,c(t)D(t)\cos(2\pi f_0 t). \tag{2.5}$$

The direct sequence spread spectrum (DSSS) of the signal $s(t)$ is visible in Fig. 2.1. The notation of a BPSK signal is often given as BPSK(n) defined by the parameter n, the ratio between the frequency of the spreading code f_c and a reference frequency f_r

$$n = \frac{f_c}{f_r}. \tag{2.6}$$

The reference frequency f_r is typically set to 1.023 MHz considering GNSS signals (e. g. GPS and Galileo).

The characteristics of a signal is generally described by its autocorrelation function (ACF) and the directly related power spectral density (PSD). Let us consider an infinite perfectly random code $c(t)$ based on rectangular pulses according to Eq. (2.1) with pulse length T_c. The ACF of an ergodic process $c(t)$ is defined as

$$R_c(\tau) = \overline{c(t)\,c(t+\tau)} = \lim_{T\to\infty} \frac{1}{2T} \int_{-T}^{T} c(t)\,c(t+\tau)\,\mathrm{d}t. \tag{2.7}$$

Due to the infinite sequence of independent zero-mean random binary digits the integral in Eq. (2.7) is zero for $|\tau| \geq T_c$. The integral for $|\tau| < T_c$ is equal to the area of the chip time fraction $T_c - \tau$. Therefore the result for the normalized ACF is given by

$$R_c(\tau) = \begin{cases} \left(1 - \frac{|\tau|}{T_c}\right) & |\tau| < T_c \\ 0 & |\tau| \geq T_c. \end{cases} \tag{2.8}$$

The ACF of a random signal is illustrated in Fig. 2.2 (left). It can be seen that the signal is correlated only for one specific bit (time) offset. For all other time offsets the correlation remains zero. The power spectral density $S_c(f)$ of a stochastic signal $c(t)$ is nothing else
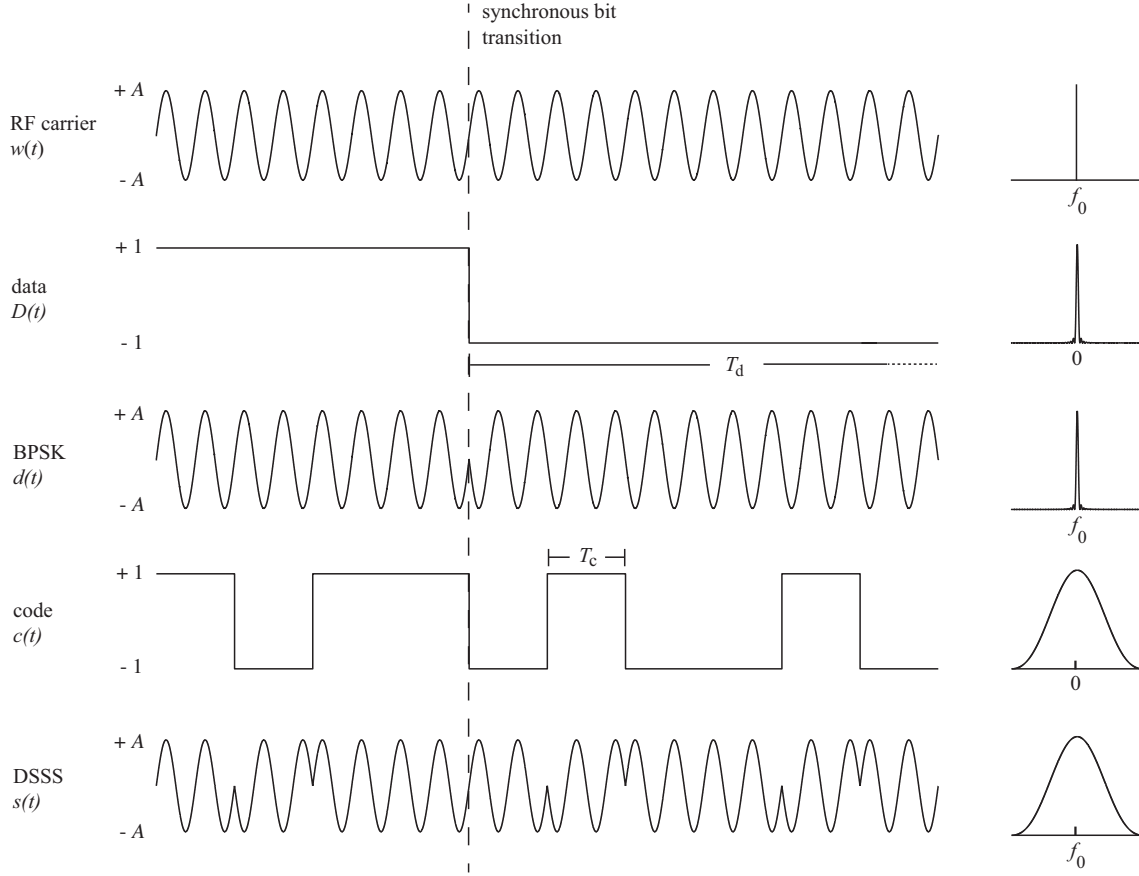
Figure 2.1: The BPSK modulation process of an RF carrier is shown as well as the corresponding power spectral densities on the right. The RF carrier with a frequency f_0 is modulated by data bits with a long chip length T_d represented as a baseband signal $D(t)$ with its main power around 0 Hz. The resulting passband signal $d(t)$ is spread by a code sequence $c(t)$ with a much shorter chip length T_c that leads to a direct sequence spread spectrum (DSSS) with a wider bandwidth around the RF center frequency f_0. Due to the synchronous bit transition the passband signal $s(t)$ has an equal power spectrum as the baseband signal $c(t)$ only shifted by the RF center frequency.

than the Fourier transform of its ACF $R_\mathrm{c}(\tau)$

$$
\begin{aligned}
S_\mathrm{c}(f) &= \int_{-\infty}^{\infty} R_\mathrm{c}(\tau)\mathrm{e}^{-j2\pi f\tau}\,\mathrm{d}\tau \\
&= \int_{-T_\mathrm{c}}^{T_\mathrm{c}} \left(1 - \frac{|\tau|}{T_\mathrm{c}}\right)\mathrm{e}^{-j2\pi f\tau}\,\mathrm{d}\tau \\
&= \int_{-T_\mathrm{c}}^{T_\mathrm{c}} \cos(2\pi f\tau)\,\mathrm{d}\tau - \underbrace{\int_{-T_\mathrm{c}}^{T_\mathrm{c}} j\sin(2\pi f\tau)\,\mathrm{d}\tau}_{=\,0} - \frac{1}{T_\mathrm{c}}\int_{-T_\mathrm{c}}^{T_\mathrm{c}} |\tau|\cos(2\pi f\tau)\,\mathrm{d}\tau \qquad (2.9) \\
&\qquad\qquad\qquad\qquad\qquad\qquad + \frac{1}{T_\mathrm{c}}\underbrace{\int_{-T_\mathrm{c}}^{T_\mathrm{c}} |\tau|j\sin(2\pi f\tau)\,\mathrm{d}\tau}_{=\,0}\,.
\end{aligned}
$$

By changing the interval of the non-zero integrals (even functions) to $[0, T_\mathrm{c}]$ and by partially
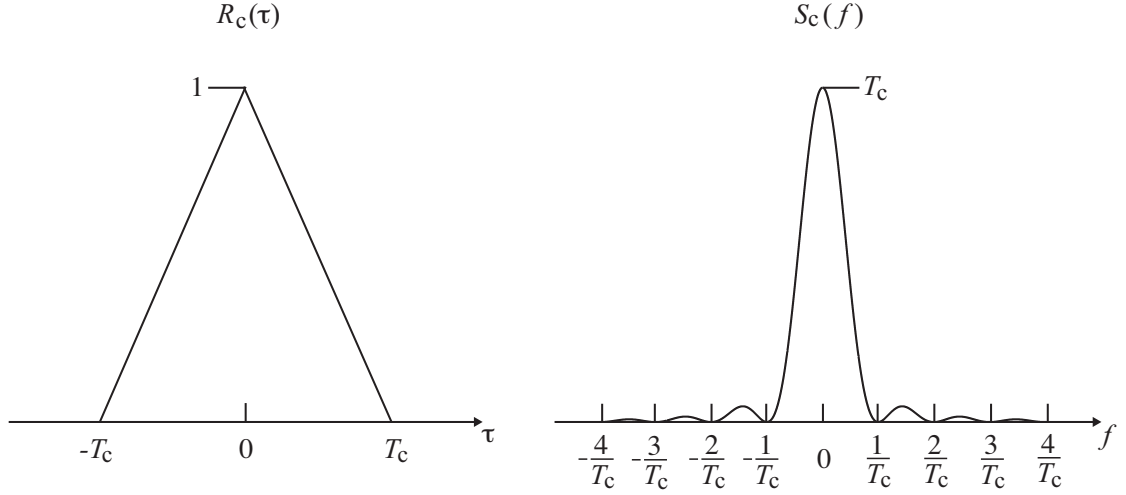
Figure 2.2: The width of the autocorrelation peak of a random code sequence is exactly 2 chips with the peak corresponding to the signal power P (left). The baseband power spectral density (right) with a peak of T_c consists of several side lobes at each multiple of $f_c = 1/T_c$.

integrating the following antiderivatives can be found

$$
\begin{aligned}
S_c(f) &= 2 \left(\frac{\sin(2\pi f \tau)}{2\pi f \tau} \right)\Bigg|_0^{T_c} - \frac{2}{T_c} \left(\frac{\cos(2\pi f \tau)}{(2\pi f \tau)^2} + \frac{\tau \sin(2\pi f \tau)}{2\pi f \tau} \right)\Bigg|_0^{T_c} \\
&= \frac{2}{T_c} \left(\frac{1 - \cos(2\pi f T_c)}{(2\pi f T_c)^2} \right) \\
&= T_c \frac{\sin^2(\pi f T_c)}{(\pi f T_c)^2} = T_c \operatorname{sinc}^2(f T_c).
\end{aligned}
\tag{2.10}
$$

with $\frac{\sin(\pi x)}{\pi x} = \operatorname{sinc}(x)$. Figure 2.2 (right) shows the two-sided power spectral density of an infinite random code with chip length T_c at baseband.

The PSD of the carrier

$$
w(t) = A \cos(2\pi f_0 t)
\tag{2.11}
$$

can also be derived by its autocorrelation function

$$
R_w(\tau) = \lim_{T \to \infty} \frac{1}{2T} \int_{-T}^{T} A^2 \cos(2\pi f_0 t) \cos(2\pi f_0 t + 2\pi f_0 \tau) \, \mathrm{d}t.
\tag{2.12}
$$

Using a trigonometric identity the expression can be simplified to

$$
\begin{aligned}
R_w(\tau) =& \frac{A^2}{2} \cos(2\pi f_0 t) \lim_{T \to \infty} \frac{1}{2T} \int_{-T}^{T} \mathrm{d}t + \frac{A^2}{2} \lim_{T \to \infty} \frac{1}{2T} \int_{-T}^{T} \cos(4\pi f_0 t + 2\pi f_0 \tau) \, \mathrm{d}t \\
=& \frac{A^2}{2} \cos(2\pi f_0 t).
\end{aligned}
\tag{2.13}
$$

The PSD $S_w(f)$ as the Fourier transform of $R_w(\tau)$ is finally given by the Dirac delta

functions

$$S_{\mathrm{w}}(f) = \mathscr{F}\left\{\frac{A^2}{2}\cos(2\pi f_0 t)\right\}$$
$$= \frac{A^2}{4}\left[\delta(f - f_0) + \delta(f + f_0)\right]. \tag{2.14}$$

The spectrum of the positive frequency part is shown in Fig. 2.1 (top right). Due to the synchronized transition between $d(t)$ and $c(t)$, the PSD of the passband (or bandpass) DSSS signal $s(t)$ is given by the frequency translation of the real signal $c(t)$

$$S_{\mathrm{s}}(f) = \frac{A^2}{4}\left[S_{\mathrm{c}}(f - f_0) + S_{\mathrm{c}}(f + f_0)\right]. \tag{2.15}$$

2.1.2 Binary Offset Carrier (BOC)

An additional modulation technique is the binary offset carrier (BOC) modulation. The concept bases on the multiplication of the modulated code signal and a rectangular sub-carrier with frequency f_{sc} that is defined by its chip length T_{sc}

$$f_{\mathrm{sc}} = \frac{1}{2T_{\mathrm{sc}}} \tag{2.16}$$

and is equal to or higher than the frquency f_{c} of the modulated signal (*Betz*, 2001)

$$f_{\mathrm{c}} = \frac{1}{T_{\mathrm{c}}} = \frac{2}{N_{\mathrm{B}}}f_{\mathrm{sc}}. \tag{2.17}$$

N_{B} is the order or the number of half-periods T_{sc} of the subcarrier during one spreading code chip T_{c} (see Fig. 2.3)

$$N_{\mathrm{B}} = 2\frac{f_{\mathrm{sc}}}{f_{\mathrm{c}}}. \tag{2.18}$$

The notation is commonly given as $\mathrm{BOC}(m,n)$ with the proportional parameter n defined in Eq. (2.6) and m dependent on the subcarrier frequency f_{sc} and the set reference frequency f_{r}

$$m = \frac{f_{\mathrm{sc}}}{f_{\mathrm{r}}}. \tag{2.19}$$

The subcarrier is either in sine-phase or cosine-phase to the BPSK code sequence $c(t)$. The resulting baseband BOC signals $b(t)$ are termed $\mathrm{BOC_s}$ and $\mathrm{BOC_c}$, respectively. Figure 2.3 shows the additional modulation of a subcarrier $sc(t)$, sine-phase (solid) and cosine-phase (dashed), on the code sequence $c(t)$. The baseband signal $b(t)$ can be added to the carrier as described for the BPSK signal $c(t)$ according to Eq. (2.5).

The power spectral density $S_{\mathrm{s}}(f)$ of a $\mathrm{BOC_s}$ modulated signal for even N_{B} is given by *Betz* (2001):

$$S_{\mathrm{s}}(f) = T_{\mathrm{c}}\,\mathrm{sinc}^2(fT_{\mathrm{c}})\tan^2\left(\frac{\pi f T_{\mathrm{c}}}{N_{\mathrm{B}}}\right) \tag{2.20}$$

and for a $\mathrm{BOC_c}$ signal respectively

$$S_{\mathrm{c}}(f) = S_{\mathrm{s}}(f)\tan^2\left(\frac{\pi f T_{\mathrm{c}}}{2N_{\mathrm{B}}}\right). \tag{2.21}$$
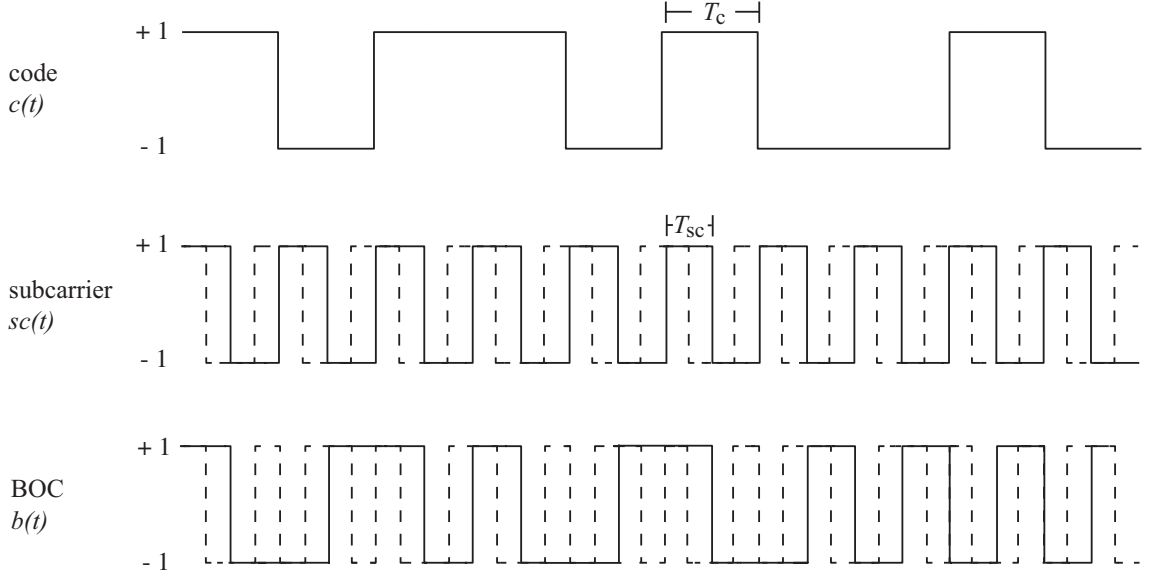
Figure 2.3: The $\mathrm{BOC_s}(1,1)$ signal (solid) and the $\mathrm{BOC_c}(1,1)$ (dashed) signals are represented as baseband signal with $f_{\mathrm{sc}} = f_{\mathrm{c}} = f_{\mathrm{r}}$. The signal $b(t)$ is the product of the subcarrier with chip-length T_{sc} and the modulated code $c(t)$. The phase state of $sc(t)$ is either sine-phase (solid) or cosine-phase (dashed).

Odd orders are currently not used in satellite navigation systems and are not even planned. The split mainlobes of the PSD of the $\mathrm{BOC_s}(1,1)$ (solid) and $\mathrm{BOC_c}(1,1)$ (dashed) in Fig. 2.4 (right) are a result of the subcarrier modulation with the half chip length compared to the spreading code. The maximum PSD values for the $\mathrm{BOC_s}(1,1)$ are about half that of BPSK(1) modulation. The $\mathrm{BOC_c}(1,1)$ maximum values are even lower due to the slightly wider spread of the main lobes and stronger side lobes.

The autocorrelation function of a BOC modulation with an infinite bandwidth shown in Fig. 2.4 (left) produces several side peaks. The ACF function of a $\mathrm{BOC_s}$ for $0 \leq \tau \leq T_{\mathrm{c}}$ is derived in (*Sousa and Nunes*, 2013) as

$$R_{\mathrm{s}}(\tau) = (-1)^k \left(\frac{2k^2 - 2kN_{\mathrm{B}} - 2k + N_{\mathrm{B}}}{N_{\mathrm{B}}} + (2N_{\mathrm{B}} - 2k + 1)\frac{|\tau|}{T_{\mathrm{c}}} \right) \qquad (2.22)$$

with

$$k = \mathrm{ceil}\left[\frac{N_{\mathrm{B}}|\tau|}{T_{\mathrm{c}}} \right]. \qquad (2.23)$$

The values for the k-th peak of a normalized autocorrelation function at τ_k with the corresponding magnitude a_k is given as follows (for $\tau \geq 0$)

$$(\tau_k, a_k) = \left(k\frac{T_{\mathrm{c}}}{N_{\mathrm{B}}}, (-1)^k \left(1 - \frac{k}{N_{\mathrm{B}}} \right) \right). \qquad (2.24)$$

The ACF is linear over each sub-interval between the given peaks, where $k = 0$ defines the main peak. Due to the symmetry of the ACF the number of peaks for a sine-phased $\mathrm{BOC_s}$ is $2N_{\mathrm{B}} - 1$. The ACF of the $\mathrm{BOC_s}(1,1)$ displayed in Fig. 2.4 (left) as a solid line contains three peaks, the main peak ($k = 0$) equal to 1, and two peaks ($k = 1$) with a magnitude

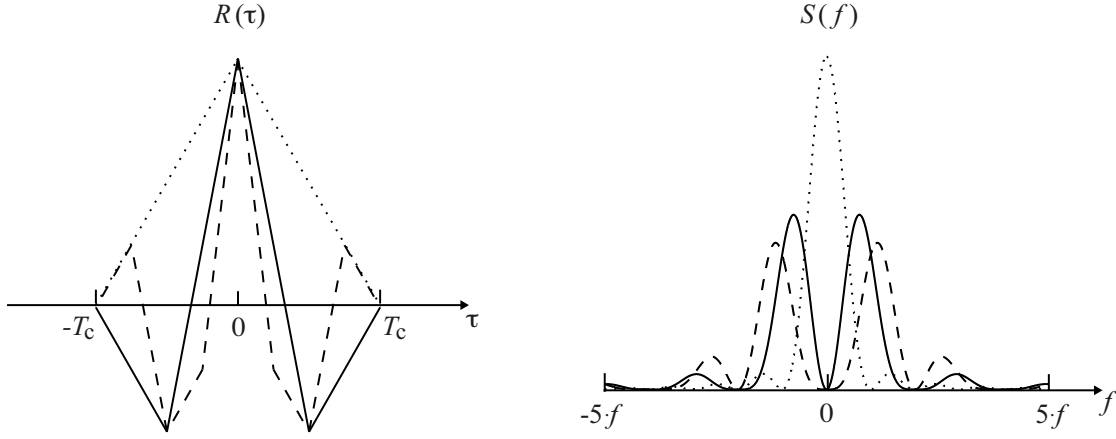**Figure 2.4:** The autocorrelation functions $R(\tau)$ for $BOC_s(1,1)$ (solid) and $BOC_c(1,1)$ (dashed) signals are visible on the left. In contrary to the BPSK(1) (dotted) the BOC ACF have several side peaks which make the correlation process in the receiver more complex. However, the sharper main peak compared to the BSPK(1) signal with the same spreading code chip length T_c promises a better multipath mitigation. The power spectral density $S(f)$ (right) shows the split main lobes for the two $BOC_s(1,1)$ (solid) and $BOC_c(1,1)$ (dashed) signals compared to the BPSK(1) modulation (dotted).

of -0.5 at $\pm T_c/2$. The ACF of the cosine-phased BOC_c is more complex with additional sub-side peaks visible in Fig. 2.4 (left) as dashed line for $k = 1$ at $\tau = \pm\frac{T_c}{4}$ in case of a $BOC_c(1,1)$ computed with the followed formula by *Sousa and Nunes* (2013)

$$R_c(\tau) = \begin{cases} (-1)^{\frac{k}{2}} \left(\frac{2kN_B + 2N_B - k^2}{2N_B} + (-2N_B + k - 1)\frac{|\tau|}{T_c} \right), & k = 0, 2, \ldots, 2N_B - 2 \\ (-1)^{\frac{k+1}{2}} \left(\frac{k^2 + 2k - 2kN_B + 1}{2N_B} + (2N_B - k - 2)\frac{|\tau|}{T_c} \right), & k = 1, 3, \ldots, 2N_B - 1. \end{cases} \tag{2.25}$$

A high order allows a large spectral separation of the two mainlobes of the PSD (e. g. Galileo PRS E1-A as $BOC_c(15, 2.5)$) and produces a huge number of side peaks in the autocorrelation function. Each additional peak poses a risk of false lock. However, the sharper main peak compared to the ACF of BPSK-modulated signals with the same spreading code frequency promises higher code tracking accuracy and better multipath mitigation while reducing the power of the side peaks during demodulation with different techniques, e. g. *Hung et al.* (2014).

2.1.3 Bandlimited Signal and Noise Representation

The PSD $S(f)$ of BPSK-modulated signals is given in Eqs. (2.10) and for the basic BOC signals in Eqs. (2.20) and (2.21). Dependent on the modulation type and chipping frequencies expressed by the parameters n and m (see Eq. (2.19)) a certain amount of power P_s is differently spread over the spectrum (see the comparison of PSDs in Fig. 2.4 as an example for BPSK(1), $BOC_s(1,1)$ and $BOC_c(1,1)$ signals). The power P_s within a two-sided bandwidth of $2B$ is given by

$$P_s = \int_{-B}^{B} S(f)\, df. \tag{2.26}$$

Considering a modulated passband signal $s(t)$ (positive and negative frequencies) with amplitude A according to Eq. (2.5) and its corresponding PSD and substituting Eq. (2.10) into Eq. (2.15), the total power within an infinite bandwidth $B = \infty$ is

$$P_{\mathrm{s}} = \int_{-\infty}^{\infty} S_{\mathrm{s}}(f) \,\mathrm{d}f = \int_{-\infty}^{\infty} \frac{A^2}{2} T_{\mathrm{c}} \mathrm{sinc}^2(fT_{\mathrm{c}}) \,\mathrm{d}f = 2 \frac{A^2}{2} \int_{0}^{\infty} T_{\mathrm{c}} \frac{\sin^2(\pi f T_{\mathrm{c}})}{(\pi f T_{\mathrm{c}})^2} \,\mathrm{d}f \qquad (2.27)$$

due to the even function. By partially integrating and substituting $a = \pi T_{\mathrm{c}}$ we get:

$$\begin{aligned} P_{\mathrm{s}} &= A^2 T_{\mathrm{c}} \left(\frac{-\sin(af)}{a^2 f} \right) \Big|_{0}^{\infty} + A^2 T_{\mathrm{c}} \int_{0}^{\infty} \frac{\sin(2af)}{af} \,\mathrm{d}f \\ &= \underbrace{\lim_{f \to 0} \frac{-A^2 T_{\mathrm{c}} \sin(af)}{a^2 f}}_{= 0} + \underbrace{\lim_{f \to \infty} \frac{A^2 T_{\mathrm{c}} \sin(af)}{a^2 f}}_{= 0} + A^2 T_{\mathrm{c}} \int_{0}^{\infty} \frac{\sin(2af)}{af} \,\mathrm{d}f. \end{aligned} \qquad (2.28)$$

The integral on the right side has no elementary antiderivative. For solving this integral the Laplace transform of the sine with $t = 2a$ is used:

$$\begin{aligned} P_{\mathrm{s}} &= \frac{A^2 T_{\mathrm{c}}}{a} \mathcal{L} \left\{ \int_{0}^{\infty} \frac{1}{f} \sin(tf) \,\mathrm{d}f \right\} = \frac{A^2 T_{\mathrm{c}}}{a} \int_{0}^{\infty} \frac{1}{f} \frac{f}{s^2 + f^2} \,\mathrm{d}f \\ &= \frac{A^2 T_{\mathrm{c}}}{a} \left(\frac{1}{s} \arctan \left(\frac{f}{s} \right) \right) \Big|_{0}^{\infty} \\ &= \frac{A^2 T_{\mathrm{c}}}{a} \left(\frac{1}{s} \frac{\pi}{2} \right). \end{aligned} \qquad (2.29)$$

With the inverse Laplace transform $\mathcal{L}^{-1} \left\{ \frac{1}{s} \right\} = 1$ and resubstitution of $a = \pi T_{\mathrm{c}}$ the final result is

$$P_{\mathrm{s}} = \frac{A^2 T_{\mathrm{c}}}{\pi T_{\mathrm{c}}} \frac{\pi}{2} = \frac{A^2}{2}. \qquad (2.30)$$

The power of $A^2/2$ is equal to the averaged power of a sine wave ($A = \sqrt{2P_{\mathrm{s}}}$) due to the normalized PSD $S_{\mathrm{c}}(f)$ in Eq. (2.10) for an unlimited baseband BSPK signal. However, the suppression of out-of-band interferences requires bandpass filters in the receiver. They produce so-called bandlimited signals with an output of a specific bandwidth. The amount of received power is therefore dependent on the modulation type and the chosen bandwidth. There are different definitions for the term bandwidth, see (*Couch II*, 2013). Several types of bandwidths are shortly introduced and illustrated in Fig. 2.5.

|	
Absolute bandwidth	$f_2 - f_1$: The spectrum is zero outside the frequency band $f_1 < f < f_2$
Null-to-null bandwidth	Two-sided bandwidth: $2W = f_2 - f_1$. The spectrum is zero outside the frequency band $f_1 < f < f_2$ where f_2 is the first null of the baseband envelope above f_0 (max. magnitude), and f_1 is the first null below f_0. This bandwidth is also called zero-crossing bandwidth (for BPSK signals: $2W = 2/T_{\mathrm{c}}$).
3-dB bandwidth	Two-sided bandwidth: $2W_{\mathrm{3dB}} = f_2 - f_1$. The power inside the frequency band $f_1 < f < f_2$ is not attenuated by more than 3 dB with respect to the maximum value (for BPSK signals: $2W_{\mathrm{3dB}} = 0.88/T_{\mathrm{c}}$).
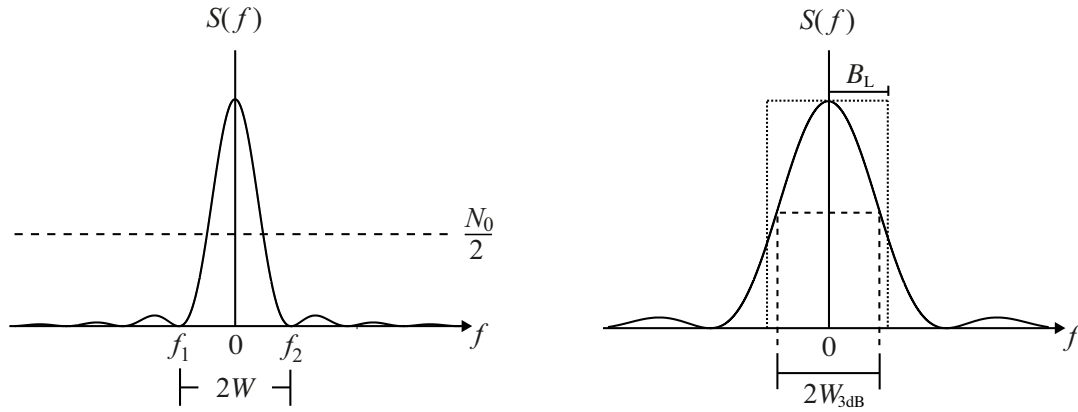
Figure 2.5: Left: PSDs of baseband BPSK signal (solid) and of white noise with a constant value of $N_0/2$ (dashed line). The two-sided bandwidth $2W$ represents the null-to-null bandwidth with $\pm W = \pm 1/T_c$ equal to twice the chipping rate of the spreading code $c(t)$. On the right the two-sided 3-dB bandwidth $2W_{\text{3dB}}$ (dashed) which includes the frequency range, where the power is not attenuated by more than half with respect to the maximum value. The single-sided equivalent noise bandwidth B_L (dotted) includes half the power of the positive spectrum, for a BPSK signal $0.5/T_c$.

Equivalent noise bandwidth	One-sided bandwidth B_L. A fictional rectangular band includes power that is equal to the power within the positive spectrum, see Sec. 4.1.3 for the mathematical definition (for BPSK signals: $B_L = 0.5/\text{T}_c$).
Bounded spectrum bandwidth	$f_2 - f_1$: Outside the frequency band $f_1 < f < f_2$, the PSD has to be below a certain amount (e. g. 40 dB, for out-of-band interference filters of antennas).

The power of a BPSK signal within the main lobe (null-to-null bandwidth of $2/T_c$) is $0.9\,P_s$. This means that a BPSK(1)-modulated signal (remember BPSK(f_c/f_r) contains about 90% of its power within $2f_r$ and a BSPK(10) modulation within $20f_r$, see Fig. 2.6 for BPSK(1) (dotted) and BPSK(10) (dash-dotted). Due to the higher side lobes, the BOC_s (solid) contains 86% and the BOC_c (dashed) 74% of their power within their split main lobes of $4f_r$. High-frequency modulations with widely separated mainlobes like the $\text{BOC}_s(10,5)$ signal (see diamonds in Fig. 2.6) require a much wider bandwidth to ensure a sufficient power receipt. Additionally, a narrow bandwidth attenuates the peaks of the autocorrelation function and finally the tracking accuracy (bandlimited effects). In order to acquire 83% of the total power of a $\text{BOC}_s(10,5)$ the bandwidth has to be expanded to $30f_r$. Therefore the bandwidth that specifies the amount of received power at the receiver is enlarged for the new satellite generations with their modern signals. Additionally, if the received power is specified within a bandwidth of $30f_r$ (for GPS and Galileo f_r is equal to 1.023 MHz), the $\text{BOC}_s(10,5)$ signal has a 90% power bandwidth of $23.6f_r$.

Based on Eq. (2.26) it could be shown that the averaged power can directly be derived by integrating the PSD over all frequencies. There are special cases of PSDs, where the value
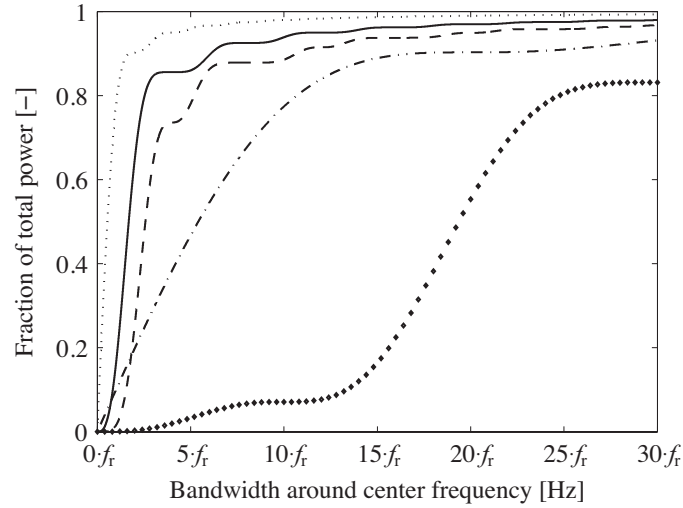
Figure 2.6: The power distributions of different modulation types are compared dependent on the two-sided bandwidth. The bandwidth is represented as multiples of a reference frequency f_r. The BPSK(1) (dotted) contains the most power within f_r, followed by $BOC_s(1,1)$ (solid), $BOC_c(1,1)$ (dashed), and BPSK(10) (dash-dotted). The $BOC_s(10,5)$ (diamonds) only contains 83% of its power within this bandwidth.

N_0 is constant over the whole frequency spectrum, e. g. white noise

$$S_n(f) = \begin{cases} \frac{N_0}{2} & f_0 - W \leq |f| \leq f_0 + W \\ 0 & \text{otherwise.} \end{cases} \tag{2.31}$$

The factor $1/2$ indicates that one half of the power is within the negative and the other half in the positive frequency spectrum. Noise plays an important role in communication systems. Several types of noise with different properties and from different sources have to be considered. For the case of signal transmission through a medium and the subsequent receipt, demodulation, and measurement extraction in a receiver, external and internal noise sources are roughly distinguished. The propagation through the external medium (external to the receiver system) is affected by many noise sources such as ionosphere, troposphere, background radiation, producing all types of noise (e. g. coloured noise, flicker noise, white noise). The internal system noise is mainly induced by random motions (thermal noise) and random arrivals (shot noise) of electrons in the receiver conductors (*Couch II*, 2013). Thermal noise is caused by thermal agitation within the electronic components while the random electron arrival at semi-conductors produces randomly fluctuating currents known as shot noise. The main amount of internal noise is induced by thermal noise, but in the following mathematical representation both noise types are combined in $n(t)$ because both are Gaussian distributed with zero mean, also known as Johnson-Nyquist noise (for the physical modeling see Sec. 3.1.3). The noise added to the received signal passes different bandpass filters with a two-sided bandwidth of $2W$ in the receiver simultaneously with the signal. The noise power P_n within the bandwidth $2W$ around the center frequency f_0 at filter output (with unity gain) is according to Eq. (2.26)

$$P_n = \int_{-W}^{W} S_n(f)\,df = \int_{-W}^{W} N_0\,df = 2N_0W. \tag{2.32}$$

Note the additional factor 2, in contrary to the representation in Eq. (2.31), caused by adding the positive and negative center frequencies (f_0 and $-f_0$). Finally, the passband representation of noise $n(t)$ is given by

$$n(t) = n_{\mathrm{I}}(t) \cos(2\pi f_0 t) + n_{\mathrm{Q}}(t) \sin(2\pi f_0 t) \tag{2.33}$$

where the noise is centered at the carrier frequency f_0 with the two baseband components $n_{\mathrm{I}}(t)$ and $n_{\mathrm{Q}}(t)$. The signal-to-noise ratio *SNR* plays an important role as a quality characteristic for communication processes. According to Eqs. (2.30) and (2.32) we get

$$SNR = \frac{P_{\mathrm{s}}}{P_{\mathrm{n}}} = \frac{A^2}{4N_0 W}. \tag{2.34}$$

The *SNR* at the receiver can be improved on the one hand by increasing the transmitted power or by reducing the bandwidth on the other hand. However, a too narrow bandwidth attenuates the signal itself dependent on the modulation type as discussed above.

Let us assume that the DSSS signal $s(t)$ is affected by white noise with a power spectral density N_0. The task of the receiver is to demodulate the noisy DSSS signal by correlating it with a synchronized replica signal generated in the receiver. The signal $s(t)$ is now dispread to the original narrow band signal $d(t)$. The spectral density of the noise is still N_0 because the convolution of a signal with a continuous spectral envelope with white noise is still white noise. This means that the spreading of a signal has no effect on the demodulated signal property in presence of thermal noise. In contrast, after the correlation a narrowband interference on the spread spectrum signal $s(t)$ has been spread and shows exactly the same spectral density as $s(t)$. Passing a bandpass filter that does not affect the signal $d(t)$, the power of the narrowband interference is decreased by a factor of f_c/f_d, the so-called processing gain. In addition to the obvious possibility to modulate a navigation signal, the DSSS is powerful in order to compress narrowband interferences.

2.1.4 Multiplexing and Multiple Access Techniques

Satellite navigation systems have to be capable of broadcasting several spread spectrum signals on the same carrier. Let us assume that two DSSS signals should be transmitted on the same carrier, e. g. two different random codes $c_1(t)$, $c_2(t)$ and two different data streams $D_1(t)$, $D_2(t)$. For this purpose the two DSSS signals according to Eq. (2.5) based on a BPSK modulation with two phase states are multiplexed with a relative phase rotation of 90 degrees. This expansion to four phase states is called quadrature phase shift keying (QPSK) and can be represented as follows:

$$s(t) = s_{\mathrm{I}}(t) \cos(2\pi f_0 t) + s_{\mathrm{Q}}(t) \sin(2\pi f_0 t) \tag{2.35}$$

with the signals $s_{\mathrm{I}}(t)$ and $s_{\mathrm{Q}}(t)$ according to Eq. (2.5):

$$s_{\mathrm{I}}(t) = \sqrt{2P_1}\, c_1(t) D_1(t) \tag{2.36}$$

$$s_{\mathrm{Q}}(t) = \sqrt{2P_2}\, c_2(t) D_2(t). \tag{2.37}$$

The two components are called in-phase I and quadra-phase Q on the corresponding cosine or sine RF carrier component. Even if the powers P_1 and P_2 are not identical, this multiplexing technique provides constant envelopes of the modulated carrier.

In addition to QPSK, time division multiplexing (TDM) is an often used technique, especially for the modern GNSS signals (e. g. L2C) in order to transmit two ranging codes (e. g. pilot and data) on the same carrier component. The concept is based on the interlacing of samples from several codes so that this information can serially be transmitted on the same channel. A detailed description of this technique can be found in *Couch II* (2013). Using BOC-modulated code sequences, the multiplexed signal is called TMBOC or CBOC (see GPS L1C or Galileo E1 OS).

AltBOC (alternative BOC) is a technique for multiplexing 4 code sequences on one carrier. It leads to a split spectrum around the center frequency and can be considered as a system consisting of two QPSK modulations (two independent sub-bands), for more details about the modulation and characteristics see *Shivaramaiah and Dempster* (2009). The Galileo E5 frequency band is modulated by an AltBOC(15,10) comprising two sub-band signals (E5a and E5b), each with a data and pilot code sequence, see Sec. 2.5.2. The PSD of the resulting non-constant envelope of an AltBOC signal is given by *Rebeyrol et al.* (2005) for odd N_{B} (e. g. Galileo E5)

$$S(f) = \frac{8}{T_{\mathrm{c}} \pi^2 f^2} \frac{\cos^2(\pi f T_{\mathrm{c}})}{\cos^2(\pi f \frac{T_{\mathrm{c}}}{N_{\mathrm{B}}})} \left(1 - \cos\left(\pi f \frac{T_{\mathrm{c}}}{N_{\mathrm{B}}} \right) \right). \tag{2.38}$$

The expression for a constant envelope is also derived and discussed in *Rebeyrol et al.* (2005) which is based on the product of two special subcarriers producing slightly different side lobe frequencies. However, the main lobes are almost identical. The PSD of the AltBOC(15,10) signal with a non-constant envelope is visible in Fig. 2.16.

One of the challenges for GNSS is to provide a multiple access capability. This means all satellites have to transmit several spread spectrum signals in the same frequency band while the receiver is simultaneously receiving those signals with minimal interferences. The code sequences should optimally have the autocorrelation properties equal to a random code (see Fig. 2.2) but with a defined code sequence for each satellite, so-called pseudorandom noise (PRN) modulations with no correlations between each other for all possible time offsets. Code sequences with rectangular chips can be generated by linear feedback shift registers with n bits of memory. The possible length N of the sequence is limited to $N = 2^n - 1$ due to the modulo-2 adders. A code with a repetition period of N is called maximum-length sequence. The restricted period NT_c, after which the code is repeated, has a direct impact on the autocorrelation properties (see Fig. 2.7). The correlation outside the correlation interval ($\tau > \pm T_c$) is $-1/N$ for a maximum-length pseudorandom code (with values of ± 1). The power spectral density $S(f)$ has a similar envelope as the random binary code in Fig. 2.2 but a discrete line spacing dependent on the sequence period and chip length ($1/(NT_c)$). The weighting of the spectral lines is given by the ACF of a periodic waveform expressed as Fourier series

$$S_{\mathrm{PRN}}(f) = \sum_{i=-\infty}^{\infty} r_i \, \delta(f - i f_{\mathrm{c}}) \tag{2.39}$$

with its coefficients r_i (see *Couch II* (2013))

$$r_i = \begin{cases} \frac{1}{N^2} & i = 0 \\[2ex] \left(\frac{N+1}{N^2} \right) \operatorname{sinc}^2 \left(\frac{i}{N} \right) & i \neq 0. \end{cases} \tag{2.40}$$
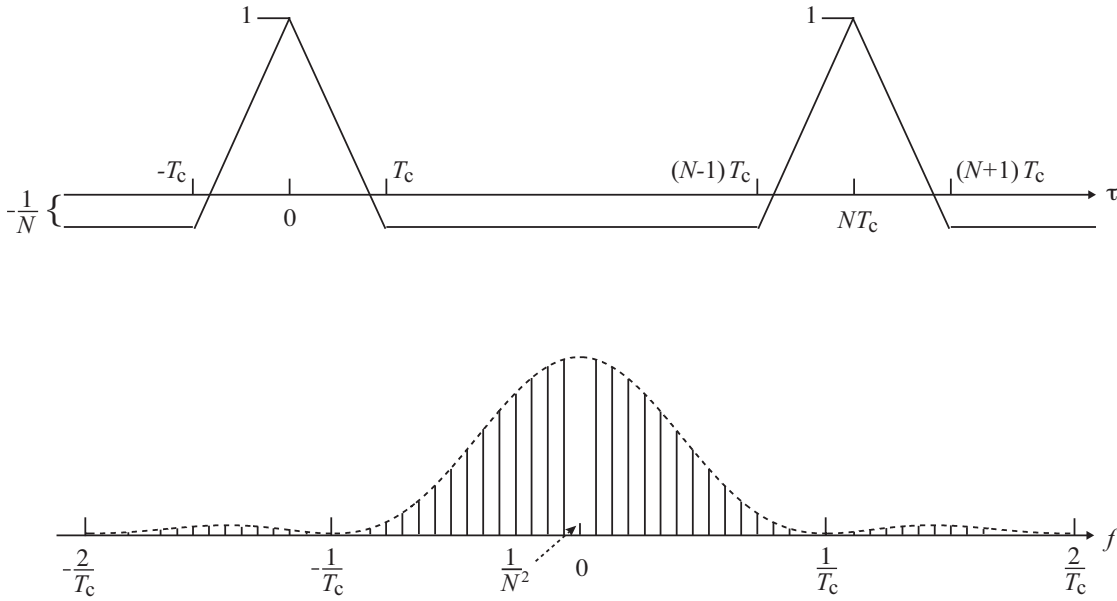
Figure 2.7: The autocorrelation function of a maximum-length PRN sequence with values ± 1 (top) and the corresponding PSD as a line spectrum with a spacing of $1/(NT_c)$ (bottom). The dashed line indicates the envelope or weighting of each spectral line.

The weighting of the spectral lines including the DC component ($i = 0$) of $1/N^2$ is shown in Fig. 2.7 (bottom) as a dashed line. A long period of the pseudorandom code implies a highly resolved envelope, but leads to a potentially longer acquisition time.

In addition to the described code division multiple access (CDMA), other methods of multiple access are possible, the so-called frequency and time division multiple access (FDMA and TDMA). The FDMA (see GLONASS in Sec. 2.4) has the advantage of completely uncorrelated code sequences due to the modulation on different frequency bands with a separation of the code bandwidth. The FDMA also has a higher robustness against narrowband interferences. A possible interference signal is affecting only one sub-band or the FDMA signal of one satellite compared to the CDMA technique, where the signals of all satellites are possibly disturbed. However, a larger bandwidth for a specific signal is required using FDMA, and the receiver needs to handle several frequency offsets that lead to extensive receiver front-end components.

2.2 Legacy GPS Signals

The chosen IEEE L-band (1–2 GHz) for GPS has the advantage of less space loss against the IEEE S-band (2–4 GHz) and C-band (4–8 GHz), and smaller ionospheric delay effects and an easier bandwidth allocation permission compared to the ultra high frequency (UHF) band (0.3–1 GHz). Both legacy GPS signals (*IS-GPS-200G*, 2012) that the satellites are transmitting, are multiples of a fundamental clock frequency $f_0 = 10.23$ MHz. For the primary signal L1 and the secondary signal L2, the following frequencies are generated by

the satellite oscillators

$$f_1 = 154 \times 10.23 \text{ MHz} = 1575.42 \text{ MHz} \tag{2.41}$$

$$f_2 = 120 \times 10.23 \text{ MHz} = 1227.60 \text{ MHz}. \tag{2.42}$$

The satellite oscillator fundamental frequency is slightly lower than the nominal frequency of 10.23 MHz which is observed by the receiver. In order to partially compensate the relativistic frequency shifts $\Delta f / f_0$ of about -4.46×10^{-10} the satellite oscillator frequency is 4.57 mHz below the fundamental frequency of 10.23 MHz. The ratio of the two frequency links is about 1.3 in order to allow the measurement of the ionospheric delay corrections.

2.2.1 Signal Structure

The L1 carrier is modulated by the data signal $D(t)$ and a long precision code $P(t)$ on the I (in-phase) component as a BPSK(10) modulation and by an additional BPSK(1) spread spectrum signal called coarse/acquisition (C/A) code $CA(t)$ with the same data signal D(t) on the 90 deg rotated quadra-phase component Q as described in Eq. (2.35)

$$s_1(t) = \sqrt{2P_\text{P}} P(t) D(t) \cos(2\pi f_1 t) + \sqrt{2P_\text{CA}} CA(t) D(t) \sin(2\pi f_1 t) \tag{2.43}$$

with the P and C/A-code signal power P_P and P_CA. The second carrier L2 with the frequency f_2 is only modulated by the P-code and the data signal

$$s_2(t) = \sqrt{2P_\text{P}} P(t) D(t) \cos(2\pi f_2 t). \tag{2.44}$$

The control segment has the possibility to replace the P-code by the C/A-code on L2. Additionally, the data signal could be deactivated if the P-code is modulated on the L2 carrier. However, during normal operations the L2 carrier is modulated in the form given by Eq. (2.44) with the P-code and the data signal.

The C/A-code for civilian users is a pseudorandom code with a chip rate of 1.023 Mbps (1/10 of the clock frequency f_0) and a period of 1 ms. This short period has been chosen to enable a fast acquisition process. The 1023-chip code sequences $CA_i(t)$ for a satellite i with its chip length T_CA are generated as Gold Codes (*Gold*, 1967) and possess good CDMA properties with some limitations due to the short period. The code generation is based on two maximum-length Gold code sequences $G1$ and $G2$ generated by a 10 bit shift register each ($N = 2^{10} - 1$). The corresponding feedback taps at stages 3 and 10 for $G1$ and at stages 2,3,6,8,9, and 10 for $G2$ are expressed by the characteristic polynomials

$$\begin{aligned} G1(x) &= 1 + x^3 + x^{10} \\ G2(x) &= 1 + x^2 + x^3 + x^6 + x^8 + x^9 + x^{10} \end{aligned} \tag{2.45}$$

with an initial state of 1 for all registers. The final C/A-code is produced by a multiplication of both generated Gold code sequences $G1$ and $G2$

$$CA_i(t) = G1(t) \, G2(t + n_i T_\text{CA}). \tag{2.46}$$

The $G2$ Gold sequence has a specific chip delay n_i that is different for each satellite i. This enables the generation of 1023 different Gold codes of this length plus $G1$ and $G2$

themselves. The assignment of the corresponding number of delayed chips to the PRN signal number is listed in *IS-GPS-200G* (2012).

The P-code is also a binary pseudorandom code with a period of one week. Its chip rate (with chip length T_P) is identical to the fundamental clock rate of 10.23 Mbps and is produced by the multiplication of the $X1$ and $X2$ sequences with the same clock rate. The produced chip delay n_i between them directly corresponds to the PRN number

$$P_i(t) = X1(t)\, X2(t + n_i T_P) \quad 0 \leq n_i \leq 36. \tag{2.47}$$

Both code sequences $X1$ and $X2$ are again generated by a modulo-2 sum of two 12 bit shift register code sequences ($2^{12} - 1 = 4095$), short-cycled by omitting the last chips to 4092 ($X1A$ and $X2A$) and 4093 ($X1B$ and $X2B$) with the following tap positions

$$
\begin{aligned}
X1A &= 1 + x^6 + x^8 + x^{11} + x^{12} \\
X1B &= 1 + x^1 + x^2 + x^5 + x^8 + x^9 + x^{10} + x^{11} + x^{12} \\
X2A &= 1 + x^1 + x^3 + x^4 + x^5 + x^7 + x^8 + x^9 + x^{10} + x^{11} + x^{12} \\
X2B &= 1 + x^1 + x^3 + x^4 + x^8 + x^9 + x^{12}.
\end{aligned}
\tag{2.48}
$$

One $X1$ period is defined as 3750 $X1A$ cycles (15'345'000 chips) while the $X1B$ register (4093) is held in the final state at its 3749th cycle. After 3750 $X1A$ cycles, which exactly corresponds to 1.5 s, the $X1A$ and $X1B$ are reset to their initial states. $X2A$ and $X2B$ are generated exactly in the same way with the only difference that the re-initialization after 3750 $X2A$ cycles is delayed by 37 chips in order to produce the $X2$ sequence (15'345'037 chips) that is 37 chips longer than $X1$. The final 37 P-codes can be generated with a length of around 2.35×10^{14} chips which are not overlapping with each other. At the beginning of each week the counter is set to zero (Z-counter counts the number of $X1$ periods since the week started), although the codes are theoretically defined for more than 38 weeks. The period of one weak makes the acquisition process still extremely difficult.

Both code sequences $P(t)$ and $CA(t)$ are modulo-2 added to the data signal $D(t)$ which has a rate of 50 bps. The data signal is divided into 5 subframes each with a length of 6 s (detailed description see *IS-GPS-200G* (2012) and *Van Dierendonck et al.* (1980)). For each subframe a hand-over-word (HOW) is streamed and indicates the beginning of a subframe. There are exactly 4 $X1$ periods per data subframe, respectively 4 Z-counts per HOW. With the timing from the really short C/A-code, the subframe timing and the HOW word, the P-code can immediately be acquired. Although the P-code is originally designed as a precise code for military purposes, the code sequences are public in *IS-GPS-200G* (2012). In order to prevent the P-code from antispoofing (AS), an additional encrypted W-code is added and results in an antispoofing P(Y)-code, still with the same chipping rate as the original P-code. During the activation of the AS-mode the P-code is unknown for civilian users, but the AS-mode can theoretically be turned off by the control segment.

2.2.2 Signal Characteristics

The received power and cross-correlation properties of the transmitted signals are shortly discussed in this section. The total noise and power budget, also taking into account

Table 2.1: This table shows the specified minimum received power at a 3 dBi linearly polarized receiver antenna for the GPS legacy signals within a 20.46 MHz. These worst case signal strengths are dependent on the SV Blocks and are valid for elevation angles of 5 and 90 deg.

SV Block	L1 C/A	L1 P(Y)	L2 P(Y)
II/IIA/IIR	-158.5 dBW	-161.5 dBW	-164.5 dBW
IIR-M/IIF	-158.5 dBW	-161.5 dBW	-161.5 dBW
III	-158.5 dBW	-161.5 dBW	-161.5 dBW

the effects induced by tracking and filtering techniques in the receiver, are described in Chapter 5.

The minimum received signal power is defined in *IS-GPS-200G* (2012) for a 3 dBi linearly polarized receiving antenna output allocated in a bandwidth of 20.46 MHz (see Tab. 2.1). The input power of the satellite antennas is chosen to compensate different maximum power losses (for Block IIR, IIR-M, and IIF satellites)

- decreased satellite antenna gain from Edge-of-Earth to nadir: 2 dB

- correlation loss: 0.6 dB

- polarization loss: 1.8 dB (L1) and 2.2 dB (L2)

- atmospheric loss: 0.5 dB

- free space propagation loss: 184.4 dB (L1) and 182.3 dB (L2)

in order to maintain the signal strengths for a worst case scenario at an elevation angle of 5 and 90 deg with a maximum power at a 40 deg user elevation angle. Dependent on the elevation angle, satellite Block, and better conditions than expected for the factors mentioned above, the received signal power is up to 5 dB higher than specified. The noise of the transmitted unmodulated carrier should have a level that allows carrier tracking with a one-sided noise bandwidth of 10 Hz with an accuracy of 0.1 rad.

The normalized power spectral densities according to Eq. (2.10) of the signal structures of L1 and L2 described by Eqs. (2.43) and (2.44) are visible in Figs. 2.8 and 2.9. Note that the maximum value of the spectral density of the C/A-code (right Fig. 2.8) is 10 dB higher than for the P-code (left Fig. 2.8) due to the 10 times lower chipping rate. Additionally, for SV Blocks IIR-M and newer the received P(Y) power is 3 dB lower than for the C/A component ($2P_\mathrm{P} = P_\mathrm{CA}$). Therefore, for a non-normalized PSD the maximum value of the C/A-code would be 13 dB higher compared to the P(Y)-code PSD. For a better visualization the PSDs are plotted over a wider bandwidth than specified.

As described in Sec. 2.1 the autocorrelation and cross-correlation properties are fundamental for a reliable CDMA as well as for an accurate code and carrier tracking. The theoretical and optimal correlation characteristics for maximum-length PRN codes are visible in Fig. 2.7. The P-code with its long period of one week and high chipping rate of 10.23 MHz can be treated as ideal and comparable to the autocorrelation and line spectrum in Fig. 2.7. The C/A-code generated by two 1023 chip Gold codes with a period of 1 ms has significantly different properties. Instead of an almost continuous power spectrum as for the P-code, the spectral lines of the C/A sequence are spaced by 1 kHz and are varying in
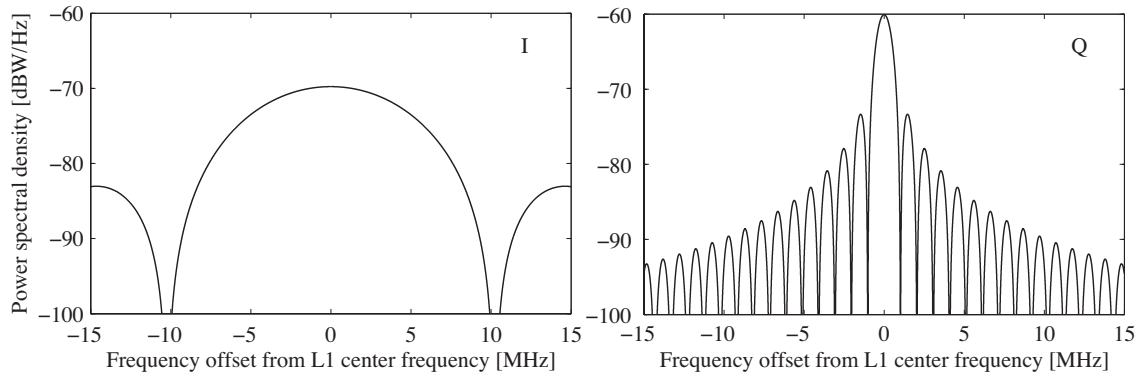
Figure 2.8: Normalized power spectral densities for the legacy signals on L1. On the I channel (left) the P(Y)-code as BPSK(10) and on the Q channel (right) the C/A-code as a BPSK(1) modulation. The PSDs are normalized to unit power over the bandwidth of 30.69 MHz.
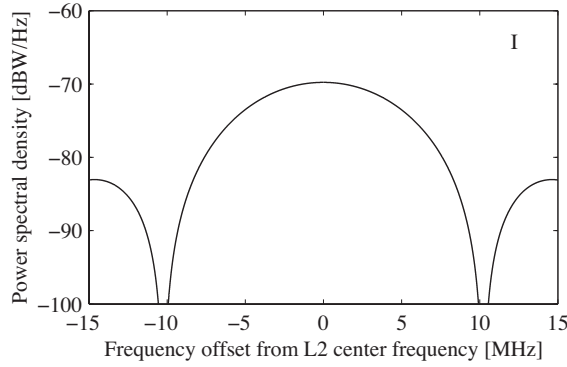
Figure 2.9: Normalized power spectral density for the legacy signal on L2. In normal mode L2 only consists of the P(Y)-code on the I component as a BPSK(10) modulation. The PSD is normalized to unit power over the bandwidth of 30.69 MHz.

power relative to the theoretical $\text{sinc}^2(x)$ envelope. Each C/A-code has some strong lines, making it more difficult to separate them from continuous wave (CW) interferences. The cross-correlation properties are affected by Doppler and time offsets because the Doppler is different for each satellite and can differ by up to ±6 kHz. The corresponding effect in the autocorrelation function is visible as fluctuations between the correlation intervals. The theoretical power of a 1023 chip maximum-length PRN sequence outside the correlation interval is −30.1 dB lower than the maximum signal power. Dependent on the time offsets between the codes and the Doppler frequency shift the cross-correlation level for a worst case scenario is only −21.1 dB below the total power (*Spilker*, 1996). An additional negative impact on the C/A-code properties is given by the integration and dump time T (see Sec. 3.2.2) in the receiver baseband functions which is usually close to the period of the C/A-code (1–20 ms).

2.3 GPS Signal Modernization

Since the first GPS Block I satellite launches between 1978 and 1985 for concept validation, upgraded satellite types Block II/IIA and IIR with general system enhancements (onboard momentum control, higher power and programmable capacity), and advanced frequency standards with more stable atomic clocks were developed and sent into orbit. Until 2004 and the last launch of a IIR satellite, only the legacy GPS signals described in Sec. 2.2 were broadcasted. In 2000 it was planned to provide new services to the growing number of worldwide GPS users. For this purpose the development of a new satellite generation IIF was planned. For the transition period (2005–2009), unlaunched but already produced Block IIR satellites were modernized (IIR-M) with some moderate hardware improvements in order to transmit a new civil signal L2C on L2 and a new military M-code on L1 and L2.

2.3.1 L2C and M-Code

The new civil signal on L2 has an overall chip-rate of 1.023 MHz and therefore a power spectrum similar to the C/A-code. In contrast to the C/A-code sequence, the L2C consists of two different codes per satellite generated at a rate of 0.5115 MHz each, the civil moderate (CM) code with a repetition period of 10'230 chips, and the civil long (CL) code with a length of 767'250 chips. The first CM-code and CL-code chips are synchronized with the X1 epoch (see P-code generation) and start with the start of week epoch. The two codes are generated by a 27-stage feedback shift register that theoretically allows a code length of 134'217'727 chips. However, both codes are short cycled to the given length of 10'230 and 767'250 chips (initial states given in *IS-GPS-200G* (2012)). The short CM-code reduces the acquisition time while the longer CL sequence improves the correlation properties. Both codes are chip-by-chip time division multiplexed (TDM) that leads to an overall rate of 1.023 MHz. The main reason of this 10 times lower chipping-rate compared to the new C5-code on L5 is the spectral separation to the military codes (see Fig. 2.10). For Block IIR-M and IIF satellites 37 CM/CL-code pairs are defined in (*IS-GPS-200G*, 2012) and assigned to the corresponding PRN numbers, expanded to additional 26 code pairs for Block III satellites in the future. The CM-code is additionally modulated by a 25 bps navigation message which makes the data demodulation process more reliable under poor conditions compared to the 50 bps data sequence on the legacy signals (bit transition). Due to the Forward Error Correction (FEC) encoding by using a rate 1/2 convolutional encoder, the resulting symbol-rate is 50 sps and is modulo-2 added to the CM-code sequence.

The additional dataless CL signal has the great advantage of better tracking capabilities (gain benefit of 6 dB, see Sec. 3.2.3, but a 3 dB loss due to the 50% power sharing with CM) and is common for the new and future DSSS signals. Due to the much longer repetition period of the CM sequences (20 ms, equal to the data chip length on the P-code) and CL (1.5 s, equal to the Z-count) compared to the 1 ms C/A-code, the maximum spectral lines are much lower than the lines in the C/A power spectrum (described in Sec. 2.2.2). Therefore, the robustness against narrowband interferences and multipath is substantially improved.

The new military signal, called M-code, is designed as a $BOC_s(10,5)$ signal on L1 and

Figure 2.10: Normalized power spectral densities for the signals on L2 since Block IIR-M. On the I channel (left) the legacy P(Y)-code as a BPSK(10) modulation, and on the Q channel (right) the L2C-code as a BPSK(1) modulation (solid) and the M-code (dashed) as a $BOC_s(10,5)$ modulation. The PSDs are normalized to unit power over the bandwidth of 30.69 MHz.

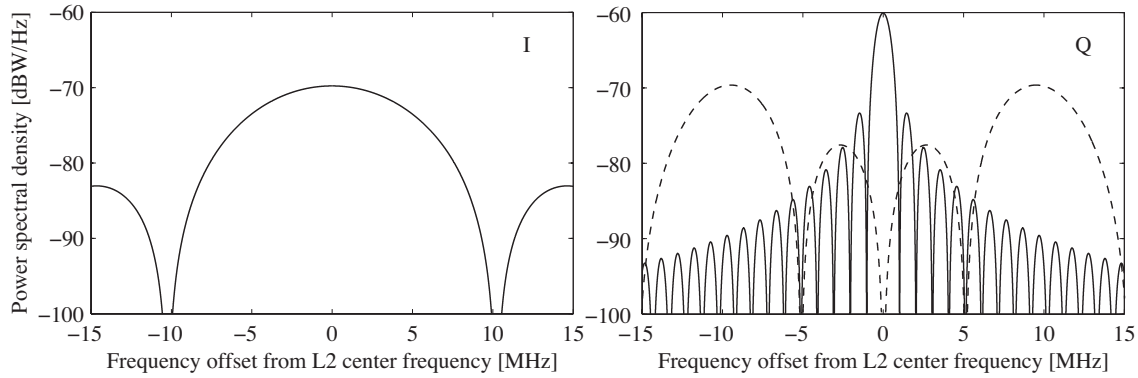L2 quadrature-phases. The BOC_s modulation is based on an encrypted BPSK spread code signal with a frequency of 5.115 MHz modulated on a subcarrier with a frequency of 10.23 MHz. The code sequence is not public in order to ensure high security and anti-jamming capability. Some limited information can be retrieved from *Barker et al.* (2006), a documentation of the M-code approved for public release. Another main requirement is the compatibility to the civil signals (see Figs. 2.10 and 2.12), due to the much higher transmitted power of the M-code component of -138 dBW (*Barker et al.*, 2006), and also with the already existing military P(Y)-code at baseband. The $BOC_s(10,5)$ modulation with main lobes separated by 20 MHz guarantees low interferences and provides a fast acquisition, and a robust data demodulation and tracking performance.

2.3.2 Carrier Frequency L5

With the first launch of a Block IIF SV in 2010 GPS finally covered the L5 band with the new center frequency f_5 of

$$f_5 = 115 \times 10.23 \text{ MHz} = 1176.45 \text{ MHz} \tag{2.49}$$

based on the same fundamental clock frequency of 10.23 MHz corrected by the relativistic shift Δf of -4.57 mHz and defined within a 24 MHz band. The carrier is modulated by two different BPSK code sequences both with a 10.23 MHz chipping-rate and a period of 1 ms which are multiplexed in phase quadrature (QPSK) according to Eq. (2.35), see Fig. 2.11. The code on the in-phase component (I5) is modulo-2 added with a 50 bps navigation message, which is rate 1/2 convolutional encoded, resulting in a 100 sps symbol rate (comparable to the navigation message on L2C). Additionally, a 10 bit synchronization code (Neuman-Hofman code) is modulated on I5 clocked with 1 kHz and starts with each 10 ms data symbol. The PRN codes on Q5 are dataless (pilot channel) and only added with a 20 bit Neuman-Hofman code also clocked at 1 kHz and synchronized with the 50 bps navigation message on I5.

Both PRN codes I5 and Q5 are modulo-2 sums of $XA(t)$ and $XBI_i(t)$ or $XBQ_i(t)$ sequences
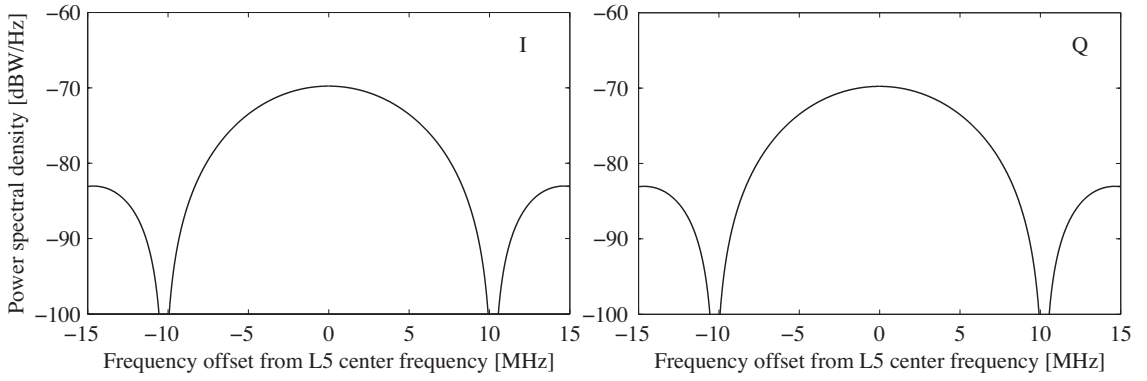
Figure 2.11: Normalized power spectral densities for the signals on L5. The C5-code is modulated as BSPK(10) on the I channel (left) and on the Q channel (right). The PSDs are normalized to unit power over the bandwidth of 30.69 MHz.

for a specific satellite i with the following polynomials referenced to the shift register input

$$
\begin{aligned}
XA &= 1 + x^9 + x^{10} + x^{12} + x^{13} \\
XBI \text{ or } XBQ &= 1 + x^1 + x^3 + x^4 + x^6 + x^7 + x^8 + x^{12} + x^{13}.
\end{aligned}
\tag{2.50}
$$

The $XA(t)$ sequence generated by a 13 bit shift register ($N = 8191$) has a length of 8190 chips, short cycled by one chip, and runs over by 2040 chips before re-initializing every 1 ms (10'230 chips). $XA(t)$ is synchronized with the C/A-code on L1. $XBI_i(t)$ and $XBQ_i(t)$ have a total length of 8191 chips and are not short cycled. The initial state of each $XBI_i(t)$ and $XBQ_i(t)$ depends on the PRN number and phase. They are re-initialized to their initial states after 1 ms (synchronized with $XA(t)$). The 128 assigned code phases and initial states for $XBI_i(t)$ and $XBQ_i(t)$ are listed in *IS-GPS-705B* (2012).

Block IIR-M and IIF antenna panel enhancements lead to higher transmitting power and finally to a higher receiving power at the user. The minimum specified received power for a 3 dBi linearly polarized antenna for the L2C signal is -160 dBW (Block IIR/IIF) and -158.5 dBW for the future Block III satellites. The L5 signal components have a minimum received power of -157.9 dBW for IIF and -157 dBW for the future Block III satellites (see Tab. 2.2).

2.3.3 L1C

The newest generation of Block III GPS satellites are designed for higher military and civil positioning, navigation, and timing performance. In addition to higher received power for the modern civil signals (L2C and L5) and the military M-code, a new civil signal L1C will be transmitted in order to improve autonomous navigation and interoperability with other GNSS signals (*Stansell et al.*, 2011). Similar to L2C and L5, the L1C characteristics base on a long spreading code of 10'230 chips, on a separated pilot and data channel, and on an overlaid code in order to improve correlation properties and to eliminate bit synchronization problems (comparable to Neuman-Hofman code on L5). Both, the pilot component $L1C_P$ and the data component $L1C_D$ consist of a 10 ms code length with a chip-rate of 1 MHz. They are not linear shift register sequences like all other GPS PRN
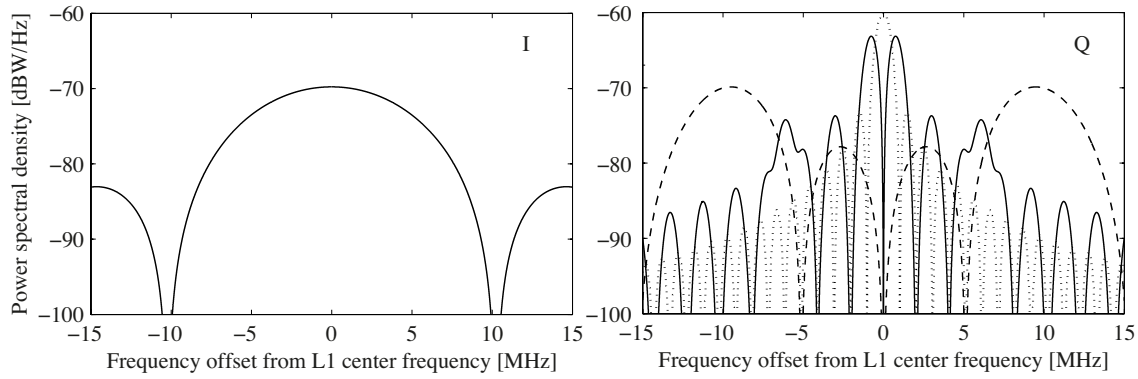
Figure 2.12: Normalized power spectral densities for the signals on L1 transmitted by the future Block III satellites. On the I channel (left) the legacy P-code BPSK(10) modulation, on the Q channel (right) the M-code (dashed) as a $BOC_s(10,5)$ modulation (since Block IIR-M) with L1C (solid) as a multiplexed $TMBOC_s(6, 1, 1/11)$. The legacy C/A-code (Q) is represented as dotted spectrum. The PSDs are normalized to unit power over the bandwidth of 30.69 MHz.

Table 2.2: This table shows the specified minimum received power at a 3 dBi linearly polarized receiver antenna for the GPS signal modernization. These worst case signal strengths are dependent on the SV Blocks and are valid for elevation angles of 5 and 90 deg.

SV Block	L2C	I5	Q5	L1C
IIR-M	-160.0 dBW	-	-	-
IIF	-160.0 dBW	-157.9 dBW	-157.9 dBW	-
III	-158.5 dBW	-157.0 dBW	-157.0 dBW	-157.0 dBW

codes, but derived from Weil sequences (*Rushanan*, 2006) with an expansion sequence identical for each PRN signal of seven bits. Additionally, a pilot overlaid code of 1800 bits unique to each satellite improves the correlation properties. The comparable overlay code of 20 ms on L5 (Neuman-Hofman) is shorter and identical for each satellite. All codes and the improved navigation messages for L1C are defined in *IS-GPS-800C* (2012).

The L1C code is additionally modulated by a synchronized 1.023 MHz square wave sine-phase. All bits of the data channel are modulated by the square carrier resulting in a $BOC_s(1, 1)$, while 4 bits of 33 of the pilot channel are being modulated by a 6.138 MHz square wave leading to a $BOC_s(6,1)$. The high-frequency $BOC_s(6,1)$ promises better tracking performance due to higher signal-to-noise ratio and advanced multipath mitigation (*Stansell et al.*, 2011). The L1C signal is multiplexed as a time-multiplexed BOC (TMBOC), where the $BOC_s(6,1)$ contains 1/11th of the power. The PSD of the L1C $TMBOC_s(6,1,1/11)$ is visible as the solid envelope in Fig. 2.12 (right). One important design aspect was a good spectral separation with low impact on the legacy GPS signals. Especially the separation to the M-code with its much higher signal power than the civil signals can be considered as key characteristics. Additionally, the higher power at high frequencies, especially at ± 6.138 MHz due to the additional 1/11th power of the $BOC_s(6,1)$ modulation, can be seen. The total power for L1C is shared by the pilot channel with 75% and the data channel with 25% of the specified minimum received power in Tab. 2.2.

2.4 Russian Global Navigation Satellite System (GLONASS)

Similar to GPS, in the mid-70s the Soviet military initiated a program for developing a global navigation satellite system for military purposes and requirements. During the design phase and preliminary tests it was decided to include civilian users by broadcasting open-access signals. After the first launch on October 12, 1982 and the following test constellation of four satellites, the gradual dissolution of the Soviet Union decelerated the further system development. Not till the Russians established a new test constellation at the beginning of the 90s, the system tests and deployment continued and reached its full operational constellation with 24 active satellites in February 1996. However, the short lifetime of the first generation GLONASS satellites and the incapability to restore the failed satellites in time led to a minimum number of about 7 active satellites in 2001 (*Feairheller and Clark*, 2006). The first start of a modified satellite type, called GLONASS-M on December 10, 2003 defined the start of rebuilding the whole system with an improved performance capability. In October 2011 the restore of the full operational constellation with 24 active GLONASS-M satellites was completed.

2.4.1 GLONASS Frequency Plan

The GLONASS-M satellites are broadcasting the ranging code sequence and navigation message on two different carrier frequencies in the L-band close to the GPS L1 and L2 bands. In contrast to GPS, the multiple access to the transmitted signals from different GLONASS satellites is based on the FDMA technique, see also Sec. 2.1.4. All simultaneously visible satellites transmit their signal on a specific frequency band separated to each other. This simplifies the generation of a sufficient number of code sequences with good cross-correlation properties because exactly the same code for all satellites can be modulated on the carrier. Additionally, the rejection of narrowband interferences is improved. Thus, if a narrowband interference degrades all the CDMA GPS signals, only the GLONASS satellite within this frequency band is affected. However, FDMA requires extended receiver front-ends in order to process the multiple frequency signals.

The nominal carrier frequencies for L1 and L2 are dependent on the frequency number K for each channel and are defined in *GLONASS ICD* (2008):

$$f_{1,K} = f_{01} + K\Delta f_1$$
$$f_{2,K} = f_{02} + K\Delta f_2$$

$$(2.51)$$

with

$$f_{01} = 1602 \text{ MHz} \quad \text{and} \quad \Delta f_1 = 0.5625 \text{ MHz}$$
$$f_{02} = 1246 \text{ MHz} \quad \text{and} \quad \Delta f_2 = 0.4375 \text{ MHz}.$$

$$(2.52)$$

In order to compensate the relativistic effects the nominal frequency of 5.11 MHz derived from a common onboard time/frequency standard is corrected by $\Delta f = -2.18$ mHz. The covered nominal frequencies for L1 are between 1598.0625 MHz (for $K = -7$) and 1605.375 MHz (for $K = 6$), each channel separated by Δf_1 of 0.5625 MHz. The L2 frequency with the given ratio of $f_{2,K} = \frac{7}{9}f_{1,K}$ covers the frequencies from 1242.9375 MHz (for $K = -7$) to 1248.625 MHz (for $K = 6$) with a channel separation of 0.4375 MHz.
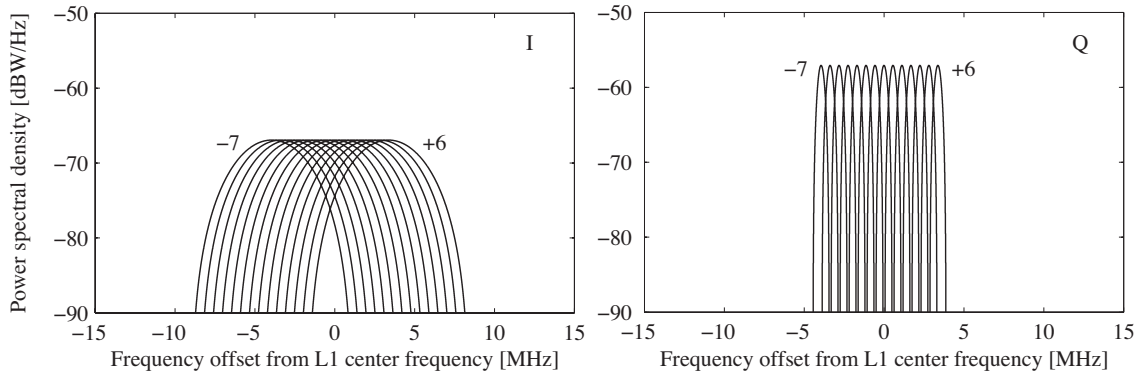
Figure 2.13: Normalized power spectral densities (only the mainlobes) for the GLONASS signals on L1. On the I channel (left) the 0.511 MHz BPSK modulated C/A-code and on the Q channel the P-code as a 5.11 MHz BPSK signal for all 14 sub-bands. The PSDs are normalized to unit power over the bandwidth of 30.69 MHz.

The allowed maximum inter-channel interference does not exceed -48 dB. Like GPS, the properties of the generated unmodulated carrier in the satellite guarantees a carrier phase tracking in the receiver with an accuracy not worse than 0.1 rad, while using a 10 Hz PLL one-sided equivalent noise bandwidth B_{L} (definition given in Sec. 2.1.3).

Originally, each of the 24 GLONASS satellites had a specific frequency number allocated from 0 to 24. After the modernization to GLONASS-M satellites only integer numbers between -7 and 6 are used in the way that the currently visible satellites at a specific site are uniquely identified by one of the 14 numbers. The channel numbers K are valid for L1 and L2. The actual active satellites and their associated frequency channel K can be found on the official website of the Russian Federal Space Agency (www.glonass-iac.ru).

2.4.2 GLONASS Signal Modulation

The standard accuracy pseudorandom-code C/A is designed as a BPSK modulation and is modulo-2 added on each L1 and L2 carrier sub-band (quadra-phase). The chipping-rate of 0.511 Mbps is about half of the GPS C/A-code with the same repetition period of 1 millisecond. The maximum length code-sequence is generated by a 9-stage shift register at the output of the 7th stage with the corresponding taps expressed by the polynomial

$$G(x) = 1 + x^5 + x^9. \tag{2.53}$$

The PSDs of the mainlobes for all 14 sub-bands are plotted in Figs. 2.13 and 2.14. The precise accuracy code P is modulated on the in-phase carrier component with a chipping-rate of 5.11 Mbps. The satellites transmit the BPSK modulation with a code duration of 1 s on both carriers. It is not encrypted like the GPS P(Y)-code. However, there is no detailed information about the code structure in the official interface control document (*GLONASS ICD*, 2008). The 50 bps navigation message is additionally modulo-2 added on the C/A- and P-codes for all L1 and L2 sub-bands.

The specified minimum L1 and L2 carrier component powers received for the current GLONASS-M satellites are listed in Tab. 2.3. The GLONASS L1 codes have a 2.5 dBW
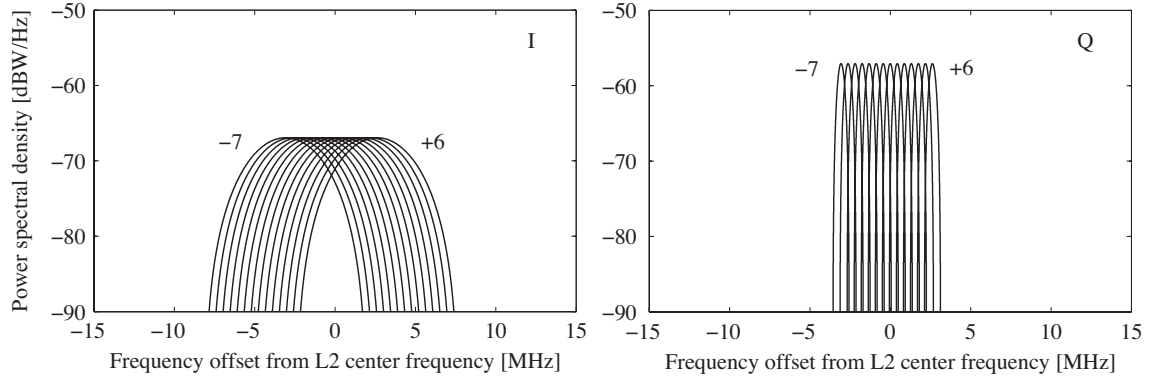
Figure 2.14: Normalized power spectral densities for the GLONASS signals on L2. On the I channel (left) the 0.511 MHz BPSK modulated C/A-code and on the Q channel the P-code as a 5.11 MHz BPSK signal for all 14 sub-bands.The PSDs are normalized to unit power over the bandwidth of 30.69 MHz.

Table 2.3: This table shows the specified minimum received power at a 3 dBi linearly polarized receiver antenna for the GLONASS signals (*GLONASS ICD*, 2008). These worst case signal strengths are dependent on the SV generation and are valid for elevation angles of 5 degrees. Nowadays (2015) only GLONASS-M satellites are active, the old GLONASS SV generation was put out of operation.

SV Type	L1	L2
GLONASS	-161.0 dBW	-167.0 dBW
GLONASS-M	-161.0 dBW	-167.0 dBW

lower power than the corresponding GPS C/A-code on L1. The GPS signals on L2 exceed the GLONASS L2 signal power by 5.5 dBW (P-code) and 7 dBW (L2C).

2.4.3 GLONASS Modernization

A new satellite generation with smaller mass and increased lifetime of 10 years compared to 7 years for GLONASS-M was developed to reduce the overall system costs. With the first launch of a new GLONASS-K1 satellite on February 25, 2011 and a second one on November 30, 2014 flight and payload tests have started. In addition to improved stability of the onboard atomic clocks, GLONASS-K1 and a modified version of GLONASS-M are able to transmit a new CDMA signal on L3 at the center frequency of 1201 MHz (*Mirgorodskaya*, 2013). The L3 band is located close to the GPS L5 and overlaps with the Galileo E5b band. Further SV generations like GLONASS-K2, and GLONASS-KM are designed for transmitting additional CDMA-based BPSK and BOC signals on L1, L2 and L3 in order to improve the tracking and range accuracy, robustness and interoperability with GPS and Galileo. However, the exact frequency plan and modulation schemes are not officially defined yet and different options exist.

2.5 Galileo

The European contribution to the already existing global navigation satellite systems
(e. g. GPS and GLONASS) is called Galileo and is currently in deployment phase while
reaching the fully operational constellation in some years. The European Commission re-
sponsible for legal and political issues and the European Space Agency (ESA) responsible
for the technology part defined the main objectives to be an open system, global, com-
patible with existing GNSS, under civil control, and service-oriented. Five services can be
distinguished (*OD SIS ICD Galileo*, 2010; *Hofmann-Wellenhof et al.*, 2008)

- **Open service (OS):** The OS signals are open to all global users. They are mainly
  designed for mass-market products and applications such as mobile phones and car
  navigation.

- **Commercial service (CS):** The controlled access CS signals support high-accuracy
  positioning, mainly for professional applications and base on encrypted data in the
  navigaton message.

- **Safety-of-life service (SOL):** The SOL service provides the same signal as OS
  with integrity information in the navigation message. SOL is especially intended for
  safety relevant applications and is compliant to aeronautical and maritime standards.

- **Public regulated service (PRS):** The PRS signals are extremely robust against
  intentional interference, jamming, and spoofing. The signals are encrypted and only
  accessible to European public authorities, especially for civil protection and national
  security.

- **Search and rescue service (SAR):** A service that is integrated into the inter-
  national COSPAS/SARSAT system, built for worldwide SAR operations. Galileo
  satellites will be able to detect emergency beacons and an additional return link
  modulated on the OS signals will confirm the ongoing rescue.

During the system development and test phase two Galileo in-orbit validation elements
(GIOVE) were launched on December 28, 2005 (GIOVE-A) and on April 26, 2008 (GIOVE-
B). The main goal was the validation of the developed payload and the allocation of the
different frequency bands. Especially the new atomic frequency standards, e. g. a passive
hydrogen maser carried by GIOVE-B should grant an extremely good short- and long-term
frequency stability and extended clock prediction validity. The deployment phase started
with the first launch of two satellites on October 21, 2011 (PRN E11 and E12) and was
followed by PRN E19 and E20 on October 12, 2012. These satellites build the system of
4 active satellites until mid 2014.

2.5.1 Galileo Frequency Bands

All the signals broadcasted by the Galileo satellites are allocated to three different frequency
bands, namely E1, E5 with two sub-bands (E5a and E5b), and E6. The upper L-band
frequency E1 is located exactly on the same center frequency as GPS L1 with a slightly
larger bandwidth (see Tab. 2.4). The center frequency of the sub-band E5a carrier is
aligned to the GPS L5 center frequency. The second sub-band E5b is allocated between
GPS L5 and L2, while overlaying the GLONASS L3 band. E6 with its center frequency

Table 2.4: This table shows the specified minimum received power at a 0 dBic circularly polarized receiver antenna for the Galileo signals with their specific center frequencies and reference bandwidths. These worst case signal strengths are valid for elevation angles larger than 10 deg.

Frequency Band	Carrier Frequency	Minimum Received Power	Reference Bandwidth
E1	1575.420 MHz	-157.0 dBW	24.552 MHz
E5a	1176.450 MHz	-155.0 dBW	20.460 MHz
E5b	1207.140 MHz	-155.0 dBW	20.460 MHz
E5	1191.795 MHz	-155.0 dBW	51.150 MHz
E6	1278.750 MHz	-155.0 dBW	40.920 MHz

of 1278.75 MHz is separated out from other GNSS signal bands. All satellites transmit on the same carrier frequencies due to the CDMA-based multiple access technique used.

The defined receiver reference bandwidths in Tab. 2.4 for E1, E5a and E5b are slightly smaller than those officially allocated for radionavigation satellite services (RNSS) at ITU. The specified minimum received power is valid for elevation angles of 10 deg and higher. Incoming signals at an elevation angle of 5 deg are typically 0.25 dB lower (*OD SIS ICD Galileo*, 2010). Similar to GPS and GLONASS the expected maximum received power does not exceed the specified minimum power by more than 3 dBW and the PSDs of the unmodulated carriers allow a carrier phase tracking with a one-sided equivalent noise bandwidth of 10 Hz with an accuracy of 0.04 rad.

2.5.2 Galileo Modulation Schemes

OS signals are available on E1, E5a, and E5b, while the E6 carrier only transmits one PRS signal for authorized users and encrypted CS signals. An additional PRS signal is modulated onto the E1 carrier (Q component). CS users have also access to all additional encrypted navigation messages on the OS signals. The OS E1 (I channel) and E5b provide integrity information for SOL services (see Tab. 2.5). Except for the PRS signals, all other signals are designed as a pair consisting of a data and pilot channel which are multiplexed onto the carrier with different techniques. Most PRN codes are built by a long primary sequence (higher robustness) and a short secondary sequence (shorter acquisition time). The PRN code sequences are defined in the *OD SIS ICD Galileo* (2010), except for the PRS signal on E1 and all E6 code sequences.

Three PRN codes are modulated onto the E1 carrier. The encrypted and controlled code sequence (E1-A) is transmitted on the quadra-phase component as a $BOC_c(15,2.5)$ modulation including an encrypted data stream. The E1 OS signal consists of E1-B (data) and E1-C (pilot) PRN codes with chip-rates of 1.023 MHz which are designed both, as a composite BOC with 10/11 of the power using a 1.023 MHz subcarrier and with 1/11 of the power using a 6.138 MHz subcarrier. The CBOC(6,1,1/11) modulated signals are chip-by-chip multiplexed onto the I channel with a power sharing of 50% referred to the value in Tab. 2.4. In contrast to the GPS L1C signal, where the high-frequency $BOC_s(6,1)$ is only added at four chips onto the pilot component with the amount of 1/11 relative power, both E1 components (E1-B and E1-C) and each PRN code chip are added by the additional
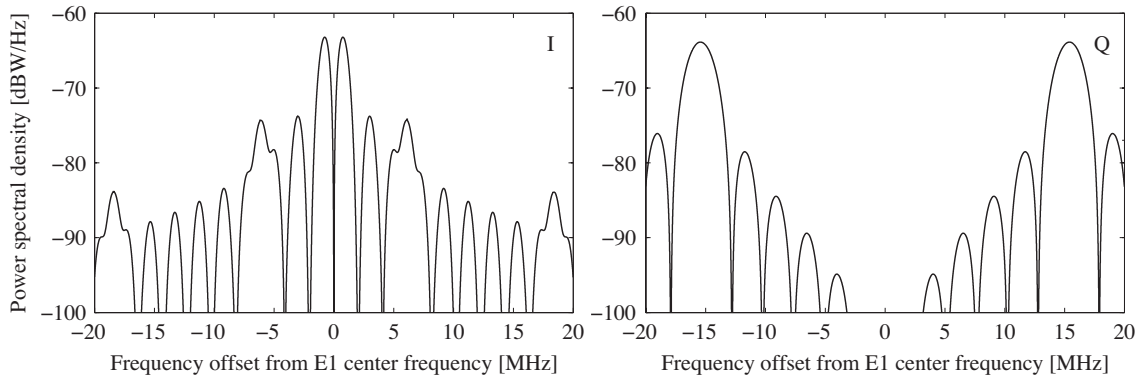
Figure 2.15: Normalized power spectral densities for the Galileo signals on E1. On the I channel (left) the open-access signal (E1 OS) which is multiplexed by E1-B and E1-C as a CBOC(6,1,1/11). The E1 PRS signal on the Q channel is based on a $BOC_c(15,2.5)$ modulation (right). The PSDs are normalized to unit power over the bandwidth of 40.92 MHz.

high-frequency subcarrier. Both primary codes have a length of 4092 chips, but only E1-C consists of a secondary code with a length of 25 chips. The primary codes are memory code sequences given as a hexadecimal representation in the Annex of *OD SIS ICD Galileo* (2010) with the assignment to the SV IDs and the corresponding fix secondary codes. The ranging codes generated by sequentially adding the primary and secondary codes lead to a repetition period of 4 ms for E1-B and 100 ms for E1-C. The navigation message I/NAV convolutional encoded with a symbol-rate of 250 sps is transmitted on E1-B. The I/NAV message type provides the OS, CS, and SOL services. The PSDs are represented in Fig. 2.15 with a larger bandwidth than defined in Tab. 2.4 for a better visualization.

The four signal components E5a-I (data), E5a-Q (pilot), E5b-I (data), and E5b-Q (pilot), each a PRN code sequence modulated as BPSK(10), are multiplexed on the I and Q carrier component as a non-constant envelope AltBOC(15,10) (Sec. 2.1.4). The wide spreading of the main lobes requires an extremely large bandwidth. Fig. 2.16 shows a 10 MHz wider bandwidth than officially defined in Tab. 2.4. However, both sub-band signals, E5a and E5b, can be demodulated independently and can approximately be considered as two BPSK(10) signals (per carrier component) shifted by -15 and $+15$ MHz with respect to the E5 center frequency. All E5 signals are unencrypted and accessible to all users (OS). Additionally, the data stream on E5b-I with a symbol-rate of 250 sps contains integrity information for the SOL service. The primary code length of all four PRN sequences is 10'230 chips. They are given as optimized memory code sequences assigned to the satellites in *OD SIS ICD Galileo* (2010) or can be generated with a linear feedback shift register. The short secondary codes of the pilot signals (E5a-Q and E5b-Q) have a length of 100 chips. For the data components secondary codes of 20 chips (E5a-I) and 4 chips for the SoL data are used. The resulting ranging code periods are 20 ms for E5a-I, 4 ms for E5b-I and 100 ms for the pilot components E5a-Q and E5b-Q. The data components provide two different navigation types. On E5a-I the F/NAV is added providing OS service, and the I/NAV on E5b-I (like E1-B) potentially providing OS, CS, and SOL services. They are convolutional encoded (FEC) on the corresponding code sequences with a resulting symbol rate of 50 sps (F/NAV) and 250 sps (I/NAV). For more details about the structure of the different navigation messages see *OD SIS ICD Galileo* (2010).
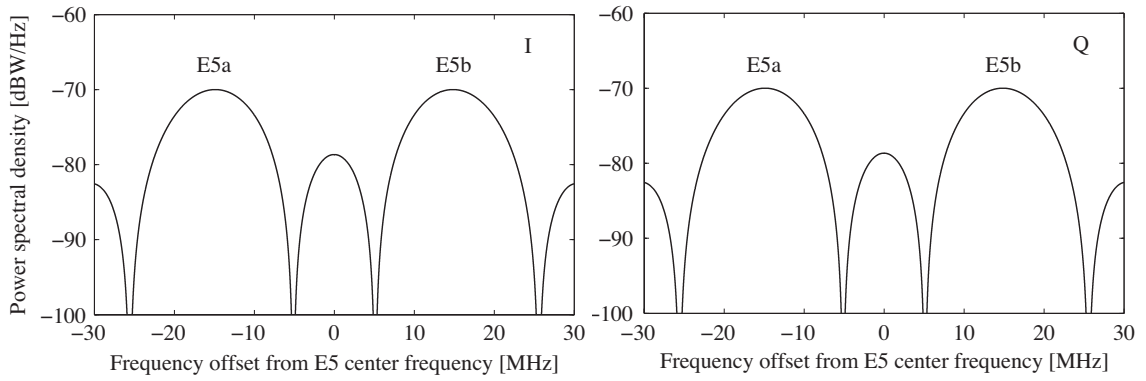
Figure 2.16: Normalized power spectral densities for the Galileo signals on E5. The four BPSK(10) PRN codes are multiplexed with an AltBOC(15,10) modulation onto the E5 carrier, the data signals onto the I channel and the pilot signals onto the Q channel. The PSDs are normalized to unit power over the bandwidth of 61.38 MHz.
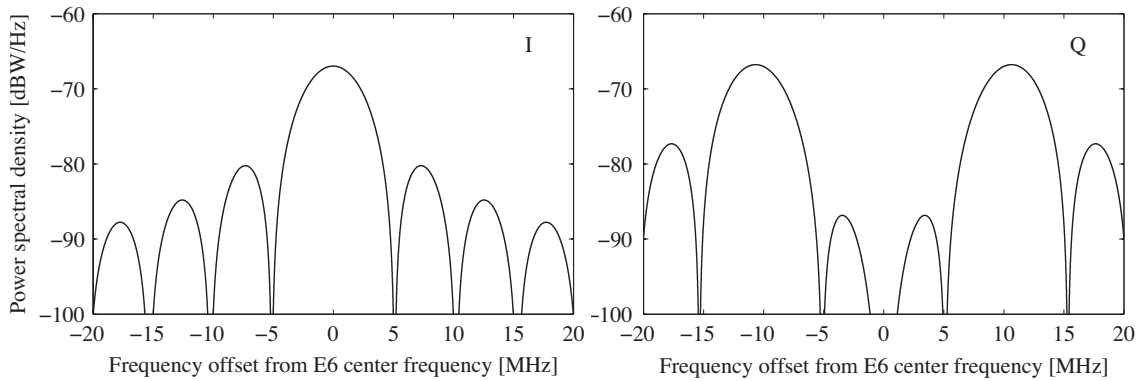
Figure 2.17: Normalized power spectral densities for the Galileo signals on E6. On the I channel (left) the signal E6 CS with a BPSK(5) modulation, which is TDM multiplexed by a pilot and data signal and on the right the E6 PRS signal with a $BOC_c(10,5)$ modulation. The PSDs are normalized to unit power over the bandwidth of 40.92 MHz.

The E6-A PRS code sequence is modulated as a cosine-phased $BOC_c(10,5)$ onto the E6 carrier. Both CS PRN codes E6-B (data) and E6-C (pilot) base on BPSK(5) and are multiplexed by TDM on the in-phase component of the carrier by a 50 % power sharing, see the E6 PSDs in Fig. 2.17. All the E6 PRN codes and navigation messages (C/NAV) are not published in *OD SIS ICD Galileo* (2010).

Table 2.5: This table gives an overview of all available Galileo PRN codes with their specific modulations.

Band	PRN Code	Service	Code Period	Modulation
E1	E1-A	PRS	not public	$BOC_c(15,2.5)$
	E1-B	OS/CS/SOL	4 ms	CBOC(6,1,1/11)
	E1-C	OS/CS/SOL	100 ms	CBOC(6,1,1/11)
E5	E5a-I	OS/CS	20 ms	BPSK(10)
	E5a-Q	OS/CS	100 ms	BPSK(10)
	E5b-I	OS/CS/SOL	4 ms	BPSK(10)
	E5b-Q	OS/CS/SOL	100 ms	BPSK(10)
E6	E6-A	PRS	not public	$BOC_c(10,5)$
	E6-B	CS	not public	BPSK(5)
	E6-C	CS	not public	BPSK(5)

3 GNSS Receiver Architecture

This chapter describes the most important hardware components and processing functions of a GNSS receiver summarized as a generic receiver diagram in Fig. 3.1. This receiver model, which is used for the introduction and explanation of the main components and functions, bases on *Van Dierendonck* (1996) and *Ward et al.* (2006).

The first part consists of the antenna, the oscillator, and the receiver front-end containing preamplification, filtering, and down-conversion to the intermediate frequency (IF), see Sec. 3.1. The antenna receives the RF GNSS signals which are filtered and amplified afterwards in order to reject out-of-band interferences. The oscillator provides the timing for the signal processing and the frequency to the frequency synthesizer that generates local oscillators (LOs). The LOs are used for the down-conversion of the RF signals to the IF and for the phase unwrapping and conversion to baseband during the signal processing. The IF processing is composed of the analog-to-digital conversion (ADC) and the automatic gain control (AGC). In addition to filtering out-of-band noise and interferences, the amplitude of the signal-plus-noise is increased to a workable level which is controlled by the AGC. The gained signal-plus-noise is split into different processing channels in order to process several satellites and signals simultaneously. This signal processing is the key function of a GNSS receiver which is mainly implemented in the receiver firmware. The main task of the signal processing is to extract the replica code phase and replica carrier Doppler phase measurements, forming the observables like pseudorange, integrated Doppler phase, and delta pseudorange to provide them to the navigation processor. In order to allow the extraction of these measurement types a lot of steps during the baseband processing are needed. The functions for a coherent tracking of the incoming signals are implemented in
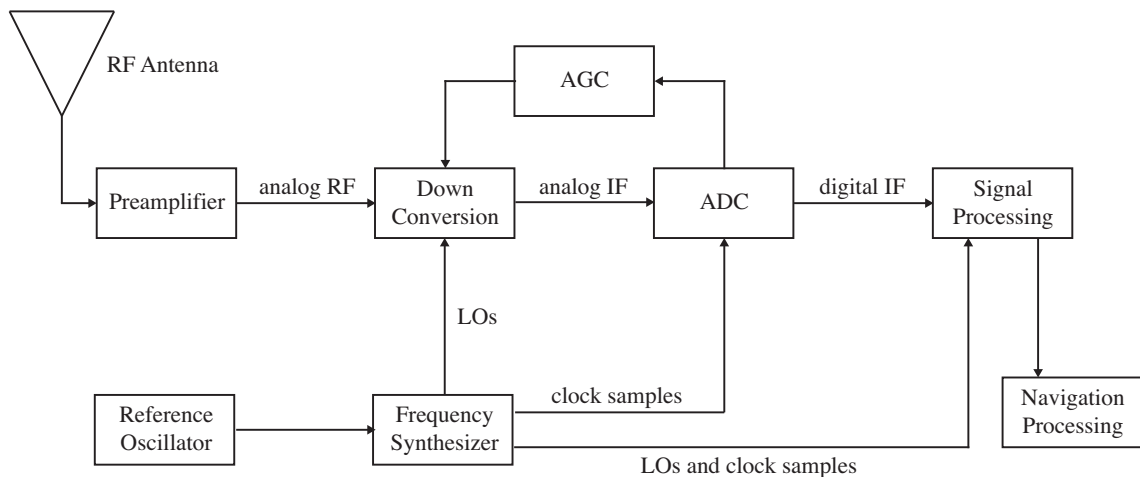

Figure 3.1: A generic receiver model with its main components and functions based on the introduction in *Van Dierendonck* (1996) and *Ward et al.* (2006).

closed tracking loops with their components described in Sec. 3.2 and their characteristics analyzed in Chapter 4. In addition to this baseband functions, the signal-to-noise ratio and the time relation to the system time (e.g. GPS time) are estimated.

3.1 Antenna and Receiver Front-end

3.1.1 Antenna

The field of antenna theory and development is extremely broad dependent on signal type and applications. For the general antenna theory we refer to *Kraus* (1988). This Section only introduces some critical aspects and parameters of common geodetic GNSS antennas based on the fundamental requirements discussed in Sec. 2. The main task of a receiving antenna is to convert the incoming RHCP electromagnetic RF wave into an electrical signal while requiring a uniform gain towards all satellites over a wide frequency band and suppressing potential multipath and out-of-band interferences. In addition to a low noise figure, the electrical phase center has to be stable and repeatable for highly accurate geodetic applications. Several requirements are contradictory and demand a compromise for the antenna design and parameters.

One important characteristic of an antenna is the gain (amplification of the incident signal) which is usually represented in dBiC, the ratio of the energy amplification compared to an isotropic circularly polarized antenna (or in dBi with respect to an isotropic linearly polarized antenna). In order to combine the requirements of a uniformly distributed gain pattern over all elevation angles and the multipath (and interference) rejection, the gain is breaking down below an elevation angle of about 20 deg because the multipath signal is dominating below this angle. The maximum gain of a GNSS antenna at the zenith is typically around 5 dBiC with a gain roll-off (from zenith to horizon) of more than 10 dB. Fig. 3.2 shows the gain pattern of a Javad GrAnt-G3T GNSS antenna that is typical for geodetic antennas. The suppression of reflected signals from ground, which are changing their polarization from RHCP to LHCP, is achieved by an extremely reduced LHCP gain pattern. The ability of multipath rejection can be expressed by the front-back ratio that describes the gain at a 90° elevation angle compared to the gain at the back ($-90°$ elevation), additionally influenced by the sensitivity to LHCP signals (*Hekmat et al.*, 1995). Typical values for a front-back ratio of GNSS antennas are in the order of 30 dB. The challenge for GNSS antennas is not only to guarantee a uniform gain distribution over the elevation and azimuth, but also over a wide frequency band. Nowadays, GNSS antennas have to receive a wide frequency spectrum in order to allow the measurements of all available satellite signals and frequencies (see Sec. 2.2 and 2.3). Different frequencies such as L1, L2, and L5 and the slightly different center frequencies in these bands of other satellite systems have to be covered, and, on the other hand, a wide bandwidth around these center frequencies has to be ensured due to the precorrelation and different power distribution, especially for the BOC signals (see Sec. 2.1). The final filtering of all the various signals preparing for the tracking process (see Sec. 3.2) is achieved at the next stage in the receiver front-end (Sec. 3.1.3). Therefore, the antennas are typically wideband, in contrast to stacked narrowband components, and cover the bands 1559–1610 MHz and 1164–1253 MHz (for E6 and B3 (Beidou) extended to 1300 MHz, e.g. Javad GrAnt-G3T).
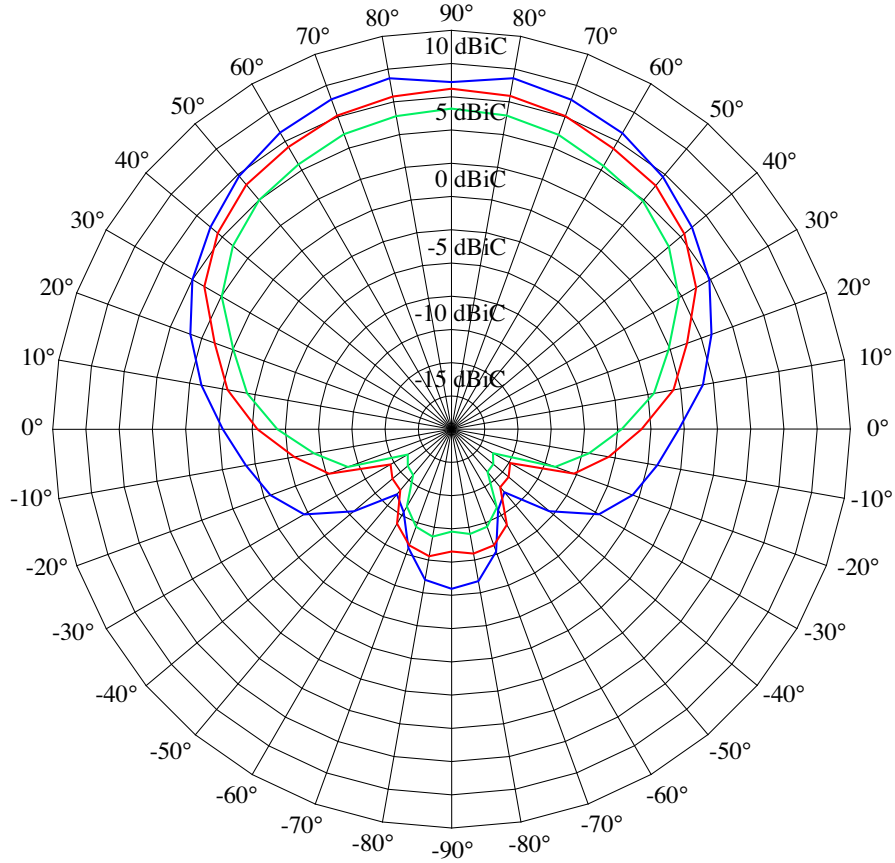
Figure 3.2: The radiation pattern dependent on the three L-band frequencies L1 (blue), L2 (red), and L5 (green) for Javad GrAnt-G3T. It represents a typical pattern for a geodetic GNSS antenna and is comparable to antennas manufactured by NovAtel or Trimble (data provided by Javad).

Out of these specific frequency bands, ideally with a constant antenna gain, the sensitivity to RHCP signals is radically reduced (more than 30 dB) in order to prevent the satellite signal being received from out-of-band interferences.

The most common antenna types are based on the basic patch design. Compared to small and low-budget single-patches, high-performance triple frequency resonance patch designs comply with the requirements for highly accurate geodetic applications mentioned above even though the size, weight, and price are increased. Further developments towards various spiral and choke ring ground planes (*Kunysz*, 2003) additionally suppress low-elevation signals while improving multipath mitigation and the antenna radiation pattern. These improvements have a direct impact on the phase pattern, and therefore on the phase center stability and variations (PCV) with respect to the antenna reference point (ARP), one of the most important characteristics for high-end geodetic reference antennas. Beside the smaller variations dependent on azimuth and elevation, a better repeatability of the phase pattern can be guaranteed between the antennas of the same product line.

Geodetic GNSS antennas are usually not directly embedded in the receiver front-end and have to be connected by a cable. Typically, a low noise amplifier (LNA) is integrated in the antenna in order to ensure a high signal strength arriving at the receiver front-end

Figure 3.3: The two concepts of an antenna architecture. On the left side a passive antenna where the received RF signal is directly sent through a cable to the receiver front-end. On the right side an active a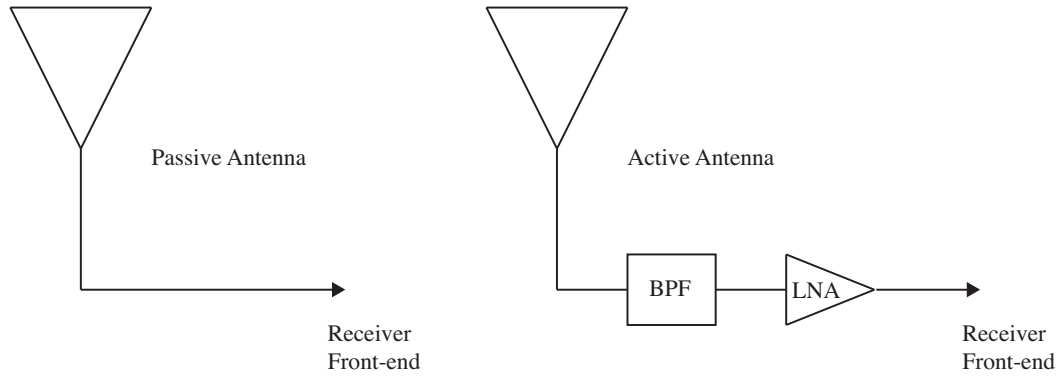ntenna with an embedded bandpass filter and LNA in the housing. The RF signal is gained before passing the cable to the receiver front-end. This is the common setup for geodetic applications.

also through long cables that increase the receiver noise. These active antennas have an LNA gain of up to 40 dB with a common noise figure at 2 dB (see Sec. 3.1.3) and need an electric power supply.

3.1.2 Oscillator and Frequency Synthesizer

The reference oscillator is a core component in a GNSS receiver that has to fulfill several requirements and determines in large part the performance of the receiver, e. g. short- and long-term stability, phase noise and acceleration sensitivity. The quality of these oscillator properties mainly decides, if the receiver is a high-end or low-cost receiver. Nowadays temperature-compensated crystal oscillators (TCXO) or oven-compensated crystal oscillators (OCXO) are relatively small and are used in most GNSS receivers. One of the most important characteristics with respect to the tracking capability is the short-term stability expressed as the dimensionless Allan deviation ($\Delta f/f$). The corresponding short-time gate time τ is usually between some milliseconds up to 1 second. The stability varies between 10^{-9} and 10^{-11} dependent on the oscillator quality. The oscillator short-time frequency variations typically set the lower boundary of applicable tracking loop filter bandwidths, see Sec. 4.2.4. Oscillators of GNSS receivers have to be additionally isolated from vibrations and should show a low g-sensitivity in order to minimize potential phase jitter and dynamic stress due to frequency changes, respectively.

The oscillator feeds the synthesizer that on the one hand is generating local oscillators (LOs) $LO(t)$ dependent on the frequency plan for the down-conversion to IF (Sec. 3.1.4) and to baseband (Sec. 3.2.2), and on the other hand provides clock samples to the analog-to-digital converter (ADC in Sec. 3.1.4) and to the numerically controlled oscillator (NCO in Sec. 3.2.5) in the signal processing unit.

3.1.3 Preamplification and Noise Figure

The first stage in the receiver front-end consists of filtering and amplification of the RF signal received from the antenna. The main goals are the limitation of the noise bandwidth of the antenna signal and the rejection of additional out-of-band interferences before down-converting the RF signal to IF. Dependent on a passive or active antenna (see Fig. 3.3) a first filter/amplifier component is already implemented in the antenna electronics. The number of further stages varies dependent on the receiver design and usually consists of a bandpass filter (BPF) followed by an LNA (see Fig. 3.4).

Each electronic component with a temperature above 0 K produces some thermal agitation (see Sec. 2.1.3). The power P_n of this thermal noise, known as Johnson-Nyquist noise (*Johnson*, 1928; *Nyquist*, 1928), is given according to Eq. (2.32)

$$P_n = N_0 2W. \tag{3.1}$$

The noise PSD N_0 expressed by the equivalent noise temperature T

$$N_0 = kT \tag{3.2}$$

leads to a noise power of

$$P_n = kT2W \tag{3.3}$$

with

$$
\begin{aligned}
k \quad &: \quad \text{Boltzmann's constant} = 1.381 \times 10^{-23} \text{ W/KHz} \\
T \quad &: \quad \text{Noise temperature [K]} \\
2W \quad &: \quad \text{Two-sided noise bandwidth [Hz].}
\end{aligned}
$$

The system noise temperature of an amplifier chain as shown in Fig. 3.4 is defined by Friis' formula (*Friis*, 1944)

$$T_{\text{sys}} = T_i + \frac{T_{i+1}}{G_i} + \frac{T_{i+2}}{G_i G_{i+1}} + \cdots \tag{3.4}$$

Note that this temperature is not a physical temperature of the device, but an equivalent temperature that might produce this amount of noise. With typical gains of much greater than one, the first stage of the receiver front-end sets the overall system noise because the impact of all subsequent stages are reduced proportionally to the first amplification. In other words, the noise applied to the second stage has already been amplified and pushed to a higher level. Due to this high noise level the noise contributions of a further stage have less impact compared to the amplification at the previous stage. If the gain of the first amplification is large, the system noise representation can be expressed only by the first stage after the input source. The increase of the noise power by the first LNA can be specified by the noise factor or noise figure NF which defines the output noise power (thermal noise and induced noise by the device) related to thermal noise with a standard input temperature T_0

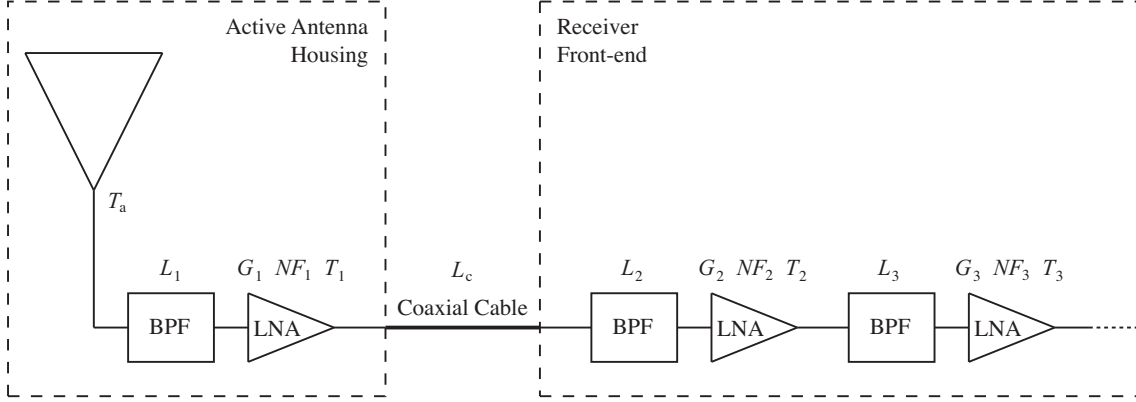$$NF = 1 + \frac{T_{\text{dev}}}{T_0} \tag{3.5}$$

Figure 3.4: A typical hardware combination of an active antenna and cable-connected receiver front-end. The shown filter/amplifier chain with filter loss $L > 1$, LNA gain G, equivalent noise temperature T (and corresponding noise figure NF) represents just an example of a possible implementation. The noise figure (NF_1) at first stage of the chain determines the noise floor of the entire system, if the gain of the first amplifier is much higher than the cable loss L_c ($G_1 >> L_c$).

and with the equivalent noise temperature T_{dev} of the device. The standard temperature T_0 is set to 290 K equal to 24.6 dBK while the noise figure is defined as the noise factor in decibel. The noise temperature at stage one ($T_{dev} = T_1$) is therefore

$$T_1 = (NF_1 - 1)T_0. \tag{3.6}$$

The noise temperature T_1 is previously affected by induced antenna noise T_a, ambient noise for the most part. The received antenna noise power is bandpass filtered before it is amplified in the housed LNA for the case of an active antenna. The power transmission and filter loss $L_1 > 1$ related to the ambient noise temperature T_0 can be applied like the noise figure in Eq. (3.6). With the total antenna noise temperature T_{ant}

$$T_{ant} = \frac{T_a}{L_1} + \frac{L_1 - 1}{L_1}T_0 \tag{3.7}$$

the total system noise temperature (according to Fig. 3.4) is defined as

$$T_{sys} = T_{ant} + T_1 = \frac{T_a}{L_1} + \frac{L_1 - 1}{L_1}T_0 + (NF_1 - 1)T_0. \tag{3.8}$$

With values of $T_a = 130$ K and $L_1 = 1.1$ (see *Spilker* (1996)) the total antenna temperature T_{ant} is 144.5 K. The noise figure NF_1 of an active antenna is typically noted in the antenna specifications. For a noise figure of 1.7 dB (e. g. Javad GrAnt-G3T) the equivalent LNA noise temperature is 139 K according to Eq. (3.6). The system temperature is finally 283.5 K or 24.5 dBK. With the Boltzmann's constant of -228.6 dBW/K-Hz, the noise spectral density N_0 (see Eq. (3.2)) can be calculated to -204.1 dBW/Hz. Comparing this value to the received spectral peak for the C/A-code signal of -218.6 dBW/Hz (see Tab. 2.1 and Fig. 2.8) it can be seen that the received signal is 14.5 dB below the calculated noise level at the receiver front-end. The PSD peak of the P(Y)-code with -231.6 dBW/Hz is additionally 13 dB lower than the C/A-code spectral peak or 27.5 dB below the noise level.

In case of an active antenna the following amplifications (G_{i+1}) of the signal-plus-noise only have an impact on out-of-band interference rejection, in order to provide a wide

correlation bandwidth to the signal processing (usually the specified two-sided bandwidth of 30.69 MHz, see Sec. 3.1.4).

3.1.4 Intermediate Frequency (IF)

After the first filter and preamplification stages (see Sec. 3.1.3) the received RF signal-plus-noise is gained and bandlimited according to the desired system frequency plan (e. g. ,L1, L2. and L5 for GPS). As already mentioned in the introduction to this chapter, nowadays the signal processor is implemented as a digital device. The analog RF signals can be digitized directly or in several steps. But there are several reasons to use an IF frequency prior to providing the signals to the analog-to-digital converter (ADC). The ADC is generally limited in sampling frequency, analog input bandwidth, and bit resolution. Even though high sampling over a wide bandwidth is available, the impact of clock and system jitter on the ADC is much larger at high frequencies. Therefore, the analog RF signal is downconverted to an analog IF by a mixer with the RF signal $s(t)$ plus noise $n(t)$, and the generated LO signal $LO(t)$ (see Sec. 3.1.2) as its inputs. Fig. 3.5 generically shows the down-conversion by an ideal mixer dependent on the frequency plan.

The following mathematical representation considers a QPSK (e. g. GPS L1) modulated signal and noise $s(t) + n(t)$ according to Eqs. (2.35) and (2.33)

$$s_{\mathrm{IF}}(t) + n_{\mathrm{IF}}(t) = [s(t) + n(t)] \cdot LO(t). \tag{3.9}$$

The signal component $s(t)$ is after the down-conversion given as

$$
\begin{aligned}
s_{\mathrm{IF}}(t) &= s(t) \cdot LO(t) \\
&= s_{\mathrm{I}}(t) \cos(2\pi(f_{\mathrm{RF}} + \Delta f)t + \theta) \cdot 2\cos(2\pi(f_{\mathrm{LO}} + \delta f)t) \\
&\quad + s_{\mathrm{Q}}(t) \sin(2\pi(f_{\mathrm{RF}} + \Delta f)t) + \theta) \cdot 2\cos(2\pi(f_{\mathrm{LO}} + \delta f)t) \\
&= s_{\mathrm{I}}(t) \left[\cos(2\pi(f_{\mathrm{RF}} - f_{\mathrm{LO}} + \Delta f - \delta f)t + \theta) \right. \\
&\quad \left. + \cos(2\pi(f_{\mathrm{RF}} + f_{\mathrm{LO}} + \Delta f + \delta f)t + \theta) \right] \\
&\quad + s_{\mathrm{Q}}(t) \left[\sin(2\pi(f_{\mathrm{RF}} - f_{\mathrm{LO}} + \Delta f - \delta f)t + \theta) \right. \\
&\quad \left. + \sin(2\pi(f_{\mathrm{RF}} + f_{\mathrm{LO}} + \Delta f + \delta f)t + \theta) \right]
\end{aligned} \tag{3.10}
$$

with the radio frequency f_{RF}, the Doppler shift Δf, the LO frequency f_{LO}, and an oscillator drift δf added by the synthesizer generated $LO(t)$. The IF signals consist of a lower sideband $(f_{\mathrm{RF}} - f_{\mathrm{LO}})$ and an upper sideband $(f_{\mathrm{RF}} + f_{\mathrm{LO}})$. The higher frequency part is not of interest, and is eliminated by a filter afterwards (see Fig. 3.5). The IF signal is finally given by

$$
\begin{aligned}
s_{\mathrm{IF}}(t) &= s_{\mathrm{I}}(t) \cos(2\pi(f_{\mathrm{IF}} + \Delta f - \delta f)t + \theta) \\
&\quad + s_{\mathrm{Q}}(t) \sin(2\pi(f_{\mathrm{IF}} + \Delta f - \delta f)t + \theta)
\end{aligned} \tag{3.11}
$$

with $f_{\mathrm{IF}} = f_{\mathrm{RF}} - f_{\mathrm{LO}}$. The noise is downconverted in the same way to

$$
\begin{aligned}
n_{\mathrm{IF}}(t) &= n_{\mathrm{I}}(t) \cos(2\pi(f_{\mathrm{IF}} + \Delta f - \delta f)t) \\
&\quad + n_{\mathrm{Q}}(t) \sin(2\pi(f_{\mathrm{IF}} + \Delta f - \delta f)t).
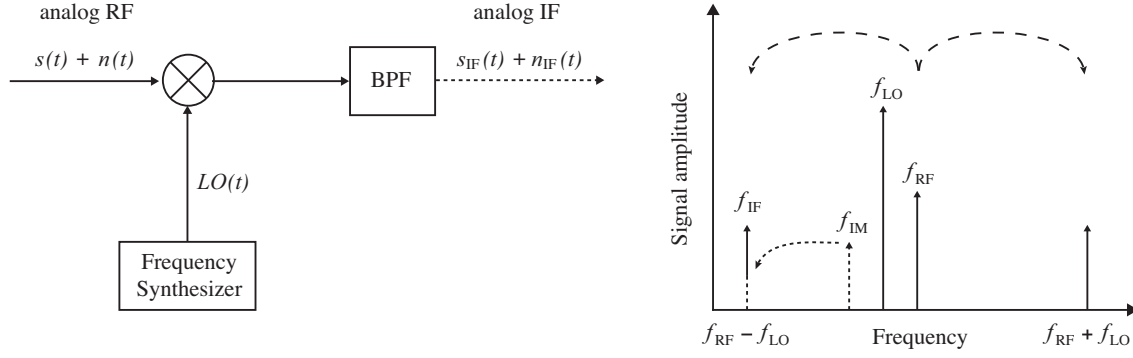\end{aligned} \tag{3.12}
$$

Figure 3.5: This figure demonstrates a one stage downconversion process to IF based on ideal mixers. The bandlimited analog RF signal-plus-noise is multiplied with the generated LOs by the synthesizer dependent on the frequency plan. In order to reject the unwanted upper band signal at $f_{\mathrm{RF}} + f_{\mathrm{LO}}$ and harmonics (not shown in this figure) induced by real not-linear mixer devices, the analog mixer output is filtered, but it still has all the properties (e. g. doppler shift, PRN codes, signal phase) of the initial RF signal. The suppression of the image signal at f_{IM} has to be applied at RF during the preamplification (see Sec. 3.1.3 and Fig. 3.4) and optimally chosen LO frequencies.

It has to be taken into account that not only the signal at frequency $f_{\mathrm{RF}} + f_{IF}$ is down-converted to IF, but also the signal at $f_{\mathrm{RF}} - f_{IF}$, the so-called image (see Fig. 3.5). The image distorts the IF signal and is difficult to filter out at IF. Therefore, the image filtering has to be carefully considered at RF before the downconversion with optimally chosen LO frequencies. Some down-conversion designs consist of two stages while two different LO frequencies are being sequentially mixed in order to reduce the signal degradation by the image. Additionally, real mixers are not linear devices as assumed in Fig. 3.5. A mixer generates several harmonics at $m f_{\mathrm{RF}} - n f_{\mathrm{LO}}$ (with integers m and n) and finally multiples of f_{IF}. The suppression of these harmonics is a key goal in mixer design, but can additionally be suppressed by a subsequent bandpass filter. All RF mixers (e. g. diode, switching mixer) are also specified by conversion gain/loss, noise figure, linearity and so on. It is important to note that the final analog IF signal contains the same properties as the analog RF signal. The signal has only been shifted to a low frequency while preserving the satellite doppler shifts Δf, the PRN codes, and the signal phase θ (see Eqs. (3.11) and (3.12)). The only term added is an oscillator drift δf which is a key issue for the coherent signal processing and the final navigation solution. Typically, an additional amplifier on IF is applied after the IF filtering in order to compensate some potential signal loss due to the mixer and to reach the required high signal level for the ADC. In order to ensure that the IF signal is arranged in an ideal dynamic range for the ADC, an automated gain control (AGC) loop with a variable gain amplifier (VGA) is implemented (*Alegre Pérez et al.*, 2011) and visible in Fig. 3.6. The ADC takes commonly place at the IF signal prior to the down-conversion to baseband (see Sec. 3.2.2 for the description of the baseband downconversion). Other designs are based on the direct baseband down-conversion using the analog RF signal to reduce the required sampling rate f_{s} at the following ADC (with the limitations mentioned above) or also at the IF, setting $f_s = 4 f_{\mathrm{IF}}$ in order to limit the phase advance to maximum 90 deg between two samples and to obtain the I and Q samples directly during the digitization process.
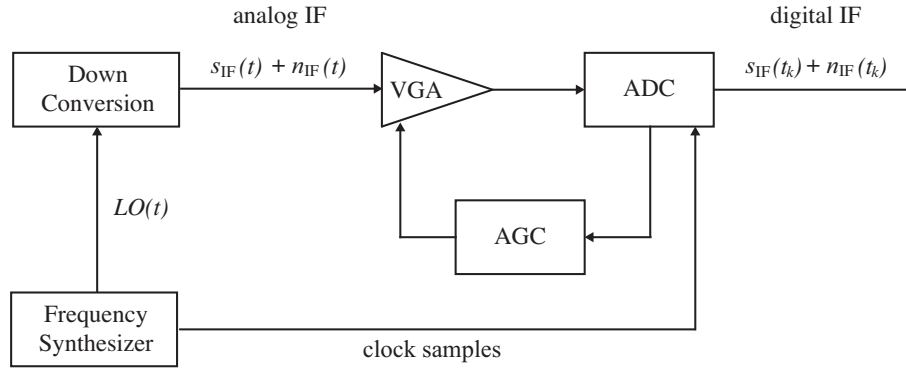
Figure 3.6: A possible implementation of the sampling of the intermediate frequency signal. After the downconversion including filtering the gain of the analog IF signal-plus-noise is controlled by an AGC containing a VGA in order to ensure an optimal dynamic signal range as input for the analog-to-digial converter (ADC).

Figure 3.6 shows the ADC after the IF down-conversion process. The generic down-conversion box includes the functions shown in Fig. 3.5. The two main tasks are the sampling and quantization of the analog IF signal, a simultaneous process in a standard ADC (*Ahmed*, 2010). The sampling rate f_s has to be carefully chosen to reduce aliasing effects based on the Nyquist theorem so that the information of the analog signal is preserved within half of the sampling frequency. Additionally, the IF filter in Fig. 3.5 with its bandwidth (also called precorrelation bandwidth) has to be wide enough in order to prevent aliasing effects and to improve the code correlation process at baseband. The two-sided bandwidth should at least correspond to the null-to-null bandwidth (see Fig. 2.5). The precorrelation bandwidth is often expanded to the specified bandwidth in the corresponding ICDs for a sharp code correlation peak with only small bandlimited effects. The second task, the quantization of the amplitude, is mainly affected by quantization noise (the finite amplitude resolution) and the clipping noise (amplitude beyond the maximum range of the ADC). These signal degradation impacts can be decreased by multi-bit ADCs. An ADC with an increased dynamic range of more than 1 bit requires an AGC to control the quantization levels. The AGC is implemented as a closed loop containing an amplifier and a filter in order to reduce the signal degradation (*Alegre Pérez et al.*, 2011; *Whitlow*, 2003). Additionally, ADCs with a high dynamic range have a better anti-jamming capability due to the minimized clipping risk during the quantization process.

It is assumed for the following description and analysis that the receiver design at IF takes optimal measures to cope with the mentioned critical aspects during the downconversion and sampling process. Therefore the signal and noise in Eqs. (3.11) and (3.12) finally represent the digitized IF signal-plus-noise $s_{IF}(t_k) + n_{IF}(t_k)$ with sample times t_k and sampling interval T_s that is fed into the signal processor.

3.2 Receiver Signal Processing

The core processes of a GNSS receiver are taking place in the signal processing unit realized by a microprocessor that consists of several integrated circuits. But the key baseband
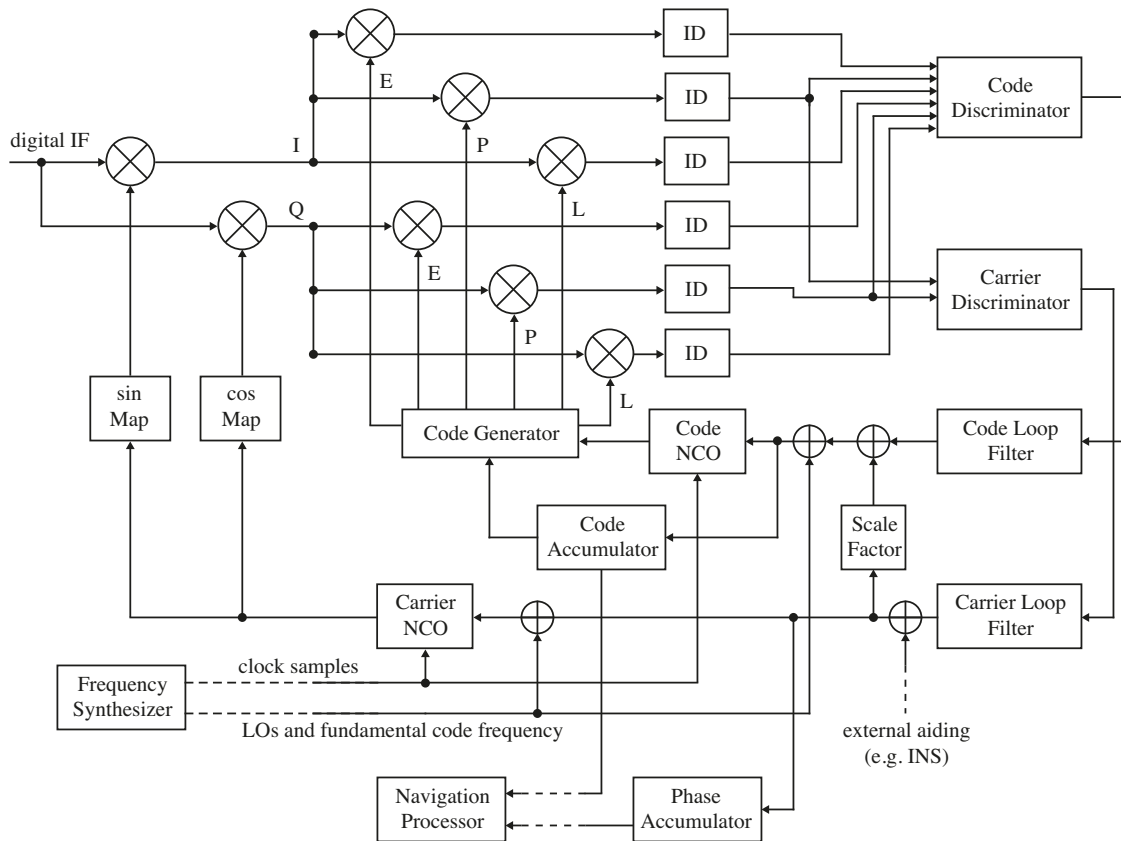
Figure 3.7: A schematic overview of one channel of the multidimensional signal processing part, a possible implementation based on *Ward et al.* (2006).

functions such as discriminators, filters, numerically controlled oscillator (NCO), and demodulation are numerically implemented, and therefore, this processing section is often called digital. The incoming sampled IF signal is buried in noise (see Sec. 3.1.3) and signals of all satellites are mixed in the same signal stream, each frequency shifted by its specific Doppler frequency. Thus the two main tasks of the receiver signal processing are the search (acquisition) of each specific satellite signal and its tracking for retrieving the desired measurements. Both processes have two dimensions which are summarized in code and carrier loops. The code loops demodulate the PRN codes from the carrier and the carrier loop estimates and tracks the doppler shifted signal. In the code loop domain the noise is much higher and requires smaller loop filter bandwidth and order. The estimated code Doppler is not accurate enough for a closed loop tracking and has to be supported by the carrier loop. In contrary, an accurate carrier measurement is not feasible without the demodulation of the PRN codes. Fig. 3.7 shows a generic simplified example of a digital channel implemented in a GNSS receiver as closed loops for the code, called code-locked loop (CLL) or delay-locked loop (DLL), and for the carrier, called phase-locked loop (PLL). For each satellite and each desired signal a single channel is used.

In order to understand the complex multi-dimensional process presented in Fig. 3.7 the basic principles of a PLL are described in the next section based on a simplified analog implementation (see Fig. 3.8). After this fundamental introduction a closer look at each

Figure 3.8: This simple implementation of a PLL contains the main signal processing steps.

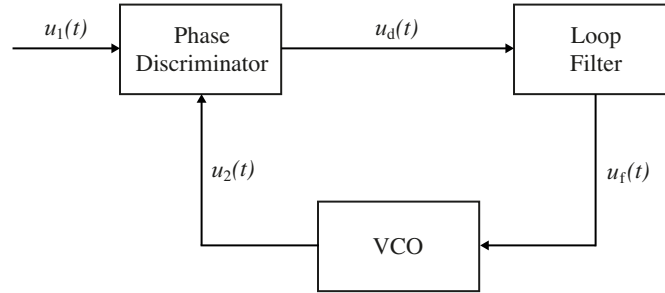processing step and component allows the formulation and analysis of the entire system and its parameters.

3.2.1 Basic Principles of a PLL

Due to existing LOS velocities such as Doppler as well as the demodulation process, a control system for a coherent phase detection has to be achieved. Assuming the incoming signal (reference signal) and the receiver signal generated by an internal oscillator are synchronized in phase as well as in frequency. If the phase difference of the reference signal and the oscillator output is zero or remains constant, they are in a *locked* state. If the phase error increases, the control mechanism acts on the oscillator in order to minimize the phase difference again. This coherent process is known as a phase-locked loop (PLL). With the progress of the space programs in the beginning of the 1960s and the development of integrated circuits (IC) the theory and application of PLLs have dramatically increased. Nowadays, most electronic devices have an implemented PLL for purposes of coherent signal demodulations, frequency synthesis, and Doppler-shift reception. It is theoretically possible to track the Doppler-shifted GNSS signals with a non-coherent approach. But the uncertainty of the Doppler frequency change requires a wide bandwidth. Due to the proportionality of the received noise power to the receiver bandwidth, a wide bandwidth induces a higher noise power and finally a bad system performance.

The three main components of an analog PLL are the phase discriminator (PD), the loop filter (LF), and the voltage controlled oscillator (VCO). For a basic understanding the functionality of a PLL is introduced as a linear process of tracking unmodulated signals (Fig. 3.8). The output signal $u_\mathrm{d}(t)$ [V] of the PD which compares the phases of the reference signal $u_1(t)$ [V] and the VCO output signal $u_2(t)$ [V] can be written as the phase difference dependent on the PD function f

$$u_\mathrm{d}(t) = K_\mathrm{d} f(\theta_1 - \theta_2). \tag{3.13}$$

K_d is the conversion gain of the PD expressed in volts per radian. The PDs are generally designed in such a way that the output signal is proportional to the phase error $\theta_\mathrm{d} = \theta_1 - \theta_2$.

The main task of the LF is to enable the tracking of a certain reference signal dynamics (including noise). Therefore, the loop filter can also be considered as a loop controller. The output voltage $u_\mathrm{f}(t)$ of the loop filter determines the angular frequency ω_2, at which the VCO is oscillating

$$\omega_2 = \omega_0 + K_\mathrm{v} u_\mathrm{f} \tag{3.14}$$

with the VCO center frequency ω_0 [rad/s] and VCO conversion gain K_v [rad/Vs]. Assumed the reference frequency and the VCO frequency are identical, the error phase θ_d is zero. Hence, the filtered output voltage u_f is zero, and the VCO is oscillating with its center frequency, thus $\omega_2 = \omega_0$. If the initial phase error θ_d is not zero, the filter produces, with a certain delay, a non-zero signal that forces the oscillator to change its frequency according to Eq. (3.14) in order to reduce the phase error to zero.

There are many different possibilities of a PD implementation dependent on the reference signal structure, on its signal characteristics (signal strength, amount of noise), and on a reasonable computational load. Some phase and code discriminators often used are described in Sec. 3.2.3. Here the PD works as a multiplier. The reference signal $u_1(t)$ (without code and data modulation) and the VCO output $u_2(t)$ as a signal shifted by 90 deg can be expressed as follows

$$\begin{aligned} u_1(t) &= U_1 \sin(\omega_1 t + \theta_1) \\ u_2(t) &= U_2 \cos(\omega_2 t + \theta_2). \end{aligned} \tag{3.15}$$

The PD output $u_d(t)$ is finally given by

$$\begin{aligned} u_d(t) &= u_1(t)u_2(t) \\ &= K_d[\sin((\omega_1 - \omega_2)t + \theta_1 - \theta_2) + \sin((\omega_1 + \omega_2)t + \theta_1 + \theta_2)] \end{aligned} \tag{3.16}$$

with

$$K_d = \frac{U_1 U_2}{2}. \tag{3.17}$$

The higher harmonic part with the doubled frequency has to be filtered out by the LF which is designed as a lowpass filter (LPF). The LF output finally has the form

$$u_f(t) = K_d \sin((\omega_1 - \omega_2)t + \theta_1 - \theta_2) \tag{3.18}$$

which determines the new angular frequency ω_2 of the VCO. When the PLL is locked, both PD input signals have almost identical frequencies ($\omega_1 \approx \omega_2$). The output of a multiplier corresponds, therefore, directly to the phase error $\theta_d = \theta_1 - \theta_2$ for small tracking errors

$$\begin{aligned} u_d(t) &= K_d \sin \theta_d \\ &\approx K_d \theta_d. \end{aligned} \tag{3.19}$$

The reference signal is often buried in noise. The PD output signal determined by the zero crossing of the signals $u_1(t)$ and $u_2(t)$ jitters around an averaged value, but the angular frequency is constant. However, it is assumed that the noise is small and the induced phase error θ_d remains in the linear range.

If the reference signal $u_1(t)$ suffers a frequency step $\Delta\omega$ at a certain time t_0 (see Fig. 3.9 left), it leads to an advanced phase at $u_1(t)$ compared to $u_2(t)$ which produces a rising phase error θ_d and voltage output at the PD $u_d(t)$ with time. With a delay the filter signal $u_f(t)$ is gained and the VCO increases its frequency ω_2. Now the phase error is getting smaller and after a certain settling time dependent on the loop filter design the VCO oscillates with the identical frequency as the reference signal. The phase error is now zero or remains at a constant value. The oscillator frequency is now higher than the center frequency by $\Delta\omega$ while $u_f(t)$ is constantly

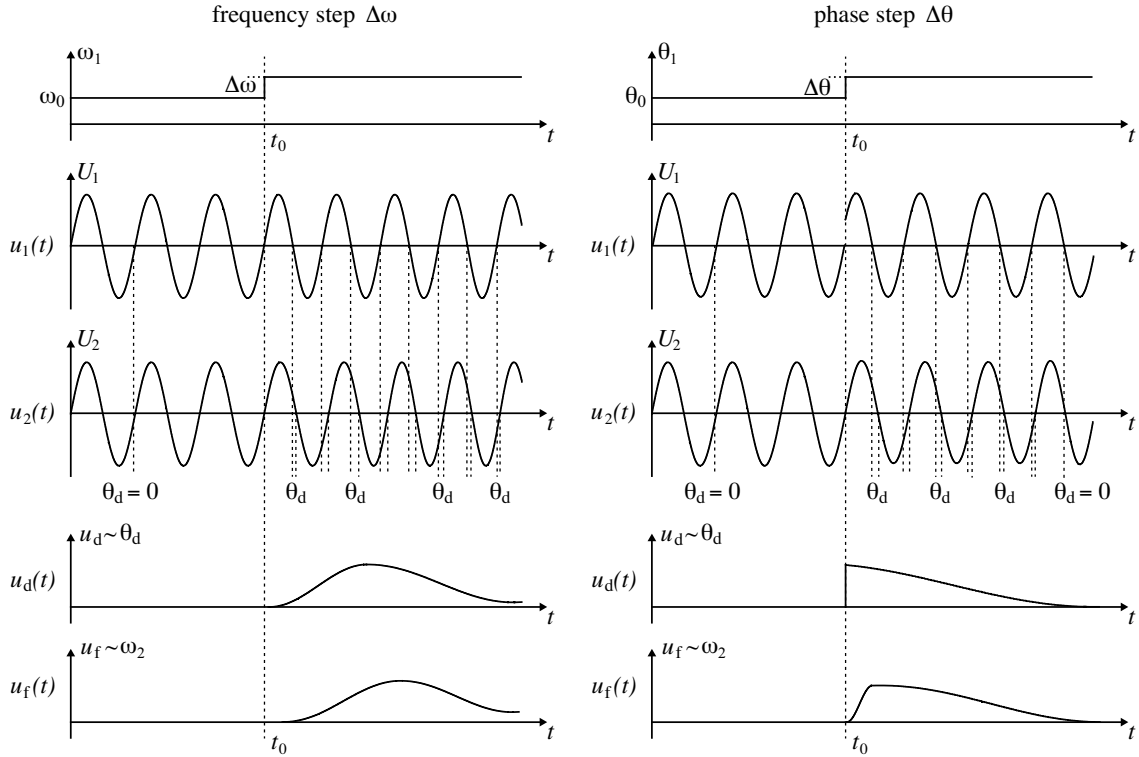$$u_f(t) = \frac{\Delta\omega}{K_v}. \tag{3.20}$$

Figure 3.9: The phase adjustment of an idealized and locked PLL is illustrated on scenarios for a frequency step (left) and a phase step (right) occurring on the reference signal $u_1(t)$. The replica signal frequency ω_2 is adjusted according to the measured phase error θ_d. The mechanism acts in order to reduce the phase error to zero or to a small constant value.

The second scenario in Fig. 3.9 (right) illustrates a phase step $\Delta\theta$ occurring on the reference signal $u_1(t)$ at t_0. The PLL works in the same way as described for the frequency step. The instantly detected phase error θ_d is constantly reduced by the filtered error signal $u_\mathrm{f}(t)$ which is gained dependent on the filter response. The replica signal frequency ω_2 is accordingly raised before it is lowered and adjusted to the initial frequency.

During the processes described in Fig. 3.9 the PLL is always in a locked state. However, there are conditions which have to be fulfilled and define the limits for different tracking states. Typically four parameters (see Fig. 3.10) are distinguished in order to describe the PLL tracking and acquisition range (*Best*, 2003). The frequency range, where a PLL statically maintains lock, is called hold range ω_H. Outside this range the PLL will not be capable of returning back to the locked state. The hold range has not really a practical relevance because it generally defines the valid range of a discriminator. The pull-in range ω_pi defines the frequency boundary, within which a PLL will always become locked (*Best*, 2003). *Encinas* (1993) and other authors use also the term capture range for ω_pi and do not distinguish between pull-in and pull-out range ω_po, which is the limit for the dynamic tracking, see *Best* (2003). Finally, the lock range ω_L defines the normal operational boundaries, where a PLL directly reaches the locked state without time consuming pull-in processes. The values are mainly dependent on the implemented discriminator and filter design, which are analyzed in Chapter 4 dependent on the baseband parameters.
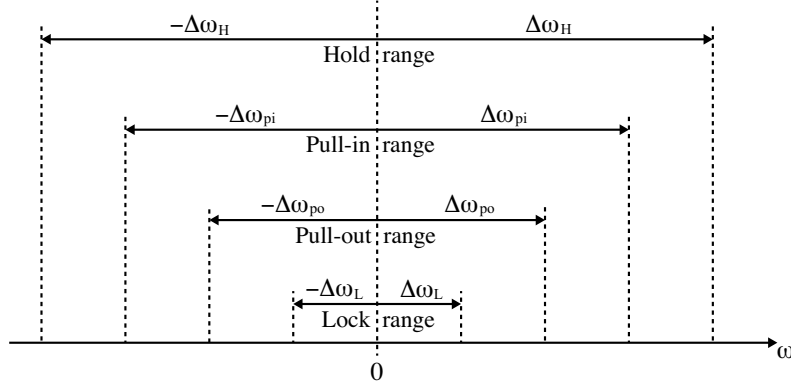
Figure 3.10: The four key values by *Best* (2003) define four frequency ranges for a stable PLL tracking.

3.2.2 Downconversion to Baseband

The given basic example from the last section is now adapted step-by-step to a possible implementation in a GNSS receiver as visible in Fig. 3.7. The signals in Eq. (3.15) are already in baseband with no modulated code and data anymore. However, the input of the channel input is a highly sampled IF signal, mixed from all visible satellites, which has to be down-converted first. Let us consider a channel that tracks the L1 carrier component with the modulated C/A-code for a satellite i according to Eq. (2.43). The P-code component does not appear anymore in the mathematical representation because there will never be a correlation above zero after the correlation with the replica code for this specific channel. The first part of the downconversion is called Doppler removal or phase rotation. The stair-case function at the carrier NCO output (NCO see Sec. 3.2.5) is mapped as sine- and cosine-phased signals and is multiplied with the incoming sampled IF signal-plus-noise to produce sampled $I(t_k)$ and $Q(t_k)$ signals

$$
\begin{aligned}
I^i(t_k) &= [s_{\mathrm{IF}}(t_k) + n_{\mathrm{IF}}(t_k)] \cdot \sqrt{2} \sin(2\pi \tilde{f}^i t_k + \tilde{\theta}_k^i) \\
Q^i(t_k) &= [s_{\mathrm{IF}}(t_k) + n_{\mathrm{IF}}(t_k)] \cdot \sqrt{2} \cos(2\pi \tilde{f}^i t_k + \tilde{\theta}_k^i)
\end{aligned}
\tag{3.21}
$$

with the IF signal being the sum of all Doppler frequencies of the available satellites j

$$
s_{\mathrm{IF}}(t_k) = \sum_{j=1}^{n} \sqrt{2P_{\mathrm{CA}}^j} CA^j(t_k) D^j(t_k) \sin(2\pi(f_{\mathrm{IF}} + \Delta f^j - \delta f)t_k + \theta_k^j).
\tag{3.22}
$$

The tilde above the frequencies and phases denotes the replica values from the carrier NCO. Under the assumption that the Doppler search (acquisition see Sec. 3.2.7) has already been successful, the replica frequency $\tilde{f}^i$ of a satellite i approximately corresponds to the IF frequency f_{IF} plus Doppler shift Δf^i of the desired satellite and the oscillator frequency shift δf

$$
\tilde{f}^i \approx f^i = f_{\mathrm{IF}} + \Delta f^i + \delta f.
\tag{3.23}
$$

This specific design of the phase rotation is required in order to prevent amplitude fading of the phasor dependent on the phase error. The phase rotation forces the main part of the signal onto the receiver I channel, thus during locked state the $I(t_k)$ samples are

maximized in signal plus the corresponding noise component, and the Q samples $Q(t_k)$ only consist of noise. The in-phase and quadra-phase samples, still dominated by noise, pass the correlator afterwards. They are compared with a code state $\tilde{CA}^i(t_k)$ for a satellite i replicated by the code generator based on the code NCO spreading code frequency. The NCO and the code generator are clocked at the same intervals T_s as the IF signal while the code generator retrieves the code state time relationship from the code accumulator (see Sec. 3.2.5). The code generator with a 2-bit shift register implemented in the DLL produces an early (E), prompt (P), and late (L) replica code with a typical spacing of 1 chip between the early and late replica. For a better multipath mitigation process correlators with more narrow spacing are used in combination with IF signals sampled higher than theoretically required. The code correlation functions R_{E}^{ji}, R_{P}^{ji}, R_{L}^{ji} between the code $CA^j(t_k)$ of the incoming satellite j and the replica code $\tilde{CA}^i(t_k)$ of satellite i are given dependent on the code phase τ_k [chips] and the chip spacing w between early-minus-late (EL) correlators

$$
\begin{aligned}
R_{\mathrm{E}}^{ji}(\tau_k) &= R_{\mathrm{c}}^{ji}(\tau_k - \frac{w}{2}) = CA^j(t_k)\tilde{CA}^i(t_k + \tau_k - \frac{w}{2}) \\
R_{\mathrm{P}}^{ji}(\tau_k) &= R_{\mathrm{c}}^{ji}(\tau_k) = CA^j(t_k)\tilde{CA}^i(t_k + \tau_k) \\
R_{\mathrm{L}}^{ji}(\tau_k) &= R_{\mathrm{c}}^{ji}(\tau_k + \frac{w}{2}) = CA^j(t_k)\tilde{CA}^i(t_k + \tau_k + \frac{w}{2}).
\end{aligned}
\tag{3.24}
$$

Due to the orthogonality of the Gold codes building the C/A-code described in Sec. 2.2.1 with their cross-correlation properties (see Sec. 2.2.2) only the functions for $j = i$ are non-zero, thus

$$
R_{\mathrm{E}} \cong R_{\mathrm{P}} \cong R_{\mathrm{L}} \cong 0 \qquad \text{if} \quad j \neq i.
\tag{3.25}
$$

For the following mathematical representation the satellite indices are dropped while looking at a specific processing channel i. If the replica code is aligned with the reference code, τ_k is equal to 0 (see Fig. 3.11 middle), the early, prompt, and late correlator output values for a one-chip spacing $w = 1$ are

$$
\begin{aligned}
R_{\mathrm{E}}(0) &\cong 1/2 \\
R_{\mathrm{P}}(0) &\cong 1 \\
R_{\mathrm{L}}(0) &\cong 1/2.
\end{aligned}
\tag{3.26}
$$

The code envelopes defined by the three code phase correlations E, P, and L dependent on different τ_k are shown in Fig. 3.11. The dependency of the chip spacing on the correlation noise is shortly described in Sec. 3.2.3 in combination with the code discriminators.

The $I(t_k)$ and $Q(t_k)$ clock samples are accumulated over a certain time period T called integrate and dump process (ID, see Fig. 3.7). The accumulation (and correlation) time T, also called predetection integration time, has to be within the data bit boundaries with an interval T_{d} of 20 ms (navigation message of the legacy GPS signals) in order to prevent bit transition (sign change) that would degrade the accumulated signal power or even average it to zero. The synchronization between the navigation data transition boundaries and the predetection integration epochs is called bit synchronization. Based on methods like the histogram approach or various powerful maximum likelihood algorithms, the data boundaries can be found and the accumulation epochs t_a with interval T can be aligned. The resulting coherent integration intervals are skewed by T_{sk} with respect to the internally clocked receiver time frame (RTF) which is used to extract the measurements
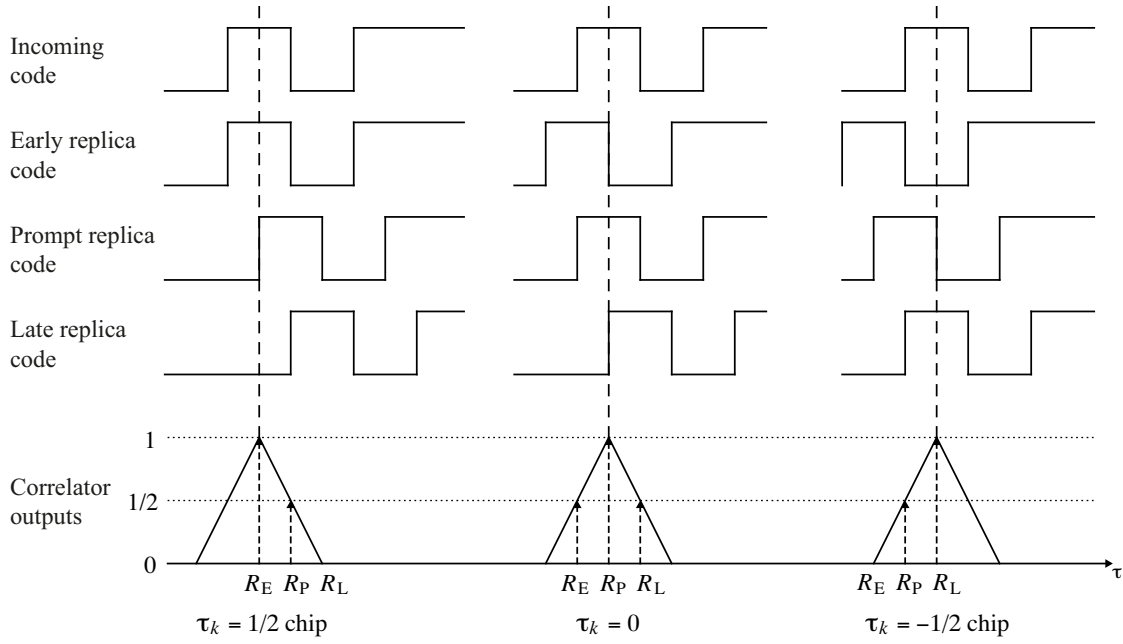
Figure 3.11: The incoming (reference) code is correlated with the early, prompt and late replica codes with a chip spacing of $w = 1$. Three different cases are illustrated. On the left, the early replica code is aligned with the incoming code with the corresponding correlator outputs $E = 1$, $P = 1/2$ and $L = 0$ while the prompt replica is being delayed by $1/2$ chip ($\tau_k = 1/2$ chip). In the middle, the prompt code is aligned with $E = 1/2$, $P = 1$ and $L = 1/2$ ($\tau_k = 0$) according to Eq. (3.26) and on the right, the late replica code matches with the incoming signal $E = 0$, $P = 1/2$ and $L = 1$ which means that the prompt replica code is premature by $1/2$ chip ($\tau_k = -1/2$ chip).

(see Sec. 3.2.6). The skew time T_{sk} is different for each satellite because the ranges from the satellites to the receiver are different and are time-dependent due to changes of the ranges. The coherent integration time T is usually set between 1 and 10 ms with the number M_{ID} of integrated samples

$$M_{\text{ID}} = \frac{T}{T_{\text{s}}} \tag{3.27}$$

with T_{s} as the IF signal sample interval or precorrelation sampling used by the ADC and clocking the NCOs. Due to the time-changing skewed integration epochs the number of samples M_{ID} varies with time. However, the variation over some milliseconds is extremely small and can be neglected (*Van Dierendonck*, 1996). This resampling by the integration and dump process acts like a lowpass filter and eliminates the high-frequency output of the algebraic product in Eq. (3.21). The integrated and dumped samples now refer to t_a that indicates the time after the integration with a normalized phasor amplitude $A = \sqrt{I^2 + Q^2} = \sqrt{2P}$. Substituting Eqs. (3.22) and (3.23) in Eq. (3.21) for $j = i$ and neglecting correlator output noise, the early (E), prompt (P) and late (L) integrated $I(t_a)$

and $Q(t_a)$ samples are

$$I_{\mathrm{E}}(t_a) = \sqrt{S}\, R_{\mathrm{E}}(\tau_a) D(t_a) \sum_{k=1}^{M_{\mathrm{ID}}} \cos(2\pi(f - \tilde{f})t_k + \theta_k - \tilde{\theta}_k) + \frac{1}{\sqrt{2}} \sum_{k=1}^{M_{\mathrm{ID}}} n_{\mathrm{I}}(t_k)$$

$$I_{\mathrm{P}}(t_a) = \sqrt{S}\, R_{\mathrm{P}}(\tau_a) D(t_a) \sum_{k=1}^{M_{\mathrm{ID}}} \cos(2\pi(f - \tilde{f})t_k + \theta_k - \tilde{\theta}_k) + \frac{1}{\sqrt{2}} \sum_{k=1}^{M_{\mathrm{ID}}} n_{\mathrm{I}}(t_k)$$

$$I_{\mathrm{L}}(t_a) = \sqrt{S}\, R_{\mathrm{L}}(\tau_a) D(t_a) \sum_{k=1}^{M_{\mathrm{ID}}} \cos(2\pi(f - \tilde{f})t_k + \theta_k - \tilde{\theta}_k) + \frac{1}{\sqrt{2}} \sum_{k=1}^{M_{\mathrm{ID}}} n_{\mathrm{I}}(t_k)$$

$$Q_{\mathrm{E}}(t_a) = \sqrt{S}\, R_{\mathrm{E}}(\tau_a) D(t_a) \sum_{k=1}^{M_{\mathrm{ID}}} \sin(2\pi(f - \tilde{f})t_k + \theta_k - \tilde{\theta}_k) + \frac{1}{\sqrt{2}} \sum_{k=1}^{M_{\mathrm{ID}}} n_{\mathrm{Q}}(t_k) \tag{3.28}$$

$$Q_{\mathrm{P}}(t_a) = \sqrt{S}\, R_{\mathrm{P}}(\tau_a) D(t_a) \sum_{k=1}^{M_{\mathrm{ID}}} \sin(2\pi(f - \tilde{f})t_k + \theta_k - \tilde{\theta}_k) + \frac{1}{\sqrt{2}} \sum_{k=1}^{M_{\mathrm{ID}}} n_{\mathrm{Q}}(t_k)$$

$$Q_{\mathrm{L}}(t_a) = \sqrt{S}\, R_{\mathrm{L}}(\tau_a) D(t_a) \sum_{k=1}^{M_{\mathrm{ID}}} \sin(2\pi(f - \tilde{f})t_k + \theta_k - \tilde{\theta}_k) + \frac{1}{\sqrt{2}} \sum_{k=1}^{M_{\mathrm{ID}}} n_{\mathrm{Q}}(t_k)$$

with the accumulated data stream $D(t_a)$ and signal power $\sqrt{S} = \sqrt{2P_{\mathrm{CA}}}/\sqrt{2}$ over T. Note the factor $1/\sqrt{2}$ which is the result of the product of the NCO gain $\sqrt{2}$ and the factor $1/2$ of the trigonometric identity. The non-zero correlator outputs $R_{\mathrm{E}}(\tau_k)$, $R_{\mathrm{P}}(\tau_k)$ and $R_{\mathrm{L}}(\tau_k)$ for $j = i$ from Eq. (3.24) are accumulated to

$$R_{\mathrm{E}}(\tau_a) = \frac{1}{M_{\mathrm{ID}}} \sum_{k=1}^{M_{\mathrm{ID}}} R_{\mathrm{E}}(\tau_k)$$

$$R_{\mathrm{P}}(\tau_a) = \frac{1}{M_{\mathrm{ID}}} \sum_{k=1}^{M_{\mathrm{ID}}} R_{\mathrm{P}}(\tau_k) \tag{3.29}$$

$$R_{\mathrm{L}}(\tau_a) = \frac{1}{M_{\mathrm{ID}}} \sum_{k=1}^{M_{\mathrm{ID}}} R_{\mathrm{L}}(\tau_k).$$

The noise components $n_{\mathrm{I}}(t_k)$ and $n_{\mathrm{Q}}(t_k)$ have the following properties

$$E[n_{\mathrm{I}}(t_k)] = E[n_{\mathrm{Q}}(t_k)] = E[n_{\mathrm{I}}(t_k)n_{\mathrm{Q}}(t_k)] = 0 \tag{3.30}$$

and, according to Eq. (2.32) with the two-sided noise bandwidth $2W$ equal to the Nyquist frequency $1/(2T_{\mathrm{s}})$,

$$E[n_{\mathrm{I}}^2(t_k)] = E[n_{\mathrm{Q}}^2(t_k)] = \frac{N_0}{T_{\mathrm{s}}}. \tag{3.31}$$

Assuming that the frequency δf_a and phase error $\delta\theta_a$ are constant over the integration time T, the frequency error is given as

$$\delta f_a = (f_a - \tilde{f}_a) - (f_{a-1} - \tilde{f}_{a-1}) \tag{3.32}$$

and the phase error as

$$\delta\theta_a = \Delta\theta_a + \pi\delta f_a T \tag{3.33}$$

which is given by the phase difference $\Delta\theta_a$

$$\Delta\theta_a = (\theta_a - \tilde{\theta}_a) - (\theta_{a-1} - \tilde{\theta}_{a-1}) \tag{3.34}$$

plus the frequency error δf_a over half the integration time T. Therefore, the discrete sum of the signal components in Eq. (3.28) can be approximated by the following integrals (*Van Dierendonck*, 1996)

$$\sum_{k=1}^{M_{\mathrm{ID}}} \cos(2\pi(f - \tilde{f})t_k + (\theta_k - \tilde{\theta}_k)) \approx \frac{1}{T_{\mathrm{s}}} \int_0^T \cos(2\pi\delta f_a t + \Delta\theta_a)\mathrm{d}t$$

$$\sum_{k=1}^{M_{\mathrm{ID}}} \sin(2\pi(f - \tilde{f})t_k + (\theta_k - \tilde{\theta}_k)) \approx \frac{1}{T_{\mathrm{s}}} \int_0^T \sin(2\pi\delta f_a t + \Delta\theta_a)\mathrm{d}t. \tag{3.35}$$

The accumulation is finally given by

$$\frac{1}{T_{\mathrm{s}}} \int_0^T \cos(2\pi\delta f_a t + \Delta\theta_a)\mathrm{d}t = \frac{1}{T_{\mathrm{s}}} \left. \left(\frac{\sin(2\pi\delta f_a t + \Delta\theta_a)}{2\pi\delta f_a} \right) \right|_0^T$$

$$= \frac{1}{T_{\mathrm{s}}} \frac{\sin(2\pi\delta f_a T + \Delta\theta_a) - \sin(\Delta\theta_a)}{2\pi\delta f_a} \tag{3.36}$$

and, using Eq. (3.27), (3.33) and a trigonometric identity, by

$$\frac{1}{T_{\mathrm{s}}} \int_0^T \cos(2\pi\delta f_a t + \Delta\theta_a)\mathrm{d}t = \frac{M_{\mathrm{ID}}}{2\pi\delta f_a T} \left[2\sin\left(\frac{2\pi\delta f_a T)}{2}\right) \cos\left(\frac{2\pi\delta f_a T + 2\Delta\theta_a)}{2}\right) \right]$$

$$= M_{\mathrm{ID}} \frac{\sin(\pi\delta f_a T)}{\pi\delta f_a T} \cos(\pi\delta f_a T + \Delta\theta_a)$$

$$= M_{\mathrm{ID}} \operatorname{sinc}(\delta f_a T) \cos(\delta\theta_a). \tag{3.37}$$

Accordingly, the accumulation of the Q samples are given by

$$\frac{1}{T_{\mathrm{s}}} \int_0^T \sin(2\pi\delta f_a t + \Delta\theta_a)\mathrm{d}t = M_{\mathrm{ID}} \operatorname{sinc}(\delta f_a T) \sin(\delta\theta_a). \tag{3.38}$$

The phase rotated noise $n_{\mathrm{I}}(t_k)/\sqrt{2}$ and $n_{\mathrm{Q}}(t_k)/\sqrt{2}$ with the statistics given by Eq. (3.31) is integrated over M_{ID} samples to

$$E[n_{\mathrm{I}}^2(t_a)] = E[n_{\mathrm{Q}}^2(t_a)] = M_{\mathrm{ID}} \frac{N_0}{2T_{\mathrm{s}}} = \frac{N_0 M_{\mathrm{ID}}^2}{2T} \tag{3.39}$$

using the relation of Eq. (3.27) with the corresponding two-sided predetection bandwidth $1/T$. For the following analyses of the baseband functions and expected tracking errors the noise components of the resampled signal streams are normalized by the factor of

Eq. (3.39). The resubstitution of Eqs. (3.37) and (3.38) in Eq. (3.28) yields

$$I_{\mathrm{E}}(t_a) = \sqrt{2T\frac{S}{N_0}}\mathrm{sinc}(\delta f_a T)R_{\mathrm{E}}(\tau_a)D(t_a)\cos(\delta\theta_a) + \hat{n}_{\mathrm{I}}(t_a)$$

$$I_{\mathrm{P}}(t_a) = \sqrt{2T\frac{S}{N_0}}\mathrm{sinc}(\delta f_a T)R_{\mathrm{P}}(\tau_a)D(t_a)\cos(\delta\theta_a) + \hat{n}_{\mathrm{I}}(t_a)$$

$$I_{\mathrm{L}}(t_a) = \sqrt{2T\frac{S}{N_0}}\mathrm{sinc}(\delta f_a T)R_{\mathrm{L}}(\tau_a)D(t_a)\cos(\delta\theta_a) + \hat{n}_{\mathrm{I}}(t_a)$$

$$Q_{\mathrm{E}}(t_a) = \sqrt{2T\frac{S}{N_0}}\mathrm{sinc}(\delta f_a T)R_{\mathrm{E}}(\tau_a)D(t_a)\sin(\delta\theta_a) + \hat{n}_{\mathrm{Q}}(t_a) \qquad (3.40)$$

$$Q_{\mathrm{P}}(t_a) = \sqrt{2T\frac{S}{N_0}}\mathrm{sinc}(\delta f_a T)R_{\mathrm{P}}(\tau_a)D(t_a)\sin(\delta\theta_a) + \hat{n}_{\mathrm{Q}}(t_a)$$

$$Q_{\mathrm{L}}(t_a) = \sqrt{2T\frac{S}{N_0}}\mathrm{sinc}(\delta f_a T)R_{\mathrm{L}}(\tau_a)D(t_a)\sin(\delta\theta_a) + \hat{n}_{\mathrm{Q}}(t_a)$$

with the normalized noise and its properties

$$E[\hat{n}_{\mathrm{I}}(t_a)] = E[\hat{n}_{\mathrm{Q}}(t_a)] = E[\hat{n}_{\mathrm{I}}(t_a)\hat{n}_{\mathrm{Q}}(t_a)] = 0 \qquad (3.41)$$

and

$$E[\hat{n}_{\mathrm{I}}^2(t_a)] = E[\hat{n}_{\mathrm{Q}}^2(t_a)] = 1 \qquad (3.42)$$

The code stripping with the integrate and dump process is the last stage of the hardware part and the parameters are not simply changeable by the firmware. The following baseband functions are implemented in firmware and performed by a microprocessor. This allows different designs and parameters to be directly adapted to the specific task (acquisition or tracking) and to the signal conditions (e.g. poor signal-to-noise environment).

The integrated $I_{\mathrm{E}}(t_a)$, $I_{\mathrm{P}}(t_a)$, $I_{\mathrm{L}}(t_a)$, $Q_{\mathrm{E}}(t_a)$, $Q_{\mathrm{P}}(t_a)$, and $Q_{\mathrm{L}}(t_a)$ samples are passing the code and carrier discriminators (see Fig. 3.7). The following section describes a small selection of possible discriminator implementations with their different characteristics.

3.2.3 Discriminator

The error detector on baseband called discriminator, as briefly discussed in Sec. 3.2.1, can be implemented in different ways dependent on the properties of the reference signal and the desired error signal (code phase, carrier phase, or carrier frequency). The baseband signals after the phase rotation, code correlation, and resampling by the integration and dump stages have the form of Eq. (3.40) and are comparable with the basic formulation of Eq. (3.15), the data modulation excepted. For the carrier tracking only the prompt signal of Eq. (3.40) is used with the prompt phasor amplitude

$$A_{\mathrm{P}}(t_a) = \sqrt{I_{\mathrm{P}}^2(t_a) + Q_{\mathrm{P}}^2(t_a)} \qquad (3.43)$$

and the noise properties of Eqs. (3.41) and (3.42). The phasor tends to be aligned with the receiver I channel which means that the maximum signal part and noise are on the I_{P} component while Q_{P} is only consisting of noise. However, the phasor is switching by 180 deg at each data bit transition and would cause a loss of phase lock. A carrier loop discriminator that is insensitive to data modulation belongs to the group of so-called Costas discriminators.

Costas Loop Discriminators

One possible implementation is the accumulation of the $I_\mathrm{P}(t_a)$ samples within a data bit and the determination of the corresponding sign by the signum function

$$\theta_{\mathrm{d},a} = Q_\mathrm{P}(t_a)\,\mathrm{sign}(I_\mathrm{P}(t_a)). \tag{3.44}$$

The expectation value of the phase error θ_d at the discriminator output is

$$
\begin{aligned}
E[\theta_{\mathrm{d},a}] &= E[Q_\mathrm{P}(t_a)]\,\mathrm{sign}(E[I_\mathrm{P}(t_a)]) \\
&= \sqrt{2T\frac{S}{N_0}}\,\mathrm{sinc}(\delta f_a T)\,R_\mathrm{P}(\tau_a)\sin(\delta\theta_a) + E[\hat{n}_\mathrm{Q}(t_a)].
\end{aligned} \tag{3.45}
$$

For small frequency errors and code and phase tracking errors the linearized form of the discriminator can be approximated by

$$E[\theta_{\mathrm{d},a}] \approx \sqrt{2T\frac{S}{N_0}}\,\delta\theta_a \tag{3.46}$$

with a discriminator gain K_d depending on the signal amplitude

$$K_\mathrm{d} = \sqrt{2T\frac{S}{N_0}}. \tag{3.47}$$

The computational load for this discriminator is minimal, but the error slope is proportional to the signal amplitude. However, for high *SNR* it provides good results.

The product (IQP) has similar low computational requirements as the discriminator with the signum function of Eq. (3.44) and allows better results for low *SNR* environments

$$\theta_{\mathrm{d},a} = Q_\mathrm{P}(t_a)\,I_\mathrm{P}(t_a) \tag{3.48}$$

with the expected output value for small frequency and tracking errors

$$
\begin{aligned}
E[\theta_{\mathrm{d},a}] &= E[Q_\mathrm{P}(t_a)]\,E[I_\mathrm{P}(t_a)] + E[Q_\mathrm{P}(t_a)]E[\hat{n}_\mathrm{I}(t_a)] \\
&\quad + E[I_\mathrm{P}(t_a)]E[\hat{n}_\mathrm{Q}(t_a)] + E[\hat{n}_\mathrm{Q}(t_a)]E[\hat{n}_\mathrm{I}(t_a)] \\
&= 2T\frac{S}{N_0}\mathrm{sinc}^2(\delta f_a T)R_\mathrm{P}^2(\tau_a)\frac{1}{2}[\sin(\delta\theta_a - \delta\theta_a) + \sin(\delta\theta_a + \delta\theta_a)] \\
&= T\frac{S}{N_0}\mathrm{sinc}^2(\delta f_a T)R_\mathrm{P}^2(\tau_a)\,\sin(2\delta\theta_a) \\
&\approx 2T\frac{S}{N_0}\,\delta\theta_a
\end{aligned} \tag{3.49}
$$

The slope of this classic analog Costas discriminator according to Eq. (3.48) is proportional to the square signal amplitude with a discriminator gain of

$$K_\mathrm{d} = 2T\frac{S}{N_0}. \tag{3.50}$$

Nowadays, in the digital domain, the two-quadrant arctangent discriminator is an often used Costas discriminator, implemented as a lookup table in order to reduce the computational burden. The error phase is linear over ± 90 deg and not amplitude-dependent

$$\theta_{\mathrm{d},a} = \arctan\left(\frac{Q_\mathrm{P}(t_a)}{I_\mathrm{P}(t_a)}\right) \tag{3.51}$$
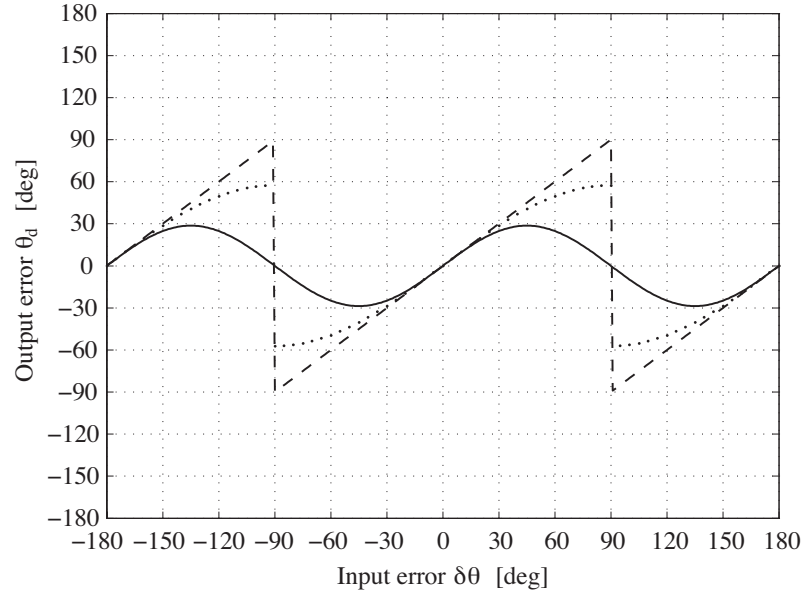
Figure 3.12: The normalized Costas discriminator output $\theta_{\mathrm{d},a}$ dependent on the input phase error $\delta\theta_a$ for the data bit sign decision function in Eq. (3.44) (dotted), the product from Eq. (3.48) (solid) and the two-quadrant arctangent function of Eq. (3.51) (dashed).

with

$$
\begin{aligned}
E[\theta_{\mathrm{d},a}] &\approx \arctan\left(\frac{\sin(\delta\theta_a)}{\cos(\delta\theta_a)}\right) \\
&\approx \delta\theta_a.
\end{aligned}
\tag{3.52}
$$

The normalized output $\theta_{\mathrm{d},a}$ of the three described Costas discriminators are visible in Fig. 3.12 dependent on a range of the input phase error $\delta\theta_a$ of ± 180 deg. Simulations of the stability and threshold behavior done by *Humphreys et al.* (2005) show that the classic Costas discriminator of Eq. (3.48) resembles the discriminators described in Eqs. (3.44) and (3.51) in all the properties. All the Costas discriminators have still a data ambiguity of 180 deg. The extracted data stream is either correct or has to be inverted. This check is achieved by comparing the data bit sign of the preamble at the beginning of each subframe of the navigation message. The Costas discriminators allow the most accurate phase measurements in presence of data modulation. However, this advantage has to be paid by a lower signal tracking threshold of 6 dB compared to a dataless signal tracking by a classical PLL because the Costas PLL tracks only half of the two-quadrant range of the incoming signal.

PLL Discriminators

The modern GNSS signals consist of a data and pilot (dataless) channel and are multiplexed with QPSK (e. g. C5/L5 in Sec. 2.3.2) or TDM (e. g. C2/L2 in Sec. 2.3.1). This allows the tracking of the pilot channel over the full four-quadrant signal range by a classical PLL discriminator, e. g. four-quadrant arctangent (ATAN2) function

$$
\theta_{\mathrm{d},a} = \mathrm{ATAN2}\left(Q_{\mathrm{P}}(t_a), I_{\mathrm{P}}(t_a)\right).
\tag{3.53}
$$

The expected value for the discriminator output assuming small tracking errors is

$$E[\theta_{\mathrm{d},a}] \approx \delta\theta_a \tag{3.54}$$

with a validity over ± 180 deg. The tracking signal power gains up to 6 dB compared to the tracking of the legacy C/A-code component on the L1 signal with a Costas PLL. The signal power of the pilot channel is often shared with the data signal and represents only half of the fully available signal reducing the benefit from 6 dB to 3 dB (e.g. L2C on L2 and most of the Galileo signals).

The following discriminator shows an alternative to the computationally intensive ATAN2 function while normalizing the $Q_{\mathrm{P}}(t_a)$ component by a long-term average of the prompt envelope

$$\theta_{\mathrm{d},a} = \frac{Q_{\mathrm{P}}(t_a)}{\mathrm{ave}\sqrt{I_{\mathrm{P}}^2(t_a) + Q_{\mathrm{P}}^2(t_a)}} \tag{3.55}$$

and

$$\begin{aligned} E[\theta_{\mathrm{d},a}] &\approx \sin(\delta\theta_a) \\ &\approx \delta\theta_a. \end{aligned} \tag{3.56}$$

The normalized output $\theta_{\mathrm{d},a}$ of the PLL discriminators from Eqs. (3.53) and (3.55) are visible in Fig. 3.12 dependent on the input phase error $\delta\theta_a$ over a range of ± 180 deg.

In the presence of noise all described Costas and classical PLL discriminators are only linear near zero degree and even though they are not proportional to the signal amplitude, a code replica not perfectly aligned suffers a signal degradation by $R_{\mathrm{P}}(\tau_a)$. It has been mentioned already at the beginning of this chapter (visible in Fig. 3.7) that the code loop is strongly related to the carrier tracking loop.

Code Loop Discriminators

Due to the coherent phase tracking by the PLL and the aiding of the DLL, the code discriminator is often implemented as a non-coherent function of the early-minus-late correlator output (see also Fig. 3.11)

$$\tau_{\mathrm{d},a} = I_{\mathrm{E}}^2(t_a) + Q_{\mathrm{E}}^2(t_a) - I_{\mathrm{L}}^2(t_a) - Q_{\mathrm{L}}^2(t_a). \tag{3.57}$$

The variance of the integrated noise samples for the early-minus-late integrated correlations $R_{\mathrm{E}}(\tau_a) - R_{\mathrm{L}}(\tau_a)$ from Eq. (3.24) is given, according to Eq. (3.39), by

$$\begin{aligned} E[n_{\mathrm{I,EL}}^2(t_a)] &= E[n_{\mathrm{I,E}}^2(t_a)] + E[n_{\mathrm{I,L}}^2(t_a)] - 2[n_{\mathrm{I,E}}(t_a)\, n_{\mathrm{I,L}}(t_a)] \\ &= \frac{N_0 M_{\mathrm{ID}}^2}{2T}(2 - 2\rho_{\mathrm{EL}}) \\ E[n_{\mathrm{Q,EL}}^2(t_a)] &= E[n_{\mathrm{Q,E}}^2(t_a)] + E[n_{\mathrm{Q,L}}^2(t_a)] - 2[n_{\mathrm{Q,E}}(t_a)\, n_{\mathrm{Q,L}}(t_a)] \\ &= \frac{N_0 M_{\mathrm{ID}}^2}{2T}(2 - 2\rho_{\mathrm{EL}}) \end{aligned} \tag{3.58}$$

with the correlation ρ_{EL} and an expectation value of zero. The early and late samples are generally independent even though the incoming noise is identical and filtered. But
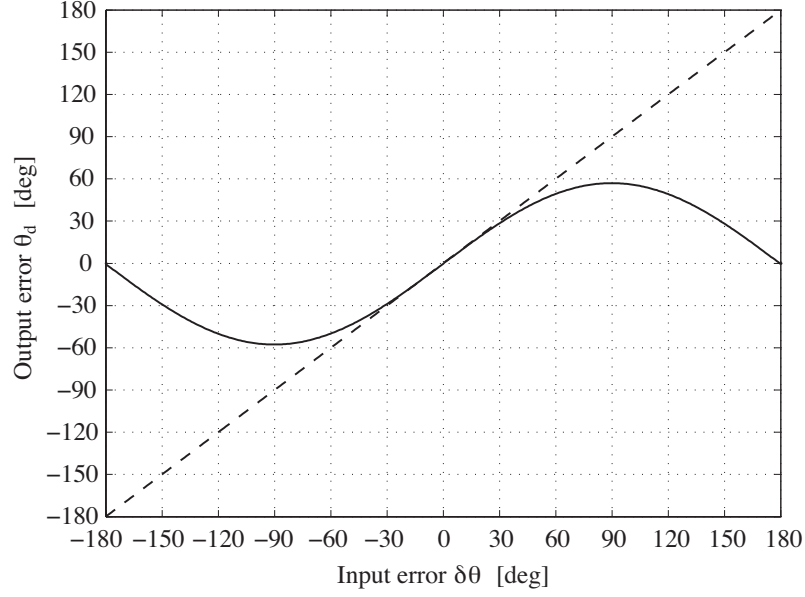
Figure 3.13: The normalized PLL discriminator output $\theta_{\mathrm{d},a}$ dependent on the input phase error $\delta\theta_a$ for four-quadrant ATAN2 function from Eq. (3.53) (dashed) and the $Q_{\mathrm{P}}(t_a)$ function with normalized power from Eq. (3.55) (solid).

they are spread by a different code phase. A chip spacing of one produces no correlations between the early and late samples, however, the correlation is increased while reducing the chip spacing w (*Van Dierendonck et al.*, 1992)

$$\rho_{\mathrm{EL}} = 1 - w. \tag{3.59}$$

The normalization of the noise components in Eq. (3.40) leads to the normalized early-minus-late noise samples

$$E[\hat{n}_{\mathrm{I,EL}}^2(t_a)] = E[\hat{n}_{\mathrm{Q,EL}}^2(t_a)] = 2 - 2(1 - w) = 2w \tag{3.60}$$

and finally to the expectation value for the code discriminator output $\tau_{\mathrm{d},a}$

$$
\begin{aligned}
E[\tau_{\mathrm{d},a}] &= 2T\frac{S}{N_0}[R_{\mathrm{E}}^2(\tau_a) - R_{\mathrm{L}}^2(\tau_a)] \\
&= 2T\frac{S}{N_0}[R_{\mathrm{c}}^2(\tau_a - w/2) - R_{\mathrm{c}}^2(\tau_a + w/2)] \\
&\approx 2T\frac{S}{N_0}(2 - |\tau_a - w/2| - |\tau_a + w/2|)(|\tau_a - w/2| - |\tau_a + w/2|) \\
&\approx 4T\frac{S}{N_0}(2 - w)\tau_a
\end{aligned}
\tag{3.61}
$$

with $|\tau_a| \leq w/2$ and $w \leq 1$. A small chip spacing reduces the noise as visible in Eq. (3.60) and improves the robustness against multipath shown by *Van Dierendonck et al.* (1992). Due to the non-conherence the early-minus-late discriminator is extremely robust. However, a more accurate code measurement is possible with a coherent approach, but only if the carrier phase is in *locked* state

$$\tau_{\mathrm{d},a} = [I_{\mathrm{E}}(t_a) - I_{\mathrm{L}}(t_a)]\,\mathrm{sign}(I_{\mathrm{P}}(t_a)). \tag{3.62}$$

The principle bases on an equal power for the early and late in-phase code samples if the prompt code is aligned with the reference code where the signum function of the prompt signals denotes the data bit sign demodulated by the PLL. When we assume that the PLL is in phase-lock the expectation value for the coherent DLL discriminator output is finally

$$E[\tau_{\mathrm{d},a}] \approx \sqrt{2T\frac{S}{N_0}}[R_{\mathrm{c}}(\tau_a - w/2) - R_{\mathrm{c}}(\tau_a + w/2)]$$
$$\approx \sqrt{2T\frac{S}{N_0}}[|\tau_a - w/2| - |\tau_a + w/2|] \qquad (3.63)$$
$$\approx 2\sqrt{2T\frac{S}{N_0}}\tau_a.$$

Both discriminator functions in Eqs. (3.61) and (3.63) can also be normalized with the corresponding envelope or power. Some receivers take advantage of a changeable chip spacing at the code correlator and switching between non-coherent and coherent DLL discriminators, e.g. $w = 1$ in combination with a non-coherent approach for a fast acquisition or robust code tracking under poor conditions (if no phase tracking is possible, but the frequency error is small compared to the predetection bandwidth $1/T$) and a small correlator spacing of $w = 0.1$ for the coherent tracking.

3.2.4 Loop Filter

As described in Sec. 3.2.1 the discriminator output passes a filter that generates the input signal for the VCO (or NCO). The low pass filter (LPF) implemented in a PLL is a crucial tool that determines the behavior of the entire loop and accordingly the capability and quality of the phase measurements. The loop filter has to ensure that the PLL remains in lock in presence of noise (poor S/N_0) and is able to track a certain signal dynamics (Doppler shift and user dynamics) with a minimized filter response. The challenge in filter design is the combination of these conflictive requirements: on the one hand, for a noisy reference signal, the filter bandwidth has to be narrow with a low filter order, on the other hand high signal dynamics require higher filter orders and a wider bandwidth. Nowadays the loop filters are designed as digital filters. The filter parameters can, however, directly be derived from the analog implementation especially for low orders. In the following some examples of possible filters with different characteristics and the transformation into the digital domain are shortly described.

A zero order filter with a magnitude 1 would imply a PLL without any filter. Due to the sensitivity to velocity, a zero order filter that leads to a first order closed loop is not applicable for tracking signals affected by frequency Doppler shifts. Therefore, at least first order filters have to be used. Different types of first order filters are suitable and are described in the following. All analyzed filters are dimensionless voltage-mode filters. Note that the following convention of dB refers to the convention typically using from Electrical engineers which defines $V\,[\mathrm{dB}] = 20\log_{10}(V/V_0)$ where the power is proportional to the square of the applied voltage, equal to $V\,[\mathrm{dB}] = 10\log_{10}(V^2/V_0^2)$.

Passive First Order Lag Filter

The most simple analogy for a first order passive LFP is given by a single RC component (see Fig. 3.14 (a)). With Kirchoff's current law indicating that the current $i(t)$ (in Ampère) through the resistor (with resistance R in Ohm) is equal to the current charging the capacitor (with the capacitance C in Farad), we get the following linear differential equation (see Fig. 3.14 for $u_d(t)$ and $u_f(t)$)

$$\begin{aligned} u_f(t) &= u_d(t) - Ri(t) \\ &= u_d(t) - RC\frac{du_f(t)}{dt}. \end{aligned} \tag{3.64}$$

Taking the Laplace transforms

$$\begin{aligned} u_d(s) &= \mathcal{L}\left\{u_d(t)\right\} \\ u_f(s) &= \mathcal{L}\left\{u_f(t)\right\} \\ s\,u_f(s) &= \mathcal{L}\left\{\frac{du_f(t)}{dt}\right\} \end{aligned} \tag{3.65}$$

and substituting $\tau = RC$

$$u_f(s) = u_d(s) - \tau s\,u_f(s) \tag{3.66}$$

the filter transfer function $F(s)$ can be formed

$$F(s) = \frac{u_f(s)}{u_d(s)} = \frac{1}{1 + \tau s}. \tag{3.67}$$

This first order filter has one pole at $s = \frac{-1}{\tau}$ and no zero. The filter behavior is shown in Fig. 3.14 (a) with the cutoff angular frequency equal to the 3 dB angular frequency ω_{3dB} (see also the definition of the 3 dB bandwidth in Sec. 2.1.3)

$$\omega_{3dB} = \frac{1}{\tau} = 2\pi f_{3dB} \tag{3.68}$$

In *Encinas* (1993) it is demonstrated that the optimization of bandwidth, damping factor and gain for this type of filter is severely limited when considering stability aspects. Therefore, this filter type is not applicable for a PLL implementation.

Passive and Active First Order Lead-Lag Filter

These types of 1st order filters have an additional phase-leading component (zero) and are typical for analog PLLs. The passive lead-lag filter in Fig. 3.14 (b) shows an ideal behavior with no nonlinearity. In accordance to Eq. (3.64), the voltage output $u_f(t)$ is

$$u_f(t) = u_d(t) - R_1 i_c(t) \tag{3.69}$$

and

$$u_f(t) = u_c(t) + R_2 i_c(t) \tag{3.70}$$

with the voltage $u_c(t)$ at the capacitor and the equal current i_c through the resistors with resistances R_1 and R_2 charging the capacitor

$$i_c = C\frac{du_c(t)}{dt}. \tag{3.71}$$

Taking the relation from Eq. (3.69)

$$\frac{u_d(t) - u_f(t)}{R_1} = C\frac{du_c(t)}{dt} \tag{3.72}$$

and $u_c(t)$ from Eq. (3.70)

$$u_c(t) = u_f(t) - \frac{R_2}{R_1}(u_d(t) - u_f(t)) \tag{3.73}$$

the relation between output and input voltage can be written as

$$\begin{aligned} u_d(t) - u_f(t) &= R_1C\frac{du_f(t)}{dt} - R_2C\frac{du_d(t)}{dt} + R_2C\frac{du_f(t)}{dt} \\ &= (R_1 + R_2)C\frac{du_f(t)}{dt} - R_2C\frac{du_d(t)}{dt}. \end{aligned} \tag{3.74}$$

The transfer function is finally given by the Laplace transforms from Eq. (3.65) and by the substitution of $\tau_1 = R_1C$ and $\tau_2 = R_2C$

$$F(s) = \frac{u_f(s)}{u_d(s)} = \frac{1 + \tau_2 s}{1 + (\tau_1 + \tau_2)s}. \tag{3.75}$$

This filter has a pole at $s = \frac{-1}{\tau_1 + \tau_2}$ and a zero at $s = \frac{-1}{\tau_2}$, see Fig. 3.14 (b). The zero is responsible for the phase-leading and is directly related to the damping factor ζ (see Sec. 4.1.1). An infinite frequency (short-circuit) accordingly produces a magnitude response defined by the two resistances

$$|F(\infty)| = \frac{\tau_2}{\tau_1 + \tau_2} = \frac{R_2}{R_1 + R_2} \tag{3.76}$$

The active lead-lag filter with its schematic diagram in Fig. 3.14 (c) consists of an operational amplifier, which is assumed to be ideal. This means the open-loop gain has to be infinite, the voltage difference between the negative $u_-(t)$ and positive $u_+(t)$ poles of the amplifier has to be zero (zero input voltage offset)

$$u_-(t) = u_+(t) \tag{3.77}$$

and no current at its input

$$i_-(t) = i_+(t) = 0. \tag{3.78}$$

The current through the resistor with resistance R_1 and charging the capacitor with capacitance C_1 is equal to the current through the resistor with resistance R_2 and charging the capacitor with capacitance C_2

$$\frac{u_d(t) - u_+(t)}{Z_1} = \frac{u_+(t) - u_f(t)}{Z_2} \tag{3.79}$$

with the corresponding impedances

$$Z_1 = R_1 + \frac{1}{j\omega C_1}$$
$$Z_2 = R_2 + \frac{1}{j\omega C_2}$$

(3.80)

Assuming $u_+(t) = 0$ and replacing $j\omega$, which corresponds to the Laplace operator s, the filter transfer function is

$$F(s) = \frac{u_f(s)}{u_d(s)} = -\frac{R_2 + \frac{1}{C_2 s}}{R_1 + \frac{1}{C_1 s}}$$
$$= -\frac{C_1}{C_2} \frac{1 + R_2 C_2 s}{1 + R_1 C_1 s}.$$

(3.81)

With the substitution of $\tau_1 = R_1 C_1$ and $\tau_2 = R_2 C_2$ the final form of the active lead-lag transfer function is given

$$F(s) = \frac{u_f(s)}{u_d(s)} = -K_f \frac{1 + \tau_2 s}{1 + \tau_1 s}$$

(3.82)

with the gain

$$K_f = \frac{C_1}{C_2}.$$

(3.83)

The pole of the transfer function is at $s = \frac{-1}{\tau_1}$ and the zero at $s = \frac{-1}{\tau_2}$, see also Fig. 3.14 (c). The filter response for an infinite frequency is accordingly

$$|F(\infty)| = K_f \frac{\tau_2}{\tau_1} = \frac{R_2}{R_1}.$$

(3.84)

A typical coefficient setting of $\tau_2 << \tau_1$ changes the transfer function of the passive lead-lag filter from Eq. (3.75) to

$$F(s) = \frac{1 + \tau_2 s}{1 + \tau_1 s}$$

(3.85)

which is equal to the active lead-lag transfer function in Eq. (3.82) except for the gain K_f.

Active First Order PI Filter

The active proportional-integral (PI) filter taken from control theory is visible in Fig. 3.14 (d) and is also a lead-lag filter. The operational amplifier is assumed as ideal with the properties of Eqs. (3.77) and (3.78).

Therefore, the current through the resistor with resistance R_1 is equal to the current through the resistor with resistance R_2

$$\frac{u_d(t) - u_+(t)}{R_1} = \frac{u_+(t) - u_{temp}(t)}{R_2}$$

(3.86)

with $u_{temp}(t)$ as an auxiliary voltage quantity between the second resistor and capacitor

$$u_{temp}(t) = u_+(t) - \frac{R_2}{R_1}(u_d(t) - u_+(t)).$$
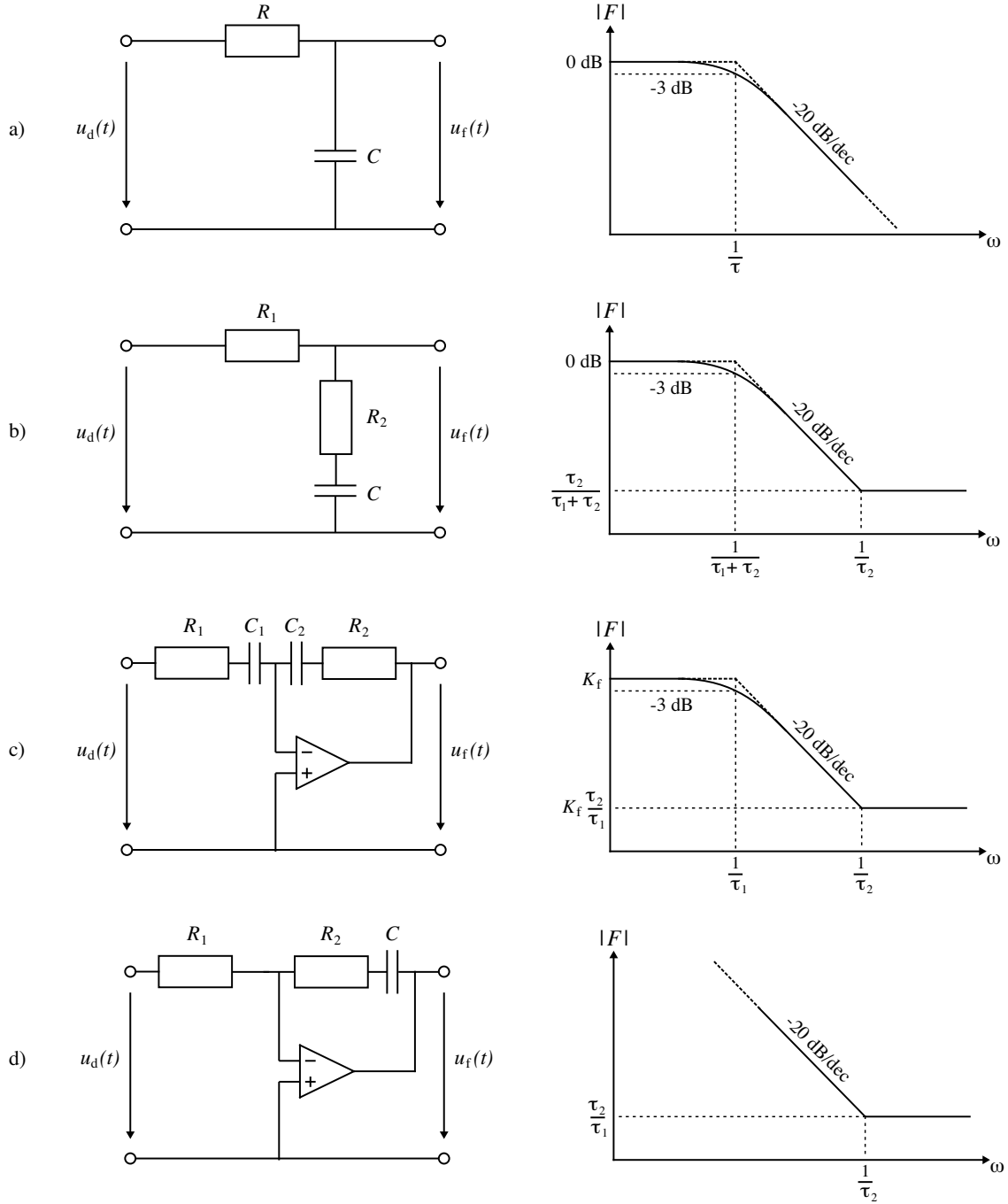
(3.87)

Figure 3.14: Schematic diagrams (left) and the corresponding magnitude responses in dB (right) for different first order LPF used in linear PLLs: A passive lag filter dependent on a simple RC component (a), a passive (b) and active (c) lead-lag filter, and an active proportional-integral (PI) filter (d).

The current charging the capacitor is equal to the current through the resistor with resistance R_2

$$C\frac{\mathrm{d}}{\mathrm{d}t}[u_{\text{temp}}(t) - u_{\text{f}}(t)] = \frac{u_+(t) - u_{\text{temp}}(t)}{R_2}. \tag{3.88}$$

Substituting $u_\text{temp}(t)$ from Eq. (3.87) into Eq. (3.88) we get

$$C\frac{\mathrm{d}}{\mathrm{d}t}[R_1 u_+(t) + R_2 u_+(t) - R_2 u_\text{d}(t) - R_1 u_\text{f}(t)] = u_\text{d}(t) - u_+(t). \tag{3.89}$$

The differential equation is finally given assuming $u_+(t) = 0$

$$R_1 C\frac{\mathrm{d}u_\text{f}(t)}{\mathrm{d}t} = -R_2 C\frac{\mathrm{d}u_\text{d}(t)}{\mathrm{d}t} - u_\text{d}(t). \tag{3.90}$$

With the corresponding Laplace transforms and the substitution of $\tau_1 = R_1 C$ and $\tau_2 = R_2 C$ the transfer function for an active second order PI filter is

$$F(s) = \frac{u_\text{f}(s)}{u_\text{d}(s)} = -\frac{1 + \tau_2 s}{\tau_1 s}. \tag{3.91}$$

The zero is at $s = \frac{-1}{\tau_2}$ according to the lead-lag filters with an ω_∞ equal to the ratio of the resistances

$$|F(\infty)| = \frac{\tau_2}{\tau_1} = \frac{R_2}{R_1}. \tag{3.92}$$

The transfer function has a pole at $s = 0$ with a theoretically infinite magnitude and behaves like an integrator (*Best*, 2003), see Fig. 3.14 (d). The DC gain $K_\text{DC} = F|(0)|$ is an important value for the system behavior concerning steady state errors (see Sec. 4.2.1). Approximately the same properties can also be achieved by an active lead-lag filter shown in Fig. 3.14 (c) with a large gain due to a large capacitance C_1, see Eq. (3.82). Compared to the passive filter, the active lead-lag and PI filters can be affected by noise of the operational amplifier and by a non-ideal behavior causing nonlinearity.

In contrast to the single path electric circuit as described above and shown in Fig. 3.14, the filter transfer function can also be found by two parallel paths in analogy to the control theory

$$F(s) = K_1 + \frac{K_2}{s} \tag{3.93}$$

with the coefficient K_1 [-] of the proportional path and K_2 [s^{-1}] of the integral path through the filter. The relationships to the electric quantities are finally

$$K_1 = \frac{\tau_2}{\tau_1} \quad \text{and} \quad K_2 = \frac{1}{\tau_1} \tag{3.94}$$

The impact of the filter parameters in dependency on mechanical analogies like the damping factor ζ and the natural frequency ω_n for the closed loop in the analog and digital domain are described in Sec. 4.1.1.

Second Order PI Filter

In addition to the insensitivity against Doppler frequency shifts, which is already guaranteed by first order loop filters, a GNSS receiver has an implemented second order loop filter in order to allow a stable tracking of LOS accelerations at least for the strong loop (signal tracking at high S/N_0), which guides the DLL and the PLL of weak signals. Second order filters and even higher orders can be built in exactly the same filter variants as described

for first order loop filters (passive, active lead-lag and active PI) adding an additional capacitor or impedance. Due to the large number of possible implementations as electric circuits, the direct relationship to electric quantities will not be discussed in the following. However, the additional poles of high order loop filters and accordingly of the entire loop are a stability issue (see Sec. 4.1). Taking the expression of the 1st order PI filter from Eq. (3.93), the expansion of the two parallel paths trough the filter to a third one with an additional integrator leads to a general description of a 2nd order PI filter (neglecting high frequency effects)

$$F(s) = K_1 + \frac{K_2}{s} + \frac{K_3}{s^2} \tag{3.95}$$

with its filter parameters K_1 [-], K_2 [s^{-1}], and K_3 [s^{-2}]. This is a general definition and can be theoretically expanded to an arbitrary number of integrators. Note that this formulation increases not only the number of poles, but also the number of zeros. The influence of different PLL types is shortly described in Sec. 4.1 and 4.2.

For the corresponding implementation into the discrete time domain, see Sec. 7.1.1.

3.2.5 Numerically Controlled Oscillator and Accumulator

The digital complement to an analog voltage controlled oscillator (VCO), that generates the new estimate of the replica code and carrier phase, is the numerically controlled oscillator (NCO) or also called digital controlled oscillator (DCO). The NCO is one of the baseband functions implemented in hardware and consists of a bit adder and of a hold register that overflows at a specific time interval which is corresponding to the estimated replica code chipping rate in the case of a code NCO or to the Doppler-shifted frequency for the carrier NCO. The fundamental NCO frequency is given by the frequency synthesizer that generates clock samples with a frequency f_s and a constant value M (see Fig. 3.7) that sets the output frequency equal to the spread code frequency f_c (code NCO) and to the IF frequency f_{IF} (carrier NCO), comparable to the fundamental VCO angular frequency ω_0 in Eq. (3.14). Dependent on the NCO bit number N, the bias M_c for the code NCO is given by

$$M_c = f_c \frac{2^N}{f_s} \tag{3.96}$$

and M_p for the carrier NCO by

$$M_p = f_{IF} \frac{2^N}{f_s}. \tag{3.97}$$

These increments are summed and build a staircase function that overflows and sets the counter to zero if the total count length 2^N is reached, which corresponds to a phase state of 2π (see Fig. 3.15). Assuming a first order digital filter according to Eq. (7.10) preserving the doppler shift frequency, the filter output signal $\theta_{f,a}$ after each loop update T

$$\theta_{f,a} = b_0\,\theta_{d,a} + b_1\,\theta_{d,a-1} - a_1\,\theta_{f,a-1} \tag{3.98}$$

can be set per clock cycle increment T_s due to the constant value over the loop update T

$$\Delta\theta_{f,a} = \theta_{f,a} \frac{T_s}{T}. \tag{3.99}$$

The filtered phase increment $\Delta\theta_{\mathrm{f},a}$ is added to the constant value M_{p}

$$M_{\theta}(t_a) = 2^N \Delta\theta_{\mathrm{f},a} + M_{\mathrm{p}} \tag{3.100}$$

in order to obtain the new NCO phase state $\tilde{\theta}_{a+1}$ and frequency $\tilde{f}_{a+1}$ for the next loop iteration

$$\tilde{f}_{a+1} = \frac{f_{\mathrm{s}}}{2^{\mathrm{N}}} M_{\theta}(t_a). \tag{3.101}$$

The carrier NCO staircase functions are finally mapped onto the trigonometric sine and cosine functions by a phase-to-amplitude converter (PAC) visible in Fig. 3.15. Between a loop update the NCO ejects the synthesized signals for each fundamental clock sample T_{s} with its constant frequency increments $\tilde{f}_k$ and phase state $\tilde{\theta}_k$ for the downconversion process in Eq. (3.21).

After each loop output to the NCO the filtered replica Doppler phase increment $\Delta\theta_{\mathrm{f},a}$ is maintained by a phase accumulator that consists of a fractional ϕ [cycles] and integer N_ϕ part [cycles]. The accumulator status at t_a is according to *Ward et al.* (2006)

$$
\begin{aligned}
\phi_{\mathrm{temp},a} &= \phi_{a-1} + \Delta\theta_{\mathrm{f},a}\frac{T}{T_{\mathrm{s}}} \\
\phi_a &= \mathrm{frac}(\phi_{\mathrm{temp},a}) \\
N_{\phi,a} &= N_{\phi,a-1} + \mathrm{floor}(\phi_{\mathrm{temp,a}}).
\end{aligned}
\tag{3.102}
$$

where the subscript temp indicates a temporary variable in order to simplify the formalism. The phase accumulator is initialized after a successful acquisition and first lock $t_{a=0}$. The initial values for ϕ_0 and $N_{\phi,0}$ are typically zero. Note that the constant value M_{P} is not added to the accumulator because it represents an offset referred to the artificial intermediate frequency, which would be eliminated anyway during the differential processing.

The code NCO works in a similar way as the frequency synthesizing by the carrier NCO. The code NCO input composed of the filtered fractional chip error $\Delta\tau_{\mathrm{f}}$ per clock cycle according to Eq. (3.99)

$$\Delta\tau_{\mathrm{f},a} = \tau_{\mathrm{f},a}\frac{T_{\mathrm{s}}}{T} \tag{3.103}$$

and the constant offset M_{c}

$$M_{\tau}(t_a) = 2^N \Delta\tau_{\mathrm{f},a} + M_{\mathrm{c}} \tag{3.104}$$

is added until the hold register overflows at one code chip with a final output frequency $\tilde{f}_{\mathrm{c}}$, which is used by the code generator for the next loop iteration

$$\tilde{f}_{\mathrm{c},a+1} = \frac{f_{\mathrm{s}}}{2^{\mathrm{N}}} M_{\tau}(t_a). \tag{3.105}$$

In order to enable the correlation with early and late code replicas dependent on a early-minus-late chip spacing w, a second code NCO output frequency for the 2-bit shift register is required that is $2/w$ faster than the nominal code frequency $\tilde{f}_{\mathrm{c}}$. The code phase increments $\Delta\tau_{\mathrm{f},a}$ plus the code bias increment ΔM_{c} per clock cycle

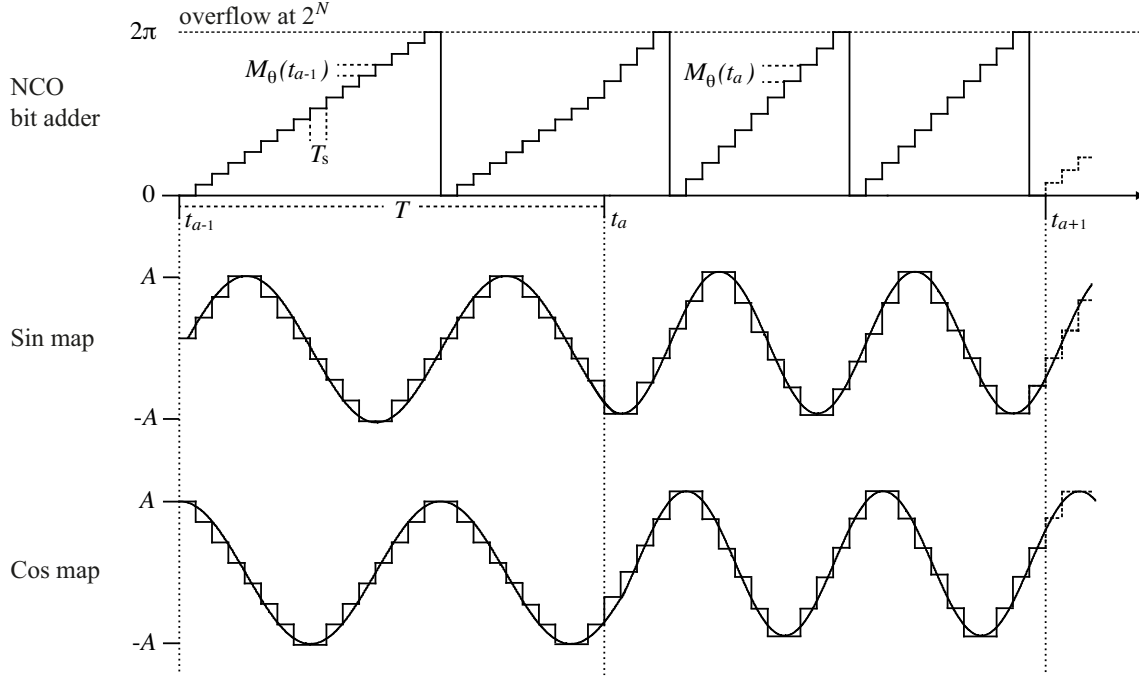$$\Delta M_{\mathrm{c}} = \frac{M_{\mathrm{c}}}{2^N} \tag{3.106}$$

Figure 3.15: The carrier NCO staircase adder with a holding register that overflows reaching the phase state 2π which is equal to the 2^N with bit number N. The phase increments M_θ per clock cycle T_s for each loop update after T define the new NCO frequency for the next loop iteration while mapping the staircase function on the trigonometric sine and cosine functions.

are accumulated and preserved in the code accumulator (in contrary to the carrier phase accumulator without the constant offset). A typical code accumulator contains three counters (*Ward et al.*, 2006), the Z, X1 and P counters, see also the legacy GPS code descriptions in Sec. 2.2.1. The Z counter accumulates the GPS increments of 1.5 s and sets the count to zero one step before the maximum is reached (one week = 403'200 Z counts). The X1 (10 X1 per one C/A-code chip) counts the integer P chips per Z count (1.5 s) and rolls over one short of the maximum value 15'345'000. The P counter containing the fractional code chip increments has the same length as the code NCO adder

$$
P_{\text{temp},a} = P_{a-1} + (\Delta\tau_{\text{f},a} + \Delta M_{\text{c}})\frac{T}{T_s}
$$

$$
P_a = \text{frac}(P_{\text{temp},a})
$$

$$
X_{\text{temp},a} = X1_{a-1} + \text{floor}(P_{\text{temp},a}) \tag{3.107}
$$

$$
X1_a = X_{\text{temp},a} \text{ modulo } 15'345'000
$$

$$
Z_a = [Z_{a-1} + \text{floor}(X_{\text{temp},a}/15'345'000)] \text{ modulo } 403'200.
$$

The initial states of the code accumulator are set during the acquisition process and are initially ambiguous for the C/A-code with a period of 1 ms, see time relationship in Sec. 3.2.6.

The spreading code frequency $\tilde{f}_c$ from the code NCO and the code state time relationship from the code accumulator are the inputs for the code generator with its code setter and shift register in order to produce a new set of replica codes $\tilde{CA}(t_k)$ for each NCO clock sampling interval T_s.

The code NCO is often aided by the carrier loop due to the high DLL jitter. The filter outputs of the PLL have to be scaled first by a scale factor r because the Doppler effect is inversely proportional to the wavelength, and therefore much smaller for the spreading code with frequency f_c. Even if the carrier is downconverted to IF the Doppler is still referred to the L-band frequency f_{RF}

$$r = \frac{f_c}{f_{RF}}. \tag{3.108}$$

The converted code phase error from the PLL is already included in $\tau_{f,a}$ of Eq. (3.103). Due to the support of the PLL that basically covers all LOS dynamics, the DLL order can be lowered and the filter bandwidth narrowed what is additionally reducing the DLL noise and increasing the measurement accuracy if the carrier tracking is locked. Additionally, the code filter update can be reduced while summing the code discriminator outputs. However, the code NCO has to be updated at each PLL NCO update even though the code filter output is not updated, but aided by the carrier tracking (*Ward et al.*, 2006).

This aiding concept is also used for weak carrier tracking, e. g. carrier phase derived from the P(Y)-code component (see Sec. 5.3.2). The estimates derived from a strong signal tracking channel (e. g. L1 based on the C/A-code component) are scaled to the corresponding weak signal wavelength. Finally, the tracking performance of dynamics is guaranteed while the reliability of tracking low signal strength (e. g. low elevation angles) is being improved. For extremely high dynamics, even too large for the strong loops, an external sensor can be coupled to the PLL, e. g. leading to inertia-aided carrier tracking loops (*Chiou*, 2005).

3.2.6 Measurement Extraction and Forming of the Observables

As described in the previous sections the natural measurements of a GNSS receiver are replica code phases and replica carrier Doppler phases in case of a DLL and PLL. The measurements are retrieved from the discriminators ($\tau_{d,a}$ and $\theta_{d,a}$), are filtered ($\tau_{f,a}$ and $\theta_{f,a}$) and finally maintained by the accumulators according to Eqs. (3.102) and (3.107). The main concepts of position computation for code based navigation or highly accurate differential surveying and geodetic applications include pseudoranges and integrated carrier Doppler phases in their corresponding observation equations (see Sec. 4.3). Additionally, delta pseudoranges can be formed by the replica carrier Doppler phase measurements for velocity based applications. The relationships between the replica code phases in the receiver and the pseudoranges and between the replica carrier Doppler phases and the integrated Doppler phases and delta pseudoranges are described in the following.

The pseudorange $R^i(t_n)$ [m] at a specific measurement output epoch t_n referred to the internal receiver time frame (RTF) can be expressed as the difference between the receive time $T_r(t_n)$ and the transmit time $T_t^i(t_n)$ of a satellite i

$$R^i(t_n) = c\left[T_r(t_n) - T_t^i(t_n)\right] \tag{3.109}$$

with the speed of light c [m/s]. While successfully correlating the transmitted PRN code with a replica PRN code in the receiver, the transmit time corresponds to the code phase offset with respect to the beginning of the week. If the receiver is able to retrieve the

satellite transmit time from the DLL, the pseudorange according to Eq. (3.109) can be formed. Each transmitted PRN code epoch is synchronized to GPS time by the satellite timing hardware with a maximum deviation of 1 ms specified in the corresponding ICDs. This deviation (satellite clock offset) is still included in $T_t^i(t_n)$ and has to be corrected later during the navigation process (the satellite clock bias is transmitted within the navigation message). Therefore the input to the navigation processor is typically the transmit time and the receive time instead of the pseudorange. The measurements are scheduled at a receiver epoch t_n (counter) which is internally clocked and corresponds to a receive time maintained by the navigation processor. Especially at the beginning of a measurement session, the receive time is not perfectly aligned to the true GPS time. If this time offset is not known, a first approximation of the receive time can be obtained by adding a mean propagation time to the first extracted satellite transmit time of about 75 ms (the propagation time changes from horizon to zenith from about 85 ms to about 65 ms). Afterwards, the receiver clock bias can be extracted from a first navigation solution in order to adjust the receive time.

As already described in Sec. 3.2.5 the code phase state time keeping is achieved by the code accumulator which is skewed to the RTF in order to prevent the predetection integration over the navigation bit transitions. The skew time T_{sk} is obtained from the bit synchronization process described in Sec. 3.2.2. Due to the constant NCO frequency and code phase state during a loop update the transmit time measurement $T_t^i(t_n)$ can be obtained by an error-free forward propagation of the last code accumulator update to the nearest measurement epoch t_n by the skew time T_{sk}

$$
\begin{aligned}
P_{\text{temp},n} &= P_a + (\Delta\tau_{f,a} + \Delta M_c)\frac{T_{sk}}{T_s} \\
P^i(t_n) &= \text{frac}(P_{\text{temp},n}) \\
X_{\text{temp},n} &= X1_a + \text{floor}(P_{\text{temp},n}) \\
X1^i(t_n) &= X_{\text{temp},n} \text{ modulo } 15'345'000 \\
Z^i(t_n) &= [Z_a + \text{floor}(X_{\text{temp},n}/15'345'000)] \text{ modulo } 403'200
\end{aligned}
\tag{3.110}
$$

with a measurement resolution of 2^{-N} of a code chip (N is the bit number of the NCO adder) and the corresponding time conversion

$$
T_t^i(t_n) = [P^i(t_n) + X1^i(t_n)]/(10.23 \times 10^6) + Z^i(t_n) \times 1.5.
\tag{3.111}
$$

The ambiguity of the C/A-code phase state in the accumulator can be solved by the following GPS time relationship. Each subframe (6 s) of the navigation message modulated on the C/A-code starts with a TLM word followed by a HOW containing the first Z-count (1.5 s) of each subframe. Assuming the bit synchronization is concluded within 1 ms, one of the C/A-code periods is synchronized with the beginning of the navigation data bit of 20 ms. However, there are still 20 C/A-codes within a data bit. The ambiguity is solved when the X1-count rolls over (X1 = zero), and the Z-count is set to the HOW value at the beginning of the next subframe (X1 = zero). The C/A-code is now perfectly aligned to the first bit of the TLM word at data bit transition (*Ward et al.*, 2006).

The replica Doppler phase extraction from the phase accumulator is similar to the measurement extraction from the code accumulator. In order to build the integrated Doppler

phase observables $\Phi^i(t_n)$ [cycles] for a satellite i

$$\Phi^i(t_n) = N^i_\phi(t_n) + \phi^i(t_n), \tag{3.112}$$

the fractional $\phi^i(t_n)$ and integer $N^i_\phi(t_n)$ Doppler phase can be obtained by forward propagation of the replica Doppler phase increment per clock cycle $\theta_{\mathrm{f},a}$ by the skew time T_{sk} after the last accumulator update

$$
\begin{aligned}
\phi_{\mathrm{temp},n} &= \phi_a + \Delta\theta_{\mathrm{f},a}\frac{T_{\mathrm{sk}}}{T_{\mathrm{s}}} \\
\phi^i(t_n) &= \mathrm{frac}(\phi_{\mathrm{temp},n}) \\
N^i_\phi(t_n) &= \mathrm{floor}(\phi_{\mathrm{temp},n}).
\end{aligned}
\tag{3.113}
$$

The Doppler output $D(t_n)$ [cycles/s] from the receiver baseband processor for velocity dependent applications corresponds to the delta pseudorange over a defined (smoothing) period, which is at least the scheduled RTF measurement interval T_{RTF} or a multiple integer m. It is theoretically possible to retrieve the delta pseudoranges from the code tracking loop and its accumulator or directly from a frequency locked loop (FLL), see acquisition in Sec. 3.2.7. However, the measurements from a DLL and FLL are magnitudes more noisy than those derived from a PLL. Therefore, the delta pseudorange $D_\phi(t_n)$ is formed by the measurement extraction of $\phi^i(t_n)$ and $N^i_\phi(t_n)$ from the carrier accumulator according to Eq. (3.113)

$$D_\phi(t_n) = \frac{1}{mT_{\mathrm{RTF}}}[N^i_\phi(t_n) - N^i_\phi(t_{n-m}) + \phi^i(t_n) - \phi^i(t_{n-m})]. \tag{3.114}$$

It has been shown that the measurements are extracted with an interval of T_{RTF}. This is the highest sampling the receiver processor cooperates with the navigation processor for position computation and receiver clock error estimation. The output sampling interval T_{p} of pseudoranges, integrated Doppler phases, and delta pseudoranges (Doppler) to an external user or navigation solution is at least T_{RTF} or an integer multiple

$$T_{\mathrm{s}} << T \le T_{\mathrm{RTF}} \le T_{\mathrm{p}}. \tag{3.115}$$

3.2.7 Acquisition

The acquisition is a search process in the range and frequency dimension. The range search is typically started with the C/A-code or another short PRN code (see modern GNSS signals) due to the limited phase states, e.g. 1023 replica phase states for the C/A-code. In the frequency domain a large Doppler range has to be scanned. A frequency locked loop (FLL) consists of a frequency discriminator instead of a phase discriminator in case of a PLL. During the acquisition a FLL is often used because the speed during frequency search is higher compared to a PLL and not the highest accuracy is required. Each search bin for the code phase and Doppler is statistically tested by a search algorithm comparing the estimated envelopes with a specific threshold, e.g. a tong search detector or an M of N search detector described by *Ward et al.* (2006). The time to first lock is strongly dependent on the initial knowledge about the available satellite constellation (almanac), the user

position and velocity, and the receiver time offset to true GPS time. The search pattern is correspondingly smaller or larger. Modern multichannel GNSS receivers use a huge number of correlators in parallel in order to speed up the search process. However, time to first fix (navigation solution) can take up to 30 seconds when only reading the ephemeris data. If the ephemeris data is not available, the whole almanac has to be acquired over 12.5 minutes. The almanac data is valid over several days for the requirements of a satellite search process. Therefore, the receivers store the almanac data and user position from the last operating session. With the knowledge about the satellite and user positions the Doppler frequency can approximately be calculated, otherwise the Doppler search commonly starts at zero Doppler which is equal to the IF frequency defined by the LOs. After the detection of the corresponding code phase and Doppler frequency and successful bit synchronization, the initial states of the accumulators can be set with the time relationships explained in the previous section, while actually coherently tracking the code phases and carrier Doppler phases. With a least 4 acquired satellites a first position and receiver time error computation is possible.

4 Carrier Tracking Modeling

The different components, their functionalities, and a possible implementation in a GNSS receiver for the tracking of PRN codes and carrier phases have been introduced in the previous section. For the characterization of the whole system containing different components, a good model is essential while understanding the limitations due to applied assumptions. In the literature (*Gardner*, 2005; *Best*, 2003; *Stensby*, 1997; *Encinas*, 1993) good models of different complexity are existing. A simple linear model is described in Sec. 4.1 for 2nd and 3rd order PLLs focusing on the behavior dependent on commonly used loop parameters. The expected tracking errors and limitations, especially LOS dynamics and the carrier jitter induced by thermal noise and oscillators, are analyzed in Sec. 4.2 followed by the geodetic observation equations including all internal and external signal perturbations in Sec. 4.3.

4.1 Linear PLL Modeling

Even though PLLs are inherently nonlinear systems, the approximation by a linear model is valid for small phase errors in case of a stable tracking. The linear assumption has the huge advantage of allowing the description of the PLL functionalities by transfer functions. The concept of transfer functions has already been used in Sec. 3.2.4 related to the loop filters which define the relationship between an input and output of a linear system for a specific domain of transformation. Further, the overall loop transfer function can be built by the transfer functions of each single system component. For the linear modeling of the analog closed-loop, the baseband system with the three main components described in Sec. 3.2.1 and illustrated in Fig. 3.8 is used with the corresponding notations. In case of the PLL the phase is the most interesting variable for the system and performance characterization while using the Laplace domain with its transformation notation $\mathcal{L}\{\cdot\}$. The transform domain of the phases is indicated by its arguments in the brackets,

$$
\begin{aligned}
\theta_1(s) &= \mathcal{L}\left\{\theta_1(t)\right\} \\
\theta_2(s) &= \mathcal{L}\left\{\theta_2(t)\right\} \\
\theta_{\mathrm{d}}(s) &= \mathcal{L}\left\{\theta_{\mathrm{d}}(t)\right\} \\
\theta_{\mathrm{f}}(s) &= \mathcal{L}\left\{\theta_{\mathrm{f}}(t)\right\}.
\end{aligned}
\tag{4.1}
$$

The filter transfer function $F(s)$ is already defined in Sec. 3.2.4 as

$$
F(s) = \frac{u_{\mathrm{f}}(s)}{u_{\mathrm{d}}(s)}
\tag{4.2}
$$

with the Laplace transforms from Eq. (3.65). The VCO angular frequency offset $\Delta\omega$ to the center frequency is given in Eq. (3.20) which is equal to the time derivative of the VCO output phase $\mathrm{d}\theta_2(t)/\mathrm{d}t$. The VCO output phase in the Laplace domain is finally

$$\theta_2(s) = \frac{K_\mathrm{v} u_\mathrm{f}(s)}{s} \tag{4.3}$$

that acts like a perfect integrator. Taking Eq. (4.2) and introducing it into Eq. (4.3) we get

$$\theta_2(s) = \frac{K_\mathrm{v} F(s)}{s} u_\mathrm{d}(s). \tag{4.4}$$

The phase discriminator was introduced as a simple multiplier in Eq. (3.19) with its output signal u_d directly proportional to the phase error θ_d

$$u_\mathrm{d}(s) = K_\mathrm{d}\theta_\mathrm{d}(s). \tag{4.5}$$

The same assumption of small tracking errors has been applied to the discriminator outputs in Sec. 3.2.3 in order to guarantee linearity. Combining Eq. (4.5) and (4.4) the open-loop transfer function $G(s)$ can be built as

$$G(s) = \frac{\theta_2(s)}{\theta_\mathrm{d}(s)} = \frac{K_\mathrm{d} K_\mathrm{v} F(s)}{s}. \tag{4.6}$$

With the substitution of the discriminator output phase by

$$\theta_\mathrm{d}(s) = \theta_1(s) - \theta_2(s) \tag{4.7}$$

and rearranging the terms, the closed-loop transfer function or system transfer function is finally given by

$$\begin{aligned} H(s) &= \frac{\theta_2(s)}{\theta_1(s)} = \frac{G(s)}{1 + G(s)} \\ &= \frac{K_\mathrm{d} K_\mathrm{v} F(s)}{s + K_\mathrm{d} K_\mathrm{v} F(s)}. \end{aligned} \tag{4.8}$$

The closed-loop transfer function from Eq. (4.8) represents the linear model used in the next sections assuming linear discriminator output and perfect VCO and filter integrators. The order and type of the PLL is defined by the loop filter transfer function $F(s)$. The degree of the numerator of $H(s)$ (number of poles) defines the order of the PLL. Taking a first order loop filter, the PLL is finally of 2nd order due to the additional VCO integrator. A 2nd order loop filter leads to a 3rd order PLL, respectively. As already mentioned in Sec. 3.2.4, the zero is essential for loop stability. The number of zeros of $H(s)$ is termed as the type of a PLL. The lead-lag or PI filters lead to type-2 PLLs which are discussed in the following.

4.1.1 2nd Order Type-2 PLL

Taking the 1st order lead-lag filter transfer function from Eq. (3.85) (assuming $\tau_2 << \tau_1$) the transfer function according to Eq. (4.8) is

$$H(s) = \frac{\frac{K_\mathrm{d} K_\mathrm{v}(\tau_2 s + 1)}{(\tau_1 s + 1)}}{\frac{(\tau_1 s + 1)s + K_\mathrm{d} K_\mathrm{v}(\tau_2 s + 1)}{(\tau_1 s + 1)}} = \frac{K_\mathrm{d} K_\mathrm{v}\tau_2 s + K_\mathrm{d} K_\mathrm{v}}{\tau_1 s^2 + (K_\mathrm{d} K_\mathrm{v}\tau_2 + 1)s + K_\mathrm{d} K_\mathrm{v}} \tag{4.9}$$

and with an additional filter gain K_f for the active lead-lag filter from Eq. (3.82) we get the transfer function

$$H(s) = \frac{\frac{K_\mathrm{d}K_\mathrm{v}K_\mathrm{f}(\tau_2 s+1)}{(\tau_1 s+1)}}{\frac{(\tau_1 s+1)s+K_\mathrm{d}K_\mathrm{v}K_\mathrm{f}(\tau_2 s+1)}{(\tau_1 s+1)}} = \frac{K_\mathrm{d}K_\mathrm{v}K_\mathrm{f}\tau_2 s + K_\mathrm{d}K_\mathrm{v}K_\mathrm{f}}{\tau_1 s^2 + (K_\mathrm{d}K_\mathrm{v}K_\mathrm{f}\tau_2 + 1)s + K_\mathrm{d}K_\mathrm{v}K_\mathrm{f}}. \tag{4.10}$$

For the 1st order active PI filter with $F(s)$ from Eq. (3.91) the closed-loop transfer function is accordingly

$$H(s) = \frac{\frac{K_\mathrm{d}K_\mathrm{v}(\tau_2 s+1)}{\tau_1 s}}{\frac{\tau_1 s^2+K_\mathrm{d}K_\mathrm{v}(\tau_2 s+1)}{\tau_1 s}} = \frac{K_\mathrm{d}K_\mathrm{v}\tau_2 s + K_\mathrm{d}K_\mathrm{v}}{\tau_1 s^2 + K_\mathrm{d}K_\mathrm{v}\tau_2 s + K_\mathrm{d}K_\mathrm{v}}. \tag{4.11}$$

Note that the minus sign in $F(s)$ (see Eq. (3.82) and (3.91)), indicating a phase inversion in the active filters, is neglected assuming that it will be canceled out and the loop is poled correctly. This is crucial for a stable feedback loop (*Gardner*, 2005). The 2nd order type-2 transfer functions in Eq. (4.9), (4.10) and (4.11) are overparameterized. Typically a set of two parameters is used in analogy to mechanical systems, the natural frequency ω_n [rad/s] and the dimensionless damping factor ζ

$$\omega_\mathrm{n} = \sqrt{\frac{K_\mathrm{d}K_\mathrm{v}}{\tau_1}} \quad \text{and} \quad \zeta = \frac{\omega_\mathrm{n}\tau_2}{2}. \tag{4.12}$$

or

$$\omega_\mathrm{n} = \sqrt{\frac{K_\mathrm{d}K_\mathrm{v}K_\mathrm{f}}{\tau_1}} \tag{4.13}$$

for the active lead-lag filter. In practice, PLLs are designed as so-called high-gain loops which fulfill the following conditions (*Best*, 2003)

$$K_\mathrm{d}K_\mathrm{v} >> \omega_\mathrm{n} \quad \text{or} \quad K_\mathrm{d}K_\mathrm{v}K_\mathrm{f} >> \omega_\mathrm{n} \tag{4.14}$$

Therefore, all three transfer functions of a 2nd order type-2 PLL are now given in the well known form

$$H(s) = \frac{2\zeta\omega_\mathrm{n}s + \omega_\mathrm{n}^2}{s^2 + 2\zeta\omega_\mathrm{n}s + \omega_\mathrm{n}^2}. \tag{4.15}$$

The DC gain $K_\mathrm{DC} = K_\mathrm{d}K_\mathrm{v}|F(0)|$ for a type-2 loop is infinite due to the additional integrator compared to the finite K_DC for a type-1, which is achieved by a lag filter from Eq. (3.67). An infinite DC gain is important in order to reduce the steady-state error θ_ω from a frequency step $\Delta\omega$ (see Sec. 4.2.1) to zero. This is the reason why type-2 PLLs are popular and widely-used.

The magnitude $|H(j\omega)|$ and phase $\arg(|H(j\omega)|)$ of the response dependent on different damping factors are illustrated as a Bode plot in Fig. 4.1 for a 2nd order type-2 PLL. The frequency is normalized by the natural frequency ω_n. It is evident that the transfer function $H(s)$ performs as a lowpass operator with a small amplitude response for small frequencies and attenuation outside the loop bandwidth. The damping factor is crucial for the dynamic tracking capability and performance. A small damping (< 0.5) generates a large overshoot in contrary to a large damping (> 1) that shows a sluggishness against dynamics (see Fig. 4.1). A damping of $1/\sqrt{2} = 0.707$ is an often preferred value in practice which corresponds to a 2nd order Butterworth lowpass filter. Due to the large dependency on the damping factor, the natural frequency ω_n as a measure for the loop bandwidth is often replaced by the equivalent noise bandwidth B_L defined in Sec. 4.1.3.
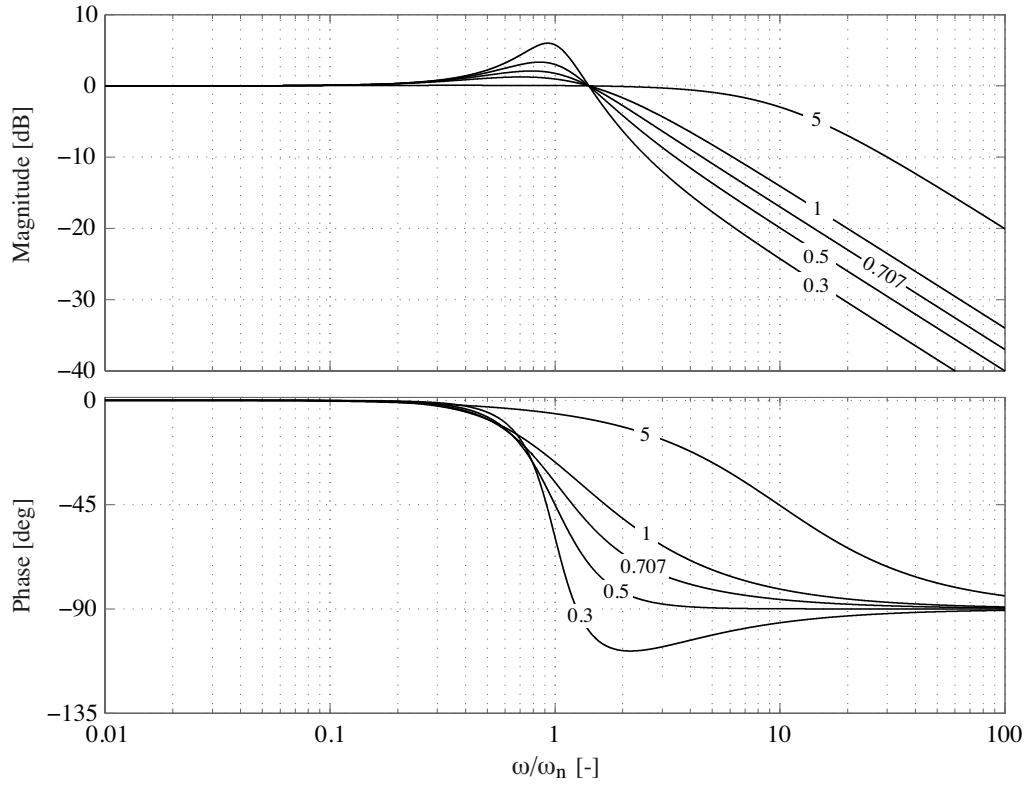
Figure 4.1: The magnitude and phase response of a 2nd order type-2 PLL according to Eq. (4.15) with damping factors ζ [-] of 0.3, 0.5, 0.707, 1 and 5. The frequency is normalized by the natural frequency ω_n.

4.1.2 3rd Order Type-3 PLL

The parameter set of natural frequency and damping is applicable for all 2nd order PLLs. For higher orders the mechanical analogy is meaningless even though the definition of the natural frequency is expanded. If the filter transfer function $F(s)$ of the second order PI filter from Eq. (3.95) is put into Eq. (4.6), the close-loop 3rd order type-2 PLL is expressed by its system transfer function as follows

$$\begin{aligned} G(s) &= \frac{K_\mathrm{d}K_\mathrm{v}}{s}\left(K_1 + \frac{K_2}{s} + \frac{K_3}{s^2}\right)\\ &= \frac{K}{s}\left(1 + \frac{K_2}{K_1 s} + \frac{K_3}{K_1 s^2}\right) \end{aligned} \tag{4.16}$$

with the loop gain K [rad/s]

$$K = K_\mathrm{d}K_\mathrm{v}K_1. \tag{4.17}$$

The loop gain is mainly determined by the proportional filter parameter K_1 and is the key value for loop response and bandwidth, see also *Gardner* (2005). The loop gain can also be applied to 2nd order type-2 PLLs introduced in Sec. 4.1.1.

The closed loop transfer function for a 3rd order type-3 PLL is according to Eq. (4.16) and

(4.8)

$$H(s) = \frac{Ks^2 + K\frac{K_2}{K_1}s + K\frac{K_3}{K_1}}{s^3 + Ks^2 + K\frac{K_2}{K_1}s + K\frac{K_3}{K_1}}. \qquad (4.18)$$

An example of setting the parameters in close analogy to a 2nd order loop is given by *Karras* (1965) with the values

$$\begin{aligned} \frac{K_2}{K_1} &= \frac{2}{3}\omega_{\mathrm n} \\ \frac{K_3}{K_1} &= \left(\frac{1}{3}\omega_{\mathrm n}\right)^2. \end{aligned} \qquad (4.19)$$

Even though a damping factor does not appear in a cubic equation, setting

$$K = \frac{9}{4}\omega_{\mathrm n} \qquad (4.20)$$

and putting the coefficients into Eq. (4.18), the analogy to a 2nd order PLL is visible in its denominator. Compared to Eq. (4.15), the denominator corresponds to a damping $\zeta = 1$

$$H(s) = \frac{\frac{9}{4}\omega_{\mathrm n}s^2 + \frac{6}{4}\omega_{\mathrm n}^2 s + \frac{1}{4}\omega_{\mathrm n}^3}{(s^2 + 2\omega_{\mathrm n}s + \omega_{\mathrm n}^2)(s + \frac{1}{4}\omega_{\mathrm n})} \qquad (4.21)$$

and in a general form

$$H(s) = \frac{c_2 s^2 + c_1 s + c_0}{d_3 s^3 + d_2 s^2 + d_1 s + d_0} \qquad (4.22)$$

with

$$\begin{aligned} c_0 = d_0 &= 0.25\,\omega_{\mathrm n}^3 \\ c_1 = d_1 &= 1.50\,\omega_{\mathrm n}^2 \\ c_2 = d_2 &= 2.25\,\omega_{\mathrm n} \\ d_3 &= 1. \end{aligned} \qquad (4.23)$$

Another set of coefficients, which can often be found in GNSS literature and publications, is provided by *Ward et al.* (2006) as follows

$$\begin{aligned} c_0 = d_0 &= 1\,\omega_{\mathrm n}^3 \\ c_1 = d_1 &= 1.1\,\omega_{\mathrm n}^2 \\ c_2 = d_2 &= 2.4\,\omega_{\mathrm n} \\ d_3 &= 1. \end{aligned} \qquad (4.24)$$

The 3rd order type-3 PLLs magnitude and phase responses with the coefficients from Eq. (4.23) (solid) and (4.24) (dashed) are given in Fig. 4.2 dependent on the normalized natural frequency $\omega_{\mathrm n}$. The peak gain frequency for the 3rd order PLL by Ward (dashed) is below $\omega_{\mathrm n}$ with a slightly higher magnitude compared to the solid curve. However, the transient response is within a more narrow bandwidth than for the PLL from *Karras* (1965) which strongly attenuates after $2\omega_{\mathrm n}$. The phase response is significantly different. The dashed curve shows a small positive phase shift at the beginning with a strong phase response below $\omega_{\mathrm n}$. The solid curve with the coefficients from Eq. (4.23) shows a similar behavior as the 2nd order type-2 PLL in Fig. 4.1.
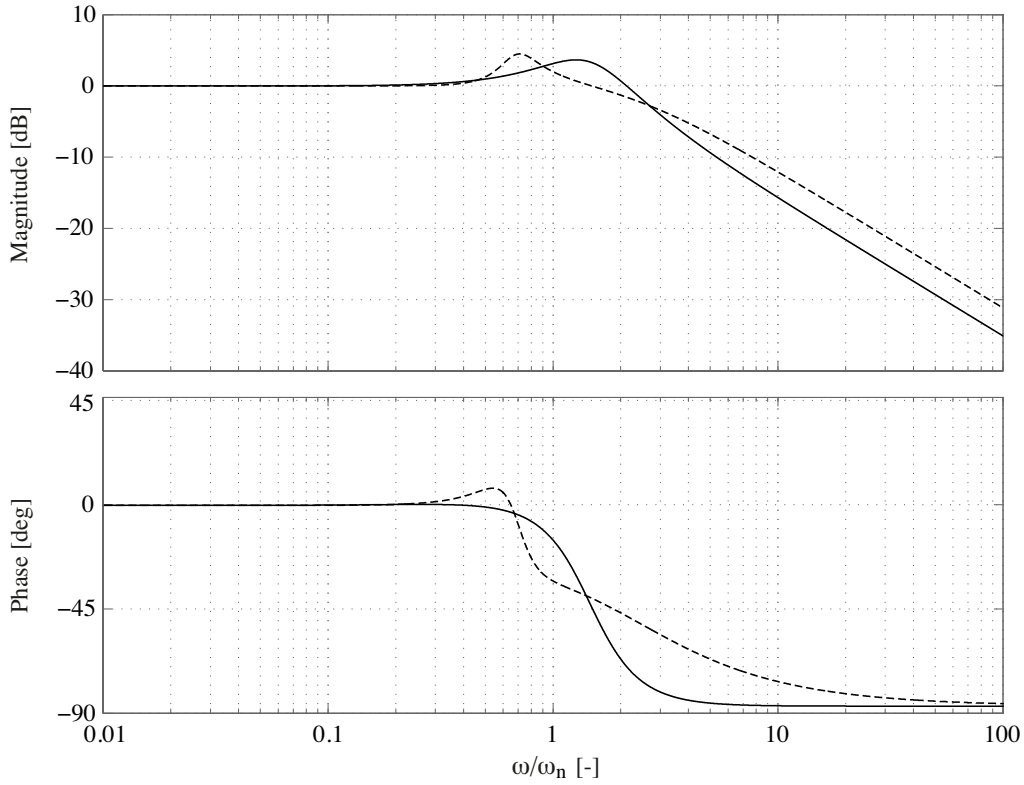
Figure 4.2: The magnitude and phase responses of a 3rd order type-3 PLL with the coefficient set from Eq. (4.23) (solid) and Eq. (4.24) (dashed). The frequency is normalized by the natural frequency ω_{n}.

4.1.3 Equivalent Noise Bandwidth of Linear PLL Models

In combination with a PLL and its filter, an equivalent noise bandwidth is an often used concept for describing the tracking characteristics instead of the 3-dB bandwidth (see Sec. 2.1.3). The relationship between the single-sided equivalent noise bandwidth B_{L} and the 3-dB bandwidth W_{3dB} dependent on the natural frequency ω_{n} of the loop is described in *Karras* (1965) for different loop orders and filter transfer functions.

As defined in Sec. 2.1.3 and visualized in Fig. 2.5 (right) the bandwidth B_{L} includes the positive frequencies representing an equivalent rectangular filter. For the closed loop filter transfer functions $H(s)$ derived in Sec. 4.1, the following relationships are given for the determination of B_{L}

$$
\begin{aligned}
B_{\mathrm{L}} &= \int_0^\infty |H(s)|^2 \mathrm{d}f \qquad [\mathrm{Hz}] \\
&= \frac{1}{2\pi j} \int_0^{j\infty} |H(s)|^2 \mathrm{d}s \qquad [\mathrm{Hz}] \\
&= \int_0^\infty |H(s)|^2 \mathrm{d}\omega \qquad [\mathrm{rad/s}]
\end{aligned}
\tag{4.25}
$$

for unity filter gain. If $H(s)$ contains a filter gain K_{f}, Eq. (4.25) has to be divided by K_{f}^2 or

$|H(j\omega)|^2$ with $\omega = 0$ for lowpass filters (*Karras*, 1965). For a second order PLL according to Eq. (4.15), put into Eq. (4.25), the equivalent noise bandwidth is

$$
\begin{aligned}
B_{\mathrm{L}} &= \frac{1}{2\pi j} \int_0^{j\infty} |H(s)|^2 \mathrm{d}s \\
&= \frac{1}{2} \left[\frac{1}{2\pi j} \int_{-j\infty}^{j\infty} |H(s)|^2 \mathrm{d}s \right] \\
&= \frac{1}{2} \left[\frac{1}{2\pi j} \int_{-j\infty}^{j\infty} \frac{c(s)c(-s)}{d(s)d(-s)} \mathrm{d}s \right] \\
&= \frac{1}{2} I_N
\end{aligned}
\tag{4.26}
$$

if $|H(s)|^2$ is an even function. The integral I_N is dependent on the polynomial degree N of $d(s)$, which is one higher than for $c(s)$

$$
\begin{aligned}
c(s) &= c_0 + c_1 s + \cdots + c_{N-1} s^{N-1} \\
d(s) &= d_0 + d_1 s + \cdots + d_N s^N.
\end{aligned}
\tag{4.27}
$$

For this type of integrals, the antiderivatives for 2nd order can be found in integral tables

$$
I_2 = \frac{c_1^2 \, d_0 + c_0^2 \, d_2}{2 \, d_0 \, d_1 \, d_2}
\tag{4.28}
$$

and for 3rd order

$$
I_3 = \frac{c_2^2 \, d_0 \, d_1 + (c_1^2 - 2 \, c_0 \, c_2) \, d_0 \, d_3 + c_0^2 \, d_2 \, d_3}{2 \, d_0 \, d_3 \, (d_1 \, d_2 - d_0 \, d_3)}.
\tag{4.29}
$$

For the closed loop 2nd order transfer function according to Eq. (4.15), put into Eq. (4.26) and with I_2 from Eq. (4.28), the equivalent noise bandwidth B_{L} [Hz] is finally

$$
\begin{aligned}
B_{\mathrm{L}} &= \frac{1}{2} I_2 \\
&= \frac{1}{2} \frac{4\zeta^2 \omega_{\mathrm{n}}^4 + \omega_{\mathrm{n}}^4}{4\zeta \omega_{\mathrm{n}}^3} \\
&= \frac{4\zeta^2 + 1}{8\zeta} \omega_{\mathrm{n}}.
\end{aligned}
\tag{4.30}
$$

The bandwidth B_{L} is minimal for a damping factor $\zeta = 0.5$ and increases while enlarging ζ. A typical value is $\zeta = 1/\sqrt{2} = 0.707$ that leads to

$$
\begin{aligned}
B_{\mathrm{L}} &= 0.53 \, \omega_{\mathrm{n}} \qquad \text{[Hz]} \\
B_{\mathrm{L}} &= 3.33 \, \omega_{\mathrm{n}}. \qquad \text{[rad/s]}
\end{aligned}
\tag{4.31}
$$

The loop bandwidth for the 3rd order loop coefficients from Eq. (4.23) can be computed with Eq. (4.26) and the polynomial relationship from Eq. (4.29)

$$
\begin{aligned}
B_{\mathrm{L}} &= \frac{1}{2} I_3 \\
B_{\mathrm{L}} &= 0.74 \, \omega_{\mathrm{n}} \quad \text{[Hz]} \\
B_{\mathrm{L}} &= 4.67 \, \omega_{\mathrm{n}} \quad \text{[rad/s]}
\end{aligned}
\tag{4.32}
$$

and for the coefficients from Eq. (4.24) (*Ward et al.*, 2006)

$$
\begin{aligned}
B_{\mathrm{L}} &= \frac{1}{2}I_3 \\
B_{\mathrm{L}} &= 0.78\,\omega_{\mathrm{n}} \quad [\mathrm{Hz}] \\
B_{\mathrm{L}} &= 4.93\,\omega_{\mathrm{n}}. \quad [\mathrm{rad/s}]
\end{aligned}
\tag{4.33}
$$

The corresponding 3-dB bandwidth $W_{\mathrm{3dB}} = \omega_{\mathrm{3dB}} - 0$ with its definition

$$
20\log(|H(j\omega)|) = -3\ \mathrm{dB} \tag{4.34}
$$

can be found by looking for the value ω_{3dB} so that

$$
\begin{aligned}
\left|\frac{\omega_{\mathrm{n}}^2 + j2\zeta\omega_{\mathrm{n}}\omega_{\mathrm{3dB}}}{\omega_{\mathrm{n}}^2 - \omega_{\mathrm{3dB}}^2 + j2\zeta\omega_{\mathrm{n}}\omega_{\mathrm{3dB}}}\right|^2 &= \frac{1}{2} \\
\frac{\omega_{\mathrm{n}}^4 + 4\zeta^2\omega_{\mathrm{n}}^2\omega_{\mathrm{3dB}}^2}{\omega_{\mathrm{n}}^4 + \omega_{\mathrm{3dB}}^4 - 2\omega_{\mathrm{n}}^2\omega_{\mathrm{3dB}}^2 + 4\zeta^2\omega_{\mathrm{n}}^2\omega_{\mathrm{3dB}}^2} &= \frac{1}{2}
\end{aligned}
\tag{4.35}
$$

for the 2nd order transfer function from Eq. (4.15). With $\zeta = 0.707$, Eq. (4.35) can be simplified to

$$
\begin{aligned}
\frac{\omega_{\mathrm{n}}^4 + 2\omega_{\mathrm{n}}^2\omega_{\mathrm{3dB}}^2}{\omega_{\mathrm{n}}^4 + \omega_{\mathrm{3dB}}^4} - \frac{1}{2} &= 0 \\
\omega_{\mathrm{n}}^4 + 4\omega_{\mathrm{n}}^2\omega_{\mathrm{3dB}}^2 - \omega_{\mathrm{3dB}}^4 &= 0
\end{aligned}
\tag{4.36}
$$

with the following roots

$$
\omega_{\mathrm{3dB}} = \pm\sqrt{2 \pm \sqrt{5}}\,\omega_{\mathrm{n}}. \tag{4.37}
$$

The only applicable root is

$$
\omega_{\mathrm{3dB}} = \sqrt{2 + \sqrt{5}}\,\omega_{\mathrm{n}} = 2.06\,\omega_{\mathrm{n}} \qquad [\mathrm{rad/s}]. \tag{4.38}
$$

Analog to the 2nd order PLL, ω_{3dB} based on Eq. (4.22) is found for the 3rd order by

$$
\begin{aligned}
\left|\frac{c_0 - c_2\,\omega_{\mathrm{3dB}}^2 + jc_1\,\omega_{\mathrm{3dB}}}{d_0 - d_2\,\omega_{\mathrm{3dB}}^2 + j(d_1\,\omega_{\mathrm{3dB}} - \omega_{\mathrm{3dB}}^3)}\right|^2 &= \frac{1}{2} \\
\frac{c_0^2 + c_2^2\,\omega_{\mathrm{3dB}}^4 - 2\,c_2\,c_0\,\omega_{\mathrm{3dB}}^2 + c_1^2\omega_{\mathrm{3dB}}^2}{d_0^2 + d_2^2\omega_{\mathrm{3dB}}^4 - 2\,d_0\,d_2\,\omega_{\mathrm{3dB}}^2 + d_1^2\omega_{\mathrm{3dB}}^2 + \omega_{\mathrm{3dB}}^6 - 2\,d_1\omega_{\mathrm{3dB}}^4} &= \frac{1}{2}
\end{aligned}
\tag{4.39}
$$

and, with the coefficients of *Karras* (1965) and *Ward et al.* (2006), can be simplified to

$$
c_0^2 + c_2^2\,\omega_{\mathrm{3dB}}^4 - 2\,c_2\,c_0\,\omega_{\mathrm{3dB}}^2 + c_1^2\omega_{\mathrm{3dB}}^2 + 2\,c_1\,\omega_{\mathrm{3dB}}^4 - \omega_{\mathrm{3dB}}^6 = 0. \tag{4.40}
$$

The only applicable root for the coefficient set of *Karras* (1965) is

$$
\omega_{\mathrm{3dB}} = 2.86\,\omega_{\mathrm{n}} \qquad [\mathrm{rad/s}] \tag{4.41}
$$

and for *Ward et al.* (2006)

$$
\omega_{\mathrm{3dB}} = 2.74\,\omega_{\mathrm{n}}. \qquad [\mathrm{rad/s}]. \tag{4.42}
$$

4.2 Carrier Tracking Errors

The PLL models and their parameters have been derived in Sec. 4.1 without noise based on the assumption of linearity due to small phase errors. The validity of linearity and finally a stable tracking with good performance is defined by the values from Fig. 3.10, which are dependent on the PLL model and parameters themselves. A deep look into non-linear analog PLL models and their analyses is given by *Stensby* (1997). For the analytical description of the tracking errors, the additive white noise $\hat{n}_\text{I}$ and $\hat{n}_\text{Q}$ with the properties from Eq. (3.41) and (3.42) will be considered as small in order to allow the PD output to be considered as linear. In addition to the thermal noise induced jitter (see Sec. 4.2.3), dynamic impacts on the reference signal as introduced in Sec. 3.2.1 generate a dynamic stress which is mainly split into a steady-state error and the transient response. For this evaluation the error transfer function $E(s)$ is built by substituting Eq. (4.6) into (4.7)

$$E(s) = \frac{\theta_\text{d}(s)}{\theta_1(s)} = \frac{1}{1 + G(s)} = \frac{s}{s + K_\text{d}K_\text{v}F(s)}. \tag{4.43}$$

4.2.1 Steady-State Error

The steady-state error is the remaining value after a transient response caused by a phase step, frequency step, or frequency ramp. It is not always easy to separate the transient state (see Sec. 4.2.2) from the steady state. A typical definition for the transition is the time at which the VCO is finally running with a new frequency after the transients died out. If the PLL is linear and is able to track the new frequency under the corresponding dynamics without additional steady-state errors, exactly the same frequencies (for periodic signals) are produced during the steady-state as the input frequencies and the amplitude and phase amplifications correspond to the frequency response. The limits of the steady-state and potentially increased errors are directly dependent on the PLL design, especially on the order and type.

For each transform domain used the time domain phase error $\theta_\text{d}(t)$ can be expressed with respect to the final value theorem (*Gardner*, 2005). For the Laplace domain

$$\lim_{t \to \infty} x(t) = \lim_{s \to 0} s\, x(s) \tag{4.44}$$

applies and accordingly for the error phase from Eq. (4.43)

$$\lim_{t \to \infty} \theta_\text{d}(t) = \lim_{s \to 0} \frac{s^2 \theta_1(s)}{s + K_\text{d}K_\text{v}F(s)}. \tag{4.45}$$

Let us consider a phase step $\Delta\theta$ on the reference signal phase θ_1 as illustrated in Fig. 3.9 (right). The phase change of the reference signal $\Delta\theta = \text{d}\theta_1(t)/\text{d}t$ corresponds to $\Delta\theta = \theta_1(s)s$ in the Laplace domain. The steady-state error θ_p after a phase step

$$\theta_\text{p} = \lim_{t \to \infty} \theta_\text{d}(t) = \lim_{s \to 0} \frac{s\Delta\theta}{s + K_\text{d}K_\text{v}F(s)} = 0 \tag{4.46}$$

is always zero for all PLLs.

A frequency step $\Delta\omega$ on the reference signal as illustrated in Fig. 3.9 (left) corresponds to a phase ramp on the reference phase $\Delta\omega = \theta_1(s)s^2$. The steady-state error θ_ω caused by a frequency step is finally

$$\theta_\omega = \lim_{t\to\infty} \theta_\mathrm{d}(t) = \lim_{s\to0} \frac{\Delta\omega}{s + K_\mathrm{d}K_\mathrm{v}F(s)} = \frac{\Delta\omega}{K_\mathrm{d}K_\mathrm{v}F(0)} \tag{4.47}$$

with the DC gain $K_\mathrm{DC} = K_\mathrm{d}K_\mathrm{v}F(0)$ already introduced for the filters in Sec. 3.2.4. The DC gain $[s^{-1}]$ determines the ability of velocity tracking, which is essential for PLLs in GNSS receivers while tracking Doppler affected carriers. A type-1 PLL has a finite DC gain in contrast to a type-2 PLL as derived in Sec. 4.1.1 with $K_\mathrm{DC} = \infty$. Therefore, at least a 2nd order type-2 PLL is necessary for GNSS receivers in order to avoid a steady-state error due to Doppler-shifted signals.

An additional important capability of a PLL implemented in a GNSS receiver is the capability of tracking a certain user dynamics which can possibly cause an accelerated LOS between satellite and receiver. Such a frequency ramp $\Delta\dot{\omega}$ $[\mathrm{rad/s^2}]$ with the reference phase $\theta_1(s) = \Delta\dot{\omega}/s^3$ leads to an acceleration steady-state error θ_a. If K_DC is finite (e. g. type-1 PLL), the error will increase without limit. Taking the 2nd order type-2 PLL from Eq. (4.15) with the relationship between $H(s)$ and $E(s)$ from Eqs. (4.8) and (4.43), the error transfer function is given by

$$E(s) = \frac{s^2}{s^2 + 2\zeta\omega_\mathrm{n}s + \omega_\mathrm{n}^2} \tag{4.48}$$

and, finally, for the acceleration steady-state error by

$$\theta_\mathrm{a} = \lim_{t\to\infty} \theta_\mathrm{d}(t) = \lim_{s\to0} \frac{s^2\theta_1(s)}{s^2 + 2\zeta\omega_\mathrm{n}s + \omega_\mathrm{n}^2} = \lim_{s\to0} \frac{\Delta\dot{\omega}}{s^2 + 2\zeta\omega_\mathrm{n}s + \omega_\mathrm{n}^2}. \tag{4.49}$$

For a second order type-2 PLL the dynamic steady-state error is dependent on the natural frequency ω_n

$$\theta_\mathrm{a} = \frac{\Delta\dot{\omega}}{\omega_\mathrm{n}^2} \tag{4.50}$$

or on the loop bandwidth B_L with the relationship from Eq. (4.30), respectively. Obviously a large bandwidth reduces the dynamic steady-state error by its square. In order to reduce θ_a to zero, the filter transfer function $F(s)$ has to include a factor $1/s^2$, which corresponds to a 2nd order loop filter that leads to a 3rd order type-3 PLL (see Sec. 4.1.2). In contrast to a type-2 PLL that requires a large bandwidth for the reduction of the dynamic steady-state error, a type-3 PLL is able to work with a smaller bandwidth and a vanishing steady-state error induced by accelerations.

4.2.2 Transient Response

The transient response is the second important dynamic signal tracking error. As shown for the steady-state error in Sec. 4.2.1, a 3rd order PLL (used in GNSS receivers) tracking accelerated motions on the reference signal is able to track without any remaining steady-state errors. The responses in magnitude and phase for 2nd order type-2 and 3rd order type-3 PLLs are plotted in Figs. 4.1 and 4.2 normalized to the natural frequency ω_n. It

can be seen that the main magnitude response for a 2nd order type-2 PLL with $\zeta = 0.707$ is beyond $0.2\,\omega_{\mathrm{n}}$ rad/s and is strongly attenuated beyond $2\,\omega_{\mathrm{n}}$ rad/s. The phase shift reaches 90 deg beyond $10\,\omega_{\mathrm{n}}$ rad/s. Analytical solutions of the transient response caused by phase offset, frequency offset, and ramp for a 2nd order type-2 PLL can be found in *Gardner* (2005). However, for quantifying the transient response for GNSS receivers, 3rd order PLLs should mainly be considered. The main magnitude response is reached beyond $0.3\,\omega_{\mathrm{n}}$ rad/s and is attenuated above $2\,\omega_{\mathrm{n}}$ rad/s. Taking applicable loop bandwidths B_{L} between 10 and 50 Hz with the relation to ω_{n} given by Eqs. (4.32) and (4.33), the main transient response is exactly in the frequency range beyond 1 Hz of the expected main contribution of 100 sps GNSS measurements. Therefore, the transient response is a critical issue of high-rate GNSS measurements. It is analyzed in detail in Sec. 7.1.

4.2.3 Carrier Phase Jitter

The main part of the overall carrier tracking measurement error is the carrier phase jitter σ_{PLL} induced by thermal noise. As already mentioned, a precise quantification is only possible with Monte-Carlo simulations due to the non-linearity of the PLLs, especially for large phase errors. The characteristics of σ_{PLL} is dependent on the discriminator type used. Simulations by *Humphreys et al.* (2005) show that the behavior of the I and Q channel product of Eq. (3.48) is representative for the class of Costas discriminators. Assuming small phase errors and accordingly a linearized PLL model, the noise is directly additive to the input signal as already assumed in the signal representation of Sec. 3.2.2. The prompt $I_{\mathrm{P}}(t_a)$ and $Q_{\mathrm{P}}(t_a)$ samples from Eq. (3.40) are given by a deterministic ($s_{\mathrm{I},a}$, $s_{\mathrm{Q},a}$) and stochastic part ($\hat{n}_{\mathrm{I},a}$, $\hat{n}_{\mathrm{Q},a}$)

$$
\begin{aligned}
I_{\mathrm{P}}(t_a) &= s_{\mathrm{I},a} + \hat{n}_{\mathrm{I},a} \\
Q_{\mathrm{P}}(t_a) &= s_{\mathrm{Q},a} + \hat{n}_{\mathrm{Q},a}
\end{aligned}
\tag{4.51}
$$

with the normalized noise variance of Eq. (3.42)

$$
E[\hat{n}_{\mathrm{I},a}^2] = E[\hat{n}_{\mathrm{Q},a}^2] = 1
\tag{4.52}
$$

and the noise zero-mean condition with no correlations

$$
E[\hat{n}_{\mathrm{I},a}] = E[\hat{n}_{\mathrm{Q},a}] = E[\hat{n}_{\mathrm{I},a}\,\hat{n}_{\mathrm{Q},a}] = 0.
\tag{4.53}
$$

The variance of the PD output for the Costas discriminator of Eq. (3.48) is given by the prompt in-phase and quadra-phase samples according to Eq. (4.51) as follows

$$
\begin{aligned}
\sigma_{n_{\mathrm{d}},a}^2 &= E[I_a^2 Q_a^2] - E^2[I_a Q_a] \\
&= E[(s_{\mathrm{I},a} + \hat{n}_{\mathrm{I},a})^2 (s_{\mathrm{Q},a} + \hat{n}_{\mathrm{Q},a})^2] - E^2[(s_{\mathrm{I},a} + \hat{n}_{\mathrm{I},a})(s_{\mathrm{Q},a} + \hat{n}_{\mathrm{Q},a})] \\
&= E[(s_{\mathrm{I},a}^2 + 2s_{\mathrm{I},a}\hat{n}_{\mathrm{I},a} + \hat{n}_{\mathrm{I},a}^2)(s_{\mathrm{Q},a}^2 + 2s_{\mathrm{Q},a}n_{\mathrm{Q},a} + \hat{n}_{\mathrm{Q},a}^2)] \\
&\quad - E^2[s_{\mathrm{I},a}s_{\mathrm{Q},a} + s_{\mathrm{I},a}\hat{n}_{\mathrm{Q},a} + s_{\mathrm{Q},a}\hat{n}_{\mathrm{I},a} + \hat{n}_{\mathrm{I},a}\hat{n}_{\mathrm{Q},a}] \\
&= E[s_{\mathrm{I},a}^2 s_{\mathrm{Q},a}^2 + 2s_{\mathrm{I},a}^2 s_{\mathrm{Q},a}\hat{n}_{\mathrm{Q},a} + s_{\mathrm{I},a}^2 \hat{n}_{\mathrm{Q},a}^2 \\
&\quad + 2s_{\mathrm{I},a}s_{\mathrm{Q},a}^2\hat{n}_{\mathrm{I},a} + 4s_{\mathrm{I},a}s_{\mathrm{Q},a}\hat{n}_{\mathrm{I},a}\hat{n}_{\mathrm{Q},a} + 2s_{\mathrm{I},a}\hat{n}_{\mathrm{I},a}\hat{n}_{\mathrm{Q},a}^2 \\
&\quad + s_{\mathrm{Q},a}^2 \hat{n}_{\mathrm{I},a}^2 + 2s_{\mathrm{Q},a}^2\hat{n}_{\mathrm{I},a}^2\hat{n}_{\mathrm{Q},a} + \hat{n}_{\mathrm{I},a}^2\hat{n}_{\mathrm{Q},a}^2] \\
&\quad - E^2[s_{\mathrm{I},a}s_{\mathrm{Q},a} + s_{\mathrm{I},a}\hat{n}_{\mathrm{Q},a} + s_{\mathrm{Q},a}\hat{n}_{\mathrm{I},a} + \hat{n}_{\mathrm{I},a}\hat{n}_{\mathrm{Q},a}]
\end{aligned}
\tag{4.54}
$$

with all elements equal to zero exept for

$$\sigma^2_{n_d,a} = E[s^2_{I,a}s^2_{Q,a} + s^2_{I,a}\hat{n}^2_{Q,a} + s^2_{Q,a}\hat{n}^2_{I,a} + \hat{n}^2_{I,a}\hat{n}^2_{Q,a}] - E^2[s_{I,a}s_{Q,a}] \tag{4.55}$$

that finally leads to

$$\sigma^2_{n_d,a} = E^2[s_{I,a}]E[n^2_{Q,a}] + E^2[s_{Q,a}]E[n^2_{I,a}] + E[n^2_{I,a}n^2_{Q,a}]. \tag{4.56}$$

With the signal amplitudes of Eq. (3.40) assuming small tracking errors, the noise variance of the Costas discriminator output is

$$\begin{aligned}
\sigma^2_{n_d,a} &= 2T\frac{S}{N_0}[\cos^2(\delta\theta_a) + \sin^2(\delta\theta_a)] + 1 \\
&= 2T\frac{S}{N_0} + 1.
\end{aligned} \tag{4.57}$$

The discriminator output is normalized to 1 by the gain K_d from Eq. (3.50)

$$\begin{aligned}
\sigma^2_{\hat{n}_d,a} &= \frac{1}{K_d^2}\sigma^2_{n_d,a} \\
&= \frac{N_0}{2T\,S} + \frac{N_0^2}{4T^2\,S^2} \\
&= \frac{1}{2T\,S/N_0}\left(1 + \frac{1}{2T\,S/N_0}\right).
\end{aligned} \tag{4.58}$$

The noise variance $\sigma^2_{\hat{\theta}}$ of the carrier loop output is assumed to be stationary. Therefore the noise is independent from a and can be modeled in the continuous time domain dependent on the two-sided predetection bandwidth $1/T$ and the one-sided equivalent noise bandwidth B_L of the loop filter. The variance can be calculated by the loop transfer function $H(\omega)$ and the noise power spectral density $S_{\hat{n}_d}$:

$$\sigma^2_{PLL} = \int_{-\infty}^{\infty}|H(f)|^2 S_{\hat{n}_d}\mathrm{d}f \tag{4.59}$$

with

$$S_{\hat{n}_d} = T\sigma^2_{\hat{n}_d}. \tag{4.60}$$

According to Eq. (4.25) the noise variance for a closed tracking loop with a predetection integration time T and an equivalent noise bandwidth B_L using a Costas discriminator is

$$\sigma^2_{PLL} = 2B_L S_{\hat{n}_d} = \frac{B_L}{S/N_0}\left(1 + \frac{1}{2T\,S/N_0}\right). \tag{4.61}$$

The unit of the carrier-to-noise spectral density S/N_0 is often given in dB and is termed C/N_0 [dB-Hz]. The carrier phase jitter in cycles for a Costas loop is finally given by

$$\sigma_{PLL} = \sqrt{\frac{B_L}{C/N_0}\left(1 + \frac{1}{2T\,C/N_0}\right)} \qquad \text{[cycles]} \tag{4.62}$$

or in meters by

$$\sigma_{PLL} = \frac{\lambda}{2\pi}\sqrt{\frac{B_L}{C/N_0}\left(1 + \frac{1}{2T\,C/N_0}\right)} \qquad \text{[m]} \tag{4.63}$$
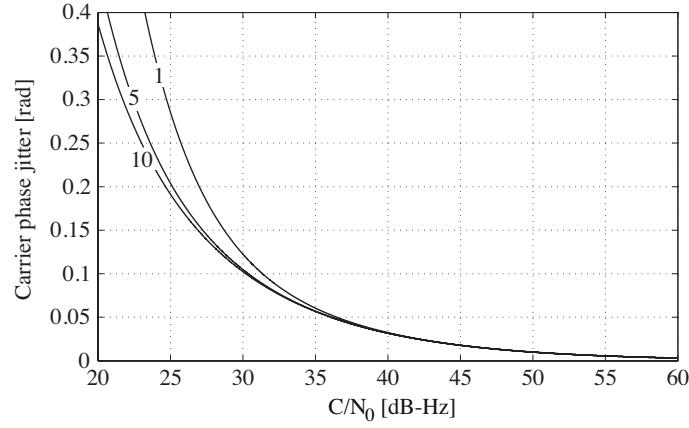
Figure 4.3: The carrier phase jitter according to Eq. (4.62) dependent on different predetection integration times of 1 ms, 5 ms, and 10 ms. For high C/N_0 (> 35 dB-Hz) the impact of T on the jitter is negligible.

with the signal wavelength λ [m]. Looking at Eq. (4.62), the induced jitter in the PLL is independent from its order and from the frequency of the tracked signal, when expressing σ_{PLL} in cycles. The predetection integration T has only an impact on extremely poor signals at low C/N_0, visible in Fig. 4.3 for typically used T of 1 ms, 5 ms and 10 ms. Therefore, this formulation of the thermal noise induced jitter at high signal strength (> 35 dB-Hz) is also applicable for the classical PLLs and modern GNSS signals without the requirement of integrating within the data bits. In contrast to T, the loop bandwidth B_{L} determines the final carrier jitter in combination with the signal strength C/N_0. In Fig. 4.4 the carrier jitter dependent on a typical range of possible bandwidths B_{L} from 5 Hz to 50 Hz is presented. A narrow bandwidth reduces the jitter significantly, at least a factor of two between 10 and 50 Hz. However, the bandwidth is limited at a lower boundary of about 5–10 Hz due to existing oscillator dynamics even for a non-moving (static) receiver (see Sec. 4.2.4). The higher boundary is mainly determined by the C/N_0 itself, for poor signal environments or demodulation and decryption algorithm consuming signal strength, the bandwidth B_{L} has to be dramatically reduced. A thorough study about the carrier jitter for almost all available GNSS signals is achieved in Chapter 5 dependent on the main factors C/N_0 and B_{L}.

4.2.4 Oscillator Jitter

The oscillators involved, especially the receiver oscillator introduced in Sec. 3.1.2, are critical issues with respect to a stable tracking and induced tracking errors. The PLL implemented in a GNSS receiver has to be capable of tracking the oscillator frequency changes as visible in Eq. (3.22). As mentioned in Sec. 3.1.2, the oscillator is a main component that defines a GNSS receiver as high-end or low-cost. Especially for low-cost receivers with a moderate oscillator quality, the tracking of oscillator-induced frequency changes is a main challenge in receiver design. Additionally, the final quality of the measurements can dramatically differ only because of the oscillator-induced jitter. Concentrating on the receiver oscillator, the tracking error caused can be distinguished in short-term stability described by the Allan deviation and in vibration and acceleration stress errors (*Ward et al.*, 2006).
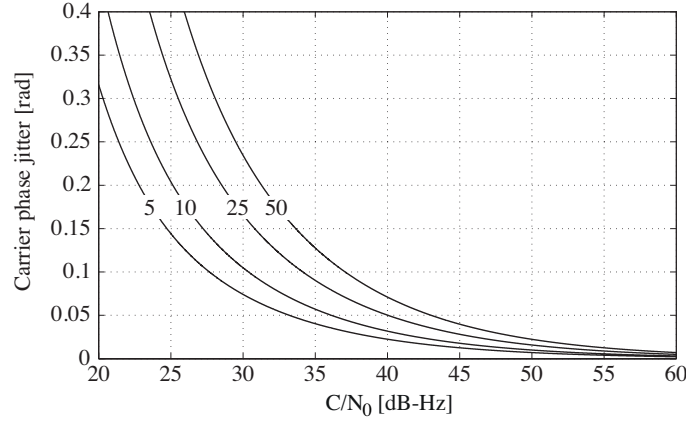
Figure 4.4: The carrier phase jitter according to Eq. (4.62) dependent on different loop bandwidths B_L of 5 Hz, 10 Hz, 25 Hz, and 50 Hz. The jitter difference between a 10 Hz and 50 Hz B_L is at least a factor of two, even for high signal strengths.

All these error sources are directly dependent on the oscillator quality. However, the short-term stability is the most critical part concerning tracking reliability and finally defines the lower boundary of the loop bandwidth B_L (see Fig. 4.5). The frequency stability and short-term oscillator jitter $\Delta\theta_A$ [rad] with respect to the oscillator Allan deviation $\sigma_A(\tau)$ [-] is discussed in *Klepczynski and Ward* (2000) based on the equations derived by *Fuchser* (1976) for a 2nd order PLL

$$\Delta\theta_A = \frac{\sigma_A(\tau)2\pi f_{RF}}{2.5\,B_L} \tag{4.64}$$

and for a 3rd order PLL

$$\Delta\theta_A = \frac{\sigma_A(\tau)2\pi f_{RF}}{2.25\,B_L}. \tag{4.65}$$

These equations are valid under the assumption of small Allan deviation changes during the gate times τ which have to be evaluated within the loop bandwidth ($\tau = 1/B_L$). This short-term gate time is applicable for all PLLs (*Klepczynski and Ward*, 2000). The impact of the receiver oscillator Allan deviation $\sigma_A(\tau)$ on $\Delta\theta_A$ is shown in Fig. 4.5 dependent on the loop bandwidth B_L. The three different oscillator qualities with $\sigma_A(\tau)$ of 10^{-11}, 10^{-10} and 10^{-9} demonstrate their significantly different influence on the carrier jitter. For an extremely good $\sigma_A(\tau)$ of 10^{-11} the induced jitter is completely negligible compared to the existing jitter induced by thermal noise shown in Fig. 4.4, even for small B_L. An Allan deviation of 10^{-10} shows also no dominant jitter contribution beyond a B_L of 5 Hz. Only at extremely high C/N_0 (compare Fig. 4.4) the oscillator-induced jitter could become noticeable. However, this is still far from the level which is reached with a low quality oscillator of 10^{-9} which plays the dominant role for the overall PLL jitter, even for wide B_L. The comparison of Figs. 4.5 and 4.4 with the contradictory requirement on B_L shows the importance of the receiver short-term stability with respect to the overall PLL jitter. A low quality oscillator let increase the PLL jitter in general and requires a wider B_L which additionally amplifies the thermal noise induced jitter.

The sensitivity of the oscillator to dynamic stress and vibrations is typically not given in the corresponding receiver specifications. The only value that might be found is the maximum acceleration, the tolerance for the electronic components. In general the PLL cannot
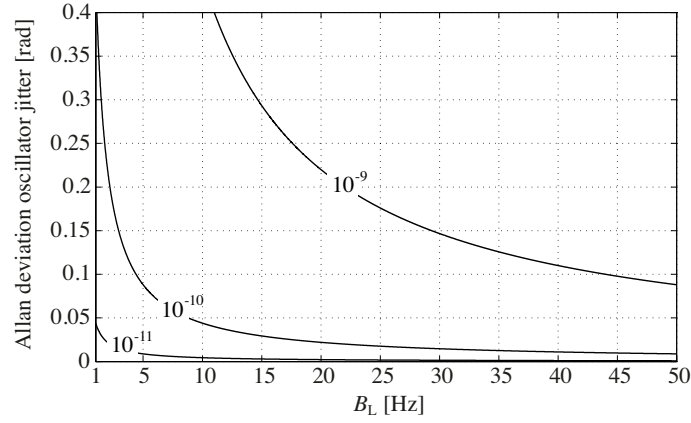
Figure 4.5: The Allan deviation oscillator jitter $\Delta\theta_A$ for GPS L1 dependent on the loop bandwidth B_L for three different receiver oscillator Allan deviations $\sigma_A(\tau)$ of 10^{-11}, 10^{-10} and 10^{-9}. The influence of the short-term oscillator quality on the jitter is significant.

separate between the LOS dynamics and the frequency change caused by an accelerated oscillator. The oscillator stress has therefore at least an impact on the tracking threshold. The g-effects on GNSS receiver oscillators are discussed in *Pratt* (1989). However, the oscillator error is equal to all tracking channels and therefore not geometry-dependent and can be considered as a part of the receiver clock error. The influence on the estimated coordinates is therefore small as verified in Sec. 7.2.4.

The noise on the generated and finally transmitted carrier wave by the satellite is mainly determined by the satellite oscillator itself. In the ICDs of the different GNSS the amount of tolerable noise induced by the satellite clocks is defined as at least trackable with a loop bandwidth B_L of 10 Hz. This means for typical values (except for extremely narrow bandwidths) the satellite oscillator induced jitter in the receiver is not a critical stability issue. Additionally, during a stable tracking the remaining amount of jitter is order of magnitude below the receiver oscillator jitter.

4.3 GNSS Observation Equations

The acquisition, tracking and retrieval of the GNSS receiver natural measurements for the formation of the desired observables are described in Sec. 3.2. The pseudorange from Eq. (3.109) and integrated Doppler phase from Eq. (3.112) are still affected by external and internal (antenna/receiver system) biases. In addition to internal biases like receiver and satellite clock synchronization, hardware biases, receiver and satellite antenna offsets and variations, external perturbations such as atmosphere, multipath, and relativistic effects have an impact on the estimation of the true geometric distance between satellite and receiver.

4.3.1 Code Pseudorange Observation Equation

The pseudorange equation from Eq. (3.109) with the receive time $T_{\mathrm{r}}(t_n)$ and transmit time $T_{\mathrm{t}}^i(t_n)$ of a satellite i is now expanded with additional modeling parameters. The pseudorange $R^i(t_n)$ [m] as well as the receive and transmit times refer to the same receiver epoch. This epoch is still biased compared to the true system time by δt and the transmit time includes a time bias δt_{t}^i produced by the satellite clock i. The receiver clock synchronization error δt has to be determined by a code navigation solution (some nanoseconds) in order to keep the receiver time frame (RTF) within 1 ms with respect to the corresponding system time. Some receivers correct their receive time at a high update rate up to each measurement extraction epoch. The transmit time bias δt_{t}^i of a specific satellite clock i can be derived from the navigation message as second order polynomial coefficients and is commonly added during the receiver navigation process before building the artificial pseudoranges and loosing the information about the transmit time. In practice for a post-processing position computation based on differencing measurements of two receivers with one or two satellites (see Sec. 4.3.4, especially for the processing of phase measurements), the satellite clock bias is typically considered at receive time while assuming a negligible drift of the Rubidium clocks or hydrogen masers over 20 ms, which is the maximum existing difference in the light-travel time between two stations on Earth. The pseudorange observation refers to the RTF and can be expressed by the geometric distance ρ^i in system time between satellite and receiver that includes all additional signal disturbances

$$R^i = c\,[T_{\mathrm{r}} - T_{\mathrm{t}}^i] = \rho^i + c\,\delta t - c\,\delta t^i. \tag{4.66}$$

By splitting the affected distance ρ^i into the true receiver and satellite position vectors and the main signal perturbations, the final observation equation for the pseudorange to satellite i is

$$R^i = |(\boldsymbol{r} + \boldsymbol{r}_\Delta) - (\boldsymbol{s}^i + \boldsymbol{s}_\Delta^i)| + c\,(\delta t + \alpha_{\mathrm{c}}) - c\,(\delta t^i + \beta_{\mathrm{c}}^i) + I^i + T^i + M_{\mathrm{c}}^i + U^i + \epsilon_{\mathrm{c}}^i \tag{4.67}$$

where

$\boldsymbol{r}$ corresponds to the geocentric position vector of the receiving antenna reference point (ARP),

$\boldsymbol{s}^i$ is the geocentric position vector of the satellite ARP (including satellite attitude),

$\boldsymbol{r}_\Delta, \boldsymbol{s}_\Delta^i$ are the vectors from the ARP to the receiver and satellite antenna phase centers,

δt is the synchronization error between the receiver measurement time and the true system time (e. g. GPS time),

δt^i is the synchronization error between the satellite clock and true system time (e. g. GPS time),

$\alpha_{\mathrm{c}}, \beta_{\mathrm{c}}^i$ are hardware delays in the receiver and satellite,

I^i is the signal propagation delay caused by the Earth's ionosphere

T^i is the signal delay due to the propagation through the Earth's troposphere

M_c^i is the code multipath error signal caused by reflected signals,

U^i contains relativistic correction terms, and

ϵ_c^i consists of all unmodeled code errors such as higher order terms, interferences and system noise like DLL thermal noise jitter.

The receiver position vector $\boldsymbol{r}$ includes all displacement-dependent effects which can be described by the models given in the IERS conventions (*IERS*, 2010), such as Earth and pole tides, atmospheric and ocean loading, and post-glacial rebound. The satellite position vector $\boldsymbol{s}^i$ corresponds to the time at signal transmission. The vectors $\boldsymbol{r}$ and $\boldsymbol{s}$ have to be in the same reference system. In the framework of processing the observations, which are referred to receiver time, the light-travel time τ^i has to be taken into account for the satellite position computation, which is additionally affected by the receiver clock synchronization error. This means that the receiver clock error is implicitly included in $\boldsymbol{s}^i$. However, as a result of a first code position solution (iterative process), the synchronization error δt can be retrieved with an accuracy of some nanoseconds. An uncertainty of 10 ns would imply a tolerable error in range of 0.03 mm assuming a range velocity between satellite and receiver of 3 km/s.

The antenna phase center vectors $\boldsymbol{r}_\Delta$ and $\boldsymbol{s}_\Delta^i$ include the phase center offsets between the ARP and the electrical phase center of the receiver and satellite antennas which are dependent on the signal frequency and antenna hardware. Additionally, phase center variations dependent on azimuth and elevation have to be taken into account (*Rothacher et al.*, 1996; *Rothacher and Mader*, 2003). The receiver phase center offsets and variations are determined by an antenna calibration and provided by the manufacturers, some groups at Universities or private companies while the estimation of the satellite phase center variations is described in *Schmid and Rothacher* (2003).

The influence of the ionosphere, troposphere, and multipath on the GNSS signal propagation is a well documented and discussed topic in the geodetic GNSS community. In addition to standard literature as *Hofmann-Wellenhof et al.* (2008) or *Conley et al.* (2006), a deep insight into the specific aspects is given by *Böhm et al.* (2006) for the commonly used troposphere mapping functions, or by *Schaer* (1999) and *Petrie et al.* (2011) for the modeling of the ionospheric influence. Especially multipath is a receiver/antenna and signal modulation specific issue for the most part (*Van Dierendonck et al.*, 1992; *Floc'H and Soellner*, 2007). The relativistic effects on the signal propagation, on receiver and satellite clocks, which are not yet corrected by the adjusted fundamental satellite clock frequency, are extensively discussed in *Ashby* (2003) and *Kouba* (2004).

The satellite equipment delay β_c^i contains different timing biases, which are specified in *IS-GPS-200G* (2012) such as group delay uncertainties of maximal 3 ns (95%), differential group delays between the L1 and L2 PRN signals of maximal 15 ns (bias term transmitted in the navigation message) with variations not exceeding 3 ns (95%). The signal coherence is guaranteed with an average time difference for the chip transition between different code types on the same carrier (e.g. C/A and P(Y) on L1, or P(Y) and L2C on L2) with maximal 10 ns and variations of 1 ns (95%). The new navigation messages on the modern GPS signals also broadcast these intersignal corrections.

The receiver bias term α_c is mainly induced by hardware delays through the electronic components such as antenna, filters, LNAs, mixers etc. Not the entire delay caused by variable components can be calibrated. The rest is finally absorbed into the estimation of the receiver clock synchronization error and negligible for the positioning accuracy (but not for timing relevant applications). Additionally, *Hegarty et al.* (2004) show that receiver hardware biases contain group delays of several nanoseconds between different modulation types on the same carrier frequency or signals with the same types, but differently processed in the DLL (different loop filters). Differential group delays are especially important combining different systems on the same frequency, e. g. GPS C/A-code on L1 and Galileo E1-OS.

4.3.2 Carrier Phase Observation Equation

The integrated carrier Doppler phase Φ^i [cycles] of Eq. (3.112) retrieved from the carrier accumulator in receiver time is still ambiguous in contrast to the code pseudorange. Apart from this ambiguity term specific to carrier phase, the observation equation is similar to Eq. (4.67) while multiplying the integrated phases with the corresponding carrier wavelength λ in order to get the phase observation P^i to satellite i in meters

$$P^i = \lambda\,\Phi^i \tag{4.68}$$

and split up by the additional modeling parameters

$$\begin{aligned} P^i = {}& |(\boldsymbol{r} + \boldsymbol{r}_\Delta) - (\boldsymbol{s}^i + \boldsymbol{s}^i_\Delta)| + c\,(\delta t + \alpha) - c\,(\delta t^i + \beta^i) + \lambda N^i \\ & - I^i + T^i + M^i + U^i + \lambda W^i + \epsilon^i \end{aligned} \tag{4.69}$$

where

α, β^i are phase biases during the generation of the replica carrier signal in the receiver and generation and modulation of the carrier signal in the satellite,

N^i is a constant and arbitrary ambiguity term,

M^i is the phase multipath signal caused by reflected signals,

W^i is the phase polarization effect, called phase wind-up, and

ϵ^i consists of all unmodeled phase errors such as higher order terms, interferences and system noise like carrier phase thermal noise jitter.

As described in Sec. 3.2.5 for the carrier phase accumulator and the following measurement extraction, the initial accumulator values (fractional and integer) are set to zero after the acquisition, which is completed at different times for each tracking channel. The first measurement extraction from the accumulator occurs at the same receiver epoch and outputs arbitrary initial phase cycles for all channels to the navigation processor or external user. The determination of each integer ambiguity term N^i (not to be confused with the value N_ϕ form Eqs. (3.102) and (3.113)) is called ambiguity resolution. This integer cycle value is constant unless a cycle slip occurs or the receiver restarts the signal acquisition with a subsequent reinitialization of the accumulator values. There is a huge amount of publications in scientific journals for ambiguity resolution techniques under all aspects of applications and observation characteristics.

The phase-wind up caused by the satellite motion relative to the receiving antenna can be precisely modeled, assuming no additional receiver antenna rotation caused by the user on Earth is present(*Wu et al.*, 1993; *Häberling*, 2009). Note that the ionospheric refraction term I has the opposite sign compared to the code pseudorange equation due to the difference in the phase advance and code delay (group velocity).

4.3.3 Linear Combinations of Observations

The zero-difference (ZD) observation equations (4.67) and (4.69) contain a lot of parameters which are difficult to model with the required accuracy or to estimate due to existing correlations between the parameters. A linear combination (LC) between different observation types can be formed to obtain advantages for the processing, e. g. elimination or minimization of a specific parameter influence and changing the signal characteristics with respect to a specific preprocessing step or ambiguity resolution. Beside the combination of different carrier frequencies and different types of spreading codes, differences of observations between different receivers and different satellites or between different measurement epochs are possible. This special class of linear combinations is separately examined in Sec. 4.3.4. A linear combination L can be expressed in a general form by m involved ZD phase observations P of the same epoch between one receiver and one satellite and by their corresponding coefficients κ

$$L = \sum_{n=1}^{m} \kappa_n P_n. \tag{4.70}$$

Code LCs can be formed in a similar way. Frequently used LCs for phase observations are introduced in the following.

The ionosphere-free linear combination L_c between the L1 carrier and L2 carrier (or in the future with other carrier frequencies) is one of the most common combinations in order to reduce the influence of the dispersive Earth's ionosphere. Assuming P_1 as the phase observation of the carrier L1 with frequency f_1 and P_2 as the phase observation of the L2 carrier wave with frequency f_2, the corresponding coefficients are

$$\kappa_{1,\mathrm{c}} = \frac{f_1^2}{f_1^2 - f_2^2} \quad \text{and} \quad \kappa_{2,\mathrm{c}} = \frac{-f_2^2}{f_1^2 - f_2^2}. \tag{4.71}$$

The influence of the ionosphere in L_c is finally eliminated up to the order 1. However, the ambiguity term N_c is not an integer value anymore and therefore not accessible for a direct ambiguity fixing. For the purpose of ambiguity resolution for long baselines the widelane linear combination L_w has the advantage of integer ambiguities and a long wavelength of 86 cm (between GPS L1 and L2) which improves the ambiguity resolution under strong ionospheric disturbances. The coefficients for L_w are

$$\kappa_{1,\mathrm{w}} = \frac{f_1}{f_1 - f_2} \quad \text{and} \quad \kappa_{2,\mathrm{w}} = \frac{-f_2}{f_1 - f_2} \tag{4.72}$$

In order to obtain only the widelane ambiguity term N_w, L_w of the phase observation P can be combined with the corresponding widelane code pseudorange observation $L_\mathrm{w}(R)$, building the so-called Melbourne-Wübbena linear combination L_MW

$$L_\mathrm{MW} = L_\mathrm{w}(R) - L_\mathrm{w}(P). \tag{4.73}$$

An additional, often used linear combination is the geometry-free linear combination L_I with the coefficients

$$\kappa_{1,\mathrm{I}} = 1 \quad \text{and} \quad \kappa_{2,\mathrm{I}} = -1 \tag{4.74}$$

which finally consists of the ionospheric refraction, phase wind-up, and a linear combination ambiguity term. This LC is commonly used for the determination of ionosphere models and cycle slip detection. The different linear combinations have their specific advantages and are involved and combined in the standard geodetic processing strategies of GNSS observations. The variance σ_L^2 of a LC including more than one observation equation according to Eq. (4.70) is given by the corresponding error propagation

$$\sigma_\mathrm{L}^2 = \sum_{n=1}^m \kappa_n^2 \sigma_{\mathrm{P}_n}^2 + \sum_{n=1}^m \sum_{k=1,k\neq n}^m \kappa_n \kappa_k \rho_{nk} \sigma_{\mathrm{P}_n} \sigma_{\mathrm{P}_k} \tag{4.75}$$

with the correlation coefficient ρ_{nk}. Often, the correlation between different observation types is assumed to be zero ($\rho_{nk} = 0$). However, this assumption is generally not valid, especially between code pseudorange and phase measurements and between strong and weak loop phase measurements, due to the guiding as described in Sec. 3.2.5. The impact of the guiding on the correlation of weak signals (e. g. L2 phase observations from the P2 component) and on the ionosphere-free linear combination is demonstrated and analyzed in Sec. 5.

4.3.4 Differences of Observations

The expansion of the definition of Eq. (4.70), allowing observation differences between different receivers, satellites, and measurement epochs, opens further possibilities for reducing parameters from the ZD observation equations (4.67) and (4.69). Typically, observation equation differences are classified in single-differences (SDs), double-differences (DDs), and triple-differences (TDs). In the following only phase observations are considered. However, all equations are also valid for ZD code pseudorange observations.

Single-Differences

A SD can be built by ZD observations between two receivers with respect to the same satellite, between two satellites to the same receiver, or between two (subsequent) epochs referred to the same receiver and satellite. The equation of the difference between two receivers A and B according to Eq. (4.69) and with $\rho^i = |(\boldsymbol{r} + \boldsymbol{r}_\Delta) - (\boldsymbol{s}^i + \boldsymbol{s}_\Delta^i)|$ is given by

$$\begin{aligned}
\Delta P_{AB}^i = P_A^i - P_B^i = {} & \Delta\rho_{AB}^i + c\,(\Delta\delta t_{AB} + \Delta\alpha_{AB}) + \lambda\Delta N_{AB}^i \\
& - \Delta I_{AB}^i + \Delta T_{AB}^i + \Delta M_{AB}^i + \Delta U_{AB}^i + \lambda\Delta W_{AB}^i + \Delta\epsilon_{AB}^i.
\end{aligned} \tag{4.76}$$

The receiver independent terms like the satellite clock error and phase bias (assuming identical wavelengths between the differenced observations) vanish from the observation equation. However, the satellite clock is not completely eliminated because it is referred to the time epoch of transmission which is not identical for both receivers due to different light-travel times and receiver clock synchronization errors.

Combining two satellites i and j, the satellite single-difference can be formed

$$
\begin{aligned}
\Delta P_A^{ij} = P_A^i - P_A^j &= \Delta \rho_A^{ij} + c\left(\Delta \delta t^{ij} + \Delta \beta^{ij}\right) + \lambda \Delta N_A^{ij} \\
&\quad - \Delta I_A^{ij} + \Delta T_A^{ij} + \Delta M_A^{ij} + \Delta U_A^{ij} + \lambda \Delta W_A^{ij} + \Delta \epsilon_A^{ij}.
\end{aligned}
\tag{4.77}
$$

In this configuration the receiver clock synchronization error and bias are canceled out from the observation equation even though the synchronization error has to be known for the correction of the satellite position by the light-travel time as already mentioned. The assumption of identical wavelengths for the differenced observations is also required for Eq. (4.77). Considering the GLONASS system based on FDMA that consists of different carrier frequencies for all visible satellites from one site

$$
\lambda^i \neq \lambda^j,
\tag{4.78}
$$

single-difference GLONASS biases are included in the observation equation.

Double-Differences

The combination of both types of single-differences and accordingly the elimination of both, the receiver and satellite synchronization error and additional biases, is achieved by building double-differences, equivalent to the difference of two single-difference observation equations of Eq. (4.76) or (4.77)

$$
\begin{aligned}
\nabla \Delta P_{AB}^{ij} = \Delta P_{AB}^i - \Delta P_{AB}^j = \Delta P_A^{ij} - \Delta P_B^{ij} \\
= \nabla \Delta \rho_{AB}^{ij} + \lambda \nabla \Delta N_{AB}^{ij} - \nabla \Delta I_{AB}^{ij} + \nabla \Delta T_{AB}^{ij} \\
+ \nabla \Delta M_{AB}^{ij} + \nabla \Delta U_{AB}^{ij} + \lambda \nabla \Delta W_{AB}^{ij} + \nabla \Delta \epsilon_{AB}^{ij}.
\end{aligned}
\tag{4.79}
$$

The DD ambiguity term $\lambda \Delta N_{AB}^{ij}$ is finally an integer value, assuming equal wavelengths (which is not valid for GLONASS) and for building observation differences between different systems.

The noise $\nabla \Delta \epsilon_{AB}^{ij}$ of the DD observations is two times larger than that of the ZD observations assuming no correlations. While differencing two consecutive epochs of a DD observation, so-called triple-difference observations are obtained, where the time constant ambiguity term (no cycle slip assumed) is eliminated.

5 Analysis of the GNSS Signal Noise

Concluding from the previous sections the expected main error sources in the high frequency band above 1 Hz can be split into carrier noise, mainly white noise induced by thermal agitation in the electronic components of antenna and receiver, and into the dynamic stress due to the LOS accelerations and jerks. This chapter focuses on the analysis of the carrier noise. In order to prevent uncertainties about the expression "noise" often used in different context, it is introduced as carrier jitter σ_{PLL} defined in Sec. 4.2.3. According to Eq. (4.62), the jitter on the carrier phase measurements depends mainly on the PLL bandwidth B_{L} and the carrier-to-noise spectral density C/N_0. As described in Chapter 2, a lot of GNSS signals with different characteristics are available which put diverging demands on the carrier tracking, e. g., different B_{L}, guiding, and code/data demodulation techniques, and determine the final jitter of the carrier phase measurements.

Additionally, a short comparison of the jitter for different baseline lengths demonstrates the expected additional perturbations on the carrier phase in the frequency spectrum dependent on the baseline length.

The terminology used in this and following sections for the specific GNSS signals does not correspond to the official RINEX 3.02 convention (*IGS*, 2013). On one hand the chosen terms have been simplified because only carrier phase measurements were taken into account for the noise analysis, on the other hand the corresponding carrier channel, from which the carrier phase is derived, is defined by the modulated code. This definition is ambiguous considering all available signal components, but unique for the investigated carriers in the following sections:

CA/L1   GPS L1 carrier phase derived from the C/A-component (Q channel)
        RINEX 3.02 code: L1C

P1/L1   GPS L1 carrier phase derived from the P(Y)-component (I channel)
        RINEX 3.02 code: L1W

C1/L1   GPS L1 carrier phase derived form the L1C-component (Q channel), not
        available yet. RINEX 3.02 code: L1X

P2/L2   GPS L2 carrier phase derived form the P(Y)-component (I channel)
        RINEX 3.02 code: L2W

C2/L2   GPS L2 carrier phase derived form the L2C-component (Q channel)
        RINEX 3.02 code: L2X

C5/L5   GPS L5 carrier phase derived from I + Q channel
        RINEX 3.02 code: L5X

CA/R1   GLONASS L1 carrier phase derived from the C/A-component (Q channel)

              RINEX 3.02 code: L1C

P1/R1   GLONASS L1 carrier phase derived from the P-component (I channel)
              RINEX 3.02 code: L1P

C2/R2   GLONASS L2 carrier phase derived from the C2-component (Q channel)
              RINEX 3.02 code: L2C

P2/R2   GLONASS L2 carrier phase derived from the P-component (I channel)
              RINEX 3.02 code: L2P

E1   Galileo E1 carrier phase derived from I channel (E1-B and E1-C)
              RINEX 3.02 code: L1X

E5a   Galileo E5a carrier phase derived from I + Q channel (E5a-I and E5a-Q)
              RINEX 3.02 code: L5X

5.1 Measurement Setup and Equipment

In order to analyze the system noise above 1 Hz of high-rate GNSS receivers, zero-baseline measurements with a static antenna were performed (see Fig. 5.1). The signal from the antenna is split into two identical signals as input for the two receivers using a Huber+Suhner BNC-resistive power divider (*Huber+Suhner*, 2014). This configuration allowed a detailed study of receiver-induced errors because all other external error sources were eliminated or minimized.

For this experiment two different receiver types were used, two Javad Sigma-G3TAJ receivers with 100 sps (*Javad*, 2013) and two Leica GX1200 GNSS receivers with 20 sps (*Leica*, 2008). Almost all currently available GNSS signals were measured and analyzed with one or several receiver combinations visible in Fig. 5.1. All the signals for which the carrier jitter was determined and compared between each other are summarized in Tab. 5.1. Additionally, different PLL loop bandwidths B_L were tested, see Sec. 4.1.3 for the definition. The chosen CA/L1 PLL B_L of 10 Hz and 50 Hz for the Javad receivers defines the stable range for our experiments. Under good conditions (high signal strength) also higher bandwidths up to 100 Hz (*Moschas and Stiros*, 2014) allow a reliable phase tracking. The lower limit for the CA/L1 PLL bandwidth of about 5 Hz is mainly defined by the oscillator noise (in case of a static antenna). The Leica GX1200 receivers with the NovAtel OEM board have a fixed CA/L1 PLL B_L of 15 Hz. The predetection integration time T is not changeable for both receiver types. Due to the additive data sequences for the legacy GNSS signals the practical range of T is restricted to 1 - 20 ms (see Sec. 3.2.2) with low impact on the jitter according to Eq. (4.62) and visible in Fig. 4.3. Therefore, the difference between the 5 ms used by the Javad and 10 ms by the Leica receiver is negligible.

The receivers were connected to a Javad GrAnt-G3T GNSS antenna (*Javad*, 2014). The antenna is capable of covering a broad frequency range, 1555–1610 MHz and 1164–1253 MHz. The gain patterns for the three GPS frequency bands are illustrated in Fig. 3.2.
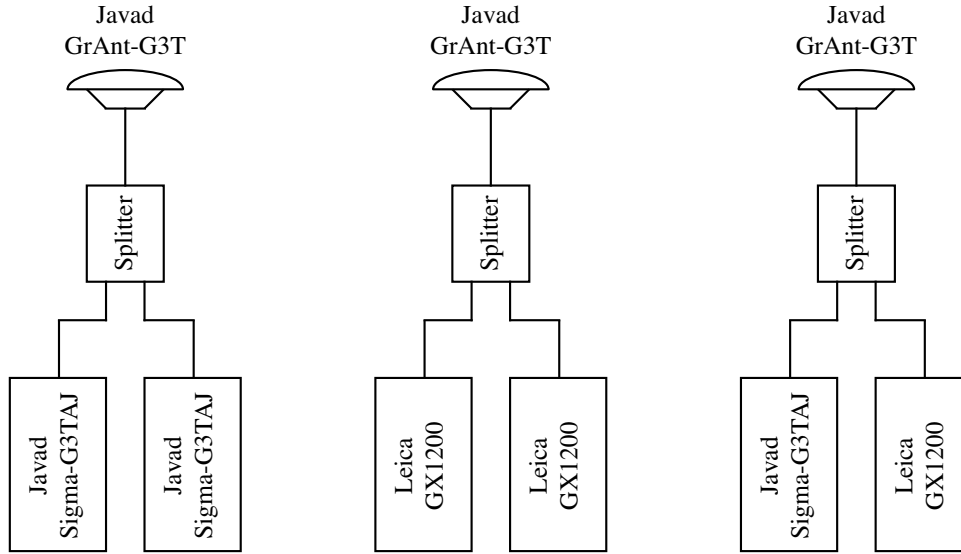
Figure 5.1: Different zero-baseline configurations were used for the high-frequency noise determination of the different signals listed in Tab. 5.1. The main analyses were performed with two Javad receivers (left), the only receivers which are capable of providing measurement outputs with 100 sps. In order to ensure a good comparison of the thermal noise induced carrier jitter the receivers were always connected to the Javad GrAnt-G3T GNSS antenna.

Table 5.1: Parameters and signals which were analyzed in this section.

Parameters and Signals	Javad Sigma-G3TAJ	Leica GX1200
GPS signals	CA/L1, P1/L1, C2/L2, P2/L2, C5/L5	CA/L1, P2/L2
GLONASS signals	CA/R1, C2/R2, P2/R2	-
Galileo signals	E1, E5a	E1, E5a
Loop bandwidth B_L [Hz]	10, 25, 50	15
Predetection integration T [ms]	5	10

5.2 Processing Strategies

The processing of the measurements in the configurations described in the previous section follows the common approach based on double-differences that eliminate almost all GNSS signal perturbations in case of a zero-baseline. According to the double-difference carrier phase Eq. (4.79), the formed zero-baseline equation between receiver A and B only comprises error sources which generate random processes in both receivers or are induced by different receiver configurations. Due to the connection to the same antenna the geometric range to the satellite is equal for both receivers. Additionally, the receiver and satellite clock offsets, the ionospheric and tropospheric delays are eliminated. Even though all these terms are canceled out, the time synchronization between both receivers or the synchronization of the receiver clocks to GPS time has to be known with a certain accuracy. The used receiver types are instantaneously determining the receiver clock offset to GPS time by several nanoseconds (code accuracy). The resulting range error due to

the different satellite positions and drifting satellite clocks during some nanoseconds is less than 0.1 mm and can be neglected. Also the atmospheric changes over this short timespan are far below the receiver induced noise. Finally, we get the following equation building a zero-baseline based on double-differences for satellites i, j and receivers A, B according to Eq. (4.79)

$$\nabla\Delta\Phi_{AB}^{ij} = \nabla\Delta N_{AB}^{ij} + \nabla\Delta\epsilon_{AB}^{ij}. \tag{5.1}$$

The double-difference ambiguity term $\nabla\Delta N_{AB}^{ij}$ is a constant integer offset (not for GLO-NASS). The second term $\nabla\Delta\epsilon_{AB}^{ij}$ contains the receiver and antenna system electronics induced noise. Based on the explanations in the previous chapters the carrier phase jitter due to thermal noise can be expected as the main part remaining in $\nabla\Delta\epsilon_{AB}^{ij}$. The carrier jitter in Eq. (4.63) is defined for a zero-difference observation between a receiver r and a satellite s

$$\sigma_{\mathrm{PLL}} = \sqrt{\frac{B_{\mathrm{L}}}{C/N_0}\left(1 + \frac{1}{2TC/N_0}\right)} \cong \sigma(\epsilon_r^s). \tag{5.2}$$

Note that the C/N_0 depends on the receiver and the satellite. With error propagation the double-difference jitter $\sigma(\nabla\Delta\epsilon_{AB}^{ij})$ can be calculated that finally corresponds to the standard deviation of the double-difference measurement after the reduction by $\nabla\Delta N_{AB}^{ij}$ (see Eq. (5.1))

$$\sigma(\nabla\Delta\epsilon_{AB}^{ij}) = \sigma(\nabla\Delta\Phi_{AB}^{ij}) = \sqrt{\sigma^2(\epsilon_A^i) + \sigma^2(\epsilon_A^j) + \sigma^2(\epsilon_B^i) + \sigma^2(\epsilon_B^j)} \tag{5.3}$$

assuming no correlations. In order to plot the measured carrier jitter $\sigma(\nabla\Delta\Phi_{AB}^{ij})$ with respect to C/N_0, a theoretical double-difference C/N_0 was calculated based on the square of the reciprocal sum of each zero-difference C/N_0. The measurements of the GNSS signals listed in Tab. 5.1 dependent on different tracking loop bandwidths B_{L} were averaged over a time window of 300 seconds and compared with the theoretical carrier jitter σ_{PLL} for double-differences according to Eqs. (5.2) and (5.3).

5.3 GPS Noise Representation

The analysis of the different GPS zero-baseline measurements is split into three sections. The first shows the fundamental characteristics of the legacy civil L1 signal (CA/L1) dependent on different loop bandwidths and receiver types. The second section focuses on the GPS carrier phases retrieved from P(Y)-code tracking, and finally the modern GPS signals with their possible property enhancements are directly compared to the jitter and signal strength of the legacy GPS signals. Several results were already published in *Häberling et al.* (2015).

5.3.1 GPS L1

Until the launch of Block IIR satellites, the modulated C/A-code on L1 (normal operation) was the only civil signal that could be received. The specifications in *IS-GPS-200G* (2012) guarantee a tracking of the CA/L1 carrier phase with a PLL B_{L} of 10 Hz. Under common
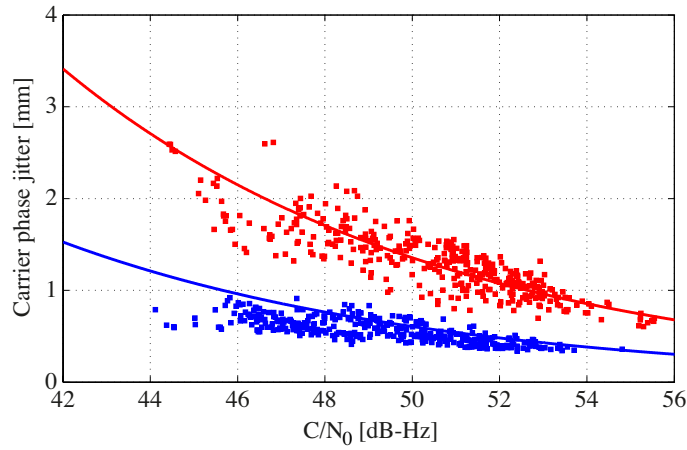
Figure 5.2: Each square shows the 100 sps double-difference carrier phase jitter averaged over a 300 s time window measured with Javad receivers with a CA/L1 B_{L} of 10 Hz (blue) and 50 Hz (red). The solid lines represent the theoretical σ_{PLL} calculated by Eq. (5.3) for double-differences. The decreased carrier phase jitter as a consequence of a narrow bandwidth is well visible.

conditions the bandwidth can be enlarged to at least 50 Hz in order to improve the dynamic tracking capabilities. Figure 5.2 shows the double-difference carrier phase jitter of 100 sps CA/L1 measurements with a B_{L} of 10 Hz (blue) and 50 Hz (red) dependent on the carrier-to-noise density ratio C/N_0 averaged over each 300 s window. The solid lines represent the theoretical jitter according to Eq. (5.2) for the double-difference case in Eq. (5.3). The final C/N_0 is between 44 and 56 dB-Hz with a corresponding double-difference jitter of 0.5–1 mm for a B_{L} of 10 Hz (blue) and 1–2 mm for a B_{L} of 50 Hz (red). The benefit from a better dynamic tracking using a wide bandwidth comes at the expense of doubled carrier jitter. But both match very well with the theoretically expected values. The small deviations of the estimated σ_{PLL} from the theoretical value can be explained by the oscillator jitter or uncertainties in the C/N_0 measurements. In geodesy the term carrier phase noise is often used and can finally be considered as the zero-difference jitter with the estimated values between 0.25 mm and 1 mm dependent on signal strength and the loop bandwidth used.

The carrier phase jitter CA/L1 σ_{PLL} estimated from two Leica GX1200 receivers with their fixed B_{L} of 15 Hz is visible in Fig. 5.3 as blue squares. Compared to the Javad measurements (red) with a B_{L} of 50 Hz (the same as in Fig. 5.2) the C/N_0 of the Leica measurements are about 3–4 dB-Hz lower. This demonstrates the receiver specific impact on C/N_0, especially the receiver front-end (see Sec. 3.1.3) with its different bandwidths and amplifications. The jitter is slightly higher than expected for a B_{L} of 15 Hz which could be explained by a significant oscillator jitter.

Performing the autocorrelation of the L1 zero-baseline measurements, the bandwidths B_{L} of the CA/L1 PLL are directly visible (see Fig. 5.4) as the zero-crossing of the autocorrelation function. The setup of the bandwidth for the Javad receiver only defines the upper limit. The receiver is able to reduce its PLL bandwidth automatically in order to improve the tracking capability under weak conditions (see Sec. 5.3.2). However, the CA/L1 loops with a nominal signal strength of more than 45 dB-Hz are generally working with stable bandwidths. The ACF of the Leica GX1200 CA/L1 zero-baseline measurements
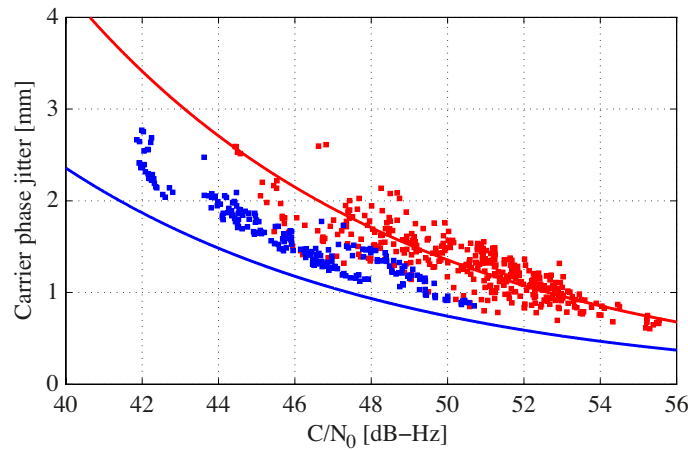
Figure 5.3: The blue squares show the 20 sps double-difference carrier phase jitter during a 300 s time window measured by a Leica receiver with a CA/L1 B_{L} of 15 Hz. The 100 sps jitter of the Javad measurements with a 50 Hz B_{L} (red) are exactly the same as plotted in Fig. 5.2. The solid lines represent the theoretical σ_{PLL} calculated by Eq. (5.3) for double-differences.

are shown in Fig. 5.8 (top). The bandwidth B_{L} visible as the zero-crossing rather corresponds to 20 Hz than the specified 15 Hz and would additionally explain the higher jitter in Fig. 5.3 (blue). However, the sampling rate is too small to determine the exact value.

The impact of the correlations induced by the loop filter on dynamic applications is demonstrated by the shake table experiments in Sec. 7. Additionally, these CA/L1 tracking loops with relatively wide bandwidths support the narrow loop bandwidth for code tracking and weak carrier phase tracking such as P1/L1 and P2/L2 (see Sec. 5.3.2).

5.3.2 GPS L1 and L2 Based on P(Y)-Code Tracking

For geodetic applications the utilization of an additional carrier phase with a different frequency is essential while processing long baselines or single receiver measurements (single point positioning). The building of the ionosphere-free linear combination of L1 and L2 allows the reduction of the influence of the dispersive ionosphere. The L1 and L2 carriers are modulated by the P-code which is generally known for civilian users and specified in *IS-GPS-200G* (2012). In order to prevent spoofing of the P-code, the Department of Defense modulates an encrypted W-code onto the P-code. The resulting antispoofing P(Y)-code, still with the same chipping-rate as the original P-code, is not available to civilian users. The received minimum signal power of the P(Y) component on L2 (P2/L2) at the user antenna is 6 dB (for Block IIR) and 3 dB (for Block IIR-M and newer) lower than the received signal power of CA/L1. Contrary to L1, L2 has no additional C/A-code and the reconstruction of the L2 carrier phase has to be performed without the knowledge of the modulated P(Y)-code. For this purpose, several codeless or semi-codeless methods for carrier tracking of L2 were developed (*Woo*, 2000). However, all the demodulation methods produce an additional squaring loss, at least 8 dB for high signal strength, which dramatically increases at low C/N_0. Due to the significantly reduced C/N_0 the P2/L2 PLL requires a much narrower bandwidth than the CA/L1 PLL.
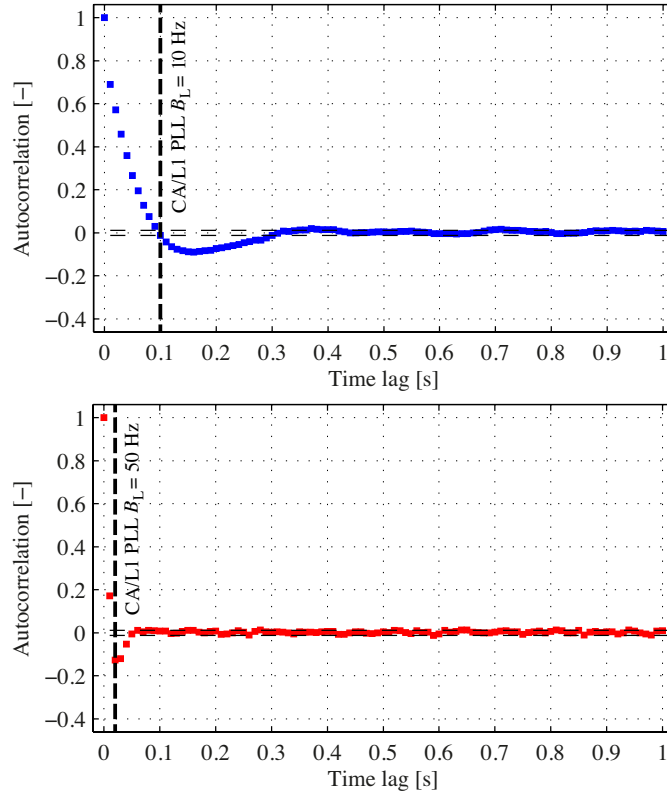
Figure 5.4: Correlations between subsequent epochs for a CA/L1 B_L of 10 Hz (top) and 50 Hz (bottom). The vertical dashed lines mark the bandwidths which exactly correspond to the zero-crossing of the autocorrelation function. The horizontal dashed lines represent the 95% confidence bounds.

The higher carrier phase jitter of L2 (black) compared to L1 (red) shown in Fig. 5.5 mainly results from the lower C/N_0, although the P2/L2 loop bandwidth of 3 Hz is significantly lower than the 50 Hz of the CA/L1 PLL. As already mentioned some receivers (e.g. Javad) take advantage of changeable weak loop bandwidths to allow a reliable tracking of signals with an extremely low signal strength at low elevation angles. This strategy of a decreased P2/L2 loop bandwidth for low C/N_0 is visible in Fig. 5.5 as a lower carrier jitter than theoretically expected. The dashed line corresponds to the theoretical jitter induced by a loop filter bandwidth linearly reduced from 3 Hz to 1.5 Hz over the tracked C/N_0 from 40–25 dB-Hz. Additionally, these characteristics can be demonstrated by the corresponding bandwidths in Fig. 5.6 calculated by the zero-crossing for each 300 s window. On the one hand the 10–20 dB-Hz lower C/N_0 of P2/L2 (black) compared to CA/L1 (blue) is significant due to the decryption algorithm, on the other hand the reduction of the B_L (black) to about 1.5 Hz is well visible dependent on C/N_0. In order to ensure the dynamic tracking ability, the CA/L1 PLL is aiding the tracking of P2/L2 with its narrow loop bandwidth. The impact of the CA/L1 PLL aiding on P2/L2 is shown in Fig. 5.7 marked as vertical dashed lines. The reduction of the P2/L2 PLL B_L can reach remarkable values of 0.2 Hz as visible for the Leica GX1200 in Fig. 5.8 (bottom) and the corresponding CA/L1 guiding at 15 Hz (first epochs). However the thermal noise induced jitter σ_{PLL} for a 0.2 Hz B_L does not correspond to the theoretical, extremely low value which is expected for a narrow B_L For
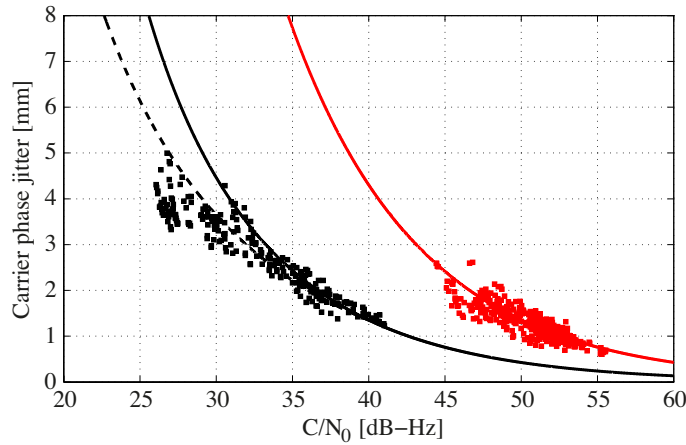
Figure 5.5: The squares show the 100 sps double-difference carrier phase jitter for 300 s time windows measured with Javad receivers for the CA/L1 carrier phase with a B_L of 50 Hz (red) and for the P2/L2 signal with a B_L of 3 Hz (black). The solid lines represent the theoretical σ_PLL calculated by Eq. (5.3) for double-differences. The dashed line denotes σ_PLL based on a linearly decreasing bandwidth of 1.5 Hz. Even with a narrower bandwidth than the CA/L1, the P2/L2 has a higher jitter due to the significant lower signal strength.
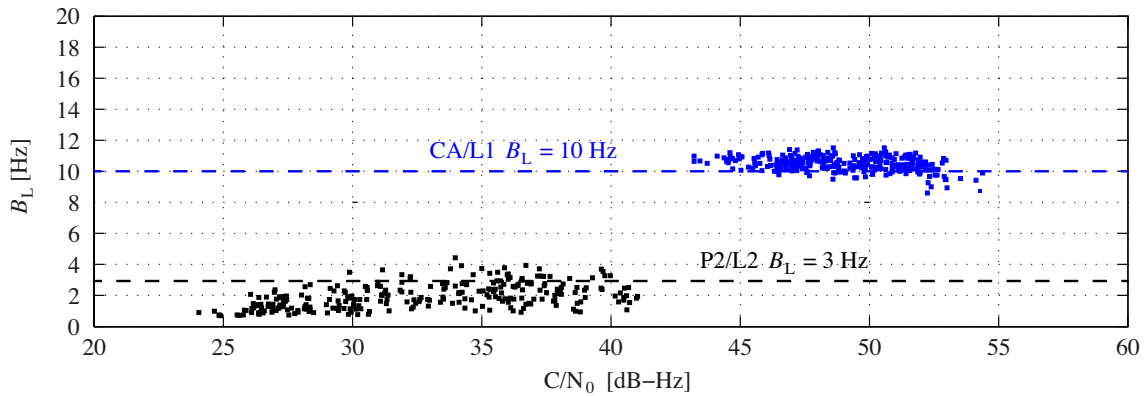
Figure 5.6: The change of the CA/L1 B_L of 10 Hz (blue) and the P2/L2 B_L of 3 Hz (black) is demonstrated dependent on carrier-to-noise density ratio C/N_0. The B_L was calculated by the zero-crossing of the autocorrelation function for each 300 s window. For a high signal strength above 40 dB-Hz the receiver operates with a stable B_L (see 10 Hz B_L). In order to ensure the tracking of extremely weak signals the already narrow bandwidth is additionally reduced.

such narrow bandwidths the oscillator jitter is the dominant factor.

There are GPS receivers which allow the retrieval of the L1 carrier phase from the P(Y)-code component (P1/L1). Apart from the incoming signal of P1/L1 being 3 dB stronger (for Block IIR) compared to P2/L2, the tracking requirements and the resulting signal characteristics are almost identical to P2/L2 (see Figs. 5.9 and 5.10). For the Javad receivers the decryption of the P(Y)-code on L1 is not independent from that on L2. Due to the related decryption logic the final C/N_0 at baseband is identical for P1/L1 and P2/L2. The black diamonds in Fig. 5.9 represent the double-difference jitter of P1/L1 compared to P2/L2 (black squares), both with a B_L of 3 Hz, and the CA/L1 jitter (red) with a B_L of
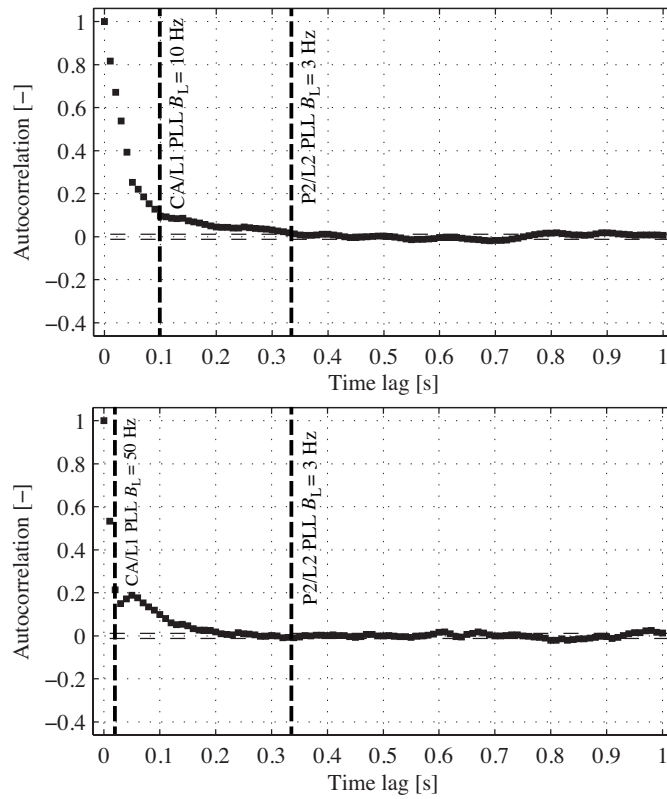
Figure 5.7: Correlations between subsequent epochs for a 3 Hz P2/L2 B_L guided by a 10 Hz CA/L1 B_L (top) and a 3 Hz P2/L2 B_L guided by a 50 Hz CA/L1 B_L (bottom). The weak loop bandwidth corresponds exactly to the zero-crossing of the autocorrelation function.

50 Hz. The only differences between P1/L1 and P2/L2 are caused by considering several partially different data sets (different observation sequences), even though the metric P1/L1 jitter should be slightly lower than that of P2/L2 due to the smaller carrier wavelength. The values for the double-difference carrier jitter based on P(Y)-code tracking are between 1–5 mm (0.5–2.5 mm for the zero-difference case), which is two times higher than the CA/L1 jitter at high C/N_0 with a narrow bandwidth (10 Hz) and up to 3 times higher at low C/N_0.

5.3.3 Modern GPS signals

In the course of the GPS modernization several additional civil signals, such as C2/L2 (since Block IIR-M) and the new frequency L5 (since Block IIF) are available and enhance the tracking capabilities. As introduced in Sec. 2.3.1 and 2.3.2 the modern signals have some fundamental advantages over the legacy signals, especially over the encrypted P(Y)-code modulation. The bit sequences building the L2C-code and the codes on L5 are public and known to all users. Therefore, the demodulation process does not suffer from signal strength loss due to the decryption logic. Compared to the C/A-code, the modern code sequences are longer for a better spectral resolution and higher robustness against narrowband interferences, and with an additional short cycled code for a short acquisition
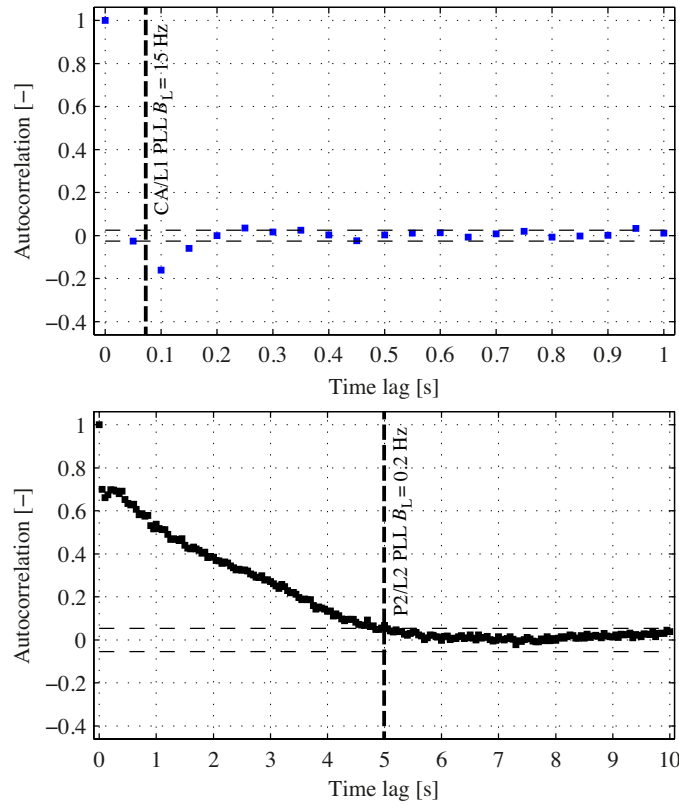
Figure 5.8: Correlations between subsequent epochs for a Leica GRX1200 receiver with a 15 Hz CA/L1 B_L (top). The P2/L2 with its extremely wide bandwidth of 0.2 Hz is guided by the CA/L1 tracking loops (bottom). The vertical dashed lines mark the bandwidths which correspond to the zero-crossing of the autocorrelation function. The horizontal dashed lines represent the 95% confidence bounds.

time. These properties in combination with a specified high received signal strength as listed in Tab. 2.2 with a dataless pilot channel, that additionally improves the C/N_0 at baseband, allow the usage of a wide tracking loop bandwidth (comparable to CA/L1). Fig. 5.11 shows the correlation of subsequent epochs for C2/L2 (left) and C5/L5 (right) with a B_L of 50 Hz each. The possible wide bandwidth makes L2C and L5 extremely interesting for a tracking combination with CA/L1 (*Salem*, 2010) and in future with L1C. The carrier jitter is improved by almost a factor of two compared to P2/L2 (and P1/L1 respectively), even with a large bandwidth of 50 Hz (see Fig. 5.12).

As demonstrated, the signal strength is a key factor for the carrier phase characteristics with respect to noise and expected receiver response (see also Sec. 7). The differences in C/N_0 for the available GPS signals are presented based on an example of a new Block IIF satellite (PRN24). In Fig. 5.13, the signal strengths of all signals transmitted by that satellite (top) are compared to the change of the elevation angle (bottom). The modern signals are represented by the red (C5/L5) and green (C2/L2) curves. In addition to the blue CA/L1, both P(Y)-code derived carrier phases (P1/L1 and P2/L2) have exactly the same signal strength due to the used decryption logic which is not independent from each other (black). The decryption methods are additionally dependent on the received signal
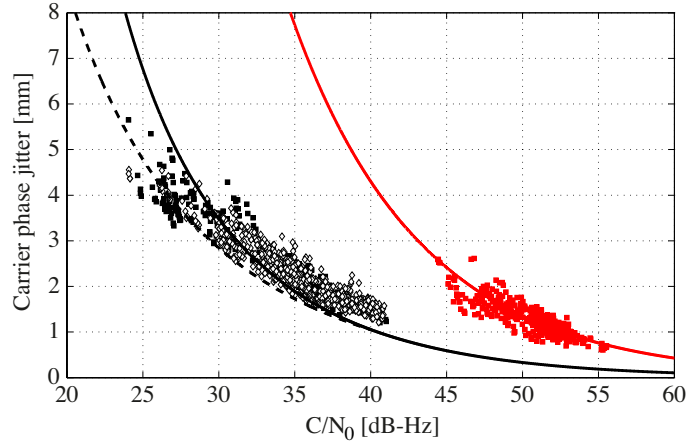
Figure 5.9: The double-difference jitter for the carrier phase retrieved from the P(Y)-component (I channel) of L1 (black diamonds) corresponds to the jitter of the P2/L2 carrier phase (black squares), both with a B_L of 3 Hz. Even though the P1/L1 tracking loops use a narrow loop bandwidth, the jitter is about 2 times higher than for the CA/L1 carrier measurements with a B_L of 50 Hz (red) due to the lower signal strength. The dashed line represents the same linear bandwidth reduction of 1.5 Hz as shown in Fig. 5.5.
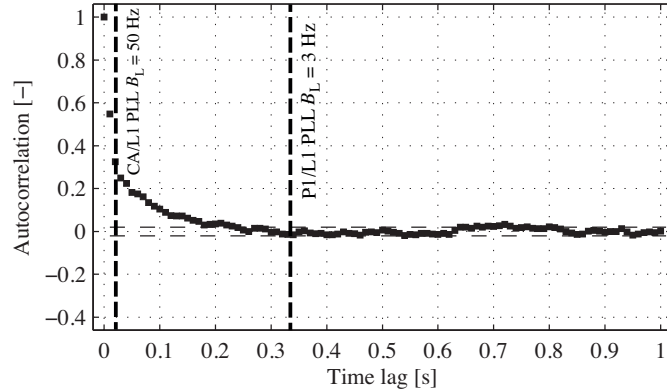
Figure 5.10: The correlations between subsequent epochs are determined by the guiding CA/L1 PLL with a B_L of 50 Hz and the P1/L1 PLL B_L of 3 Hz. This is exactly the same behavior as shown for the P2/L2 carrier in Fig. 5.7.

strength itself and produces a larger squaring loss for weak signals, which is visible as a stronger signal attenuation at lower elevation angles compared to the other GPS signals.

The expected C/N_0 differences with respect to CA/L1 are approximated and listed in Tab. 5.2. The power assumption includes the specified minimum received power, the antenna gain pattern shown in Fig. 3.2, the tracked signal component, and the tracking capability. For the loss of L2 and L5 signals due to the antenna gain pattern a mean value was taken over the elevation range. The specified received power for L2C comprises the data (50 %) and pilot (50 %) channel. Considering the received power of the pilot channel leads to a component loss of 3 dB, but to a benefit of 6 dB for the dataless tracking. The computation of the P(Y)-code carrier component power is more difficult due to the
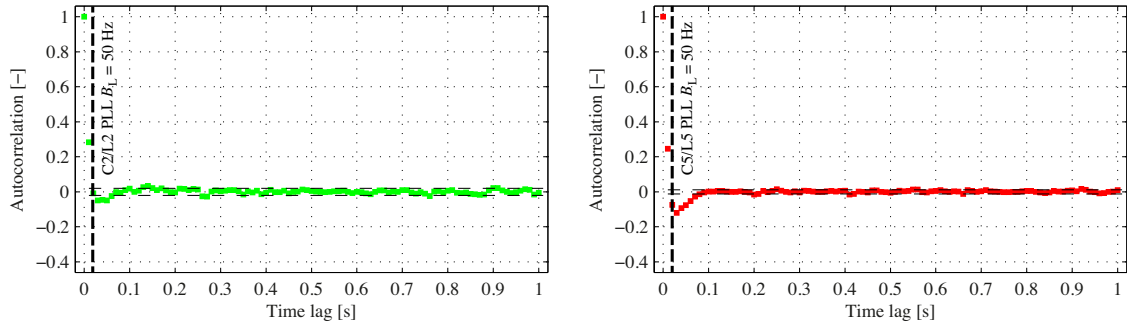
Figure 5.11: Correlations between subsequent epochs for the modern C2/L2 (left) and C5/L5 (right) which directly corresponds to the CA/L1 PLL with its 50 Hz B_L setting (see Fig. 5.4 bottom).
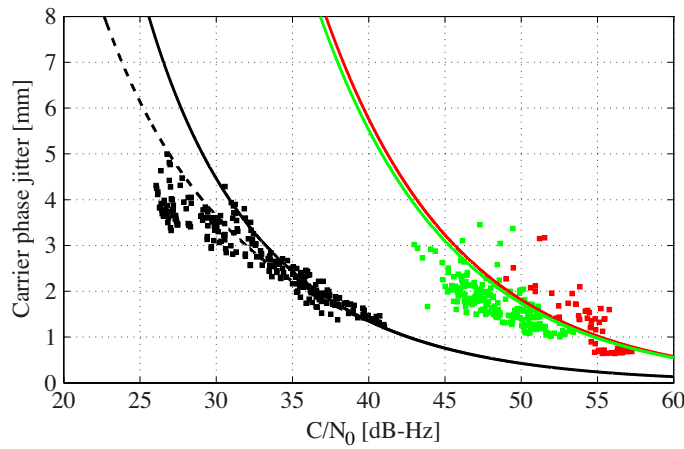
Figure 5.12: The squares show the 100 sps double-difference carrier phase jitter for 300 s time windows measured with Javad receivers for the modern GPS signals with a 50 Hz B_L (C2/L2 in green and C5/L5 in red) compared to the legacy P2/L2 with a B_L of 3 Hz (black). The solid and dashed lines represent the theoretical σ_{PLL} calculated by Eq. (5.2) for double-differences. The much higher signal strength causes a significant lower jitter even with a wider loop bandwidth (comparable to CA/L1 in Figs. 5.5 and 5.9).

dependency of the squaring loss on the received signal strength (elevation dependent) and the used decryption algorithm. In the case of the Javad receivers, the demodulation of P1/L1 and P2/L2 are not independent and finally the determination of C/N_0 produces exactly the same values. The assumed squaring loss of 8 dB assumes a high signal strength with a sophisticated demodulation procedure (e.g. maximum a posteriori (MAP) approach, see *Woo* (2000)).

The calculated values of about $+4$ dB for C5/L5, $+0.5$ dB for C2/L2, and -12 dB for the P(Y) modulated carriers are marked as dashed lines in Fig. 5.14. The figure shows the difference between the same signals as those visible in Fig. 5.13, but with respect to the C/N_0 of CA/L1. During the first 40 minutes the $\Delta C/N_0$ remain constant and range around the expected values in Tab. 5.2. It seems that an increasing multipath affects the GPS signal tracking due to the higher signal power fluctuations after 40 min (see also Fig. 5.13).
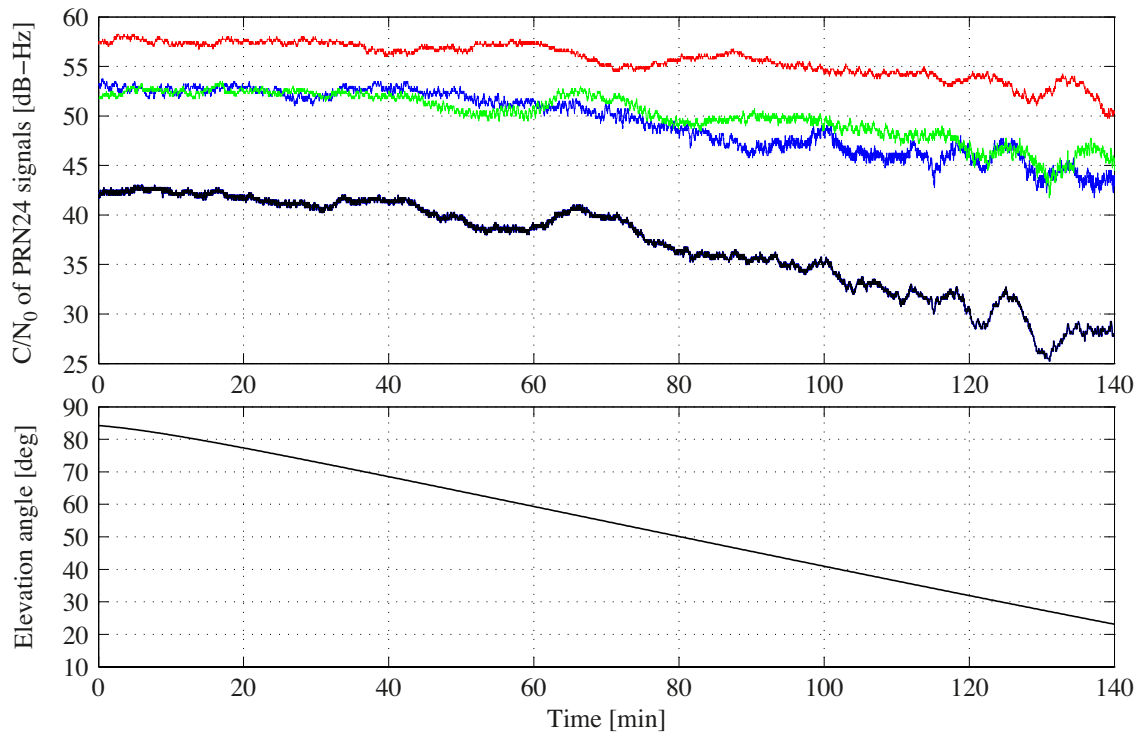
Figure 5.13: The top figure shows the baseband C/N_0 for different GPS signals transmitted by PRN24, a modern Block IIF satellite: the legacy GPS signals CA/L1 (blue), P1/L1 and P2/L2 (black) and the modern signals C5/L5 (red) and C2/L2 (green) as a function of the elevation angle (bottom).

Table 5.2: The approximated signal gain or loss with respect to the CA/L1 signal dependent on the specified minimum received power, on the antenna gain pattern (see Fig. 3.2), on the power sharing of the signal components (L2C: 50 % data channel and 50 % pilot channel), and on the tracking capabilities.

Signal	Specified [dB]	Antenna [dB]	Component [dB]	Tracking [dB]	Total [dB]
C5/L5	+0.6	−2.5	0	+6	+4.1
C2/L2	−1.5	−1	−3	+6	+0.5
P1/L1,P2/L2	−3.0	0/−1	0	min. −8	−12.0

The increased signal level of the modern GPS signals compared to CA/L1 in Fig. 5.14 demonstrates the higher robustness against multipath due to the new code designs.

5.4 GLONASS L1 and L2

The Russian satellite-based navigation system GLONASS has reached its full operational capability in 1996 with 24 satellites. However, due to technical problems and the short lifetime of the first launched satellites the Russian government planned to rebuild the system with a new satellite generation. Since mid of 2011, 21 active satellites of the type
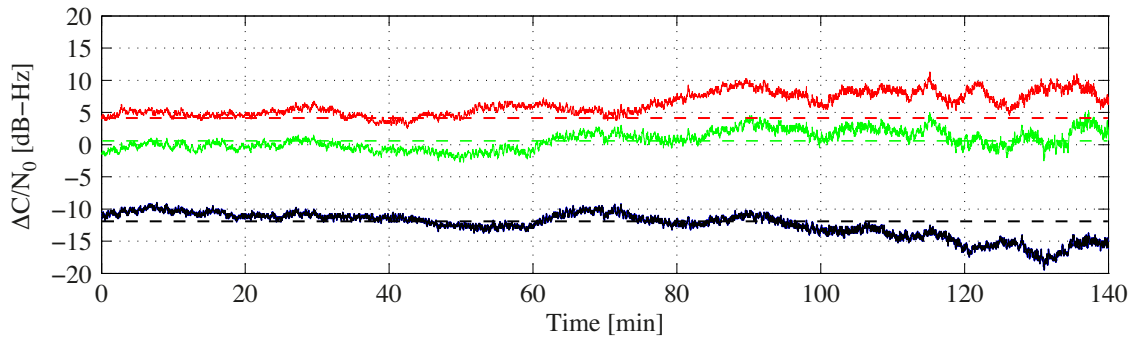
Figure 5.14: The difference in C/N$_0$ compared to CA/L1 for C5/L5 (red), C2/L2 (green), P1/L1 and P2/L2 (black) respectively transmitted by PRN24, a modern Block IIF satellite.

GLONASS-M are in orbit and grew up to 24 satellites in 2014. One of the first GLONASS-only solutions of a global network was performed by *Meindl* (2011). Additionally, it could be demonstrated that the combined GPS/GLONASS solution is preferable with respect to the single-system solutions due to the larger amount of simultaneously observable satellites, better distribution, and a different repeatability of the ground tracks.

In this section the GLONASS carrier noise compared to GPS is demonstrated by the zero-baseline measurements with two Javad Sigma-G3TAJ GNSS receivers and the Javad GrAnt-G3T GNSS antenna. The double-difference carrier phase jitter shown in Fig. 5.15 bases on the PLL setting with a B_L of 50 Hz for the CA/R1 signal (red) and 5 Hz for the P2/R2 (black) and C2/R2 signal (blue). The corresponding bandwidths for CA/R1 and for the weak signals P2/R2 and C2/R2 with the additional guiding by CA/G1 are well visible in Fig. 5.16. Due to the signal strength of CA/R1 that is 6 dB higher compared to the GLONASS L2 signals (see Tab. 2.3), the jitter for the GLONASS L1 and L2 signals in Fig. 5.15 are almost identical, even though a much more narrow bandwidth for the weak signals (black and blue) is used. The separation of the main block of the red squares to the blue and black squares corresponds to the specified 6 dB difference. C2/R2 shows a slightly higher signal strength than P2/R2, but no significantly lower jitter. As described in Sec. 2.1.4 and 2.4, the signals of GLONASS are BPSK modulated and similar to the legacy GPS signals. However, the multiple access technique based on FDMA is completely different from GPS and Galileo signals using CDMA. The FDMA technique requires extended receiver front-ends and is not fully compatible to other GNSS signals, see also Sec. 2.4.1. Typical commercial GNSS receivers and antennas are not optimized for FDMA. This can be demonstrated by the comparison of the GLONASS CA/R1 jitter (red squares) with the GPS CA/L1 (red diamonds) in Fig. 5.15. Based on the specifications of the minimum received signal power, the expected GLONASS CA/R1 signal strength would be 2.5 dB lower than the GPS CA/L1. But the measurements show an almost 10 dB lower C/N_0 and lead to a jitter more than twice the GPS carrier jitter. The GLONASS L2 weak signals can be measured in the C/N_0 range between 25 and 40 dB-Hz and correspond to the GPS carrier phases based on a P(Y)-code modulation even though the GLONASS signals are not encrypted. The GLONASS L2 signals cover the frequency range between 1242.9 MHz and 1248.6 MHz which is at the edge of the frequency band that the GrAnt-G3T GNSS antenna is specified for (see Sec. 5.1). The missing compatibility to other GNSS and their
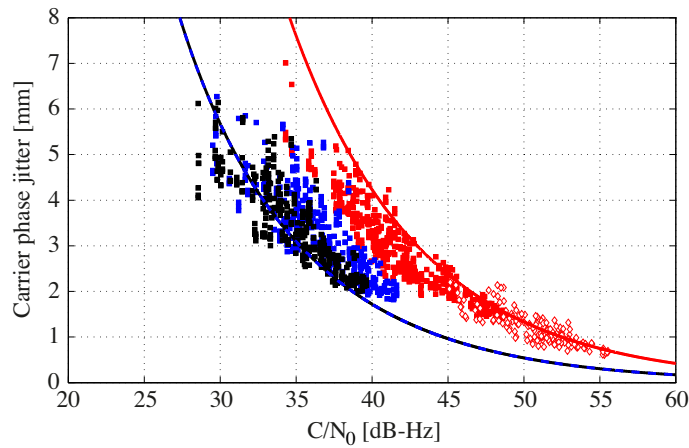
Figure 5.15: The GLONASS double-difference carrier phase jitter for CA/R1 with a B_{L} of 50 Hz (red), P2/R2 (black) and C2/R2 (blue) with a B_{L} of 5 Hz. Also the GLONASS carrier noise matches well with the theoretically expected jitter for the corresponding bandwidths (solid lines). However, due to the lower signal strength received (see Tab. 2.3), the GLONASS jitter, especially for L1 (R1), is significantly higher than that of GPS (red diamonds).

signals is one of the major reasons, why FDMA will be replaced by CDMA in the course of the GLONASS modernization.

5.5 Galileo E1 and E5a

Contrary to GLONASS, the new European navigation system Galileo is based on the newest modulation techniques and satellite hardware (e.g. hydrogen masers as satellite clocks). In addition to an improved integrity for safety relevant applications, the compatibility to GPS is a primary issue (see Sec. 2.5). The performance and characteristics of the Galileo signals E1 OS and E5a are demonstrated by zero-baseline measurements in all three receiver configurations displayed in Fig. 5.1. The Javad Sigma-G3TAJ receivers are set to the standard configuration with a 25 Hz B_{L}. In combination with the Leica receiver with a fixed B_{L} of 15 Hz the sampling rate was reduced to 20 sps. At the time of this investigation four Galileo satellites were in orbit and active: E11, E12, E19, and E20.

The 100 sps double-difference jitter for E1 (black) in Fig. 5.17 shows as expected good properties visible as a low jitter and small correlations as shown in Fig. 5.18 (left). The E5a signal (red) can be tracked at a slightly higher signal strength compared to E1 (for the specifications see Tab. 2.4), however the measured jitter is significantly above the theoretical value (solid red line). The sub-band signal E5a is multiplexed as an AltBOC modulation on the E5 carrier which can alternatively be demodulated assuming an independent BPSK(10) modulation. The Javad receiver firmware version used at the time of these measurements was not able to track the AltBOC signal, probably the implementation of the receiver tracking was not optimized yet and would explain the additional stronger negative correlations after the first zero-crossing in Fig. 5.18 (right) and a small resonance frequency outside the loop bandwidth.
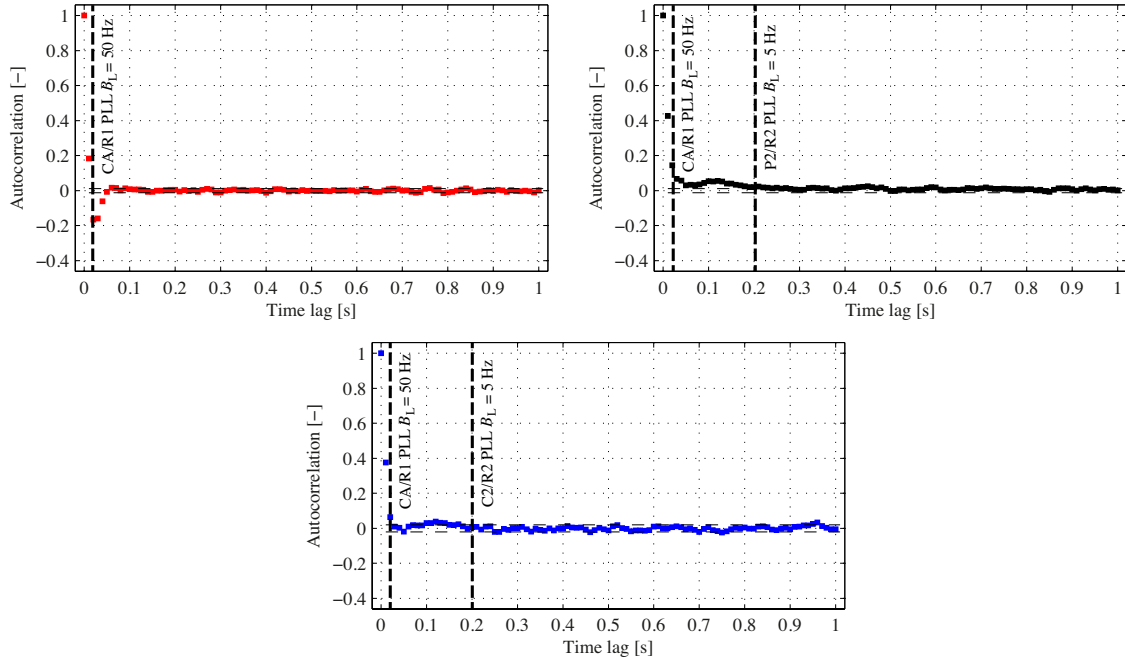
Figure 5.16: The correlations between subsequent epochs for the GLONASS CA/R1 carrier phase (top left) and the P2/R2 carrier phase measurements (top right) demonstrate the PLL setting with a B_L of 50 Hz for the CA/R1 signal as well as the guiding of the P2/R2 signal with a 5 Hz B_L (top right). At the bottom the GLONASS L2 phase ACF from the C/A component (C2/R2) with a 5 Hz PLL B_L that shows a similar behavior as P2/R2. The loop bandwidths are marked as vertical dashed lines.

Especially between 44 and 48 dB-Hz, which is dominated by the double-difference E11–E12, shows an abnormally high jitter for E5a (see Fig. 5.17). However, no significant systematic signal can be detected in the ACF dependent on different double-differences built by the same receiver types. The example of a specific double-difference is given for two Javad receivers in Fig. 5.18 and for two Leica receivers in Fig. 5.19. This behavior of the ACFs is valid for all 6 double-differences if they are built between two identical receiver types.

Building double-differences of the four Galileo satellites between two different receiver types, the usually uncorrelated jitter (only affected by the loop bandwidth) contains some significant systematic signals for Galileo E1 (Fig. 5.20) and E5a (Fig. 5.22). Only the double-difference between E19 and E20 (both launched after E11 and E12 with slightly different hardware) is not dominated by additional signals. However, the corresponding frequency spectra visible in Fig. 5.21 for E1 and in Fig. 5.23 for E5a show even for E19–E20 two small but significant spectral lines. According to the appearing significant frequencies listed in Tab. 5.3, different blocks can be distinguished. Firstly, there is no significant frequency which shows up in all double-differences. Each spectral line has a direct dependency on one of the Galileo signals and they are not independently generated by the receiver. This proposition can be confirmed by the fact, that no such significant signals appear in zero-baselines for GPS signals using two different receivers. The spectral resolution of the shown spectra is 0.36 mHz with a Nyquist frequency of 10 Hz. The E5a carrier
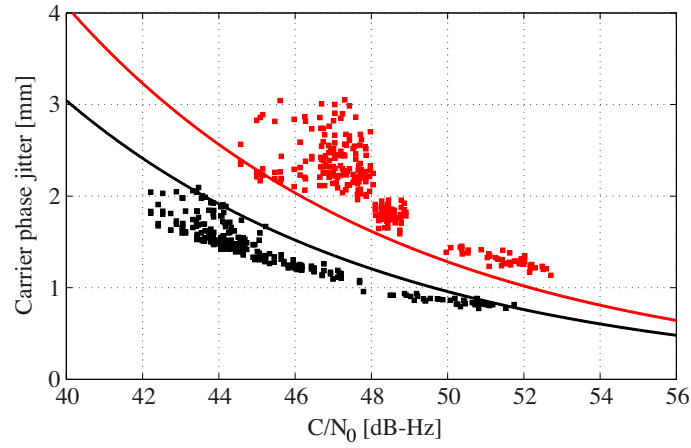
Figure 5.17: The Galileo double-difference 100 sps carrier phase jitter for E1 (black) and E5a (red) with a B_L of 25 Hz measured with the Javad Sigma-G3TAJ receivers. The carrier noise of E1 is slightly below the theoretically expected jitter for the corresponding bandwidths (solid line), but higher for the E5a signal especially at low signal strength.
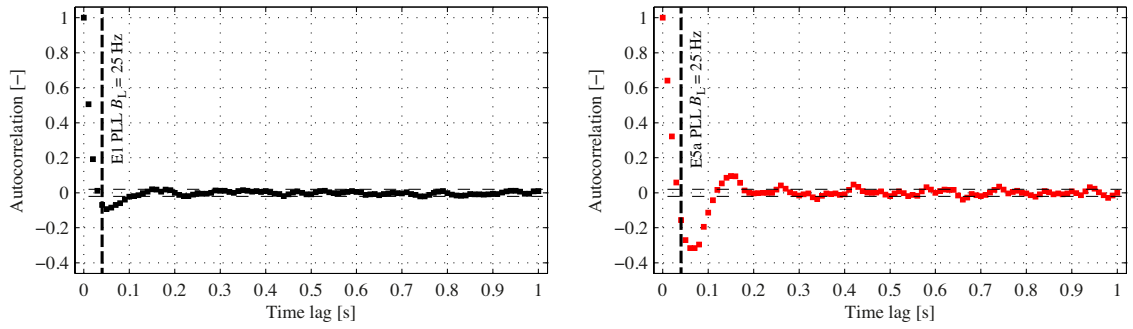
Figure 5.18: The correlations between subsequent epochs measured by two Javad Sigma-G3TAJ receivers for the Galileo E1 (black) and E5a (red) carrier phases show the PLL B_L of 25 Hz used for both signals. They are marked by the vertical dashed lines and correspond to the zero-crossing.
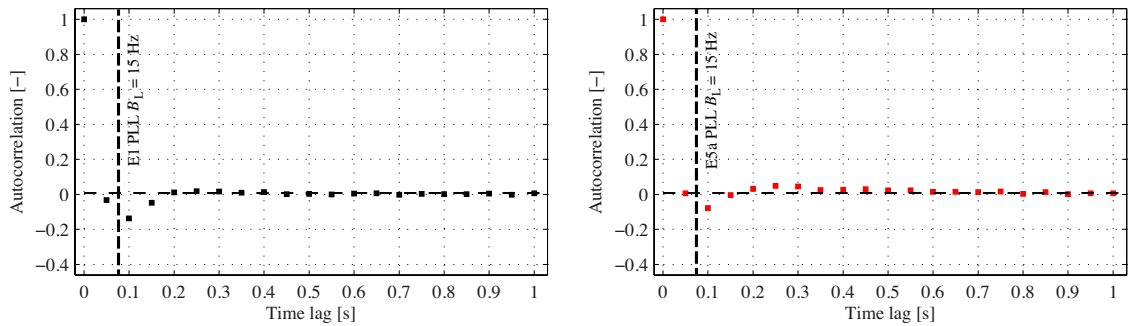
Figure 5.19: The correlation between subsequent 20 sps epochs measured by the Leica GRX1200 for the Galileo E1 (black) and E5a (red) carrier phases show the PLL B_L of 15 Hz for both signals. They are marked by the vertical dashed lines and correspond to the zero-crossing.

Table 5.3: This table shows the significant frequencies appearing in the spectra (Fig. 5.21 and Fig. 5.23) for all possible double-differences. They are separately listed for the two Galileo carrier frequencies E1 and E5a.

Frequency [Hz]	Galileo E1 amplitudes [mm] for double-differences					
	E11-E12	E11-E19	E11-E20	E12-E19	E12-E20	E19-E20
0.11703	0.03	–	–	0.02	0.02	–
1.87541	0.03	–	–	0.03	0.03	–
3.31941	–	–	0.06	–	0.06	0.06
4.00468	0.06	0.04	0.04	0.04	0.04	–
5.58804	–	0.06	–	0.05	–	0.06
5.99568	2.26	1.58	1.56	2.01	2.02	–
8.00756	0.14	0.10	0.10	0.15	0.15	–

Frequency [Hz]	Galileo E5a amplitudes [mm] for double-differences					
	E11-E12	E11-E19	E11-E20	E12-E19	E12-E20	E19-E20
0.11703	0.08	–	–	0.06	0.06	–
0.99568	0.18	0.15	0.14	0.17	0.16	–
1.87541	0.07	–	–	0.06	0.08	–
3.31941	–	–	0.08	–	0.08	0.08
4.00468	0.20	0.16	0.16	0.13	0.14	–
5.58804	–	0.09	–	0.08	–	0.09
5.99568	3.35	2.35	2.33	2.98	2.99	–
8.00756	0.11	0.08	0.08	0.13	0.13	–
8.12459	0.07	–	–	0.06	0.06	–
9.00432	0.11	0.11	0.12	0.09	0.09	–
9.88333	0.07	–	–	0.06	0.06	–

phase contains four spectral lines that are not available at E1, three higher than 8 Hz, and one dominant at a frequency of 0.99568 Hz. All other frequencies are identical for E1 and E5a up to the given spectral resolution, but with higher amplitudes for E5a. The detected frequency of 3.31941 Hz can be assigned to the PRN number E20, and 5.58804 Hz to E19. E11 has no isolated spectral lines and the lines only appear in combination with E12. While the E12 signal is generating a large amount of different frequencies (especially on E5a), the most dominant signals show up for the satellites E11 and E12, and do not show up in the double-difference E19–E20. Especially the frequency at 5.99568 Hz (for E1 and E5a) is the most dominant signal and is responsible for the behavior of the ACFs in Figs. 5.20 and 5.22 for the most part. The amplitudes of the signals at 8.00756 Hz, and 4.00468 Hz for E1 and E5a, and 0.99568 Hz and 9.00432 Hz (only for E5a) are at least one magnitude smaller.

The appearance of different significant frequencies on the Galileo carriers is attributed to a subtle cross talk of signals from two active atomic frequency standards in the clock monitoring and control unit (CMCU). The Galileo satellites are equipped with four atomic clocks, and two of these clocks operate in a redundant configuration. This phenomenon is more distinctive for the firstly launched satellites E11 and E22 than for E19 and E20.
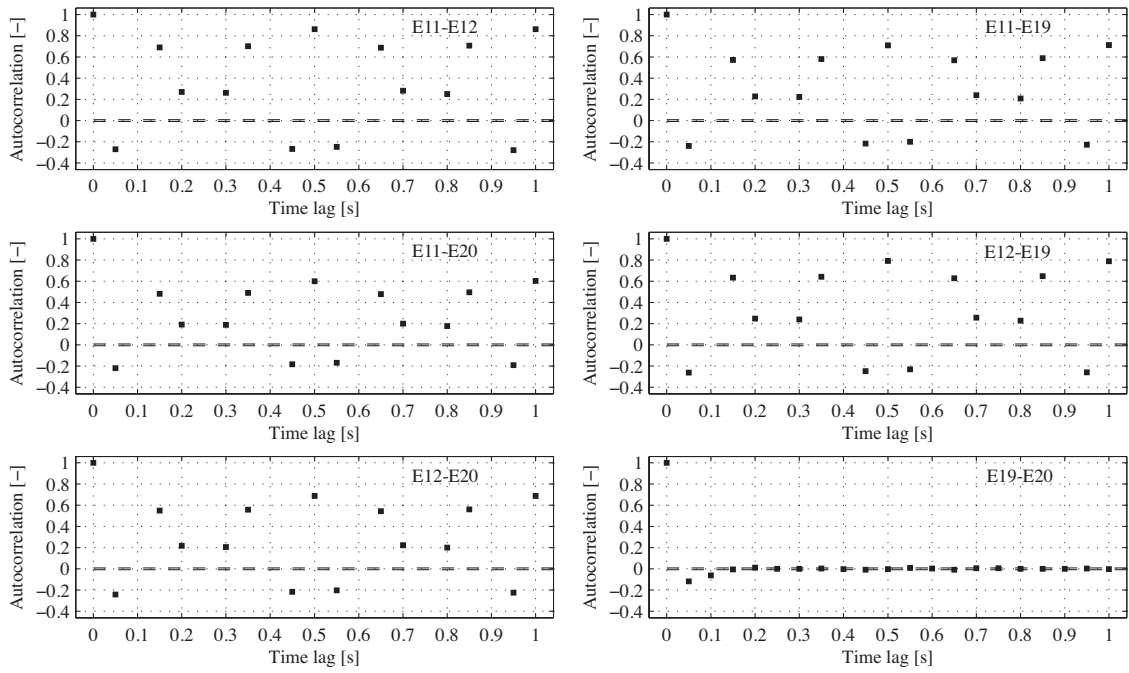
Figure 5.20: The autocorrelation functions of the E1 20 sps zero-baseline measurements between a Javad and a Leica receiver for all possible Galileo double-differences. Only the combination between the satellites E19 and E20 shows the expected behavior as shown in Figs. 5.18 and 5.19. Including measurements from E11 and E12 additional signals appear, see also the spectra in Fig. 5.21.
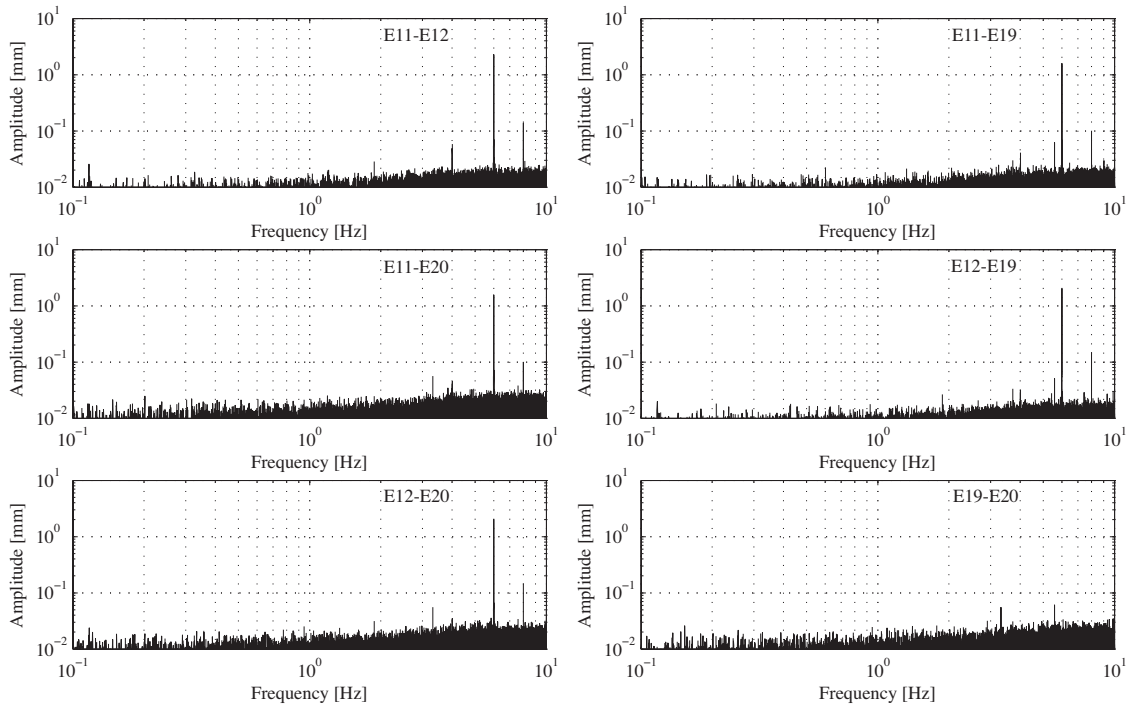
Figure 5.21: The frequency spectra of the E1 20 sps zero-baseline measurements between a Javad and a Leica receiver for all possible Galileo double-differences. The exact frequencies of the peaks are listed in Tab. 5.3.
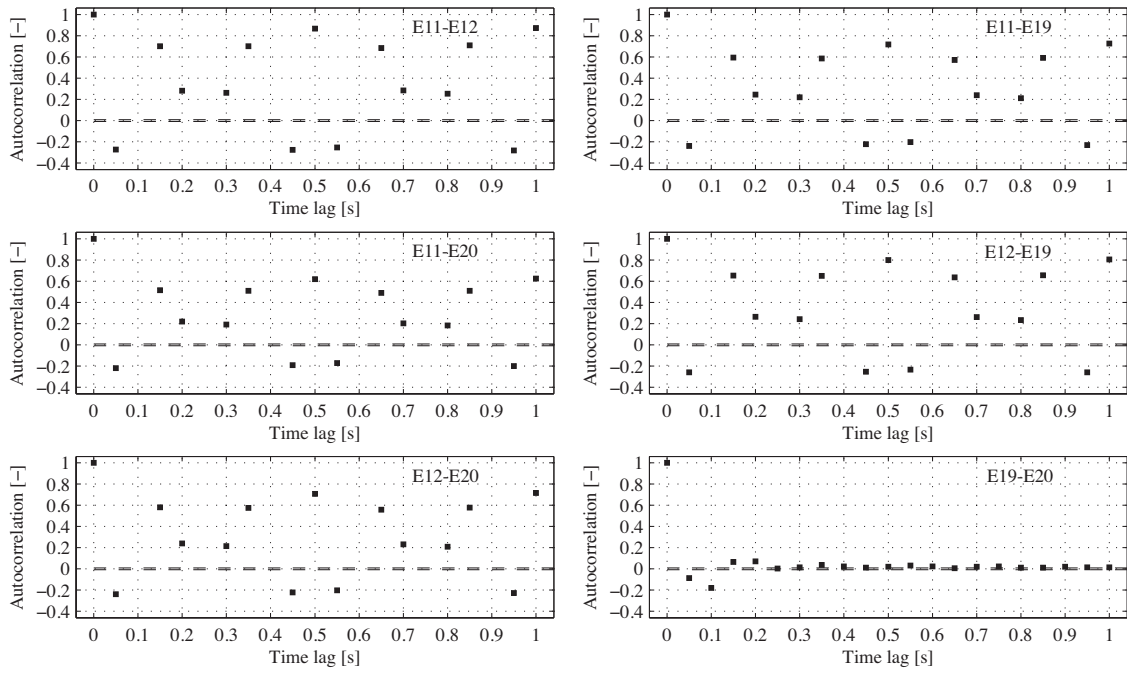
Figure 5.22: The autocorrelation functions of the E5a 20 sps zero-baseline measurements between a Javad and a Leica receiver for all possible Galileo double-differences. Only the combination between satellites E19 and E20 shows the expected behavior as shown in Figs. 5.18 and 5.19. Including measurements from E11 and E12 additional signals appear, see also the spectra in Fig. 5.23.
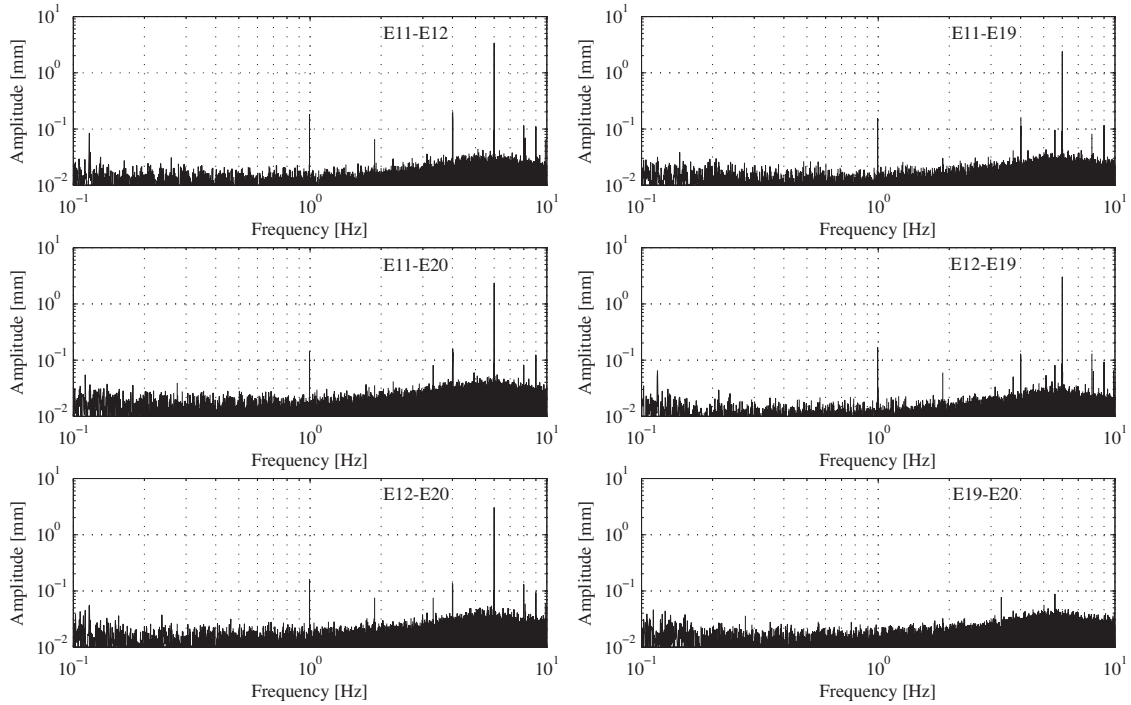
Figure 5.23: The frequency spectra of the E5a 20 sps zero-baseline measurements between a Javad and a Leica receiver for all possible Galileo double-differences. The exact frequencies of the peaks are listed in Tab. 5.3.

More details about the functionality of the CMCU and analysis of the cross talk can be found in *Montenbruck et al.* (2015).

The reason for detecting these amplitudes is caused by the different receiver response of the two receiver types (see Sec. 7.2). If the response was not different for the two receivers (Javad and Leica), the signals would not be visible in the double-differences as it has been shown in the ACFs of the Galileo zero-baselines between receivers of the same manufacturer (see Figs. 5.18 and 5.19). This means that the observed amplitudes are not identical to the originally generated signals and are additionally dependent on the frequency of each signal.

5.6 Firmware Error

As demonstrated in the previous sections the measurements based on a zero-baseline configuration provide information about some baseband functions implemented in the receiver firmware. This allows the study and verification if the receiver works as expected, especially the fundamental tracking functionalities. The following example of a wrongly implemented function in the firmware demonstrates the huge impact on the characteristics of carrier phase measurements. In Sec. 3.2.5 as well as in Fig. 3.7 it has been shown that the delay-locked loop (DLL) is guided by the strong CA/L1 PLL similar to that of weak signals, e. g. P1/L1 and P2/L2 demonstrated in the previous sections. The autocorrelation of zero-baseline CA/L1 carrier phase measurements in Fig. 5.24 shows a completely different behavior compared to the theoretically expected strong loop ACF as shown in Fig. 5.4. The 50 Hz CA/L1 PLL B_L is not visible in Fig. 5.24 which is dominated by a strongly correlated signal. This ACF is caused by the extremely narrow DLL B_L of 1 Hz (even though carrier phase measurements are processed) and produces strong correlations, because the PLL was misleadingly guided by the DLL. After the discovery of this absolutely counterproductive process, the manufacturer has been informed and the new firmware were released with the switched guiding function.
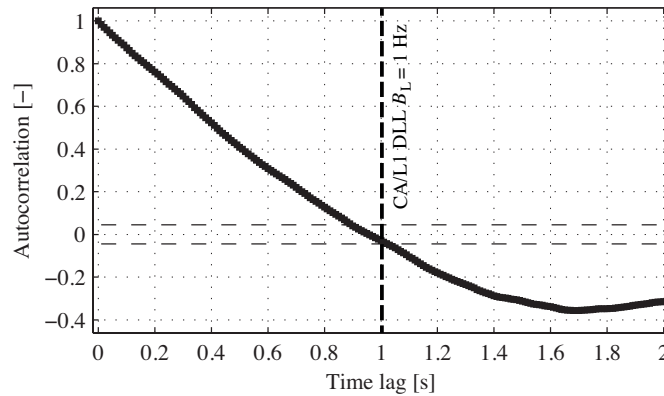
Figure 5.24: This autocorrelation function of CA/L1 GPS carrier phase measurements provides an example of a wrongly designed PLL. The loop bandwidth was set to 10 Hz and the resulting correlations should show the behavior visible in Fig. 5.4 (top). However, the strong correlation with an apparent bandwidth of 1 Hz instead of 10 Hz corresponds to the DLL B_L used for the code tracking.

5.7 Limitation on Coordinate Estimation

The impact of thermal noise on the measurements of available GNSS signals with their different characteristics were demonstrated in the previous sections. The induced jitter defines the accuracy limit for the carrier phase measurements. It has been shown that the zero-baseline configuration is able to represent the double-differences as uncorrelated noise only affected by the loop bandwidth and the signal strength. In order to give an impression of the expected limit on the estimation of final highly frequent kinematic coordinates, the 100 sps zero-baseline measurements were processed with a standard baseline procedure. In the case of a zero-baseline, it generally contains the projection of all double-differences with their properties shown in Sec. 5.3.1 and Sec. 5.3.2 into the desired coordinate system, here a topocentric system. The final jitter on the coordinates is therefore a combination of each C/N_0 which is mainly dependent on the elevation angle (see Fig. 5.13) due to the antenna gain pattern (atmosphere is only a small factor) and the dilution of precision (DOP) dependent on the number of available satellites and their distribution. The DOP can directly be retrieved from the cofactor matrix of the unknowns $\mathbf{Q}_{xx}$ which is the inverse of the normal equation matrix. Based on a geocentric coordinate system (xyz) the geometric dilution of precision (GDOP) and the position dilution of precision (PDOP) can be calculated by the diagonal elements

$$\begin{aligned} \text{GDOP} &= \sqrt{q_{xx} + q_{yy} + q_{zz} + q_{tt}} \quad \text{and} \\ \text{PDOP} &= \sqrt{q_{xx} + q_{yy} + q_{zz}}. \end{aligned} \tag{5.4}$$

where q_{ii} are the elements of the cofactor matrix. The GDOP additionally contains the receiver clock correction element q_{tt}. For the calculation of the local DOP values, e.g. in a topocentric system described by the rotation matrix $\mathbf{R}_{ENh}$, the cofactor matrix can be transformed:

$$\mathbf{Q}_{ENh} = \mathbf{R}_{ENh} \mathbf{Q}_{xx} \mathbf{R}_{ENh}^{T} \tag{5.5}$$

With the EDOP (East coordinate), NDOP (North coordinate), and VDOP (vertical/height coordinate) given by

$$\begin{aligned} \text{EDOP} &= \sqrt{q_{EE}}, \\ \text{NDOP} &= \sqrt{q_{NN}}, \text{ and} \\ \text{VDOP} &= \sqrt{q_{hh}} \end{aligned} \tag{5.6}$$

the final accuracy of each coordinate component can be calculated as

$$\begin{aligned} \sigma_E &= \text{EDOP}\,\sigma_{PLL}, \\ \sigma_N &= \text{NDOP}\,\sigma_{PLL}, \text{ and} \\ \sigma_h &= \text{VDOP}\,\sigma_{PLL}. \end{aligned} \tag{5.7}$$

Due to the time dependency of the DOP and the σ_{PLL} (corresponding to the zero-difference standard deviation), the kinematic coordinates in Figs. 5.25, 5.26, and 5.27 represent only an example for a specific satellite constellation. For a direct comparison between CA/L1-only (Fig. 5.25), P2/L2-only (Fig. 5.26), and the ionosphere-free linear combination L_c (Fig. 5.27), only the observations containing both, L1 and L2, were taken into account for the processing. The empirically estimated standard deviations of each coordinate time

series are listed in Tab. 5.4 and are used to plot the normally distributed histograms as solid red lines. The kinematic coordinates still show the properties of a normally distributed noise. The only correlation is induced by the loop bandwidths as already shown in the previous sections. This amount of noise in the kinematic coordinates induced by thermal noise defines the limit which can not be underrun. The mean DOP values calculated by Eq. (5.6) over the two-hour session are as follows: EDOP = 0.57, NDOP = 0.76, and VDOP = 1.25. The ratio between the East, North, and height components is directly given by the DOP values. The coefficients are listed in Tab. 5.5 and correspond very well to the empirically estimated values from Tab. 5.4. The small deviations are caused because on one hand the cofactor matrix used contains only the zero-difference geometry without the correlations between the double-differences and no ambiguities. On the other hand all available observations in the RINEX files are used for the calculation of the cofactor matrix which can slightly differ from the finally used observations for the position computation due to preprocessing steps (e.g. screening). The L2 noise that is about 2.5 times higher than that of L1 corresponds to a mean value over all C/N_0 in Fig. 5.5. With the factors of the linear combination L_c of Eq. (4.71) the expected noise for L_c can be calculated by error propagation using the standard deviations of L1 and L2 from Tab. 5.4. Assuming that L1 and L2 are uncorrelated, the expected $\sigma(L_c)$ for all components would be

$$\hat{\sigma}_E(L_c) = \sqrt{\kappa_{1,c}^2\, \hat{\sigma}_E^2(L_1) + \kappa_{2,c}^2\, \hat{\sigma}_E^2(L_2)} = 2.41 \quad [\text{mm}]$$

$$\hat{\sigma}_N(L_c) = \sqrt{\kappa_{1,c}^2\, \hat{\sigma}_N^2(L_1) + \kappa_{2,c}^2\, \hat{\sigma}_N^2(L_2)} = 3.67 \quad [\text{mm}] \tag{5.8}$$

$$\hat{\sigma}_h(L_c) = \sqrt{\kappa_{1,c}^2\, \hat{\sigma}_h^2(L_1) + \kappa_{2,c}^2\, \hat{\sigma}_h^2(L_2)} = 5.84 \quad [\text{mm}].$$

This values are significantly ($\approx 20\%$) higher than those listed in Tab. 5.4 from the processed L_c coordinates. As discussed in Sec. 5.3.2 and visible in the ACFs of Fig. 5.25 and 5.26, the weak P2/L2 loop is guided by the strong CA/L1 loop. The assumption of no correlation between L1 and L2 is therefore not valid. The covariances between L1 and L2 were empirically estimated from the coordinate time series as

$$\hat{\sigma}_E(L1,L2) = 0.25$$

$$\hat{\sigma}_N(L1,L2) = 0.53 \tag{5.9}$$

$$\hat{\sigma}_h(L1,L2) = 1.50.$$

The finally calculated standard deviations

$$\hat{\sigma}_E(L_c) = \sqrt{\kappa_{1,c}^2\, \hat{\sigma}_E^2(L_1) + \kappa_{2,c}^2\, \hat{\sigma}_E^2(L_2) + 2\,\kappa_{1,c}\kappa_{2,c}\, \hat{\sigma}_E(L1,L2)} = 1.96 \quad [\text{mm}]$$

$$\hat{\sigma}_N(L_c) = \sqrt{\kappa_{1,c}^2\, \hat{\sigma}_N^2(L_1) + \kappa_{2,c}^2\, \hat{\sigma}_N^2(L_2) + 2\,\kappa_{1,c}\kappa_{2,c}\, \hat{\sigma}_N(L1,L2)} = 3.05 \quad [\text{mm}]$$

$$\hat{\sigma}_h(L_c) = \sqrt{\kappa_{1,c}^2\, \hat{\sigma}_h^2(L_1) + \kappa_{2,c}^2\, \hat{\sigma}_h^2(L_2) + 2\,\kappa_{1,c}\kappa_{2,c}\, \hat{\sigma}_h(L1,L2)} = 4.72 \quad [\text{mm}]$$

$$\tag{5.10}$$

.

correspond exactly to the standard deviations from Tab. 5.4 as you expected from a mathematical point of view. This means that the correlations between L1 and L2 due to the guiding reduce the ionosphere-free linear combination noise by about 20%. The overall noise level can slightly be improved by a better satellite constellation and a more narrow

loop bandwidth. However, the main goal is to detect high frequent motions with a certain dynamic which limits the CA/L1 PLL B_L. Additionally, the impact of P2/L2 that dramatically increases the noise is playing the dominant role for L_c. In future, when the increased number of available Block IIR-M and IIF satellites allows the usage of the civil C2/L2 or C5/L5 as a second carrier phase frequency to CA/L1, the L_c noise level can be reduced by about 25% if they are treated as uncorrelated between each other.

Table 5.4: The standard deviations from the computed kinematic coordinates with a sampling rate of 100 sps measured by two Javad Sigma-G3TAJ with a CA/L1 PLL B_L of 25 Hz and a P2/L2 PLL B_L of 3 Hz.

Signal	East $\hat{\sigma}_E$ [mm]	North $\hat{\sigma}_N$ [mm]	Height $\hat{\sigma}_h$ [mm]
L1	0.52	0.75	1.26
L2	1.31	2.03	3.16
L_c	1.96	3.05	4.71

Table 5.5: The comparison between the coefficients describing the relation between the three topocentric components East, North, and height calculated by the DOP values and empirically by the coordinates from Fig. 5.25, 5.26, and 5.27.

Signal	NDOP/EDOP	$\hat{\sigma}_N/\hat{\sigma}_E$	VDOP/EDOP	$\hat{\sigma}_h/\hat{\sigma}_E$	VDOP/NDOP	$\hat{\sigma}_h/\hat{\sigma}_N$
L1	1.3	1.4	2.2	2.4	1.7	1.7
L2	1.3	1.5	2.2	2.4	1.7	1.6
L_c	1.3	1.5	2.2	2.4	1.7	1.6

The system noise that was considered to be dominated by the carrier jitter induced by thermal noise, for the most part, defines the lower boundary of GPS positioning accuracy. For a common L_c relative positioning with a longer baseline than zero, additional error sources are affecting the coordinate estimation, such as atmosphere, multipath, as described in Eq. (4.69). However for the detection of high frequent motions, the main aspect is the distribution of the noise floor and the external perturbations over the frequency spectrum. The frequency analysis of the coordinates processed with three different baseline lengths should demonstrate the expected amount of total noise between 50 Hz and 1000 seconds, see Fig. 5.28. All four receivers were Javad Sigma-G3TAJ with a CA/L1 PLL B_L of 25 Hz and a P2/L2 PLL B_L of 3 Hz. Two receivers were connected to a Leica ART20 antenna on the roof of the HPV building at ETH Hönggerberg via a splitter and built the zero-baseline (HPV1–HPV2). The short baseline of about 10 m was processed with the measurements from HPV1 and the station ETH3 which is connected to the officially inactive Agnes station ETHZ (see Sec. 8.1.2 for a short description of the site). The long baseline of about 110 km was built by HPV1 and a station at Fiescheralp in the Valais, also this station is shortly documented in Sec. 8.1.2. All measurements were collected during the same time span. The frequency spectra of the processed L_c topocentric coordinates based on the zero-baseline (black), 10 m (red), and 110 km (blue) baseline are plotted in Fig. 5.28.

The black spectrum represents the carrier jitter σ_{PLL} (black) mainly induced by thermal
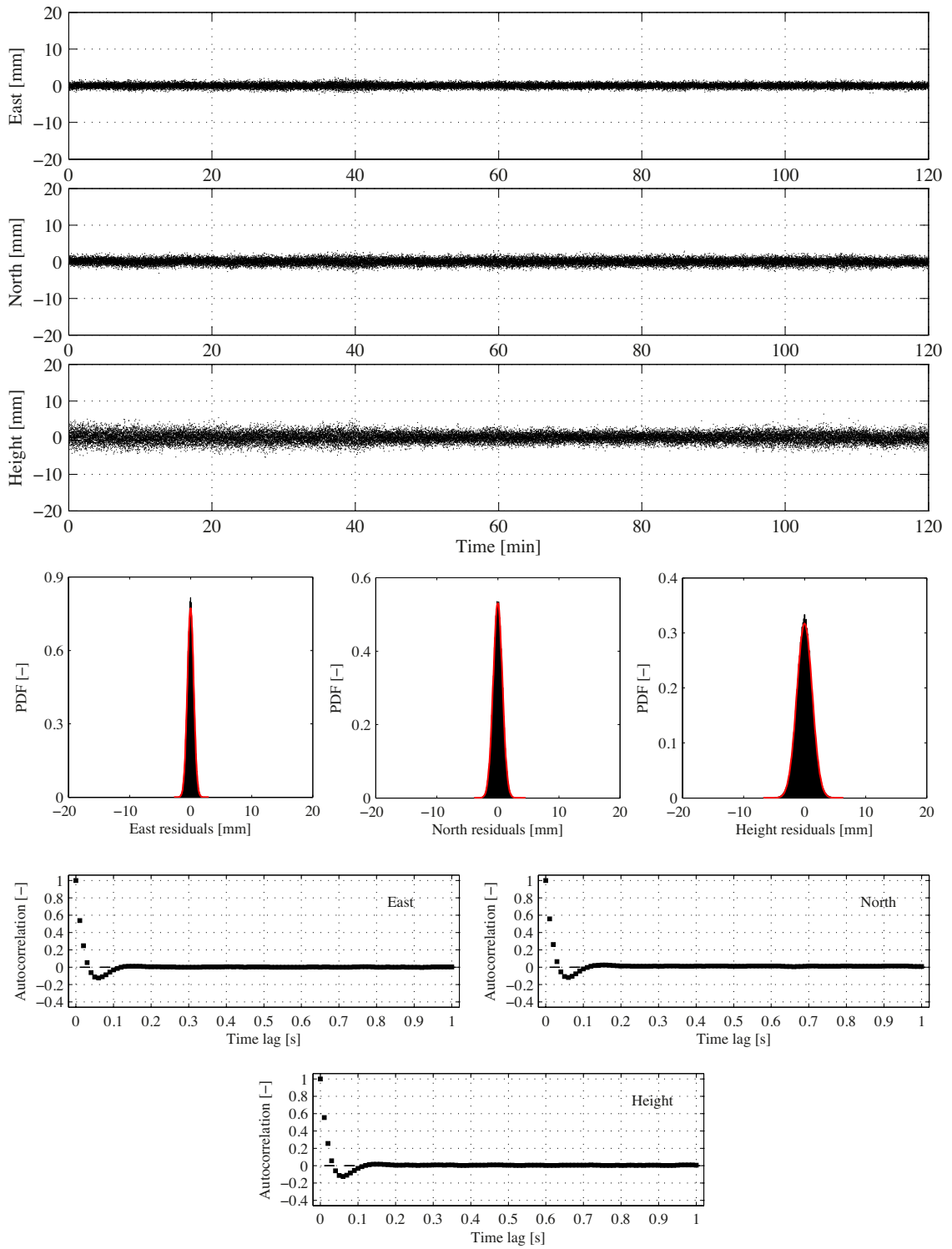
Figure 5.25: The L1 zero-baseline coordinates for the topocentric components with the corresponding histograms and autocorrelation functions. The standard deviations for each component are listed in Tab. 5.4. The red line in the histograms indicates the normal distribution dependent on the empirically estimated standard deviation from the kinematic coordinates at the top. The ACFs show the CA/L1 PLL B_{L} of 25 Hz by the zero-crossing.
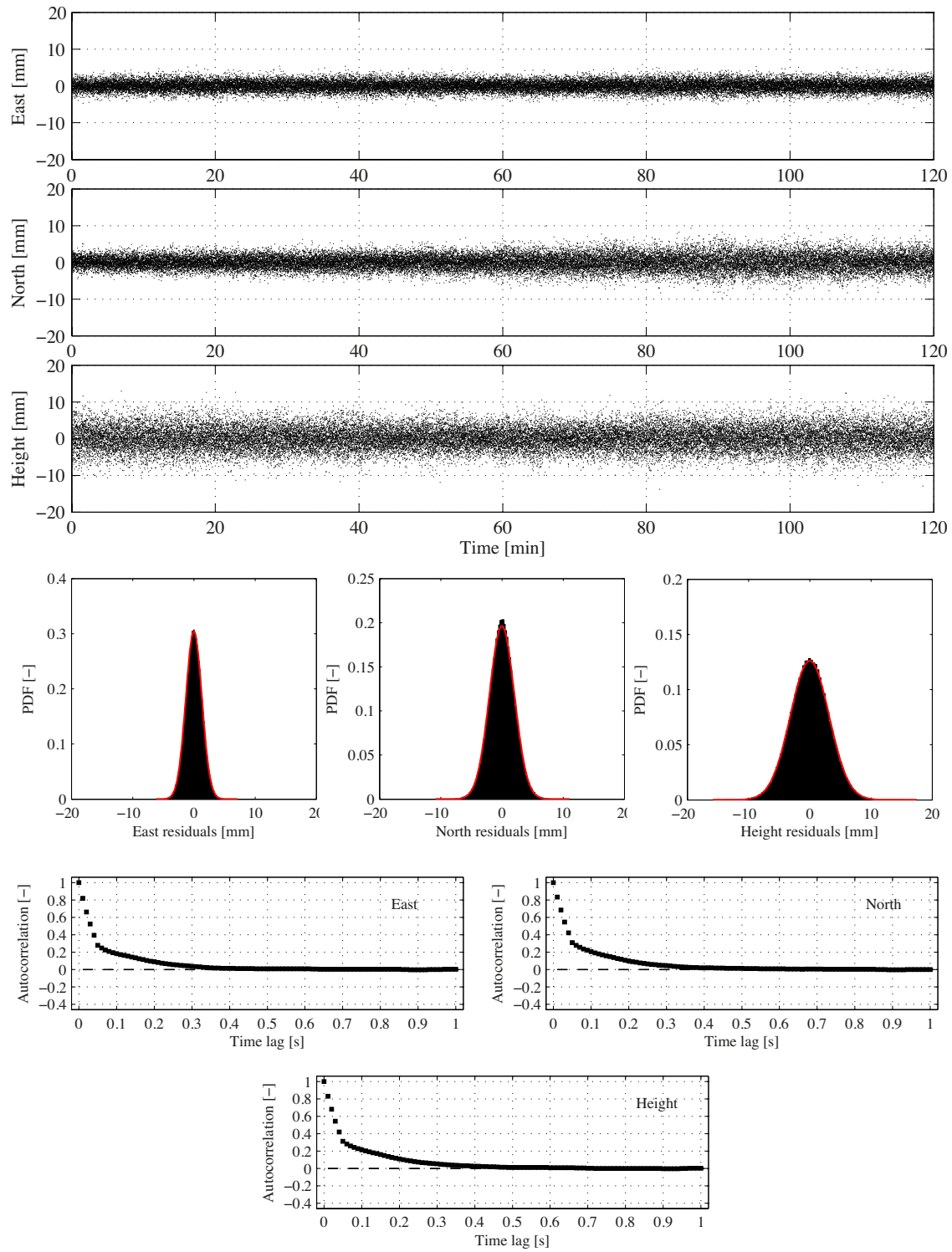
Figure 5.26: The L2 zero-baseline coordinates for the topocentric components with the corresponding histograms and autocorrelation functions. The standard deviations for each component are listed in Tab. 5.4. The red line in the histograms indicates the normal distribution dependent on the empirically estimated standard deviation from the kinematic coordinates at the top. The ACFs show the P2/L2 PLL B_L of 3 Hz guided by CA/L1 PLL B_L of 25 Hz.
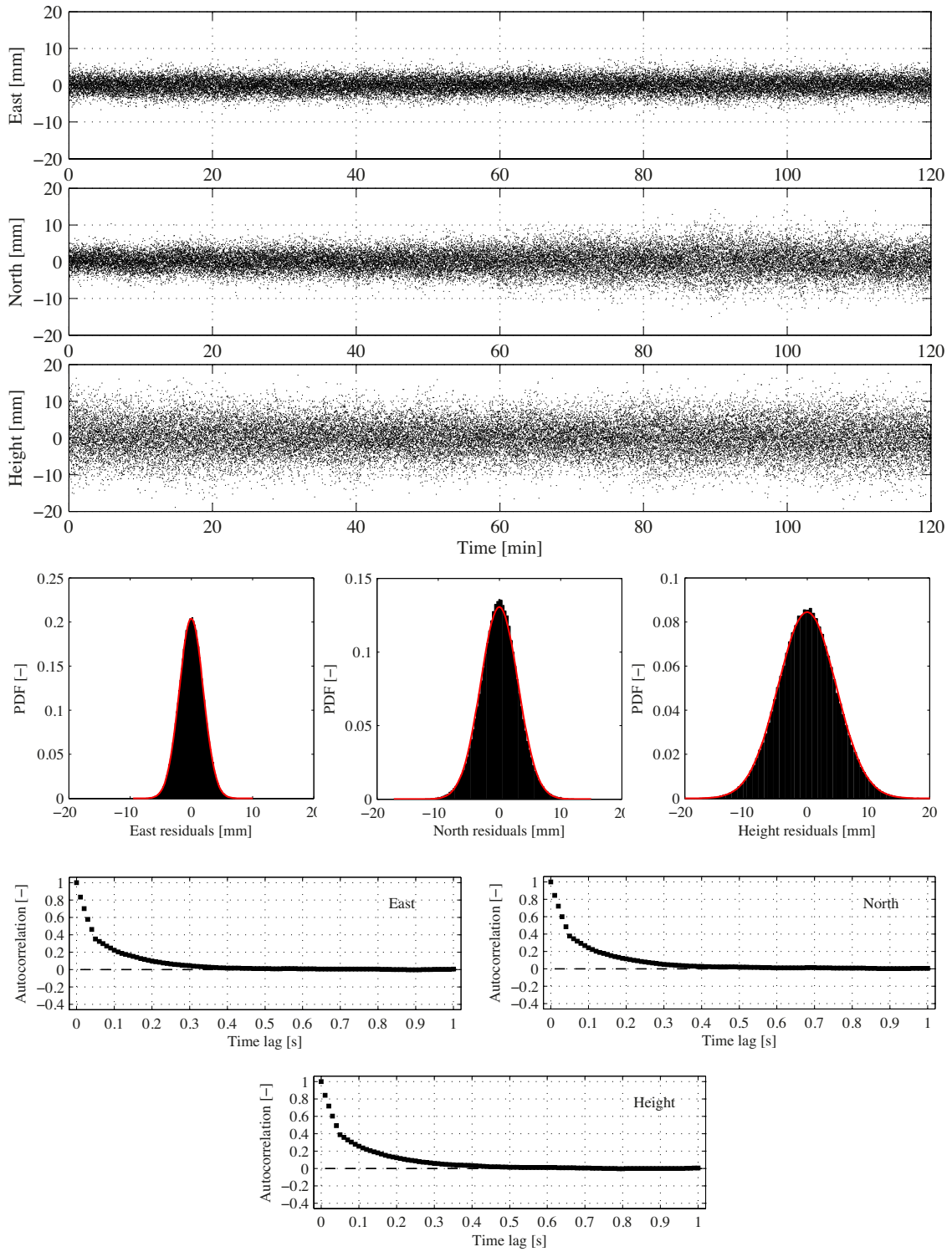
Figure 5.27: The zero-baseline coordinates of the ionosphere-free linear combination L_c for the topocentric components with the corresponding histograms and autocorrelation functions. The standard deviations for each component are listed in Tab. 5.4. The red line in the histograms indicates the normal distribution dependent on the empirically estimated standard deviation from the kinematic coordinates at the top. The ACFs show the P2/L2 PLL B_L of 3 Hz guided by CA/L1 PLL B_L of 25 Hz.
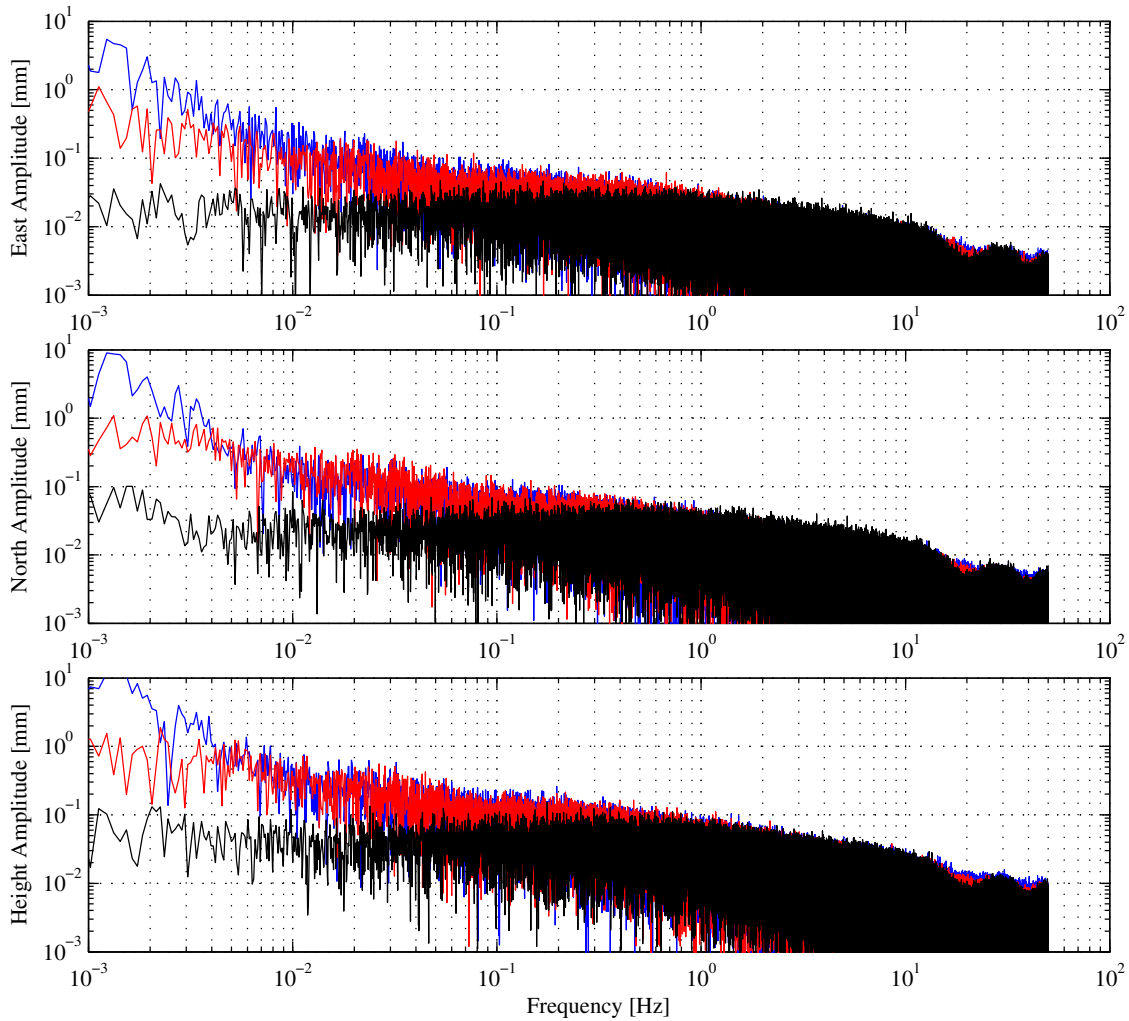
Figure 5.28: The frequency spectra of the three topocentric coordinate components for three different baseline lengths: zero-baseline (black), 10 m baseline (red), and 110 km baseline (blue).

noise. The effects of the loop bandwidths are visible between 10 and 50 Hz as a varying noise floor. After 1 Hz the carrier jitter is almost constant up to 1000 s. The thermal noise and the generated jitter are baseline independent and are system internal (antenna and receiver). All existing differences to the black spectrum have their seeds in external influences which are increasing below 1 Hz. Between 1 and 100 s the noise floor of the short and long baselines is almost equally risen while the long baseline noise (blue) especially affected by high-frequently atmospheric refraction is enlarged at frequencies below 0.01 Hz compared to the short baseline (red). Multipath is mainly site specific and independent of the baseline length and disturbs both, the short and the long baseline. However, an exact separation of the different perturbations below 1 Hz is difficult. The difference between the carrier jitter at 0.1 Hz and the total error budget for the two baselines is a mix of the high-frequently parts of the factors mentioned above, but still relatively small with a maximum factor of 2 for this receiver, antenna and satellite constellation. It can be concluded that in the spectrum at frequencies higher than 1 Hz the carrier phase jitter induced by thermal

noise is the dominant error source. This means that the baseline length has no impact on the motion detection beyond 1 Hz.

5.8 Summary and Concluding Remarks

The accuracy and reliability of a global navigation satellite system expected and required by different user groups pose high demands on the signaling techniques. In the previous sections the different modulation schemes and their impact on the signal characteristics are described and demonstrated. Especially the properties of the ranging code modulated onto the carrier determine not only the position accuracy by pseudorange measurements, but also the properties of the retrieved carrier phases as described in this section. The spread spectrum generated by the ranging code allows the receipt of the transmitted signal under interfered conditions at the first place which are caused by all available communication systems. The spreading additionally enables the transmission of a certain amount of power in agreement with ITU requirements. A higher code chipping-rate induces a better accuracy of pseudorange measurements and a wider spreading with higher robustness against interferences. Due to the BOC modulation with its split mainlobes and the sharp cross-correlation peaks, modern GNSS signals guarantee on the one hand a good spectral separation to the already existing signals and a lower sensitivity against interferences and multipath. Additionally the length of the PRN codes has a direct impact on the line spectra. Long periods generate a more highly resolved envelope containing better correlation properties, but demand longer acquisition time. In order to combine the advantages of a long and short code sequence, especially modern GNSS signals are multiplexed by codes with different lengths and additional overlaid codes for an improved correlation process. All these properties of the PRN codes are linked to those of the carrier phases because the DLL and PLL are not working independently due to the acquisition process with the synchronization between receiver and system time, and the demodulation of the codes and the data stream from the carrier.

A crucial factor for the quality of the carrier phase at receiver output is the carrier-to-noise density ratio C/N_0. This value defines (in combination with the oscillator jitter) the range of possible loop bandwidths B_L and consequently the amount of carrier phase jitter σ_{PLL} and the sensitivity against LOS dynamics. A high C/N_0 allows a wide B_L for a good dynamic tracking capability with the small handicap of a higher jitter level. The final baseband C/N_0 is the result of different factors, such as the specified received power which depends on the satellite hardware and the modulation schemes (ITU regulations and spectral separation), the receiver front-end, the robustness against interferences and multipath, the ranging code demodulation process (known or encrypted), data demodulation (existing pilot/data-less component). The disadvantage of an encrypted signal is well visible for the legacy GPS signals. The jitter for P1/L1 and P2/L2 is 2.5–3 times higher than that for CA/L1. The total amount of the thermal noise induced jitter is finally dependent on the receiver front-end and the baseband parameters, but in any case below 1 mm down to 0.25 mm at high signal strength with a narrow bandwidth (zero-difference σ_{PLL}). It is also important to note, that the guiding of the weak loops (e. g. P2/L2) by the strong loops (e. g. CA/L1) has not only an impact on the dynamic tracking capability as it will be demonstrated in the next sections, but also on building the ionosphere-free linear combination. The amount

of noise on L_c is about 20% lower due to the guiding correlations between CA/L1 and P2/L2 than if they are uncorrelated. The modern GPS signals C2/L2 and C5/L5 (and in future C1/L1) show a similar carrier noise as CA/L1 and an improved robustness against multipath. This makes them extremely interesting for building L_c with CA/L1, especially C5/L5 with its C/N_0 being almost 5 dB-Hz higher than CA/L1 and up to 20 dB-Hz higher than P2/L2. This is made possible by a high received power (no other interfering signals on the L5 carrier, above all no military signals) and the data-less component. The final jitter on L_c built by CA/L1 and C5/L5 will be about 25% lower than that of L_c between CA/L1 and P2/L2.

The interoperability between different GNSS is nowadays a crucial issue. The signaling scheme of the Russian global positioning system GLONASS bases on frequency domain multiple access instead of CDMA as GPS and Galileo. The extended receiver front-end required in order to handle a lot of different frequency sub-bands is a huge disadvantage if the receivers are not optimized for this purpose (additional inter-frequency biases). In combination with the satellite hardware not being at the level of GPS and Galileo, the C/N_0 of the GLONASS signals are far below other civil GNSS signals producing a corresponding 2 times higher carrier phase jitter.

It has been shown that the zero-baseline configuration based on double-differences is able to represent the carrier phase jitter σ_{PLL} neglecting the oscillator jitter for not too narrow loop bandwidths and high oscillator quality. This means that the carrier phase jitter σ_{PLL} induced by thermal noise defines the internal system noise $\sigma(\epsilon_r^s)$ according to Eq. (5.2) which is often called carrier phase noise in the geodetic community. This noise level defines the limit which cannot be underrun. The comparison between three different baseline lengths (0 m, 10 m and 110 km) of a test constellation demonstrates that, in the frequency spectrum above 1 Hz, only the carrier phase jitter dominates the noise on the kinematic coordinates. The detection of high-frequency signals is therefore baseline-independent.

6 Shake Table Experiments

The investigation and analysis of the high-rate GPS ground-motions and of the correspond-
ing receiver response are the main topics of this thesis and are described in Chap. 7 and 8.
For this assessment a programmable motion generator and a reliable ground-truth are key
factors and are introduced in this chapter.

6.1 Experiment Equipment

The experimental hardware is schematically illustrated in Fig. 6.1. It comprises a single-
axis shake table with all its components as a motion generator, and the equipment for
measuring and recording the generated ground motions. Two inductive displacement trans-
ducers define the ground-truth for the GPS measurements. In addition to the GPS antenna,
two strong motion seismometers were mounted on the shake table in order to validate the
ground-truth which builds a crucial part for the whole assessment.

6.1.1 Shake Table Hardware

The motion generator used in the followed experiments was a Quanser single-axis shake
table (*Quanser* 2008). The hardware consists of different components: the shake table, a
universal power module (UPM), a data acquisition card (DAC) with an external terminal
board (Q4), and a PC with the steering software, visible in Fig. 6.2. The top platform
of 45.7×45.7 cm is moved by a brushless 3-phase DC motor with 400 Watt and a ball-
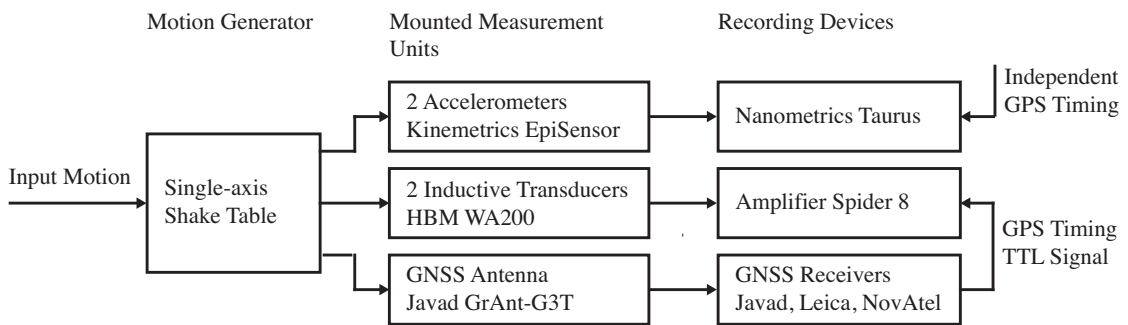
Figure 6.1: A schematic overview of the measurement equipment performing the shake table
experiments. The synchronization to GPS time of the Taurus was achieved by an independent
GPS antenna and an internal synchronization procedure. The inductive transducer amplifier and
acquisition device Spider8 received and saved the analog TTL signal from the GPS receiver involved
in the experiment. After a post-processing step the internal time could be synchronized to the GPS
reference time (see Sec. 6.2).
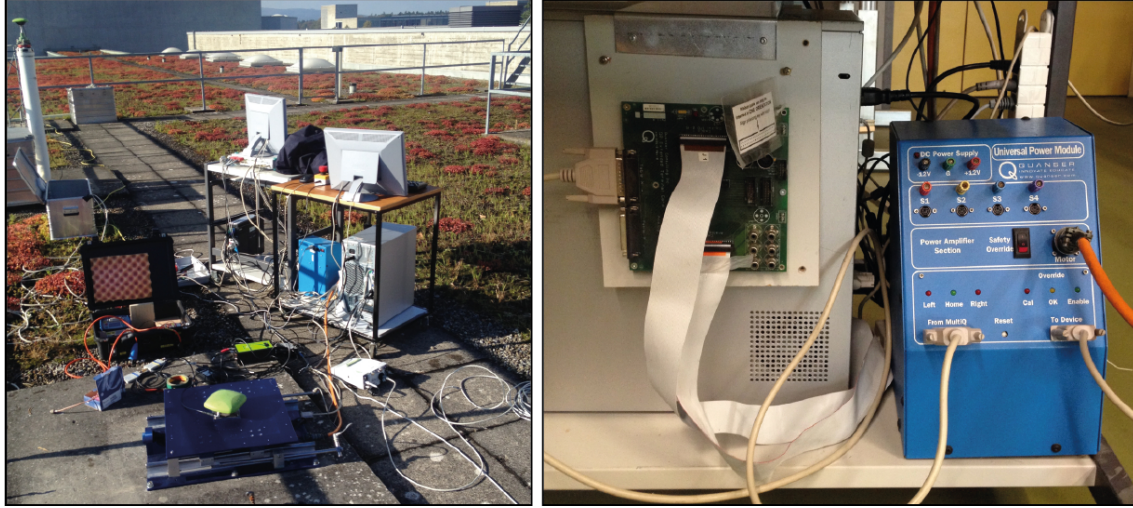
Figure 6.2: The whole equipment used during the experiments is shown on the left. The second PC was required for acquiring the measurements from the inductive transducers (see Sec. 6.1.2). In the background of the left image the white pillar with the GPS antenna is visible which mostly built the baseline to the mounted GPS antenna on the shake table (in the front) for the GPS processing and the retrieval of the receiver response (see. Sec. 6.4). On the right image the UPM (blue) and the PC with the extended terminal board (Q4) composed the main components to control the shake table.

screw. For a maximum payload of 7.5 kg an acceleration up to 2.5 g can be achieved. The maximum travel distance is 15.24 cm with a maximum linear velocity of 0.66 m/s. The position of the platform is given by the encoder embedded inside the motor with a resolution of 3 µm.

The steering of the shake table devices is based on the Quanser real-time control software (QuaRC). In order to perform experiments with the desired motions, different real-time controllers could be run by Simulink diagrams in Matlab while QuaRC is generating the corresponding executables. This enables the design of a specific experiment with all possible ground-motions within the limits described above. The used input ground-motions for the assessment in Chapters 7 and 8 are listed in Tab. 6.1.

6.1.2 Inductive Displacement Transducers

Due to mechanical uncertainties of the shake table, especially during high accelerations, an independent measurement system is necessary to establish an accurate and reliable ground-truth. For this purpose two HBM WA200 inductive displacement transducers (*HBM*, 2012a) were mounted on both sides of the shake table measuring the motion of the top platform relative to the bottom plate. The measurement output of the inductive sensors was collected by the electronic measuring system HBM Spider8 (*HBM*, 2012b) and was digitized with a rate of 2.4 kHz. The maximum sampling rate is 9.6 kHz, however the internal storage of the Spider8 is too small for collecting measurements over long time periods up to some hours and the real-time transfer to the PC was only stable with a rate of 2.4 kHz. The HBM software catman 4.5 was used for the configuration of the sensors and

the measurement process. The metric resolution of the digitized displacements is 6 µm. In nominal temperature range (-20 to +80 °C) effects of temperature on the output signal of the inductive transducers can be neglected. In principle, high temperature gradients can induce a dilatation of the shake table which affects the determination of the ground-truth. These effects were additionally investigated in a climatic chamber, see Sec. 6.3.1.

6.1.3 GNSS Receivers and Antenna

The GPS hardware for the shake table experiments is almost the same as that used for the investigation of the noise and tracking capabilities with a static antenna in Sec. 5. In addition to the Javad Sigma-G3TAJ and Leica 1200 receivers, a NovAtel DL-4plus with a maximum sampling rate of 20 sps was mounted on the shake table. The moving antenna was always a Javad GrAnt-G3T, capable of receiving three frequency bands, see the more detailed description in Sec. 5.1. During the shake table tests all available satellite systems were tracked and recorded even though GPS was the only system that is considered in the following chapters.

6.1.4 Broadband Seismometer

The equipment used was a Kinemetrics EpiSensor (*Kinemetrics*, 2005) recording on a Nanometrics Taurus (*Nanometrics*, 2012), a system with peak ground motion of 2 g, with a flat frequency response in acceleration from 200 Hz - DC, and a dynamic range of over 140 dB. A clock synchronized by GPS provided independent timing. This accelerometer type has a well-known transfer function that has zero-phase shift and a constant amplitude between 200 Hz and DC. The mounting on the shake table and the equipment used is shown in Fig. 6.3. Equally to the inductive sensors, measurements of two accelerometers should increase the confidence in the accuracy of the recorded response. The ground-motions retrieved from the seismometers were compared to those of the inductive displacement transducers to validate them as a ground-truth for the GPS measurements, see Sec. 6.3.2.

6.2 Sensor Synchronization

For the assessment of high-frequency ground motions while by comparing not only the amplitude but also the phase shift between the different sensors described above, all the sensors have to be synchronized to the same reference time. The GNSS receiver is able to generate a high-precision PPS (Pulse-Per-Second) signal by the internal oscillator based on the low-voltage TTL standard (Transistor-Transistor Logic). Dependent on the configuration, each rising (or falling) edge of the TTL signal is marked as an event and corresponds to a measured epoch of the GPS receiver. The Spider8 is theoretically able to receive a trigger signal, but only as an initial time stamp. The Spider8 oscillator bases on the common Quartz technology and produces unacceptable time drifts over the experiment duration of more than one hour. For this reason it was mandatory to generate a highly sampled 100 Hz PPS signal that was acquired by the Spider8 as an analog signal. The received voltage status allocates to its corresponding displacement measurement with a
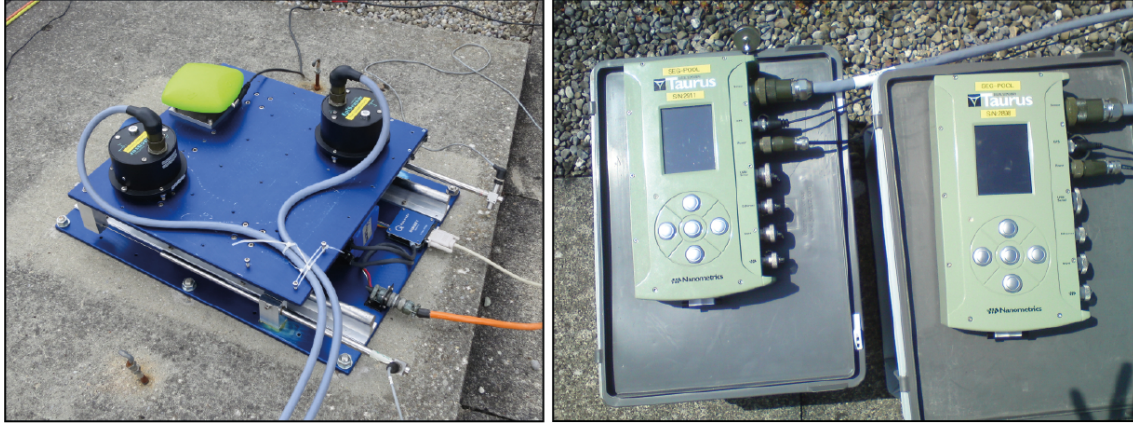
Figure 6.3: In addition to the green GPS antenna, the two EpiSensors were mounted on the shake table (left) for the ground-truth validation (see Sec. 6.3.2). On the right image the two Taurus recorded the acceleration measurements. Both were connected to an additional GPS antenna for the internal time synchronization.
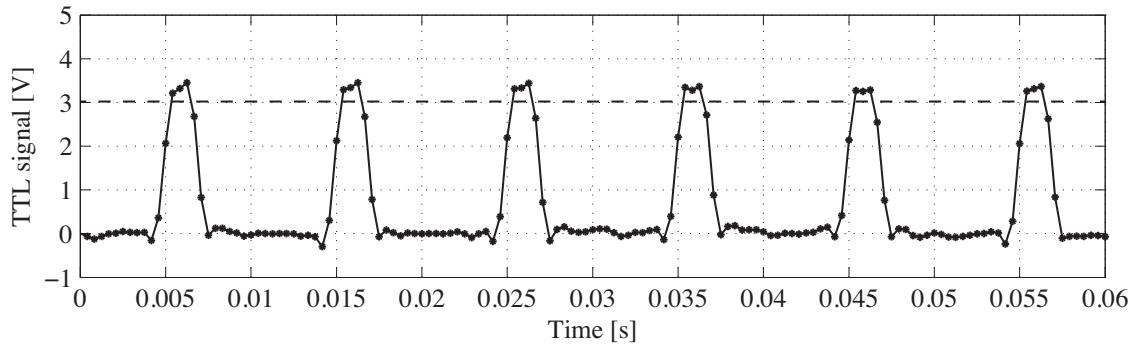
Figure 6.4: The TTL signal generated by the GPS receiver was recorded by the Spider8 as an analog signal in Volts with a sampling of 2.4 kHz. It is a standardized signal that is raising from 0 to 3.3 V if the configuration is set for rising edge detection. The horizontal dashed line defines a typical volt level threshold for the event marker.

sampling rate of 2.4 kHz. The example of a recorded low-voltage TTL signal, which is specified for 3.3 Volt power supplies is shown in Fig. 6.4. A typical voltage threshold for the event marker in the GPS receiver is between 2.8 and 3.0 V which sets the GPS time to the corresponding rising edge. After a postprocessing step allocating the first epoch above the voltage threshold (visible as a horizontal dashed line in Fig. 6.4) to the GPS receiver event, the inductive transducers were synchronized to the GPS receiver time with a time resolution of 0.4 ms. This small synchronization uncertainty produces a maximum phase shift of 1.4 degrees during the highest velocities generated by the shake table. For the comparison with the GPS measurements the mean of both inductive transducer measurements is formed and presented with a sampling rate of 100 sps in the following. The synchronization of the broadband seismometers was achieved independently by an internal synchronization process in the Taurus which was directly connected to an additional GPS antenna. The strategy used is described in *Nanometrics* (2012).

6.3 Ground-truth Validation

As discussed above the inductive transducers are able to determine the ground-truth with a sufficient accuracy for the assessment of the GPS measurements. However, the shake table deformation due to strong temperature gradients, as mentioned in Sec. 6.1.2, was tested in a climatic chamber. Additionally, the ground-truth had to be validated under real conditions at the location of our experiments. For this purpose two broadband strong motion seismometers described in Sec. 6.1.4 and visible in Fig. 6.3 were additionally mounted on the shake table as independent measurement systems to validate the inductive transducers during highly accelerated motions. Furthermore the time synchronization processes can also be verified due to the independent timing of the inductive transducers and seismometers.

6.3.1 Long-periodic drifts of the inductive transducers

The temperature tests were performed in the climatic chamber of the Institute of Geodesy and Photogrammetry at ETH Zurich. Different tests in the temperature range between 5 and 30 °C showed no significant drifts in the inductive transducer measurements when they were not fixed to the shake table. This corresponds to the technical specifications promising a good thermal stability. If the inductive sensors were mounted at the shake table, some small and long-periodic drifts could be detected due to the dilatation of the shake table. The largest drift ever measured is shown in Fig. 6.5 with 15 μm/min and a temperature gradient of 0.3 °C/min. However, for other tests in the chamber and outdoors at the location of our experiments, only extremely small and long-periodic drifts of 2 μm/min could be detected. Due to the usage of the ground-truth for assessing high-frequency motions, these effects are negligible.
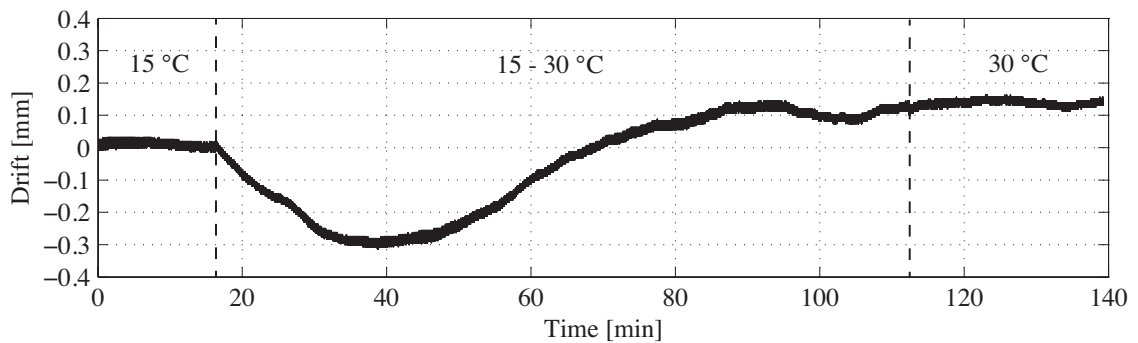
Figure 6.5: This figure demonstrates a climatic chamber test while the inductive transducers were being fixed at the shake table. The temperature was raised from 15 to 30 °C. This was the largest displacement drift with 15 μm/min that was ever detected during inductive transducer measurements, mainly caused by the deformation of the shake table. During other climatic chamber tests with stable temperature, gradients at lower temperatures, and during the experiments under real conditions maximal drifts of only 2 μm/min were observed.
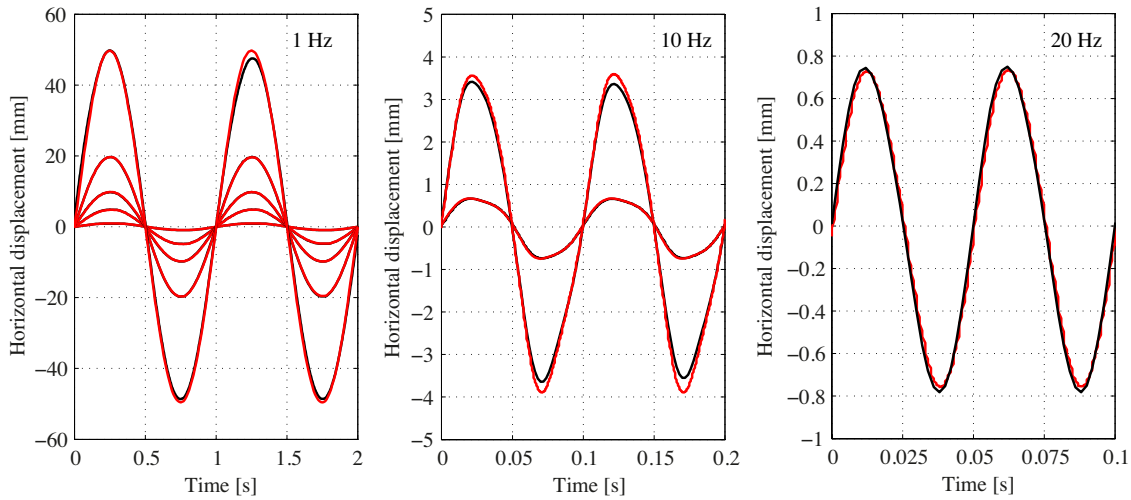
Figure 6.6: Comparison between seismometer (red) and inductive transducer (black) measurements for a set of different sine oscillations. There is no significant differences between the two signals. This demonstrates that the displacement transducer is accurately recording the ground motion of the shake table, and the accelerometer response for the frequencies tested has no frequency, phase or amplitude error.

6.3.2 Comparison with Seismometer

The main validation of the whole equipment at the final experiment site was performed in the configuration visible in Fig. 6.3 and bases on the comparison between the inductive transducers and the broadband seismometers because they are completely independent measurement systems. Fig. 6.6 shows the agreement between the averaged inductive sensors and the averaged seismometer signal across all frequencies/amplitudes tested. The raw recorded seismic accelerations were processed by removing the sensor gain and applying a third-order bandpass butterworth filter, followed by a double integration to obtain displacements. The bandpass filtering is required in order to remove long-period tilting and high-frequency spikes both induced by the shake table. In Fig. 6.6 we see that there is no shift in amplitude, frequency or phase between the seismic displacement waveforms and the inductive transducer measurements in a broadband frequency range, even at highest frequency of 20 Hz. The seismic sensor even tracks the non-linear performance of the shake table at high frequencies, where it cannot exactly produce the input sine wave. This level of performance is what can be expected from high-quality seismic instrumentation.

Additionally, it is demonstrated that the time synchronization works with a sufficient accuracy, because even for the 20 Hz sine oscillations no significant phase shift could be detected.

6.4 Experiment Setup

The shake table was fixed on a concrete base on the roof of the building HPV at ETH Hönggerberg. The motion axis of the single-axis shake table was oriented toward NE-SW. Due to the limited wire lengths of the measurement equipment, especially the power cable

connecting the shake table to the amplifier on the UPM, the whole equipment had to be installed quite close to the mounted GPS antenna. In order to minimize the blocking of available satellites the equipment was placed in the North, see also Fig. 6.2 (left) for the equipment disposition and 6.3 (left) for the shake table fixing on the concrete base.

6.4.1 Motion Generation and GPS Measurements

A large set of different motions was generated during the experiment for the assessment and determination of the GNSS receiver response. In order to cover a wide range of ground motion accelerations and jerks, sine waves with amplitudes from 1 to 50 mm and frequencies between 1 and 20 Hz were produced and build the main data set for the further analysis. The sine oscillations summarized in Tab. 6.1 were measured with the GNSS receivers described in Sec. 6.1.3. For the Javad receiver different carrier loop bandwidths B_L of 10 Hz, 25 Hz, and 50 Hz were tested.

Table 6.1: This table shows the frequencies and amplitudes with peak accelerations (brackets) of the sine oscillations generated by the shake table. The acceleration does not exactly correspond to the theoretical value because the input amplitude is not fully consistent with that finally generated by the shake table.

1 Hz	3 Hz	5 Hz	7 Hz	10 Hz	20 Hz
1 mm (0.004 g)	1 mm (0.03 g)	1 mm (0.08 g)	1 mm (0.14 g)	1 mm (0.25 g)	1 mm (1.06 g)
5 mm (0.02 g)	5 mm (0.17 g)	5 mm (0.43 g)	5 mm (0.76 g)	5 mm (1.28 g)	
10 mm (0.04 g)	10 mm (0.34 g)	10 mm (0.87 g)			
20 mm (0.08 g)					
50 mm (0.20 g)					

Further, step functions with different displacements and peak accelerations of about 2 g were generated and measured with different tracking loop parameters such as 2nd and 3rd order loops with 10 Hz and 50 Hz B_L each. These measurements were used for the representation of the tracking loop behavior and validation of the PLL modeling described in Sec. 7.1.1 and 7.1.

Table 6.2: The step function displacements with peak accelerations of about 2 g were measured with the followed PLL parameters and build the basis for the assessment of the PLL model and simulation. Only displacements of 1 cm are considered here.

Displacement [cm]	2nd order PLL B_L [Hz]	3rd order PLL B_L [Hz]
1	10	10
1	50	50

In particular, the constraint in the range of displacements limits the simulation of large earthquake ground motions. Only small M5.0 earthquake ground-motions were generated by the shake table and measured by GPS (see Sec. 8.1). Additionally, a lot of measurements had to be repeated due to firmware problems of the Javad receivers, shortly mentioned in

Sec. 5.6. The strange effects caused by the influence of the DLL on the carrier tracking led to multiple receiver parameters and combinations of different DLL and PLL bandwidths that were tested until the manufacturer fixed the problem. Finally, almost 100 hours of GPS ground-motions generated by the shake table were collected. Tables. 6.1 and 6.2 only show the measurements used for the results presented and discussed in the following chapters.

Each specific motion has been acquired over at least 10 minutes (several hundred cycles) in order to reduce noise and multipath effects for the signal representation, and to improve the amplitude and phase determination.

The major goal was the investigation and quantification of the PLL-induced errors caused by highly dynamic motions. For this purpose the majority of experiments was performed with a very short baseline of about 5 m in order to eliminate or strongly reduce most of the existing external perturbations. The static antenna was mounted on a pillar with well known coordinates visible in the background of Fig. 6.2 (left). During this project a permanent 100 sps GPS site co-located to a seismometer was installed at Fiescheralp in the Canton Valais. The station is shortly described in Sec. 8.1.2 and was used for some long baseline analysis (baseline length of 112 km).

6.4.2 GPS Processing

In order to calculate kinematic coordinates from the shake table measurements, it was the goal to perform the post-processing of the GPS raw data with the high-performance Bernese 5.1 GNSS software package (*Dach et al.*, 2007). However, all the measurements were collected with a sampling-rate of at least 20 sps.But the official version of the Bernese software is only capable of handling data sets with a sampling rate up to 1 sps. Therefore, the whole software package with all its routines and observation files had to be modified to allow the processing of kinematic GPS ground-motions up to 100 sps. Finally, the modified software version was tested by comparing the 100 sps data and the same data set downsampled to 1 sps and processed with the official version of Bernese. Thus we could verify verified that the processed 100 sps coordinates are still identical to those processed with the official version for at least every second.

Based on the state-of-the-art double-difference processing strategy (more details in *Hofmann-Wellenhof et al.* (2008)) with products provided by the IGS, the ambiguity-fixed kinematic coordinates were calculated for L1 only, L2 only, and L_c observations for the short baseline of 5 m. For the longer baseline between HPV and Fiescheralp of more than 100 km with a large impact of the ionosphere, only the usage of the L_c linear combination (see Sec. 4.3.3) enabled the estimation of amiguity-fixed coordinates. The percentage of resolved integer ambiguities was enhanced by a previous calculation of the wide-lane ambiguities with an apriori ionosphere model provided by the IGS.

Afterwards, the kinematic GPS coordinates were projected onto the movement direction NE-SW of the shake table in order to allow a direct comparison with the ground-truth defined by the inductive displacement transducers.

7 GNSS Receiver Response

In contrast to Sec. 5, which focuses on the induced jitter dependent on the signal structure and loop parameters, the potential error caused by user dynamics as proposed in Sec. 4.2.1 and 4.2.2 is the main topic of the following sections. With a precise motion generator, a single-axis shake table, and a well verified ground-truth as introduced and described in Sec. 6, the GNSS receiver response for a frequency range from 1 Hz up to 20 Hz was empirically estimated. The experiments were mainly carried out by the 100 sps Javad Sigma-G3TAJ receiver, but complemented by the Leica GX1200 and NovAtel DL-4plus, both with maximal 20 sps. It was not the primary goal to accomplish a calibration of as many receivers as possible, but to demonstrate the importance of a careful attention to the GNSS receiver response while catching signals above 1 Hz. In order to clearly verify the origin of the induced displacement errors, the empirically estimated amplitude and phase errors should be compared with the theoretically expected dynamic stress errors from Sec. 4.2.1 and 4.2.2. The tools introduced in Sec. 4.1 for the modeling of linear PLLs are adapted to a discrete transform domain with a subsequent implementation in the discrete time domain.

7.1 Simulation of the GNSS Receiver Response

7.1.1 Linear Digital PLL Model

Nowadays electronic devices are often digitally implemented such as modern GNSS receivers as described in Sec. 3. In contrast to the integrators in analog PLLs, digital integrators are invariably ideal without offsets and fabrication uncertainties. Additionally, digital PLLs (DPLL) can be theoretically designed with a tremendous complexity compared to analog implementations. However, the compatibility with other digital operations in a device like a GNSS receiver is the primary reason for using DPLLs. The problematic of non-linearity is also given for DPLLs, especially at small phase errors due to quantization effects of the limited digital number precision (*Gardner*, 2005). However, the same assumptions as for the analog PLL also apply for the DPLL with the addition of a sufficient precision and negligible quantization effects.

In analogy to the transfer functions derived and analyzed in the Laplace transform domain for the differential equations of analog PLLs, the z-transforms are used as the transform domain for converting shift-invariant difference equations of discrete signals (samples). Especially the analog loop filters are often directly taken over to the digital domain. Even though different transform approaches are possible, only two are commonly used: the impulse-invariant z-transform and the bilinear z-transform. The impuls-invariant z-

transformation $\mathcal{Z}_\mathrm{i}\{\cdot\}$ for an integrator $1/s$ is given by

$$\mathcal{Z}_\mathrm{i}\left\{\frac{1}{s}\right\} = T\frac{1}{1 - z^{-1}} \tag{7.1}$$

and for the bilinear z-transform $\mathcal{Z}_\mathrm{b}\{\cdot\}$ by

$$\mathcal{Z}_\mathrm{b}\left\{\frac{1}{s}\right\} = \frac{T}{2}\frac{1 + z^{-1}}{1 - z^{-1}}. \tag{7.2}$$

with the integration time T. The integrator in Eq. (7.1) corresponds to a difference equation of a discrete integral output $y_\mathrm{I}[n]$ of the n-th sample and its n-th sample input $x_\mathrm{I}[n]$ as follows

$$y_\mathrm{I}[n] = T\,x_\mathrm{I}[n] + y_\mathrm{I}[n - 1] \tag{7.3}$$

where z^{-1} corresponds to a shift of one sampling interval in the time domain. This describes a backward rectangular method of integration while Eq. (7.2) corresponds to the transfer function of a trapezoidal integrator. Based on the information provided by Javad about the filter implementation in the firmware, the backward rectangular integration has been chosen for the modeling, which is valid if the integration interval (see predetection integration) is small compared to the signal frequency. This is more problematic for the usage as an inverse filter applied to the output observations, especially for low sampling rates of 20 sps (see Sec. 7.3).

For the design of a linear digital PLL model the basic components of the analog PLL in Fig. 3.8 are slightly adjusted to the model in the z-domain as shown in Fig. 7.1. The VCO is exchanged by an NCO (described in Sec. 3.2.5) as an ideal integrator with a sampling interval T. The goal is to have a model in order to describe the behavior of the loop and not to implement a DPLL. Therefore the sampling interval T is equal to the loop update, even though the NCO is clocked with a much higher sampling rate (see Sec. 3.2.2 and 3.2.5). A special characteristic of a digital PLL is the usage of a delay of D samples. The loop has to have a delay of at least one sample $D = 1$, otherwise the DPLL is not computable, because building the difference between the input and output (discriminator which is needed for computing the output) has to be performed before producing the output. There are also models, especially in real PLL software implementations with high samplings (similar to the clock frequency), where larger delays are applied for each integrator (even for the proportional filter factor) due to pipelining delays (*Gardner*, 2005). The NCO transfer function $N(z)$ in the z-domain is finally

$$N(z) = T\frac{z^{-1}}{1 - z^{-1}} \tag{7.4}$$

The filter design in Fig. 7.1 corresponds to the formulation in Eq. (3.95) with the three filter parameters K_1, K_2 and K_3 in case of a 2nd order filter. For a 1st order filter the coefficient K_3 is zero. The setting and type of filter parameters are directly dependent on the filter representation. For a certain filter design different parameter types are possible, see also Sec. 3.2.4 and compare the filter transfer function from Eqs. (3.91) and (3.93). According to Fig. 7.1 with its parameter set and the rectangular integrator, the 2nd order filter transfer function $F(z)$ can be written as follows

$$F(z) = K_1 + T\frac{K_2}{1 - z^{-1}} + T^2\frac{K_3}{(1 - z^{-1})^2} = \frac{k_1 + k_2 z^{-1} + k_3 z^{-2}}{1 - 2z^{-1} + z^{-2}} \tag{7.5}$$
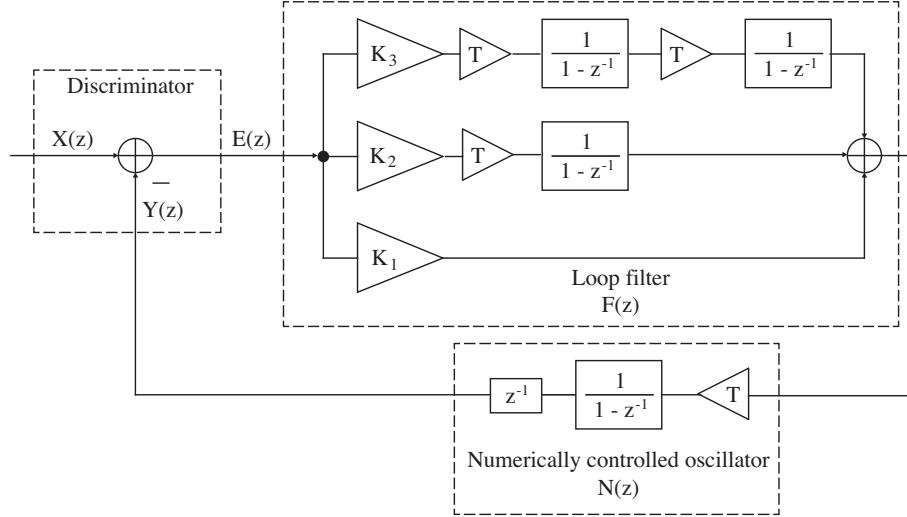
Figure 7.1: A simplified linear PLL model in the z-domain including the three main components of a tracking loop: a linear discriminator, a loop filter with its coefficients and an NCO with a reference delay of one sample.

with

$$
\begin{aligned}
k_1 &= K_1 + TK_2 + T^2K_3 \\
k_2 &= -2K_1 - TK_2 \\
k_3 &= K_1.
\end{aligned}
\tag{7.6}
$$

Due to the assumption of a linear discriminator output $E(z)$ around zero-phase and no discriminator gain, the transfer function $H(z)$ of a closed loop

$$
E(z) = X(z) - Y(z)
\tag{7.7}
$$

with its input $X(z)$ and output signal $Y(z)$ is given according to Eq. (4.8) by

$$
H(z) = \frac{Y(z)}{X(z)} = \frac{F(z)N(z)}{1 + F(z)N(z)} = \frac{b_1 z^{-1} + b_2 z^{-2} + b_3 z^{-3}}{1 + a_1 z^{-1} + a_2 z^{-2} + a_3 z^{-3}}
\tag{7.8}
$$

with

$$
b_1 = k_1 T, \ b_2 = k_2 T, \ b_3 = k_3 T, \ a_1 = b_1 - 3, \ a_2 = b_2 + 3, \ \text{and } a_3 = b_3 - 1.
$$

For the modeling of the expected dynamic GPS behavior the given ground-truth (inductive transducers) as the input $X(z)$ can directly be multiplied with the theoretical transfer function $H(z)$ with its specific parameters:

$$
Y(z) = X(z)H(z)
\tag{7.9}
$$

The back transformation into the time domain demonstrates the recursion for the output signal $y[n]$ of a 3rd order digital loop

$$
y[n] = b_1 x[n-1] + b_2 x[n-2] + b_3 x[n-3] - a_1 y[n-1] - a_2 y[n-2] - a_3 y[n-3]
\tag{7.10}
$$

for sampling instants $t = nT$.

7.1.2 Validation of the DPLL Model

For the validation of the DPLL model shown in Fig. 7.1 for a 2nd order and 3rd order loop, a step function of 1 cm has been generated with the shake table with a mounted GNSS antenna. The step has to be performed with highest possible acceleration and velocity in order to approach the properties of an ideal step covering the whole frequency spectrum and to demonstrate the transient response to a step. The acceleration at the beginning and at the end of the step function is about 2.5 g. The limiting factor of the motion generation, however, was the maximal velocity of about 0.6 m/s. Four receiver configurations were tested as already listed in Tab. 6.2. The two chosen CA/L1 PLL B_{L} of 10 Hz and 50 Hz build again the lower and upper bandwidth limit used in Sec. 5 and in the following shake table measurements. Both strong loop bandwidths were used in combination with a 2nd order and 3rd order loop, which is a selectable setting for the Javad receivers. The 2nd order loop parameters ($K_3 = 0$) can directly be taken over from the analog filter implementation of Eq. (3.93) and the parameterization of Eq. (4.15). The filter parameters K_1 and K_2 are

$$K_1 = 2\zeta\omega_{\mathrm{n}} \quad \text{and} \quad K_2 = \omega_{\mathrm{n}}^2 \tag{7.11}$$

with a damping factor ζ of 0.707. The relationship between the natural frequency ω_n [rad/s] and the 2nd order loop bandwidth B_{L} [Hz] is given by Eq. (4.30). With Eq. (7.5) for the filter transfer function, the parameters a_1, a_2, b_1, and b_2 can be calculated according to Eq. (7.8) for the closed-loop transfer function of the 2nd order DPLL and the following time domain implementation in Eq. (7.10). For a 3rd order PLL different parameter settings are possible, e. g. the filter parameters promoted by *Karras* (1965) and *Ward et al.* (2006) in Sec. 4.1.3. Typically, the filter parameters of the manufacturers are not public. Javad provides the setting on demand and uses a combination of 2nd order filter parameters (K_1 and K_2 are identical to Eq. (7.11)) and an additional empirically estimated third parameter. This design potentially simplifies the order change of a firmware implemented loop filter, e. g. during acquisition. A hybrid version of a 2nd order and 3rd order loop presented by *Tausworthe* (1971) and *Ugazio et al.* (2011) demonstrates an approach for a real-time adaptivity of the loop bandwidth (see also Fig. 5.6).

The simulated strong loop GPS signal with its response based on the derived 2nd and 3rd order discrete transfer functions $H(z)$ are calculated according to Eq. (7.9). The input signal $X(z)$ is defined by the ground-truth represented by the inductive transducers which contain a negligible amount of noise that simplifies the modeling. In the following figures, the ground-truth $X(z)$ is represented by a black line and the simulated GPS observations by black diamonds. The goal was the comparison of the simulations with the real 100 sps CA/L1 GPS measurements $\tilde{Y}(z)$. The CA/L1 GPS were processed as double-differences based on a short baseline of about 5 m, the reference pillar is visible in Fig 6.2 (left). For a better visualization of the transient response, the kinematic GPS coordinates were stacked several hundred times. In order to make this possible, the generation of the step function was repeated over a long time period. The stacking should reduce the high-frequency noise on the one hand and the dominant multipath on the other hand. The comparison of the stacked kinematic GPS coordinates measured with a narrow bandwidth B_{L} of 10 Hz (blue) with the simulated signal (black diamonds) is presented in Fig. 7.2 for the 2nd (top) and 3rd order PLL (bottom). Both PLLs generate the typical overshoot and phase shift, and
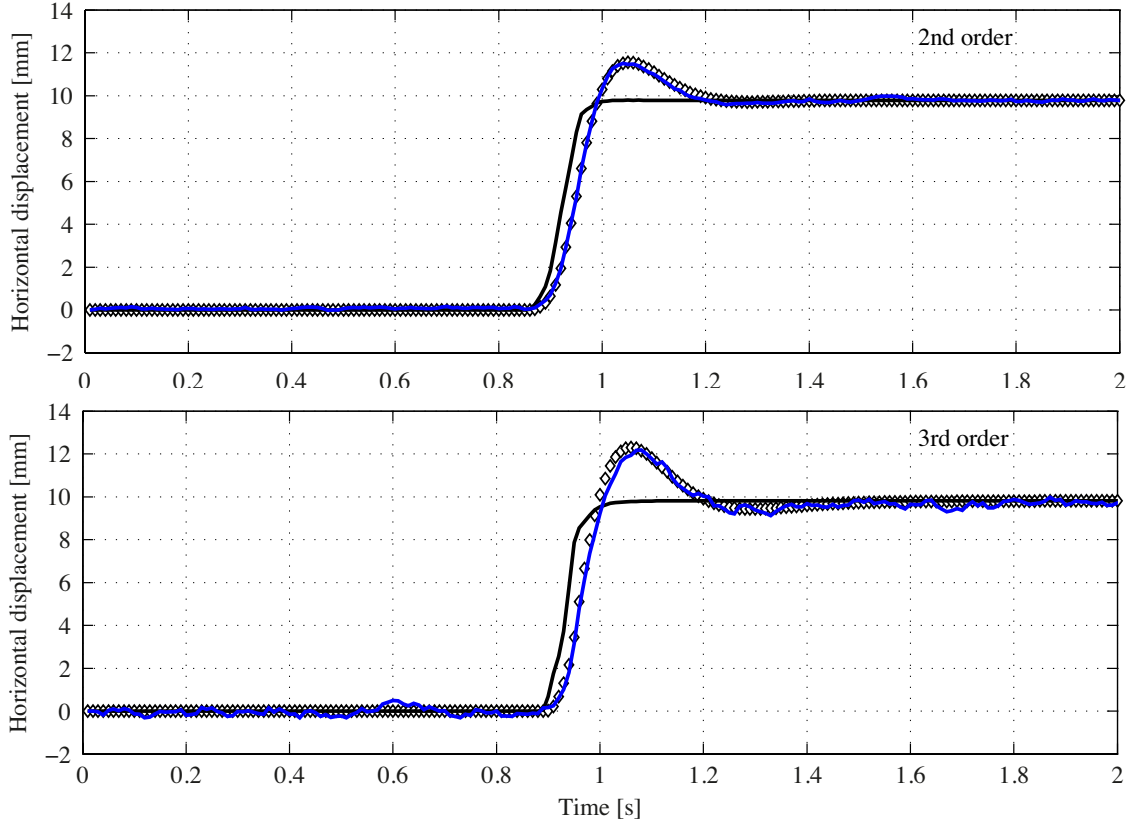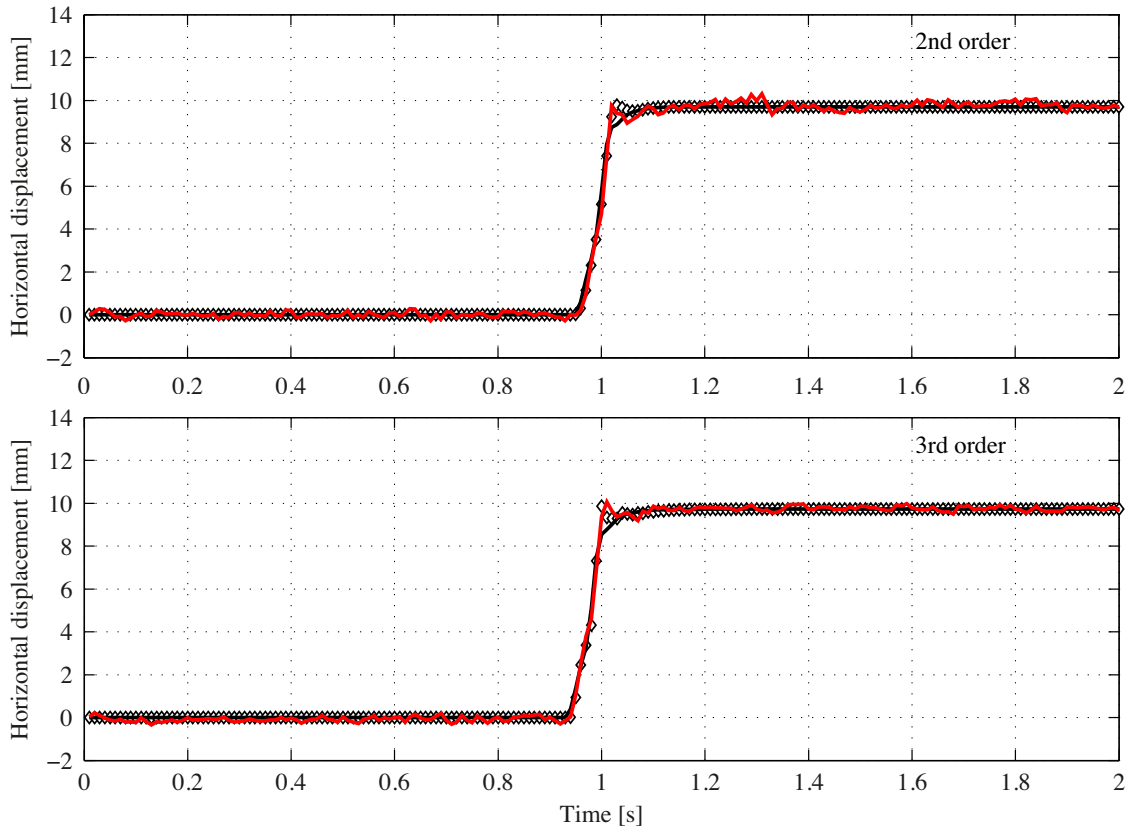
Figure 7.2: A 1 cm step in the displacements derived from 100 sps GPS data (blue) measured by a Javad Sigma-G3TAJ based on a 2nd order CA/L1 PLL (top) and a 3rd order CA/L1 PLL (bottom), both with a B_L of 10 Hz. Compared to the inductive transducers (black) the influence of the receiver transfer function can be seen by a delay and an overshooting. The simulated GPS (black diamonds) computed with Eq. (7.9) and the 100 sps CA/L1 GPS measurements (blue), both with the same PLL parameters, match well $Y(z) \approx \tilde{Y}(z)$, see also Fig. 7.4.

settling characteristics. The 3rd order loop based on the Javad parameters shows an almost identical behavior due to the close analogy to the 2nd order parameters, the overshoot is slightly larger with a more significant settling characteristic after 1.2 s. In both cases the modeled response $Y(z)$ (black diamonds) match very well with the measured 100 sps GPS signal $\tilde{Y}(z)$ (blue). The plots of the difference $\tilde{Y}(z) - Y(z)$ are visible in Fig. 7.4. The higher remaining noise for the step measured with a 3rd order PLL is caused by a significantly shorter measurement time period and accordingly less stacking intervals. The transient response of the wide B_L of 50 Hz in Fig. 7.3 for 2nd order (top) and 3rd order loops (bottom) is extremely small compared to the narrow bandwidth and at the resolution limit due to a sampling of 100 sps. The corresponding differences are presented in Fig. 7.5. However, also in this configuration the main displacement is well captured by the high-rate GPS observations, even during high dynamics between 0.9–1 s. A closer look over the whole frequency spectrum with different dynamics will follow in the next section.

The simple model of a DPLL corresponds well to the real measurements in general. The integrators of the model using a relatively long integration interval of 0.01 s are not a critical part for the step function representation. Based on the simulated step response for

Figure 7.3: A 1 cm step in the displacements derived from 100 sps GPS data (red) measured by a Javad Sigma-G3TAJ based on a 2nd order CA/L1 PLL (top) and a 3rd order CA/L1 PLL (bottom), both with a B_L of 50 Hz. Compared to the inductive transducers (black) the influence of the receiver transfer function is extremely small due to the wide bandwidth. The simulated GPS (black diamonds) computed with Eq. (7.9) and the 100 sps CA/L1 GPS measurements (red), both with the same PLL parameters, match well $Y(z) \approx \tilde{Y}(z)$, see also Fig. 7.5.

a 3rd order PLL with 10 Hz B_L the differences between the usage of backward rectangular integrators according to Eq. (7.1) and trapezoidal integrators from Eq. (7.2) are visible in Fig. 7.6.
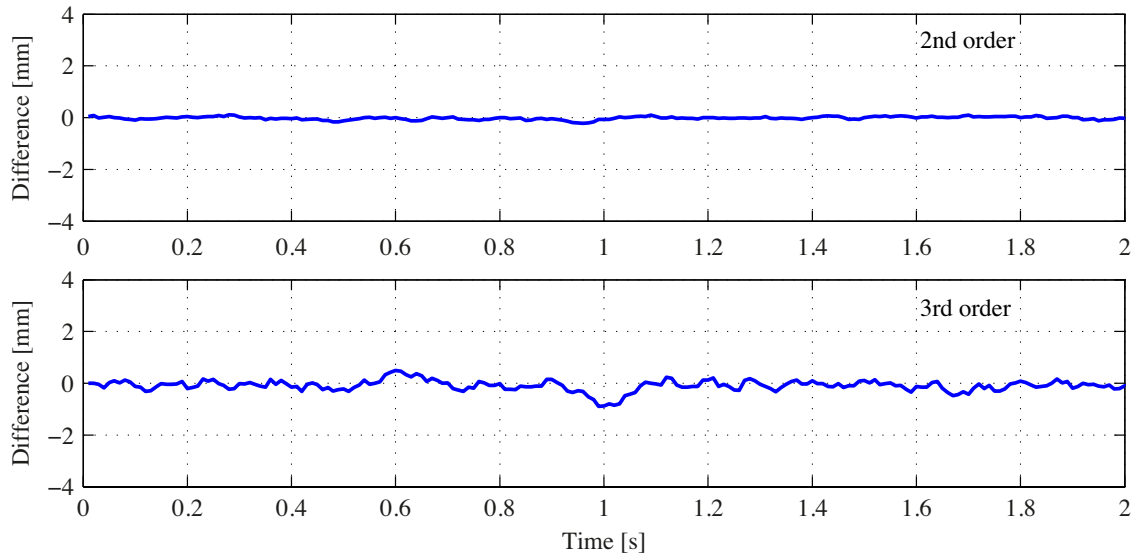
Figure 7.4: The difference in displacements between the 100 sps GPS data and the corresponding simulated response from Fig. 7.2 ($\tilde{Y}(z) - Y(z)$) for the narrow 10 Hz B_L for the 2nd order PLL (top) and 3rd order PLL (bottom).
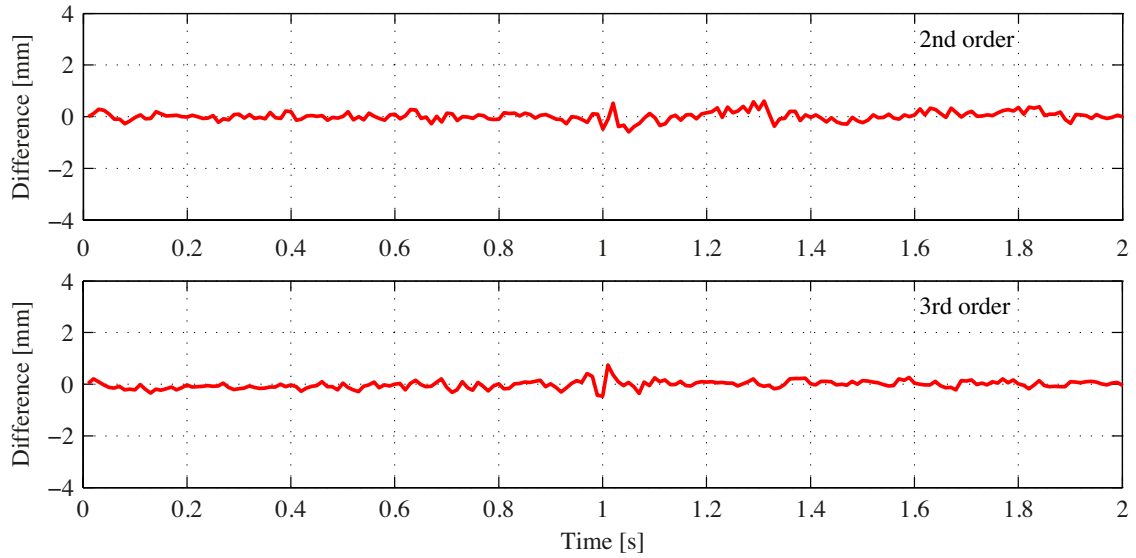
Figure 7.5: The difference in displacements between the 100 sps GPS data and the corresponding simulated response from Fig. 7.3 ($\tilde{Y}(z) - Y(z)$) for the wide 50 Hz B_L for the 2nd order PLL (top) and 3rd order PLL (bottom).

7.2 Empirical Results from the Shake Table Measurements

For the empirical determination of the receiver response, signals with high dynamics were generated by the shake table for the high-frequency spectrum above 1 Hz. In Tab. 6.1 all the sine oscillations measured with three different receiver configurations are listed. The CA/L1 PLL bandwidth was set to 10 Hz, 25 Hz and 50 Hz for the Javad Sigma-G3TAJ
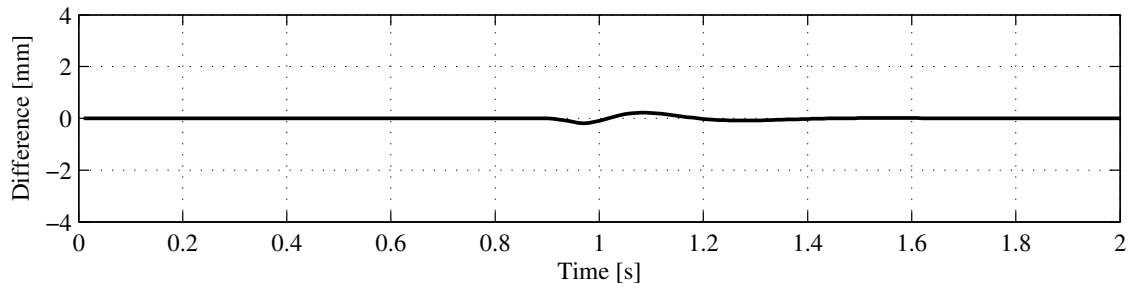
Figure 7.6: The differences of the simulated responses of a 1 cm step for a 3rd order PLL with a B_L of 10 Hz using rectangular and trapezoidal integrators from Eq. (7.1) and (7.2). The integration interval of 0.01 s is equal to the sampling rate of the kinematic GPS coordinates.

receiver. The measurements were complemented by measurements with the Leica GX1200 and NovAtel DL-4plus, both with a maximal sampling rate of 20 sps and a fixed CA/L1 PLL B_L of 15 Hz. The main configuration for the experiment makes use of a short baseline in order to minimize external perturbations of longer periods which would additionally affect an accurate determination of the baseline independent GNSS receiver response. The short baseline also allows CA/L1 and P2/L2 only solutions. However, the response based on the ionosphere-free linear combination L_c will finally demonstrate that the retrieval of the induced displacement errors is possible with a long baseline too. For more information about the processing and experiment configurations, see Chapter 6.

7.2.1 Response on CA/L1 GPS Observations

A preliminary analysis of the dynamic behavior of CA/L1 GPS measurements with a sampling rate of 100 sps is shown in Fig. 7.7 using the example of sine oscillations generated with amplitudes of 5 mm and a frequency of 1 Hz and 10 Hz. The black lines mark the ground-truth represented by the inductive transducers. Especially the 10 Hz oscillation demonstrates the mechanical limits of the shake table which is not able by far to reproduce the 5 mm input amplitude. This confirms the importance of a well defined and validated ground-truth, see also Sec. 6.3. The sine oscillations shown in Fig. 7.7 retrieved from the high-rate GPS measurements were performed with a CA/L1 PLL B_L of 10 Hz (blue) and 50 Hz (red). The corresponding spectra are given at the bottom of Fig. 7.7. The frequency can perfectly be tracked for all motions and receiver configurations. The significantly different noise levels in the spectra are caused by various measurement durations. The GPS signals were stacked for a better visualization of the dynamic behavior thus reducing the noise. For the 1 Hz oscillation a significant overshoot of the GPS measurements with a 10 Hz B_L (blue) compared to the ground-truth is already detectable. The phase is perfectly reproducible for signals of 1 Hz. The wide bandwidth of 50 Hz (red) does not show any amplitude and phase errors due to this moderate oscillation of 1 Hz. The high-frequency motion of 5 Hz in Fig. 7.7 (right) presents a completely different picture. The phase error increased for both B_L, especially the wide bandwidth generates a remarkable phase error of 64 deg. The magnitude responses between the two equivalent noise bandwidths show a contrary behavior. The wide 50 Hz B_L signal (red) significantly overshoots while the signal measured with the narrow B_L (blue) is damped by more than half of the true
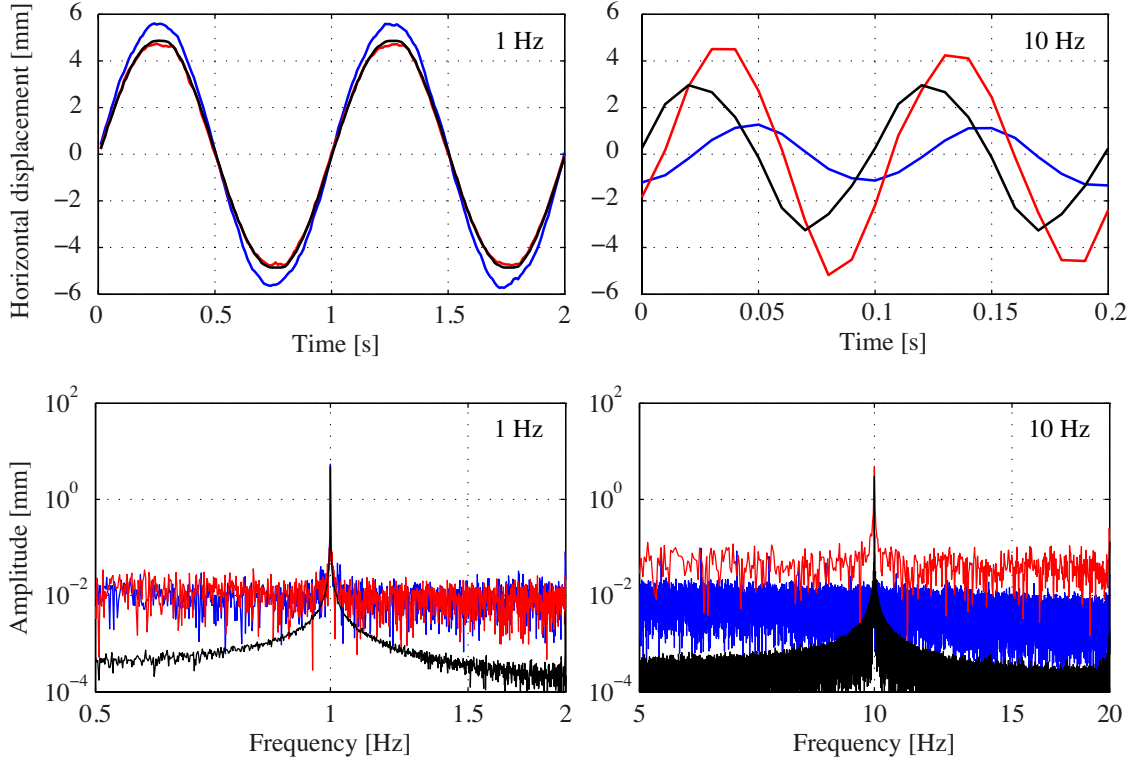
Figure 7.7: 100 sps GPS measurements of a 1 Hz (top left) and a 10 Hz (top right) sine oscillation generated by the shake table. The blue coordinates are derived from CA/L1 measurements with a 3rd order PLL and a B_L of 10 Hz compared to a B_L of 50 Hz (red) and the ground-truth (black). For the 1 Hz signal, amplitude and phase match well, though there is a degradation for the 10 Hz B_L. In the case of the 10 Hz signal, neither B_L matches phase or amplitude. At the bottom we show amplitude spectra for these motions showing that the actual frequency is tracked in all cases.

motion amplitude.

From the stacking process the standard deviation for each sample over the stacking interval can be calculated. The stacking interval corresponds to the plotted two cycles in Fig. 7.7. The standard deviations over this stacking interval are given in Fig. 7.8. On top the 1 Hz sine oscillations measured with a B_L of 10 Hz (blue) and 50 Hz (red), respectively, are shown. According to the noise analysis in Sec. 5 the narrow bandwidth shows a lower carrier phase jitter than the wide bandwidth during accelerated motions, the double-difference jitter for the CA/L1 signal of 0.75 mm for the 10 Hz B_L and of about 1.1 mm for a B_L of 50 Hz corresponds to the expected range shown in Fig. 5.2. The levels are slightly higher than the standard deviations estimated from the CA/L1 zero-baseline coordinates with a wider bandwidth of 25 Hz in Fig. 5.25, listed in Tab. 5.4. This difference is mainly caused by a slightly larger frequency spectrum involved. Even though the mean offset per stacking window is reduced, some long periodic signals are still existing and might increase the jitter above the level, where thermal noise is the only error source. Comparing the jitter before and after the motion, no significant difference to the period during the motion can be observed. For the jitter level measuring the 1 Hz signal in Fig. 7.8 no dynamic dependent variations are visible. The standard deviation of the motion with the higher frequency of 10 Hz oscillates over the two cycles. However, especially the peaks do not represent the
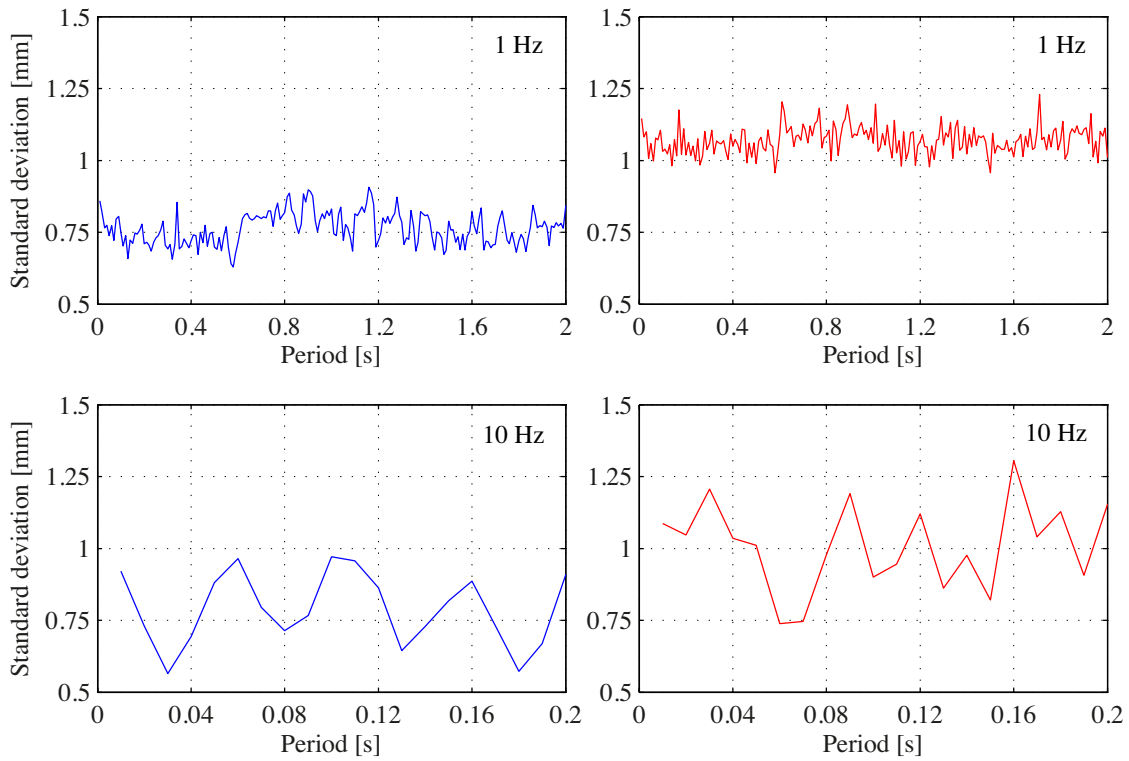
Figure 7.8: The standard deviations over the stacked period of two cycles for each sine oscillation from Fig. 7.7. On top the 1 Hz oscillation for a 10 Hz B_L (left) and 50 Hz (right). The corresponding standard deviations for the 10 Hz sine oscillation are visible at the bottom.

jitter standard deviation, but the variation of the signal amplitude over the experiment interval. Only the stacked samples at zero amplitudes are uncorrelated which are shown as the minimal values in Fig. 7.8 (bottom). For the 10 Hz B_L the jitter is about 0.65 mm and at around 0.9 mm for the 50 Hz B_L. The jitter is lower than for the 1 Hz oscillations due to the smaller stacking window and corresponds to the expected thermal noise level from Tab. 5.4 (note that the shake table motion is generated in NE-SW direction). The amplitude variations over a certain time interval while generating sine oscillations with constant amplitudes is not explainable with a linear tracking.

For the following representation of the response over the frequency spectrum between 1 Hz and 20 Hz sine oscillations in this frequency spectrum were generated by the shake table. The total error is split into a relative amplitude error η and a phase shift $\Delta\phi$:

$$\eta = \frac{A_\mathrm{GPS}}{A_\mathrm{ind}}, \quad \Delta\phi = \phi_\mathrm{GPS} - \phi_\mathrm{ind} \tag{7.12}$$

where the amplitude A and the phase ϕ were estimated by a discrete Fourier transform (DFT) for GPS and inductive transducer measurements. The frequencies determined by GPS and the inductive transducers perfectly match for all generated oscillations as already mentioned above and illustrated and confirmed by some examples in Fig. 7.7 (bottom). This is a good indication that the steady state is reached and the PLL works within a stable tracking range. The amplitudes A_GPS and A_ind are the corresponding maximal amplitudes at those frequencies. The relative amplitude error η and the phase shift $\Delta\phi$ for CA/L1
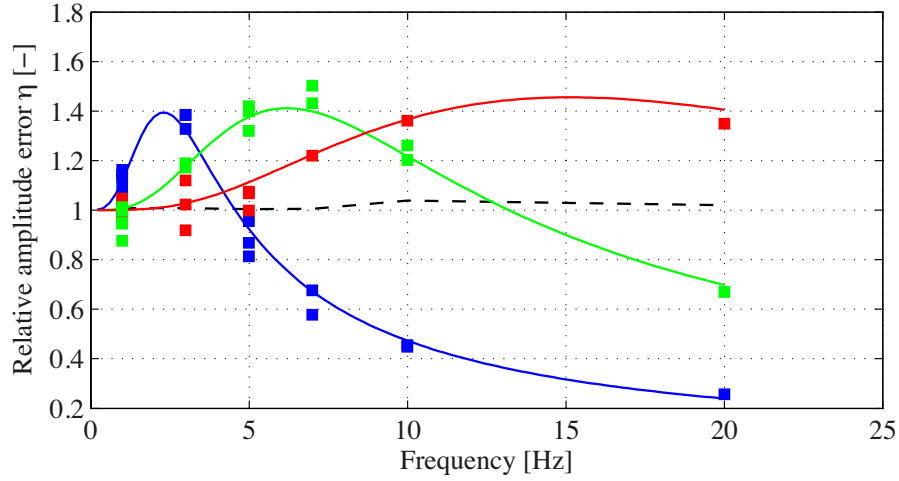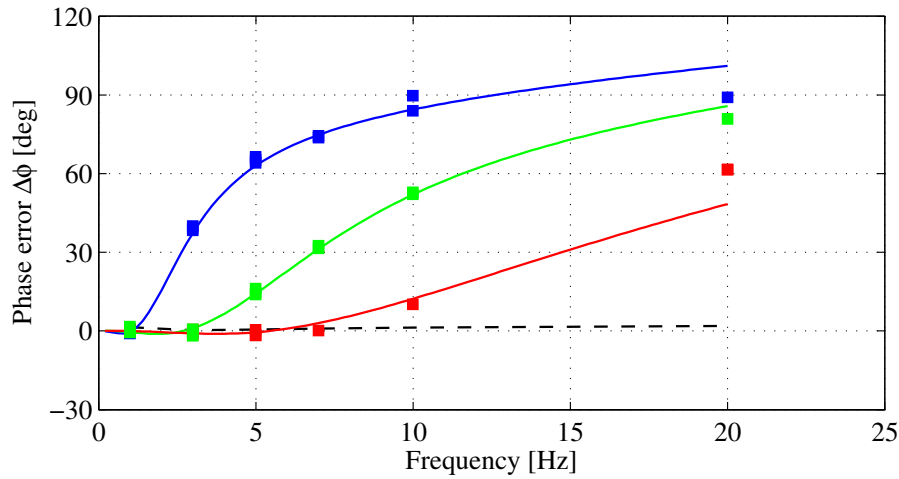
Figure 7.9: The relative amplitude error η dependent on the motion frequency for CA/L1 B_L of 10 Hz (blue), 25 Hz (green), and 50 Hz (red) measured by a Javad Sigma-G3TAJ. The solid lines represent the error η simulated by Eq. 7.9 and the parameter set provided by Javad. The dashed line marks the response of the broadband seismometer compared to the inductive transducer.

GPS measurements are presented in Figs. 7.9 and 7.10. Each square corresponds to one generated sine oscillation from Tab. 6.1. The receiver configuration is based on a 3rd order CA/L1 PLL with a B_L of 10 Hz (blue), 25 Hz (green), and 50 Hz (red). The solid lines mark the simulated response according to Eq. (7.9) with the 3rd order parameters from Javad for each loop bandwidth tested. The flat frequency response of the strong motion seismometer retrieved from the ground-truth validation experiment, visible in Fig. 6.6, is shown by the black dashed line. The variation between different amplitude responses for a specific frequency is much larger than for the corresponding phase responses. This is caused by the effect already described above for the stacking process, i. e. that the amplitude reproduced by the GPS observations is not constant over the considered time periods. The main reasons are overlaid strong signals such as high-frequency multipath and probably a non-linear behavior of the PLL which can be supported by the fact that the amplitude variations at a certain frequency are higher for the wider loop bandwidths inducing higher noise. This uncertainty is independent of the input frequency (see Fig. 7.9) and the amplitude determination method. This could be verified by a comparison of the results obtained from a DFT and a least-square adjustment estimating the amplitude and phase at the given input frequency. Both methods provide exactly the same results with differences far below the existing uncertainty level shown in Fig.7.9. However, the measured amplitude and phase responses by the shake table experiment and the corresponding simulated responses match very well. Only the phase shift $\Delta\phi$ at the highest frequency of 20 Hz slightly differs. This is caused on the one hand by a limiting phase resolution using 100 sps, and on the other hand by the integrators used for the modeling which can differ several degrees at such high frequencies with respect to an ideal integrator. The relative amplitude error reaches values up to 50% independent of the loop filter bandwidth used. A wider bandwidth helps to suppress the amplitude error only for frequencies below 5 Hz. At least the phase error for 10 Hz motions using a 50 Hz bandwidth does not exceed 10 deg.

The comparison of the receiver responses, when using a standard 2nd order PLL or the

Figure 7.10: The relative phase error $\Delta\phi$ dependent on the motion frequency for CA/L1 B_L of 10 Hz (blue), 25 Hz (green), and 50 Hz (red) measured by a Javad Sigma-G3TAJ. The solid lines represent the error $\Delta\phi$ simulated by Eq. (7.9) and the parameter set provided by Javad. The dashed line marks the response of the broadband seismometer compared to the inductive transducer.

3rd order loop with the parameters from Javad, have shown no large differences as already demonstrated for the generated step functions. The main reason can be found in the identical parameters K_1 and K_2 of a 2nd order implementation. Therefore the relationship between the equivalent noise bandwidth B_L [Hz] and the natural frequency ω_n [rad/s] for the 3rd order PLL from Javad is approximately given by Eq. (4.31). A 10 Hz B_L leads to a natural frequency of 18.9 rad/s or 3.0 Hz. Fig. 4.1 demonstrates that the peak magnitude response is slightly below ω_n, at around $0.8\,\omega_n$ for $\zeta = 0.707$. This leads to 2.4 Hz for the case of a 10 Hz B_L (blue), 6 Hz for a 25 Hz B_L (green) and 12 Hz for a 50 B_L (see Fig. 7.9). The transition frequency or the frequency with an amplitude response of 1 (not in a decibel scale) is at $1.4\,\omega_n$ for a standard 2nd order loop. In case of the Javad 3rd order PLL, the transition occurs at around $1.6\,\omega_n$ equivalent to 4.8 Hz and 12.0 Hz for a B_L of 10 Hz and 25 Hz, respectively. These values can significantly vary dependent on the implemented 3rd order loop parameters (visible in Fig. 4.2) and therefore, it is extremely hard to propagate the error over the frequency spectrum without the knowledge of the exact tracking loop parameters (see also Sec. 7.2.3).

7.2.2 Response on P2/L2 GPS Observations and on L_c

In Chapter 5 the relationship between the signal characteristics, the signal strength C/N_0, and the applicable PLL B_L has been demonstrated with respect to their impact on the carrier jitter. Especially the encryption of the P(Y)-code strongly influences the tracking behavior and performance. Due to decryption algorithm for the unknown P(Y)-code the C/N_0 at baseband suffers a huge signal strength loss of at least 10 dB compared to open-access GNSS signals. This low C/N_0 requires an extremely narrow loop bandwidth which is consequently sensitive to dynamic stress caused by receiver antenna motions and oscillator dynamics. Therefore, the P2/L2 PLL is guided by a strong signal PLL such as CA/L1, comparable to aiding the DLL PRN code tracking by the PLL, explained in Sec. 3.2.5 and
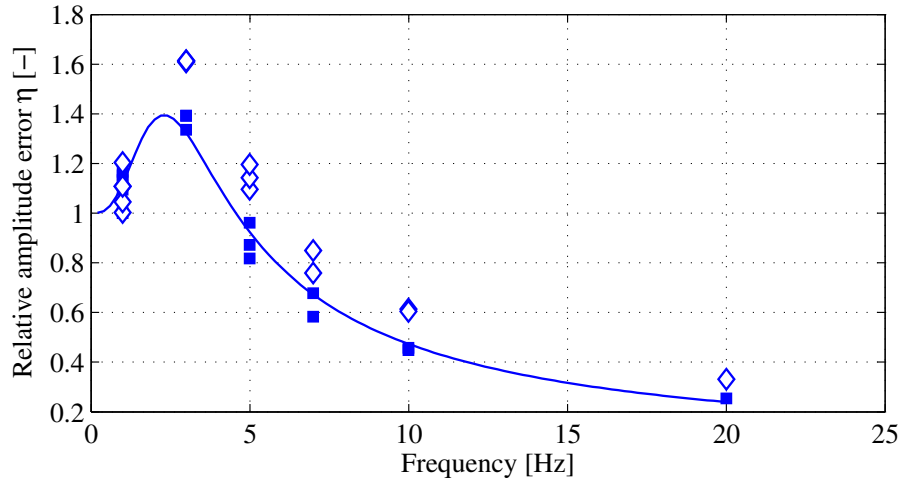
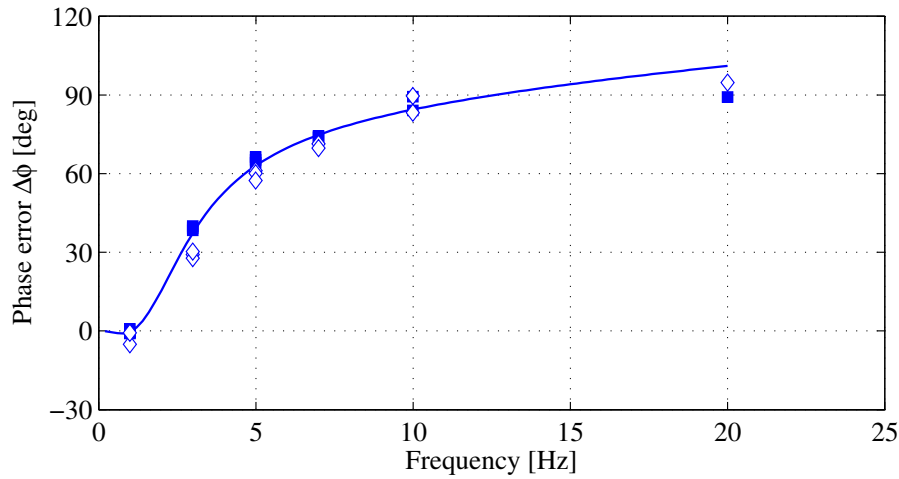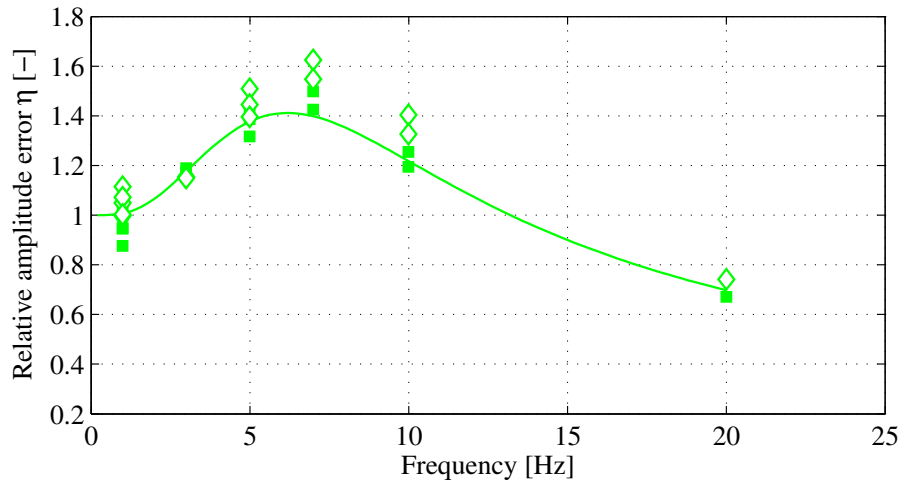**Figure 7.11:** The relative amplitude error η of CA/L1 (squares) and P2/L2 (diamonds) measurements dependent on the motion frequency for a CA/L1 PLL B_{L} of 10 Hz. The guided P2/L2 PLL has a B_{L} of 3 Hz and shows a slightly larger amplitude response. The solid line marks the simulation of the corresponding CA/L1 amplitude response.

illustrated in Fig. 3.7. The impact of the guiding is well visible in the correlations between subsequent epochs of the P2/L2 and P1/L1 GPS observations in Figs. 5.7 and 5.10. As a consequence of this, the weak loop response and resulting stress errors of P2/L2 carrier phase measurements are mainly determined by the CA/L1 PLL parameters, see Fig. 7.11 and Fig. 7.12 for an example with a CA/L1 PLL B_{L} of 10 Hz. The relative amplitude error η of P2/L2 measurements is bigger than the errors retrieved from the CA/L1 carrier phase measurements. But both transfer functions show the same frequency of maximal response and the phase errors are almost identical, which corresponds to the behavior of a proportional controller. A proportional controller generates a positive shift in the amplitude spectrum, but has no effect on the phase response. An accurate modeling and simulation of the aided PLL is difficult because the exact guiding procedure is typically not known for a GNSS receiver.

The overall P2/L2 tracking performance is an important part for geodetic observations when building the artificial ionosphere-free linear combination L_{c}, see Sec. 4.3.3. The existing correlations between CA/L1 and P2/L2 determine not only the amount of jitter on the kinematic L_{c} coordinates as shown in Sec. 5.7, but also the magnitude and phase response. Due to almost equal phase responses between CA/L1 and P2/L2 visible in Fig. 7.12, the L_{c} amplitude response directly corresponds to the amplitude differences between CA/L1 and P2/L2 scaled with the corresponding linear combination coefficients from Eq. (4.71). Let us consider the response of CA/L1 observations with a PLL B_{L} of 25 Hz (squares) and the guided P2/L2 observations (diamonds) in Fig. 7.13. The corresponding L_{c} response is shown in Fig. 7.14 (diamonds) with the solid line representing the simulated response for CA/L1. Especially at 7 Hz and 10 Hz the estimated response is significantly lower. Taking the amplitude response at 10 Hz for the sine oscillation with input amplitude 5 mm, but finally generated with A_{ind} of 3.2 mm, the relative amplitude

Figure 7.12: The phase error $\Delta\phi$ of CA/L1 (squares) and P2/L2 (diamonds) measurements dependent on the motion frequency for a CA/L1 PLL B_L of 10 Hz. The guided P2/L2 PLL has a B_L of 3 Hz and shows almost identical phase errors. The solid line marks the simulation of the corresponding CA/L1 phase response.

response $\eta(\mathrm{L_c})$ can be calculated by

$$\eta(\mathrm{L_c}) = \frac{1}{A_\mathrm{ind}} \left(\kappa_{1,\mathrm{c}} A_\mathrm{GPS}(\mathrm{CA/L1}) - \kappa_{2,\mathrm{c}} A_\mathrm{GPS}(\mathrm{P2/L2}) \right) \tag{7.13}$$

with the measured values and the coefficients for the carrier frequency of L1 and L2 the relative amplitude error is

$$\eta(\mathrm{L_c}) = \frac{1}{3.20} \left(2.55 \cdot 3.84 - 1.55 \cdot 4.24 \right) = \frac{3.22}{3.20} = 1.01. \tag{7.14}$$

This response is visible in Fig. 7.14 at 10 Hz (diamonds) which shows an η of 1, even though the CA/L1 and P2/L2 responses are at about 1.2 and 1.35 (see Fig. 7.13). The phase response in Fig. 7.15 still matches the simulated CA/L1 $\Delta\phi$ (solid line).

The black squares in Figs. 7.14 and 7.15 are the response estimates using a long baseline of 110 km. The receiver response is baseline independent , therefore the resulting responses should be identical which conforms very well to the phase errors in Fig. 7.15, but also to the relative amplitude estimates with variations within the existing uncertainties for the short baseline. The very similar determination accuracy is additionally a consequence of baseline independent noise levels for these high frequencies according to Fig. 5.28. Also multipath as the disturbance factor for the amplitude determination is independent of the baseline length.

Figure 7.13: The relative amplitude error η of CA/L1 (squares) and P2/L2 (diamonds) measurements dependent on the motion frequency for a CA/L1 PLL B_L of 25 Hz. The guided P2/L2 PLL has a B_L of 3 Hz and shows a slightly larger magnitude response.
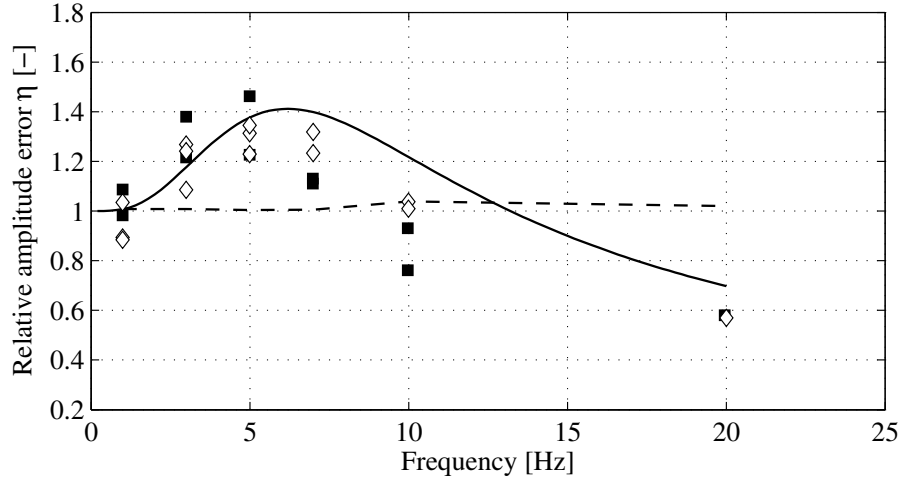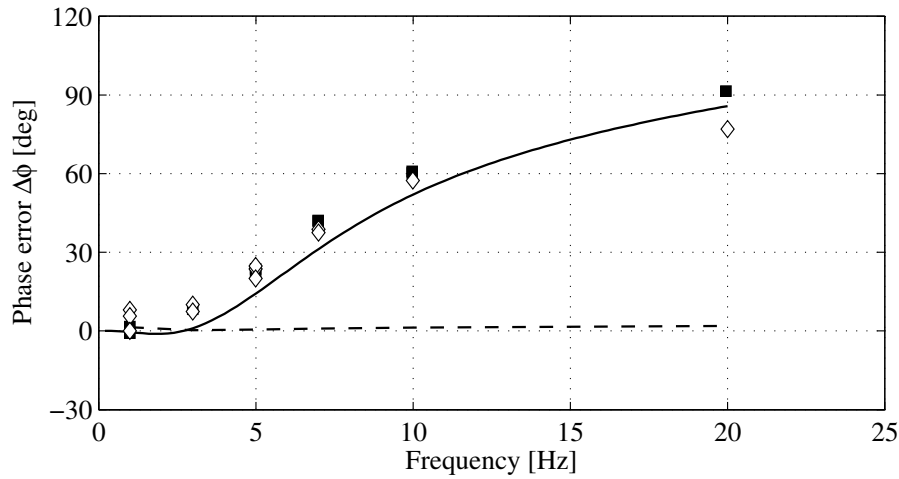

Figure 7.14: The relative amplitude error η of L_c coordinates (diamonds) estimated from the short baseline (5 m) and from a long baseline of 110 km (squares) dependent on the motion frequency. The CA/L1 PLL B_L is 25 Hz and the guided P2/L2 PLL has a B_L of 3 Hz.

7.2.3 Comparison between Different Receivers

Using different receivers, the corresponding responses differ dependent on the implemented PLL and filter parameters. Typically, these parameters are not known and not provided by the receiver manufacturers. For the tested Leica GX1200 and NovAtel DL-4plus the only information that could be obtained was the loop filter bandwidth B_L of 15 Hz and the PLL order of 3. Both receivers are based on a NovAtel OEM board and this would imply an identical parameter setting and therefore the same dynamic behavior and frequency response. Fig. 7.16 shows the relative amplitude error η for the two additional receivers, Leica GX1200 (black squares) and NovAtel DL-4plus (diamonds), both with a 3rd order CA/L1 B_L of 15 Hz. An accurate and reliable determination of the amplitudes of the 7 Hz

Figure 7.15: The phase error $\Delta\phi$ of L_c coordinates (diamonds) estimated from the short baseline (5 m) and from a long baseline of 110 km (squares) dependent on the motion frequency. The CA/L1 PLL B_L is 25 Hz and the guided P2/L2 PLL has a B_L of 3 Hz.

and 10 Hz sine oscillations was not possible anymore due to the maximum sampling rate of 20 sps, even though these frequencies are still below the Nyquist frequency. The transfer function based on the Javad parameter setting (black thick line) corresponds much better to the measured values than the function calculated with the parameters from Eq. (4.24) defined by *Ward et al.* (2006) (dashed line). The maximum amplitude response for this transfer function is at $0.70\,\omega_n$ according to Fig. 4.2. With the relationship $B_L = 0.78\omega_n$ from Eq. (4.33), the maximum response occurs at 2.14 Hz which is also visible in Fig. 7.16 (dashed line). The transition frequency is at $1.48\,\omega_n$ which leads to 4.5 Hz for a 15 Hz B_L. The different frequency response caused by different transfer functions demonstrate the necessity to know the exact parameters from the manufacturers. The knowledge of the transfer function can be used for error prediction without extensive measurement experiments on the one hand and for the correction of these errors by inverse filtering on the other hand (see Sec. 7.3).

7.2.4 g-Sensitivity of the Oscillator

The main part of the shake table experiments was performed in the configuration that only the antenna was mounted on the shake table. This is valid expecting a low impact of the accelerated oscillator on the final GPS coordinates. In Sec. 4.2.4 the oscillator induced jitter is introduced as the limiting factor for applicable B_L (for unaided loops) dependent on the oscillator quality. A physically accelerated oscillator potentially generates frequency shifts leading to an additional phase error with respect to the already accelerated reference signal. This gained phase error could move out from the linear range of the discriminator and would become a stability issue. The shake table experiments were therefore expanded to measurements with the Javad Sigma-G3TAJ mounted on the shake table. Also at highest possible dynamics (e. g. 5 Hz sine oscillation with 10 mm input amplitude as visible in Fig. 7.17) the PLL remained always locked and no additional amplitude and phase errors were induced due to the accelerated oscillator. Even though the oscillator response is not
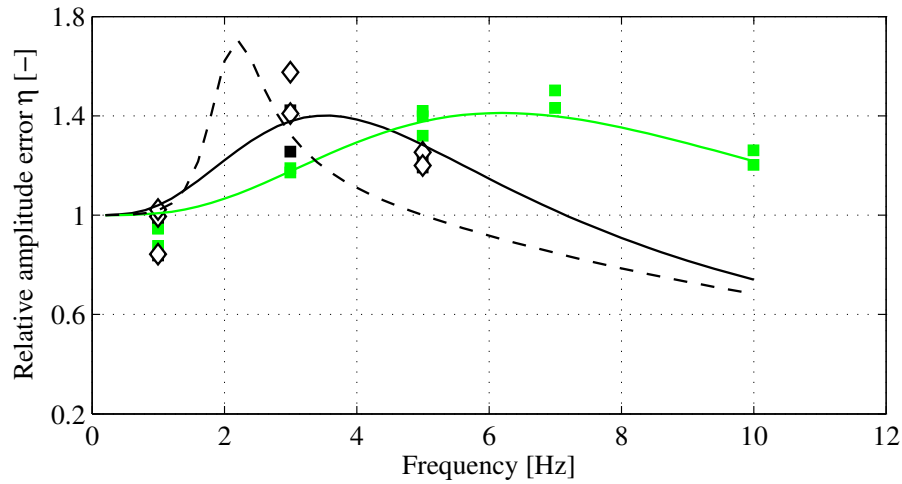
Figure 7.16: The relative amplitude errors dependent on the motion frequency for different receivers: Leica GX1200 (black squares), NovAtel DL-4plus (diamonds) both with a loop filter bandwidth of 15 Hz, and Javad Sigma-G3TAJ with a bandwidth of 25 Hz (green). The solid lines correspond to 3rd order transfer functions with the parameter setting of Javad for a B_L of 15 Hz (black) and 25 Hz (green). The dashed line marks the transfer function with the 3rd order parameters from Eq. (4.24) defined by *Ward et al.* (2006) for a B_L of 15 Hz.
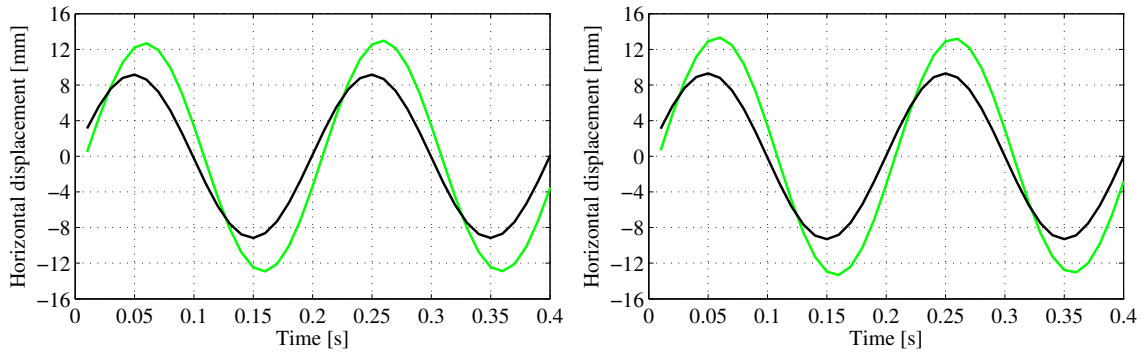
Figure 7.17: A shake table generated 5 Hz sine oscillation with an input amplitude of 10 mm with the ground-truth represented as black line and the 100 sps CA/L1 GPS measurements with a 25 Hz B_L (green). Left, the standard configuration with the GNSS antenna mounted on the shake table, and on the right the GNSS receiver additionally mounted and accelerated. No significant difference can be detected. The corresponding values for the amplitude and phase errors are listed in Tab. 7.1.

1, the error is equal for all tracking channels and would be canceled out by the receiver clock correction for the most part. As expected, especially for higher quality oscillators in geodetic receivers, no significant difference exists between the responses produced by an unaccelerated oscillator as shown in Fig. 7.17 (left) and by the accelerated oscillator (right). The quantitative comparison is given in Tab. 7.1 with small deviations far below the uncertainty existing in Figs. 7.9 and 7.10.

Table 7.1: Comparison of the amplitude response η and the phase shift $\Delta\phi$ between the two cases shown in Fig. 7.17: on the top line the measurements with only the antenna mounted on the shake table and on the bottom line the setup with the receiver additionally mounted. Both setups show the same receiver response values within the uncertainty visible in Figs. 7.9 and 7.10.

	Amp Ind [mm]	Amp GPS [mm]	η [-]	$\Delta\phi$ [deg]
only antenna	9.2	13.0	1.41	13.5
with receiver	9.3	13.3	1.43	15.3

7.3 Correction of the Receiver Response

Due to the large amplitude and phase errors, even for a wide bandwidth of 50 Hz, a minimization of these errors is only possible by inverse filtering. The measured values and the modeled transfer function for the Javad Sigma-G3TAJ match very well (see Figs. 7.9 and 7.10). This potentially allows the direct usage of the inverted transfer function from Eq. (7.8)

$$: H(z)^{-1} = \frac{1 + a_1 z^{-1} + a_2 z^{-2} + a_3 z^{-3}}{b_1 z^{-1} + b_2 z^{-2} + b_3 z^{-3}}. \tag{7.15}$$

The corrected signal $\tilde{X}(z)$ can be calculated by the displacements $\tilde{Y}(z)$ measured by GPS and the known transfer function $H(z)$

$$\tilde{X}(z) = H(z)^{-1}\tilde{Y}(z). \tag{7.16}$$

The application of the inverse filtering to a 5 Hz sine oscillation of 100 sps GPS measurements (green) is demonstrated in Fig. 7.18. The Javad Sigma-G3TAJ CA/L1 measurements $\tilde{Y}(z)$ with a 3rd order PLL and a B_{L} of 25 Hz (green) are filtered with the known transfer function $H(z)$ with the provided parameters from Javad. The resulting signal $\tilde{X}(z)$ (blue) is in good agreement with the ground-truth $X(z)$ (black) in amplitude as well as in phase apart from additional measurement noise. This works well under the condition that the signal is significantly above the noise level because the noise is additionally gained by the inverse-filter which acts like a high-pass filter. For periodic signals, such as the sine oscillations used for the frequency response determination, the best results can be obtained if a prior band-pass filter is applied for the desired frequency range. For high frequencies compared to the integration time which corresponds to the sampling-rate of the measurements, the deviation from an ideal integrator produces uncertainties. Assuming 100 sps data, the inverse-filter works up to 10 Hz within the known uncertainties, see Fig. 7.19. The 20 Hz sine oscillation with a true amplitude of 0.65 mm and a frequency of one fifth of the integration time still consists of a more than 20% damped amplitude after the inverse-filtering (about 30% before the inverse filtering, for a PLL B_{L} of 25 Hz). The phase shift $\Delta\phi$ can almost perfectly be corrected (see Fig. 7.20). Even the $\Delta\phi$ at 20 Hz is significantly reduced from about 80 deg to -10 deg.

The most important requirements for the inverse-filter are a well known transfer function and a high sampling rate. Even for the Javad receivers with the provided parameter set, only the CA/L1 PLL can be modeled with a sufficient accuracy. Due to the uncertainty
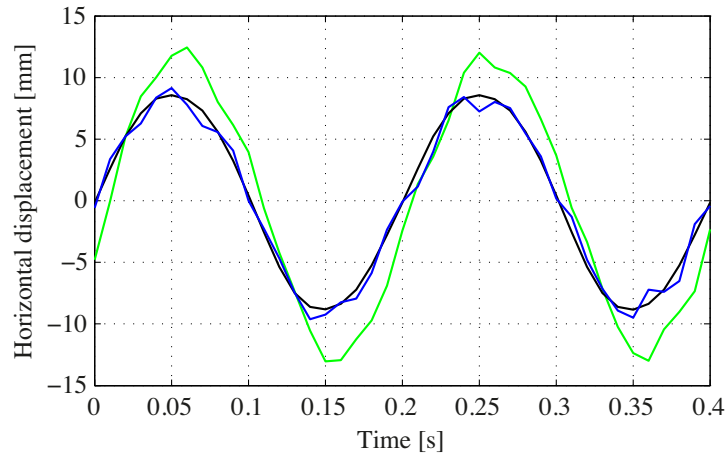
Figure 7.18: A 5 Hz sine oscillation measured by GPS with a CA/L1 3rd order B_L of 25 Hz (green) and inductive displacement transducers (ground-truth) $X(z)$ (black). The blue signal shows the inverse-filtered GPS ground motion $\tilde{X}(z)$.
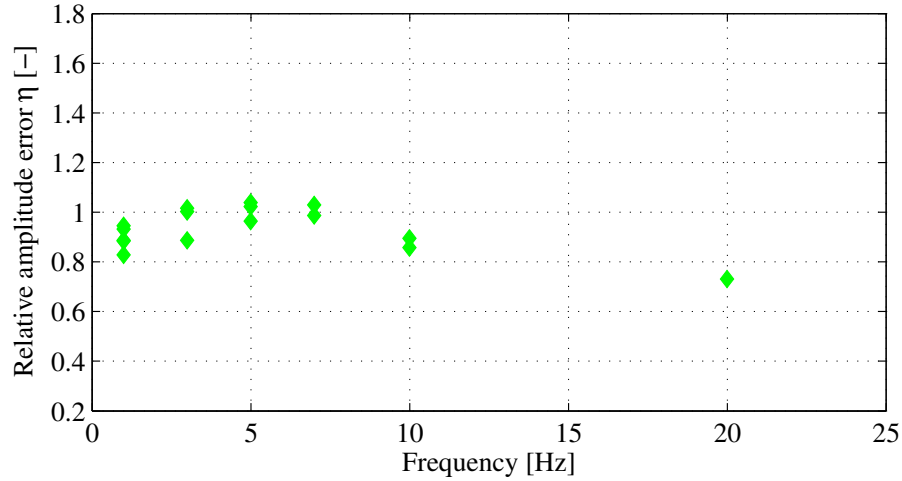

Figure 7.19: The relative amplitude errors η after the inverse filtering of the amplitude errors from Fig. 7.9 (green) for a PLL B_L of 25 Hz.

of the aiding influence, the P2/L2 amplitude response is not well known, consequently the response on L_c coordinates neither. This implies that not only the filter coefficients and bandwidth are important to know from the manufacturer, but also the precise guiding process and strategy.
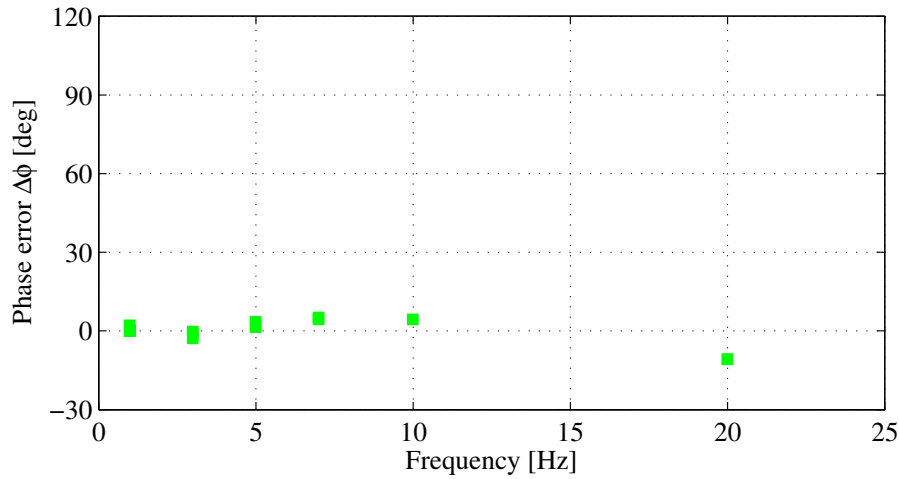
Figure 7.20: The phase shifts $\Delta\phi$ after the inverse filtering of the amplitude errors from Fig. 7.10 (green) for a PLL B_L of 25 Hz.

7.4 Summary and Concluding Remarks

The design of a PLL has to fulfill some contrary requirements. Especially the equivalent noise bandwidth B_L has a huge impact on the final characteristics of the GNSS observations, but is not selectable without limitations. In Chapter 5 the influence of a narrow and wide B_L on the carrier phase jitter has been demonstrated dependent on the signal strength, one of the limitation factors. In order to retrieve a low jitter level or even to enable a tracking of weak signals, the loop bandwidth has to be narrow. The lower boundary for unaided PLLs is typically set by the short-term stability of the oscillator. However, a narrow B_L is more sensitive against dynamic stress. Even though the tested bandwidths (10 Hz–50 Hz) in combination with the generated motions are not critical with respect to the tracking stability, the different impacts on the receiver response are significant. On the one hand the transient response of a narrow B_L is more dominant than using a wide B_L as demonstrated for the steps, which means that the tracking remains longer in the transient state and the overshoot is larger. On the other hand almost the whole frequency range beyond 1 Hz, which is the frequency band of the expected benefit of high-rate GNSS, is affected by the frequency response of the receiver. In addition to the loop bandwidth, the general design of the loop filter determines the remaining steady-state error. For the minimization of additional and in worst case growing errors after the transient state, a PLL of a GNSS receiver is at least of 2nd order and type-2. This is required in order to suppress steady-state errors caused by the permanently existing Doppler shifts on the received signals due to the satellite motions. The unguided strong loops such as CA/L1 are typically designed as 3rd order type-3 PLLs which vanish the acceleration stress induced by the receiver motion. Additionally, it minimizes the jerk induced dynamic stress or at least holds it on a constant level.

It has been shown that a simple DPLL model based on digital filter parameters provided from the manufacturer enables the reproduction of the relative amplitude errors and phase shifts of real GPS measurements. The determination of the empirical responses were achieved by signal generations with a single-axis shake table up to its limits of 20 Hz and

2.5 g. This experiment configuration can also be used as a calibration platform for the determination of receiver responses for which the filter parameters and bandwidth are unknown. The thorough investigation of the Javad receivers with a potential sampling-rate of 100 sps showed maximal amplitude errors up to about 50% and maximal phase shifts up to 90 deg independent of the loop bandwidth. The loop bandwidth determines not only the frequency with the maximum response and the transition frequency, but also the beginning of growing phase shifts. The frequencies of the generated periodic signals are always perfectly detected, which is a good indication of linear steady-state tracking for the most part. The measured amplitude variations of the generated input signals with constant amplitudes, indicates the difficulties of the amplitude determination due to strong external perturbations such as high-frequency multipath. Multipath was a dominant factor in the experiment setup, where the shake table top platform is acting as an almost perfect reflector.

The response of the guided weak loop signals as demonstrated for P2/L2 is mainly determined by the CA/L1 parameters. The amplitudes are slightly higher, but no additional phase shifts are produced compared to CA/L1. This is a typical behavior of a proportional controller. The impact on coordinates processed based on the artificial ionosphere-free linear combination is directly proportional to the coefficients of the linear combination used.

Further, the acceleration induced oscillator error is negligible and not a tracking stability issue for oscillators at the quality level of geodetic receivers. It has to be tested if a low-cost receiver with a typically lower oscillator quality.reaches an unstable tracking state during high dynamic motions.

If the transfer function is known, it can directly be applied as a inverse filter in order to correct the observations. The experiments showed that the assumption of a linear and time-invariant PLL is valid for the most part. This enabled the determination of the receiver response and also the inverse filtering directly on the processed coordinates, even though each PLL channel is referred to a specific LOS. The huge advantage of this fact is that a significant part of LOS disturbances are reduced after the processing on double-difference level. Otherwise a correction of the response is more difficult or even impossible.

8 Implications on Seismology and other Applications

In the last decades, permanent GPS stations have been operated at 30 seconds or lower sampling rates for studying long-period Earth deformations such as plate tectonics. In recent years the sampling rate has increased up to 100 sps and has sparked interest in using GNSS to record high-frequency ground motions for major earthquakes. Seismic wave fields of recent large earthquakes were successfully observed with 1 sps GNSS networks: 1999 M7.1 Hector Mine (*Nikolaidis et al.*, 2001), 2002 M7.9 Denali (*Kouba*, 2003; *Larson et al.*, 2003; *Bock et al.*, 2004; *Bilich et al.*, 2008), 2003 M8.0 Tokachi-Oki (*Miyazaki et al.*, 2004; *Clinton*, 2004; *Emore et al.*, 2007; *Larson and Miyazaki*, 2008), 2004 M9.0 Sumatra Andaman (*Kouba*, 2005; *Ohta et al.*, 2006), 2005 M8.7 Nias (*Kreemer et al.*, 2006), 2008 M8.0 Wenchuan (*Shi et al.*, 2010; *Yin et al.*, 2013), 2010 M8.8 Chile (*Wang et al.*, 2012) and 2011 M9.0 Tohoku-Oki (*Zhou et al.*, 2012; *Munekane*, 2012; *Hung and Ruey-Juin*, 2013; *Psimoulis et al.*, 2015). Beside these significant global events, moderate earthquakes have produced seismic displacements also observable by GPS: 2003 M6.5 San Simeon (*Ji et al.*, 2004; *Wang et al.*, 2007), 2004 M6.0 Parkfield (*Langbein and Bock*, 2004; *Langbein et al.*, 2006; *Houlié et al.*, 2014) and 2009 M6.3 L'Aquila (*Avallone et al.*, 2011). Events with this order of magnitude should be expected in Switzerland every 80 years (*Giardini et al.*, 2004) and have been identified as the natural hazard with the highest risk potential for Switzerland. For recording ground motion displacements during such moderate earthquakes by GPS, sites have to be installed within 100 km from the epicenter (*Clinton et al.*, 2007). Therefore, a simulated set of ground motions close to the epicenter of a M 5.0 synthetic earthquake expected for Switzerland were generated on the shake table and measured by GPS with 100 sps based on a realistic baseline configuration (Sec. 8.1). In addition to these simulated earthquakes, some actual, near-field strong motion records for moderate and large earthquakes were analyzed (Sec. 8.2) with focus on the expected GNSS receiver response and corresponding displacement errors for high-rate GNSS measurements based on the models derived in the previous sections. Due to a realistic baseline configuration for the shake table test, the existing noise level in the frequency range above 0.1 Hz can be evaluated. This allows the determination of the sensitivity of the 100 sps GPS records to high-frequency seismic signals and the comparison with the displacement errors caused by the GNSS receiver response. Assuming the same noise level for theoretically observed real events, the significance of the receiver response can be tested.

In contrast to the GNSS receiver response, the response of seismic sensors in traditional seismology practice, is provided as standard by the manufacturer. Therefore, the nominal sensor response of modern broadband instrumentation is directly proportional to velocity and acceleration, for broadband high-gain velocity sensors typically from 100 Hz – 0.01 Hz and even 200 Hz – DC for broadband strong motion accelerometers. The variations between the instruments caused by the manufacturers are small and allow a simple removal of a

gain factor or the usage of a nominal response, when working within these wide frequency bands. Nevertheless, it is typical for instrument manufacturers to deliver instruments with calibrated response information. In Fig. 6.6 it has been verified and demonstrated that a broadband strong motion instrument does not show any significant response in frequency, phase or amplitude (see also the black dashed lines in Fig. 7.9 and 7.10). Therefore, the seismic records of real events are used as a ground-truth for the GNSS receiver response simulations in Sec. 8.2 for ground motions above 0.1 Hz.

Furthermore, some example of additional applications using high-rate GNSS up to 100 sps are given in Sec. 8.4. The retrieval of high-frequency motions is required for structural monitoring and navigation, but also in the growing field of sport applications.

8.1 Synthetic Earthquake using a Shake Table

8.1.1 A synthetic M5.0 Earthquake in Switzerland

Two synthetic ground motions at epicentral distance 3 km and 24 km, respectively, shown in Figs. 8.1 and 8.2, have been used in this study. These synthetic data have been obtained deterministically from wave propagation simulations in a randomly generated heterogeneous media (*Imperatori and Mai*, 2013) using the finite difference method (FDM) of *Olsen et al.* (2009), in which a point source model for a vertical strike slip fault with moment magnitude of 5.0 is assumed. A grid size resolution of 9.98 m and a heterogeneous scattering media, are sufficient to propagates waves accurately up to 10 Hz, have been considered. Therefore, the velocity time series shown in Figs. 8.1 and 8.2 (top) were processed through a low-pass filter with a high-cut frequency of 10 Hz, and then integrated to displacements in order to use them as input for the shake table.

The ground velocities at the close site to the epicenter have the most power within 1 and 10 Hz. After the integration to displacements the main energy is shifted to lower frequencies while strongly breaking down above 3 Hz (see spectra in Fig. 8.1). The energy arriving at the station 24 km from the epicenter is mainly distributed below 1 Hz, especially for the displacements visible in the spectra of Fig. 8.2.

8.1.2 Measurement Configuration

The measurements of the earthquake ground motions generated by the shake table should be performed under realistic conditions, where GPS displacements are obtained relative to a baseline, which, as earthquakes affect a large region, must be 100's of km distant. During this project a permanent 100 sps GNSS station was installed at Fiescheralp in the Canton Valais. The site called FIES is visible in Fig. 8.3 as a black triangle. Based on the publication of *Giardini et al.* (2004) the Valais is one of the regions at highest risk with respect to potential earthquakes in Switzerland. Due to this fact, the project COupled seismogenic GEohazards in Alpine Regions (COGEAR, *Fäh et al.* (2012)) was initiated in 2006. Different institutes of the ETHZ and EPFL worked on this interdisciplinary project with its main focus on the hazard chain induced by earthquakes with the Valais as the selected study area. In addition to the seismic network in this region, a dense high-rate
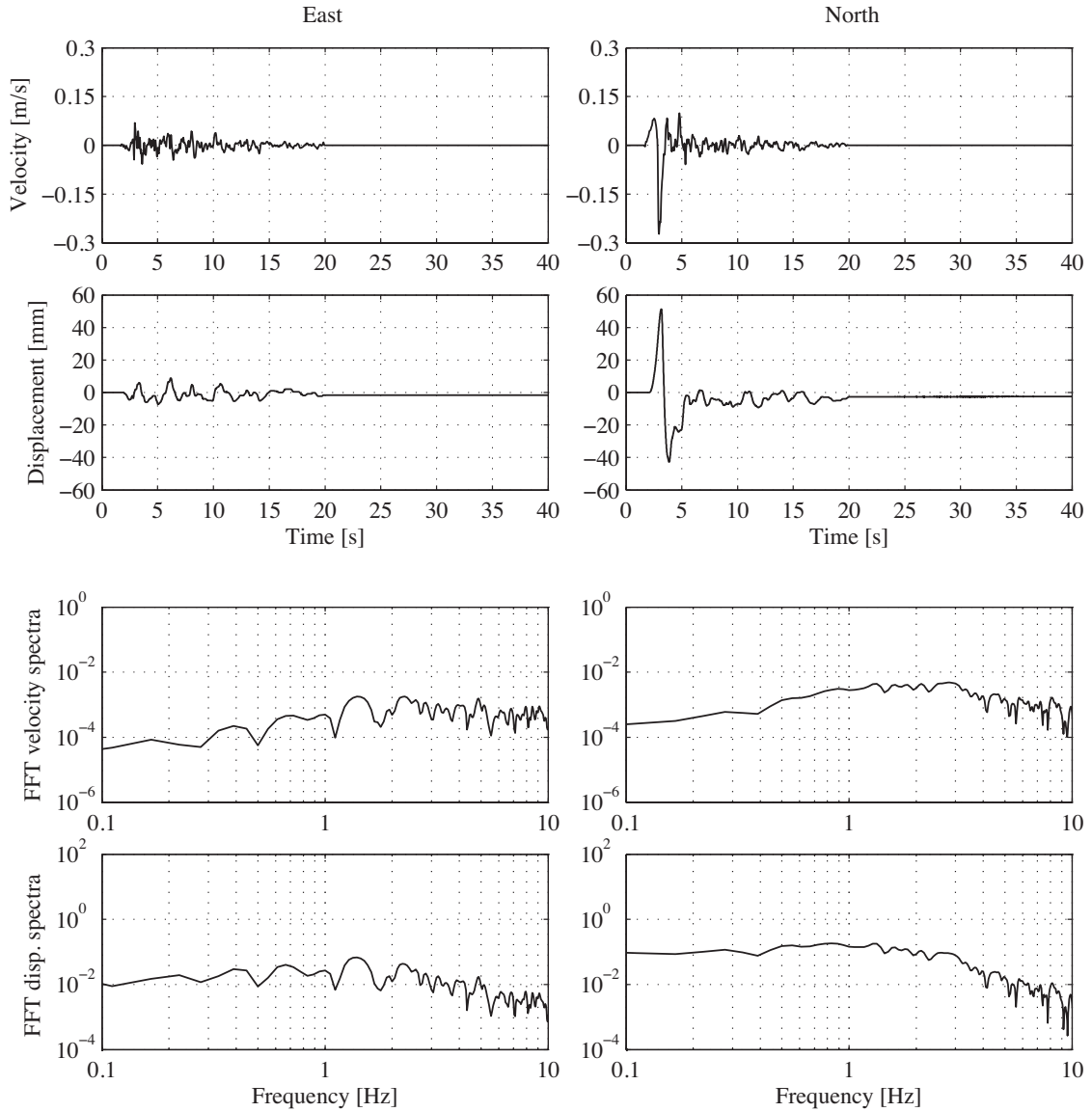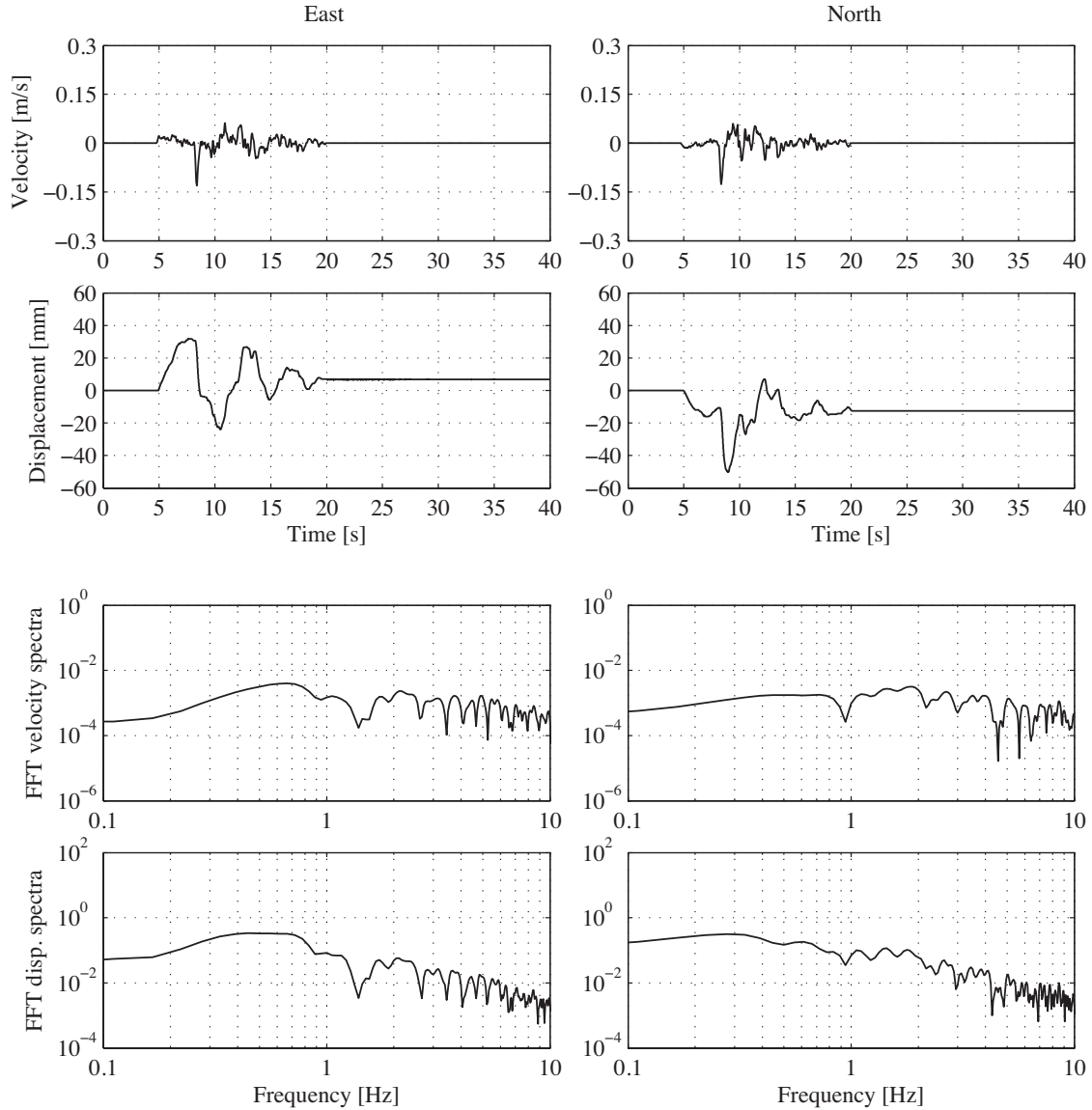
Figure 8.1: The synthetic East and North ground velocities for the M5.0 Earthquake (top) potentially measurable at a site extremely close to the epicenter (3 km). The displacements integrated from the velocities and the corresponding amplitude spectra are visible below.

GNSS network with sampling rates up to 20 sps has been installed for a continuous long-term operation (*Villiger*, 2014). These sites, including the station FIES are shown in Fig. 8.3 as black dots. Due to the infrastructure of the COGEAR GNSS network already existing (available power supply, data transmission link, GNSS antenna) and the good co-location to broadband seismometers, the site FIES was chosen for an upgrade to 100 sps. However, a processing based on accurate relative positioning is only possible with a second permanent 100 sps station. For this purpose the officially inactive AGNES station ETHZ at Hönggerberg was additionally equipped with a high-rate GNSS receiver leading to the new station ETH3 (see Fig. 8.3). On the one hand ETH3 enables a permanent 100 sps baseline, on the other hand the site is far enough from the network in the Valais (112 km

Figure 8.2: The synthetic East and North ground velocities for the M5.0 Earthquake (top) potentially measurable at a site with a 24 km epicenter distance. The displacements integrated from the velocities and the corresponding amplitude spectra are visible below.

to FIES) to be minimally affected by a potential earthquake in that region. Therefore, it can be used as a reference station not only for the baseline to FIES, but also for the other COGEAR GNSS sites with sampling rates up to 20 sps because the official permanent GNSS network AGNES operated by swisstopo is only running with 1 sps at present.

At station ETH3 the Javad Sigma-G3TAJ receiver is connected to the Trimble Antenna TRM29659-00 of the recent AGNES station by a power divider (*Huber+Suhner*, 2014). The collected 100 sps GNSS records of all available satellite systems and signals are ring-buffered on an external hard disk for 2 months. The signal from the Leica GNSS antenna AR25 at FIES is split by an identical power divider to the Javad Sigma-G3TAJ GNSS receiver and the already existing Leica GRX1200 receiver of the COGEAR network. The
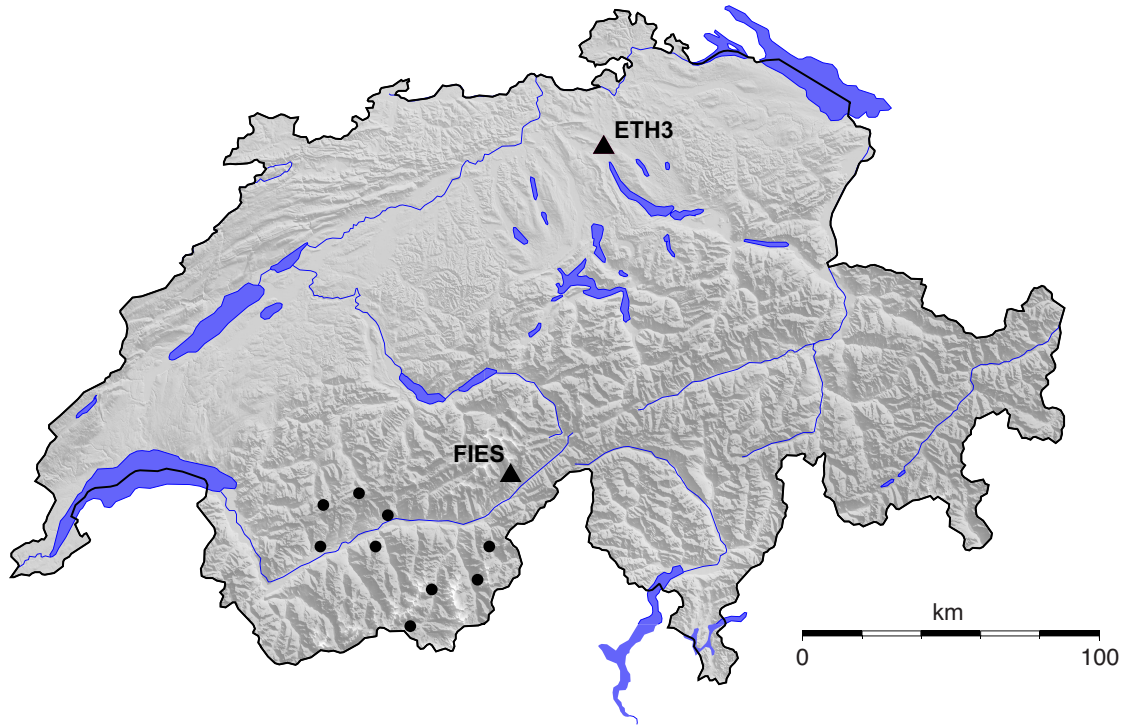
Figure 8.3: The locations of the two permanent 100 sps GNSS sites ETH3 at ETH Hönggerberg in Zurich and FIES at Fiescheralp marked as black triangles. The baseline length between the two stations is about 112 km. The black dots show the additional permanent high-rate GNSS sites with a sampling rate higher than 1 sps (up to 20 sps) installed in the framework of the COGEAR project.

Figure 8.4: Left the Leica AR25 GNSS antenna at the station FIES is mounted over the tunnel, where the GNSS receivers and the broadband seismometers are installed. The Leica GRX1200 and Javad Sigma-G3TAJ GNSS receivers are connected via a splitter to the same antenna and are placed inside the tunnel (right).

antenna is mounted about 30 m above the tunnel (see Fig. 8.4 left) where the box with the two GNSS receivers and additional equipment are placed (see Fig. 8.4 right). The Javad receiver is directly connected to a small PC in order to establish a 30 days buffer for the 100 sps data, producing huge files with a huge size. Due to the data link available, the connection to the receiver is always possible in order to change the configuration or to download the raw files on demand. Additionally, the co-location to a high-quality broadband seismometer is a key issue for the current and future combination of seismic and GNSS data.

In order to guarantee a realistic configuration for the GPS experiments, the shake table, generating the synthetic ground motions, was placed on the roof of the HPV building at Hönggerberg within meters to the ETH3 station. The GPS processing was finally based on the baseline from FIES to the shake table and corresponds to the reverse scenario of a potential event in the Valais captured by one of the GNSS stations close to the epicenter and accordingly processed with the reference station ETH3. The shake table measurements were additionally processed with ETH3, building a short baseline of 10 m in order to verify the noise behavior during an event for the spectral noise comparison between different baselines shown in Sec. 5.7. The East and North components were generated separately and the height component was not taken into account for the experiment due to the limitation of the shake table to one horizontal axis.

8.1.3 GPS Results

The 100 sps GPS processing of the earthquake records for the GNSS antenna on the shake table, including the long baseline to the station FIES, follows the standard procedure already introduced in Sec. 6.4.2. Due to the interest in the high-frequency motion, the final L_c coordinates were high-pass filtered with a low-cut frequency of 0.1 Hz in order to avoid long periodic perturbations and the static co-seismic displacement. This is valid for such a small event which has its main power above 0.1 Hz, see the spectra in Fig. 8.1 and 8.2. The measurements were performed with a Javad Sigma-G3TAJ receiver with 100 sps and three different CA/L1 3rd order PLL B_L of 10 Hz, 25 Hz and 50 Hz. The weak loop (P2/L2) bandwidth was 3 Hz for all three strong loop configurations. The processed GPS L_c coordinates compared to the ground-truth represented by the inductive transducer measurements (black) are shown in Fig. 8.5 with a PLL B_L of 10 Hz (blue), in Fig. 8.6 with a PLL B_L of 25 Hz (green) and in Fig. 8.7 with a PLL B_L of 50 Hz (red). At first view, high-rate GPS is able to well reproduce the ground-motions generated by an earthquake with magnitude 5.0 very close to the epicenter in all three receiver configurations. The small displacements of the East component are recovered by GPS only at frequencies below 1 Hz (see the spectra in Fig. 8.5, 8.6 and 8.7). Also the significant displacements of the North component are well detected by GPS from 0.1 Hz to 1 Hz. In Sec. 5.7, especially in Fig. 5.28, it demonstrated that the GNSS noise in the frequency range above 1 Hz can be described by thermal noise which is independent of the baseline length, but dependent on the B_L used. However, when building the ionosphere-free linear combination L_c the dominant noise part is induced by the weak P2/L2 signal. Therefore, there is no significant difference in the high-frequency noise and detection level above 1 Hz between the three different strong loop B_L configurations of 10 Hz, 25 Hz and 50 Hz (compare the spectra in Figs. 8.5, 8.6 and 8.7). Additionally, signals between 0.1 and 1 Hz are included in the GPS time series, which are
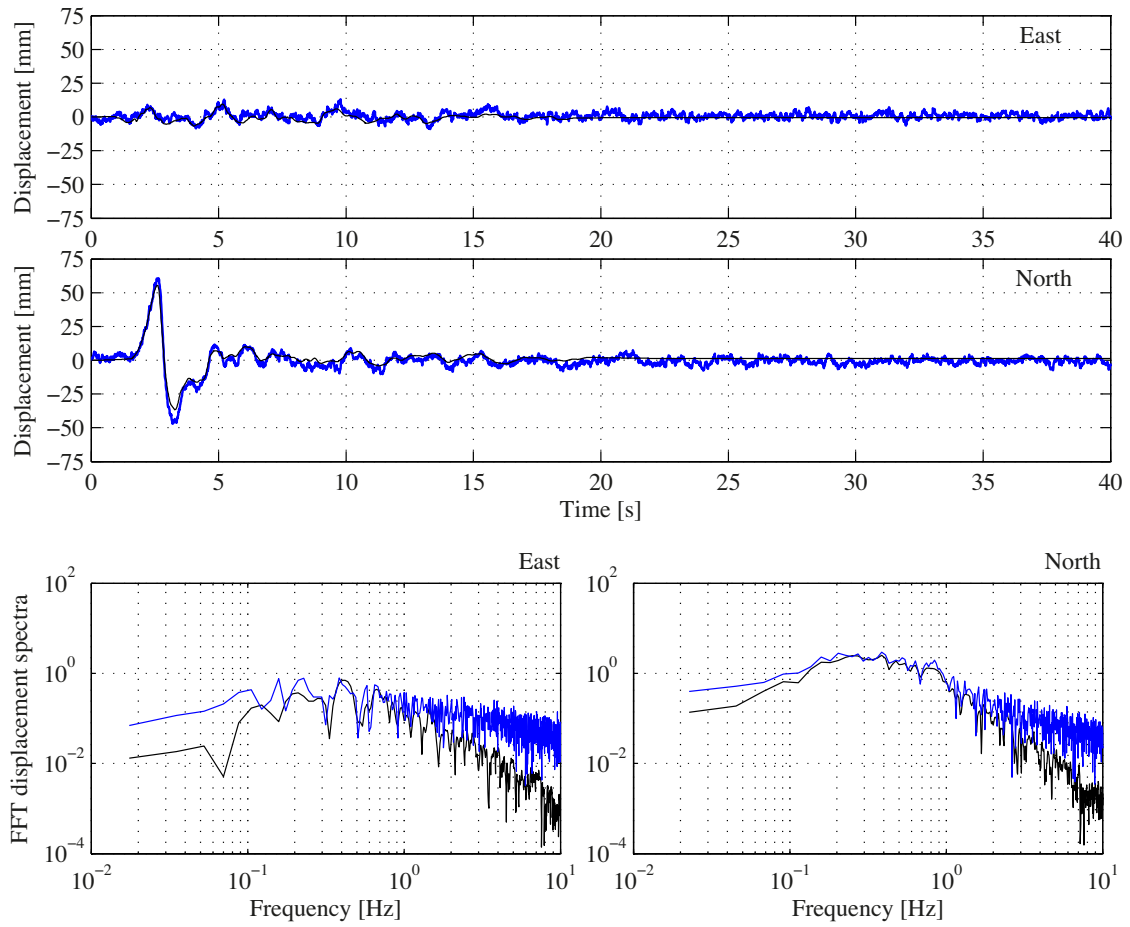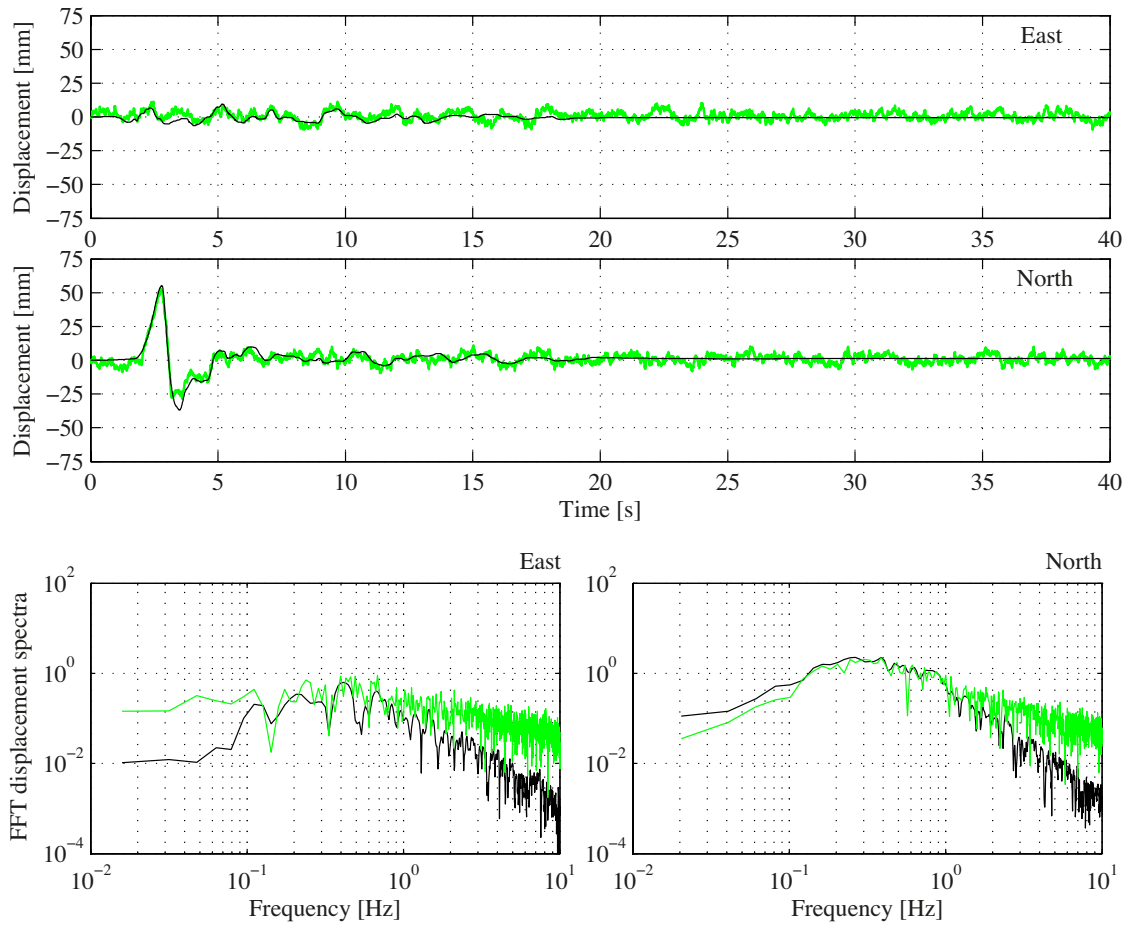
Figure 8.5: The East and North component of the simulated M 5.0 earthquake from Fig. 8.1 generated by the shake table (black) and measured with 100 sps GPS with a PLL B_{L} of 10 Hz (blue). The data is high-pass filtered with a low-cut frequency of 0.1 Hz, visible in the spectra below.

affected by external perturbations. The CA/L1 loop bandwidth has an even lower impact in that frequency range. The three different GPS L_{c} coordinate sets are therefore affected by high-frequency multipath and atmospheric refraction below 1 Hz with a changing intensity over the experiment period. These variations can be shown in the following while zooming at the North component between second 1 and 7 of the event, see Figs. 8.8, 8.9 and 8.10. In addition to the ground-truth (black) and the GPS measurements with the color of the corresponding B_{L}, the GPS displacements (dashed black line) simulated by using the transfer function of Eq. (7.9) as already demonstrated in Sec. 7.1 are shown. The differences between the ground-truth and the GPS measurements as well as the simulated responses are shown in the plots at the bottom. The horizontal dashed lines mark the 95% noise threshold equal to the 2σ standard deviation over the 40 seconds of the event after reducing the input signal. This boundary is slightly different for the three receiver configurations (independent of the loop bandwidth) due to the longer periodic signals below 1 Hz mentioned above. The 2σ (blue dashed) for the 10 Hz B_{L} in Figs. 8.8 was 5.4 mm and 6.6 mm for the GPS measurements based on a B_{L} of 25 Hz (green dashed) in Fig. 8.9.
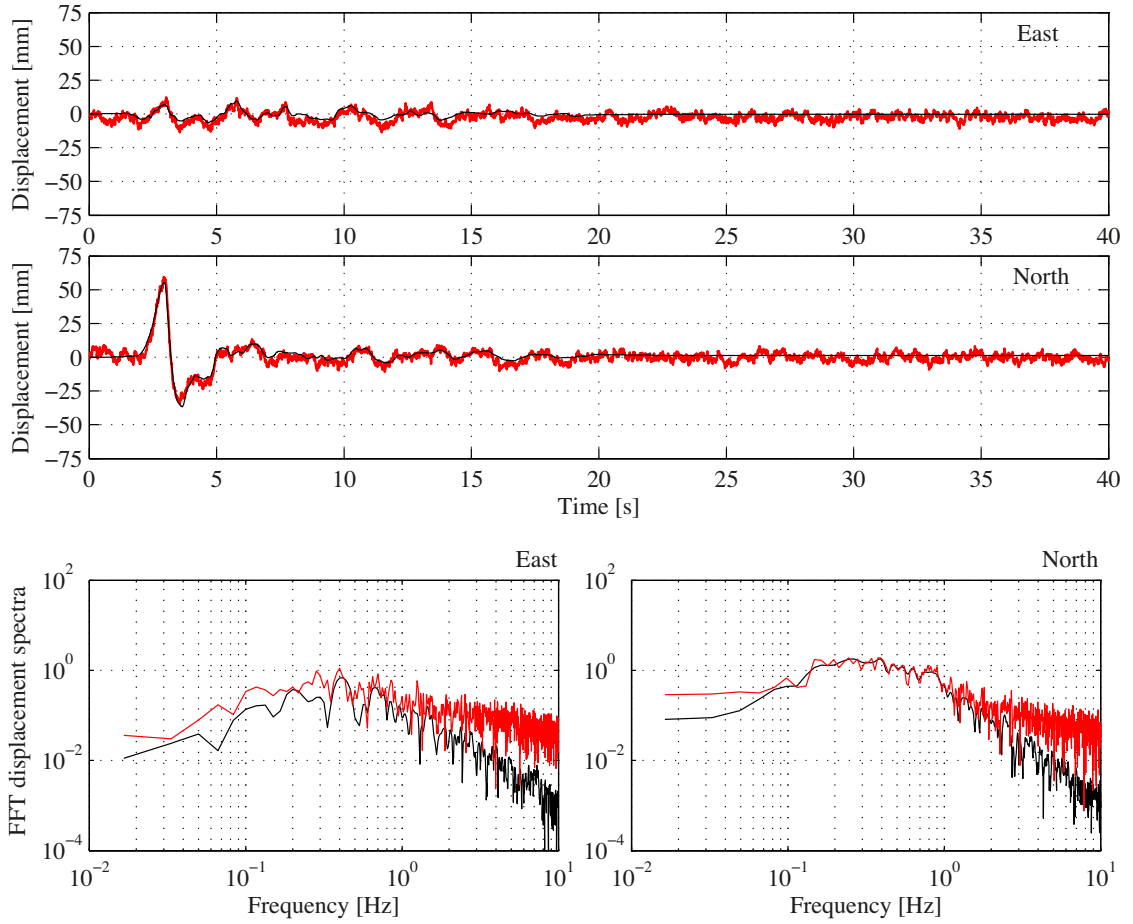
Figure 8.6: The East and North component of the simulated M 5.0 earthquake from Fig. 8.1 generated by the shake table (black) and measured with 100 sps GPS with a PLL B_L of 25 Hz (green). The data is high-pass filtered with a low-cut frequency of 0.1 Hz, visible in the spectra below.

Finally, the 95% threshold (red dashed) for the third configuration with a 50 Hz strong loop B_L reached 5.6 mm. Comparing the simulated GPS displacements (black dashed) in Figs. 8.8, 8.9 and 8.10, it can be seen, that only the displacement error caused by the response, when using a 10 Hz B_L is above the 95% boundary. The corresponding measured displacement errors (blue) in Fig. 8.8 (bottom) shows exactly this expected response. Even though this receiver response seems to be significant, the GPS coordinates in Fig. 8.9 are disturbed up to a similar level independent of the dynamics caused by the earthquake.

The response for the recordings of the generated displacements in Fig. 8.2 with an epicentral distance of 24 km is smaller due to the fact that significant displacements are mainly distributed in the lower frequency spectrum. Even when using the narrow PLL B_L of 10 Hz, the GNSS receiver response is below the 2σ threshold (see Figs. A.2 and A.3), which has also been calculated over the 40 s of the event after reducing the true input motion. The 1σ noise level for all three configurations (visible in Figs. A.1, A.4 and A.7) are in the identical range as observed for the ground-motion measurements from the station close to the epicenter (see also Tab. 8.1).

Figure 8.7: The East and North component of the simulated M 5.0 earthquake from Fig. 8.1 generated by the shake table (black) and measured with 100 sps GPS with a PLL B_{L} of 50 Hz (red). The data is high-pass filtered with a low-cut frequency of 0.1 Hz, visible in the spectra below.

An important characteristics of high-frequency GNSS noise is the baseline-length independency for the frequency range analyzed for this event above 0.1 Hz as demonstrated in Sec. 5.7. In order to verify this behavior, the GPS measurements of the M 5.0 earthquake generated by the shake table were additionally processed in parallel with the station ETH3, building a baseline of about 10 m. The comparison between the two baseline lengths are listed in Tab. 8.1. Even though the vertical component of the earthquake ground-motions was not generated, it is included in the following comparison. Note that the East and North components are referred to the earthquake component and not to the topocentric component of the GPS coordinates because the ground-motions had to be generated separately due to the limitation of the shake-table to a single axis. The variations are mainly caused by the short time interval used for estimating the standard deviations and by the measurements shifted in time over the experiment duration of more than one hour. The horizontal components with the actual satellite constellation varies around 3 mm and the vertical component around 7.5 mm, which is the typical relation between the horizontal and vertical component due to the LOS geometry as shown in Sec. 5.7. The comparison
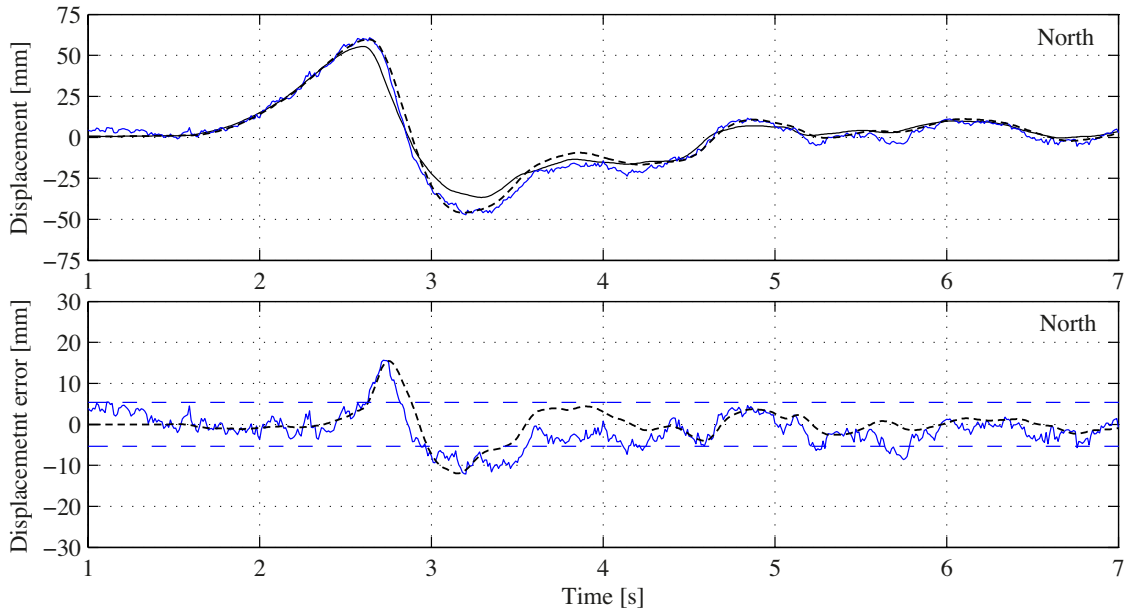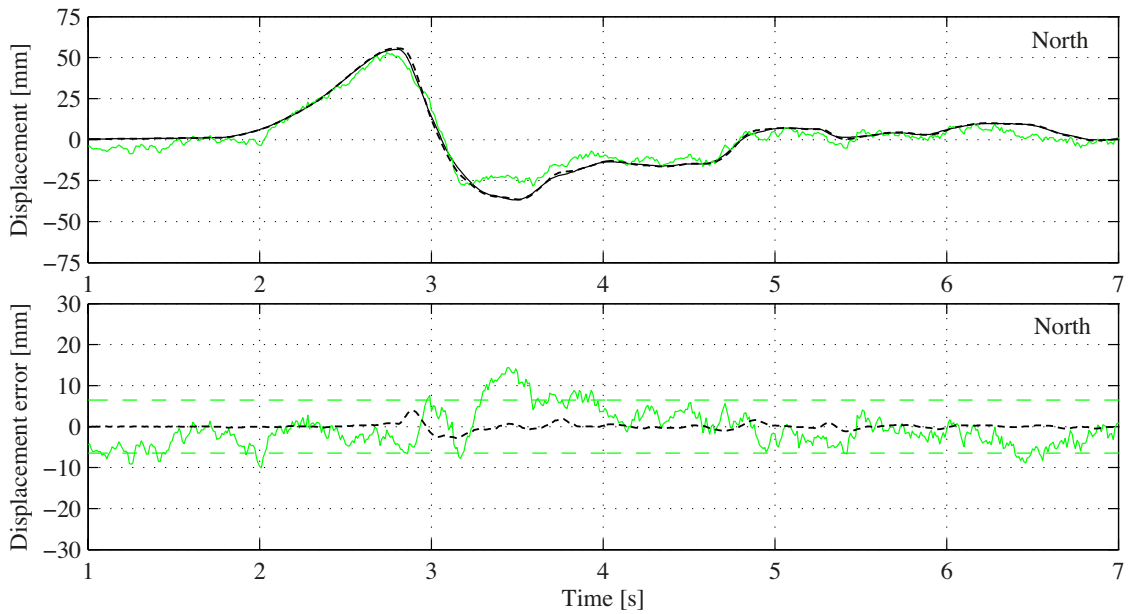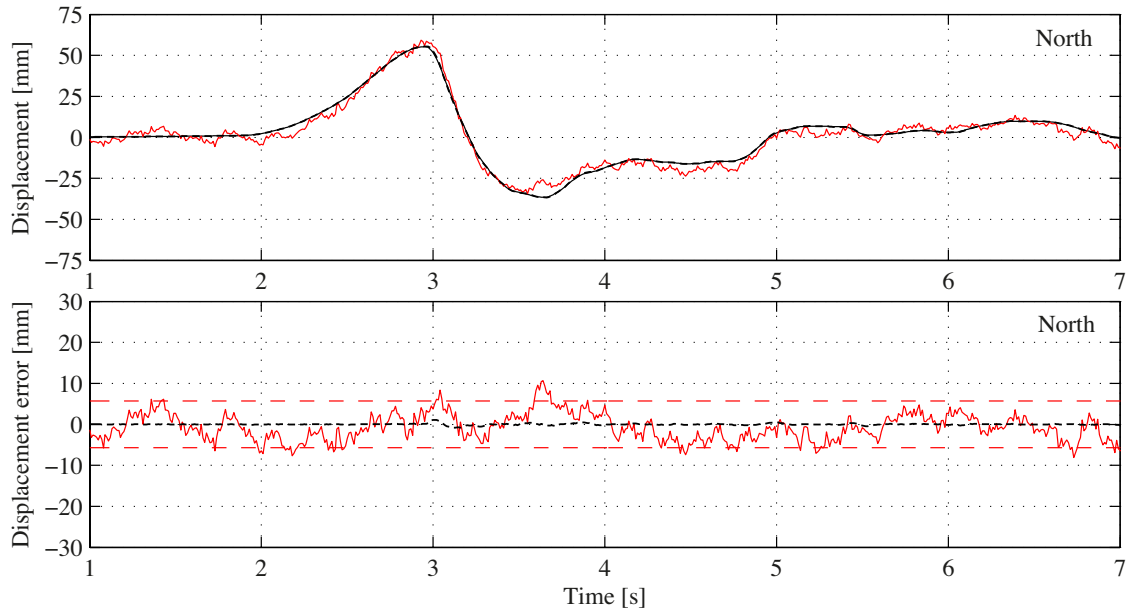
Figure 8.8: The North component from second 1 to 7 from Fig. 8.5 with the additional black dashed line representing the simulated displacements according to Eq. (7.9) with a PLL B_L of 10 Hz. At the bottom the displacement error after the subtraction of the input motion (black line on top). The horizontal dashed blue line marks the 95% threshold (2σ) of the GPS measurements estimated over the 40 s of the event.

Figure 8.9: The North component from second 1 to 7 from Fig. 8.6 with the additional black dashed line representing the simulated displacements according to Eq. (7.9) with a PLL B_L of 25 Hz. At the bottom the displacement error after the subtraction of the input motion (black line on top). The horizontal dashed green line marks the 95% threshold (2σ) of the GPS measurements estimated over the 40 s of the event.

Figure 8.10: The North component from second 1 to 7 from Fig. 8.7 with the additional black dashed line representing the simulated displacements according to Eq. (7.9) with a PLL B_L of 50 Hz. At the bottom the displacement error after the subtraction of the input motion (black line on top). The horizontal dashed red line marks the 95% threshold (2σ) of the GPS measurements estimated over the 40 s of the event.

Table 8.1: The standard deviations of the L_c coordinates estimated over a short time interval of 40 s duration of the event dependent on the different earthquake displacements, receiver configurations and baseline lengths.

	Short baseline 10 m			Long baseline 110 km		
	σ_E [mm]	σ_N [mm]	σ_{Up} [mm]	σ_E [mm]	σ_N [mm]	σ_{Up} [mm]
10 Hz B_L close	3.0	3.0	7.0	2.3	2.7	6.9
25 Hz B_L close	3.2	3.2	7.3	3.0	3.3	7.4
50 Hz B_L close	2.9	3.0	8.3	2.6	2.8	7.1
10 Hz B_L far	2.5	2.5	7.8	2.7	2.5	8.0
25 Hz B_L far	2.9	2.9	6.5	2.9	2.8	7.0
50 Hz B_L far	3.3	3.5	8.7	3.0	3.1	7.4

between the short and long baseline shows no significant differences. The noise level of the long baseline is even a bit smaller. The difference between the two processing strategies can be explained by the two different antennas used at ETH3 and FIES, and by different multipath environments and sky coverage.

8.2 Simulations of real Earthquakes

Larger displacements as expected for larger events than the M 5.0 earthquake from the previous section, could not be generated by the shake table due to the maximum possible displacement of 15 cm (see Sec. 6.1.1). However, it could be demonstrated in Chapter. 7 and Sec. 8.1.3 (especially in Fig. 8.8) that the linear PLL model is appropriate in order to determine the potential receiver response. In this section we focus on real events with moment magnitudes of 6.3, 7.0 and 9.0. We test if the GNSS receiver frequency response plays a critical role for an accurate retrieval of earthquake-induced ground-motions by high-rate GNSS. For this purpose only the acceleration recordings at the sites closest to the epicenter were considered, where the largest displacements in the higher frequency spectrum can be expected.

8.2.1 2009 L'Aquila Mw 6.3

The town of L'Aquila in the Central Appennines of Italy was hit by an earthquake of magnitude Mw 6.3 on 2009-04-06 at 01:32 UTC. The event occurred at a depth of 8.3 km, a normal faulting with strike = 139.0, dip = 48.0 and rake = -87.0. There are a lot of publications inferring the rupture process and fault modeling, e. g. *Gallovic and Zahradnik* (2012); *Ameri et al.* (2012).

The data set used for the following GPS receiver response simulations includes the L'Aquila mainshock measured at station AQK from the Italian RAN (Rete Accelerometrica Nazionale) network. Only the North-South component will be analyzed due to the much larger displacements compared to the other components. The epicentral distance is only 5.7 km. The acceleration data (from the ESM database, http://esm.mi.ingv.it) was collected by a Kinemetrics EpiSensor FBA-3 sampled with 200 sps. The accelerations provided, visible in Fig. 8.11 (top left), were already processed and filtered by a 2nd order Butterworth filter with a low-cut frequency of 0.1 Hz and a high-cut frequency of 40 Hz (see Fig. 8.11 bottom left). Due to the closeness to the epicenter the recorded peak ground acceleration (PGA) reaches 3.47 m/s^2. The strong accelerations are mainly distributed in the frequency range between 0.5 Hz and 20 Hz. The corresponding displacements obtained by a double integration of the accelerations, assuming no static coseismic displacement, show a peak ground displacement (PGD) of 0.12 m (see Fig. 8.11 top right). The main displacements are distributed between 0.1 Hz and 1 Hz (see Fig. 8.11 bottom right).

The displacement error in Fig. 8.12 (left) is calculated as the difference between the displacements from Fig. 8.11 as the input and the simulated displacements according to Eq. (7.9). The transfer function from Eq. (7.8) with the parameters from Javad is used with three different PLL B_{L} of 10 Hz (blue), 25 Hz (green) and 50 Hz (red). Only the narrow bandwidth of 10 Hz (blue) shows a significant response with a maximum difference of 5 mm. This transient response is caused by the displacements above 1 Hz, the critical frequency band with maximum amplitude response (see Fig. 7.9). However, assuming a noise level as listed in Tab. 8.1, the displacement error caused by the GNSS receiver frequency response is not really significant and a limiting factor, even for this narrow B_{L}. The responses for the wide bandwidths of 25 Hz and 50 Hz are below 1 mm because only small displacements occur at frequencies higher than 3 Hz. A GNSS receiver with a wide
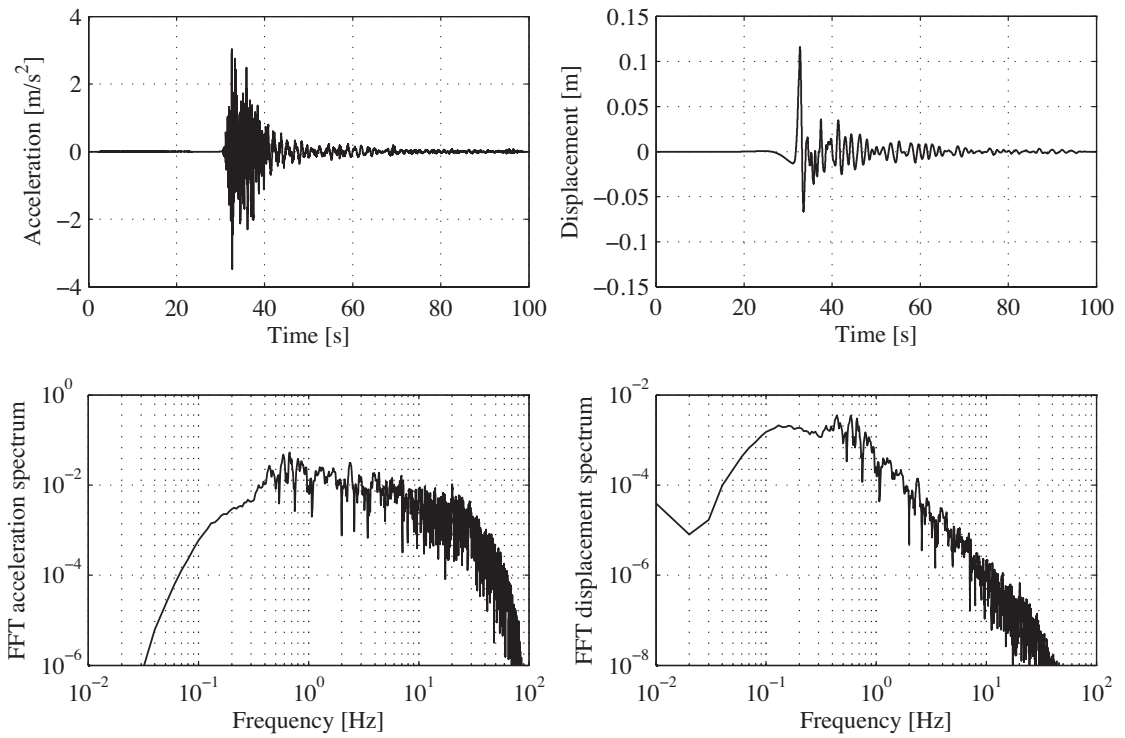
Figure 8.11: The North component recordings of the 2009 L'Aquila mainshock of Mw 6.3 at an epicentral distance of 5.7 km (left). The right plots show the displacements by doubly integrating the accelerations assuming no permanent coseismic displacement.

PLL B_L produces only negligible displacement errors for this type of event, even extremely close to the epicenter.

8.2.2 1999 Düzce Mw 7.0

The event with the ID TK-1999-0415 occurred in the Turkish province Düzce Merkez on the Düzce Fault on 1999-11-12 at 16:57:19 UTC. The Düzce fault segment, part of the North Anatolien Fault Zone (NAFZ), is located 40 km to the East of the 1999 Kocaeli earthquake rupture (*Birgören et al.*, 2004). This Düzce event, an aftershock of the Mw 7.3 earthquake, had a magnitude of Mw 7.0 at a depth of 10.4 km with an effective duration of 11.18 s followed by almost thousand aftershocks larger than Mw 2.3 during the next 5 month's time period (*Bayrak and Öztürk*, 2004). The faulting type was a strike-slip faulting with strike = 15.0, dip = 80.0 and rake = 16.0 (EMSC-CSEM-webservice). For more information about the rupture models see *Birgören et al.* (2004).

For the Düzce event several data sets from the National Strong Motion Network of Turkey (TR-NSMN) are available in the ESM database (http://esm.mi.ingv.it). 12 stations are within 100 km epicentral distance. For the following analysis the closest station AI_011_DZC (station code TK.8101) with an epicentral distance of only 5.3 km has been chosen. The station was equipped with an old Kinemetrics SMA-1 strong motion sensor sampled with 200 sps. The accelerations provided and displacements were already manually processed
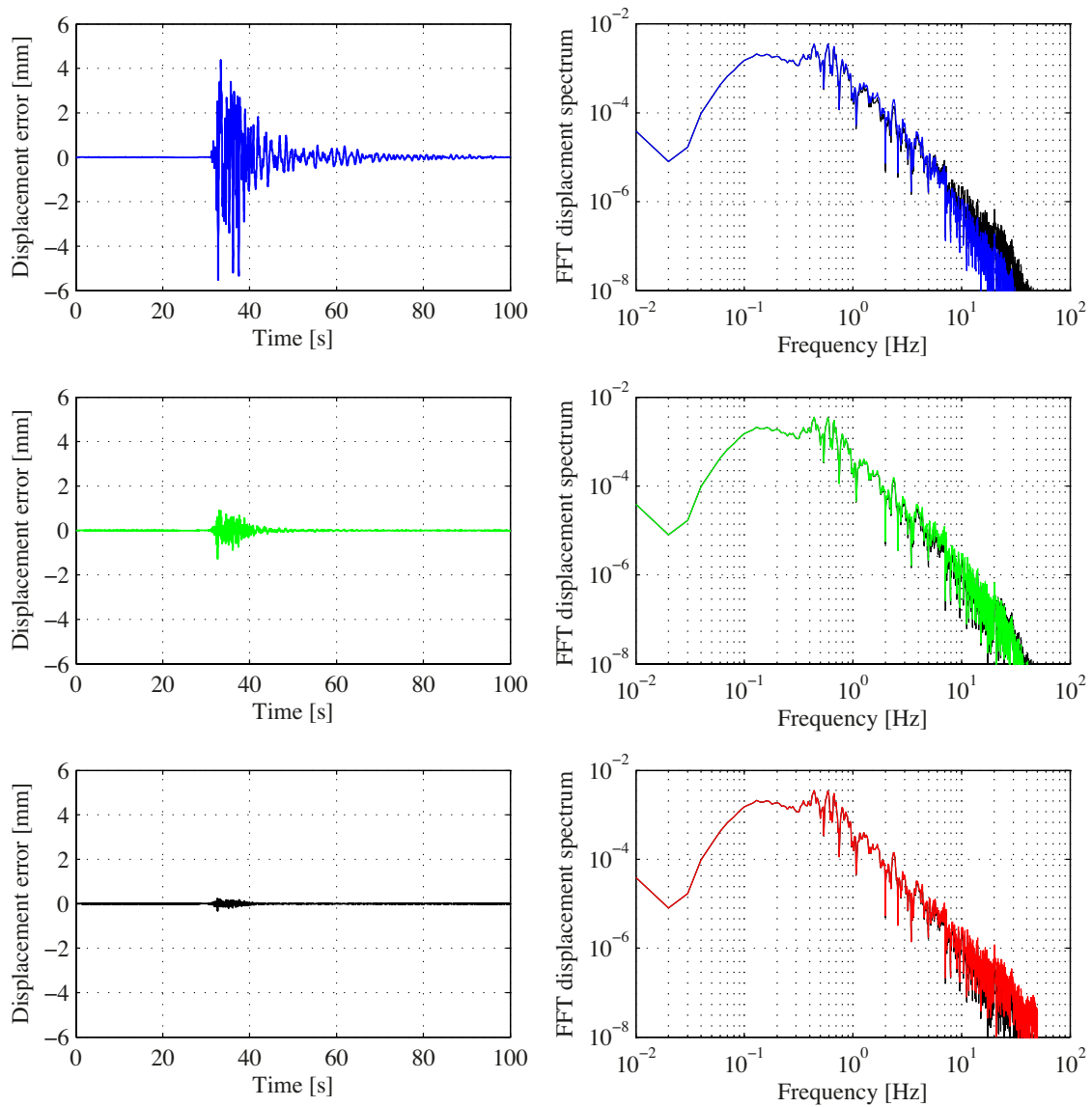
Figure 8.12: The displacement errors (left) and the spectrum comparisons (right) to the initial displacements (black) of the L'Aquila mainshock from Fig. 8.11 are calculated for three different GPS receiver PLL bandwidths B_L of 10 Hz (blue), 25 Hz (green) and 50 Hz (red). The displacement error is the difference between the initial ground motion and the receiver response simulation for all three cases.

including a filtering with a 2nd order Butterworth with a low-cut frequency of 0.07 Hz and a high-cut frequency of 40 Hz. The accelerations of the East, North and Up components are visible in Fig. 8.13 and the corresponding integrated displacements in Fig. 8.14. We show all three components in this analysis. The recorded accelerations include a remarkable PGA of 5.15 m/s^2 after 3.4 s. For the horizontal components the acceleration is almost identical between 0.2 Hz and 3 Hz, but even at higher frequencies still significantly large, especially for the vertical component, see the spectra in Fig. 8.13. At 10 Hz the accelerations are comparable to those of the L'Aquila earthquake. The largest displacements of
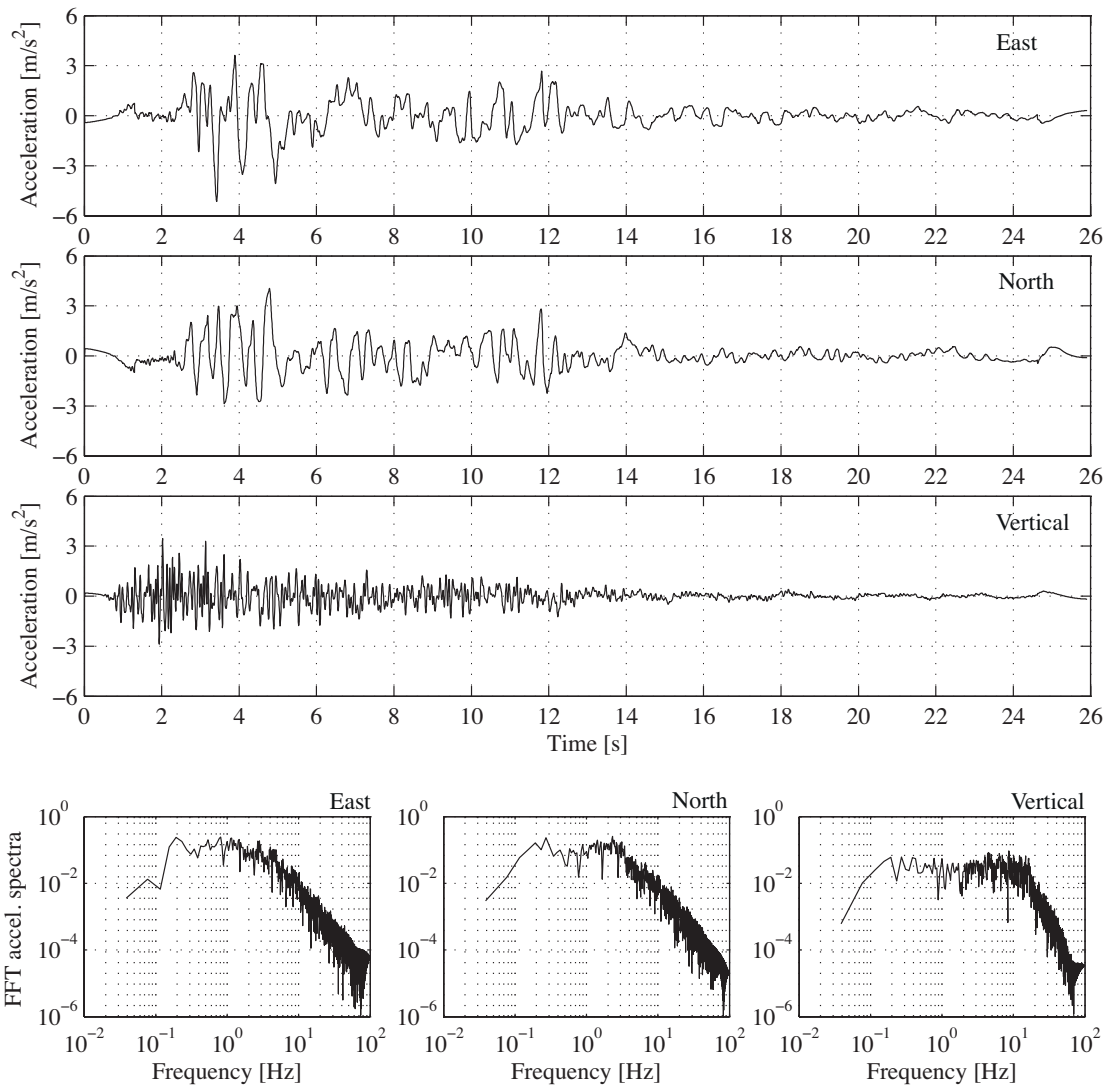
Figure 8.13: The processed accelerations of the 1999 Düzce Mw 7.0 aftershock for the East, North and Up components at station TK.8101 with an epicentral distance of only 5.3 km. The accelerations are large up to frequencies significantly above 1 Hz as visible in the spectra at the bottom.

up to more than 0.5 m have a period of several seconds (see Fig. 8.14). Compared to the displacement spectra of the L'Aquila mainshock (Fig. 8.11 right bottom) with lower magnitude but similar epicentral distance, the Düzce event has generated higher displacements at 1 Hz with similar motion magnitudes above 1 Hz. The receiver error in Fig. 8.15 (left) is calculated as the difference between the displacements (from Fig. 8.14) as the input and the simulated displacements according to Eq. (7.9). The transfer function from Eq. (7.8) with the parameters from Javad is used with three different PLL B_L of 10 Hz (blue), 25 Hz (green) and 50 Hz (red). Only the narrow bandwidth of 10 Hz (blue) shows a significant response with differences to the true input motion larger than 1 cm for the horizontal components. Similar to the L'Aquila event the motions slightly above 1 Hz are the dominant error source and are within the critical frequency range of the 10 Hz loop bandwidth (see
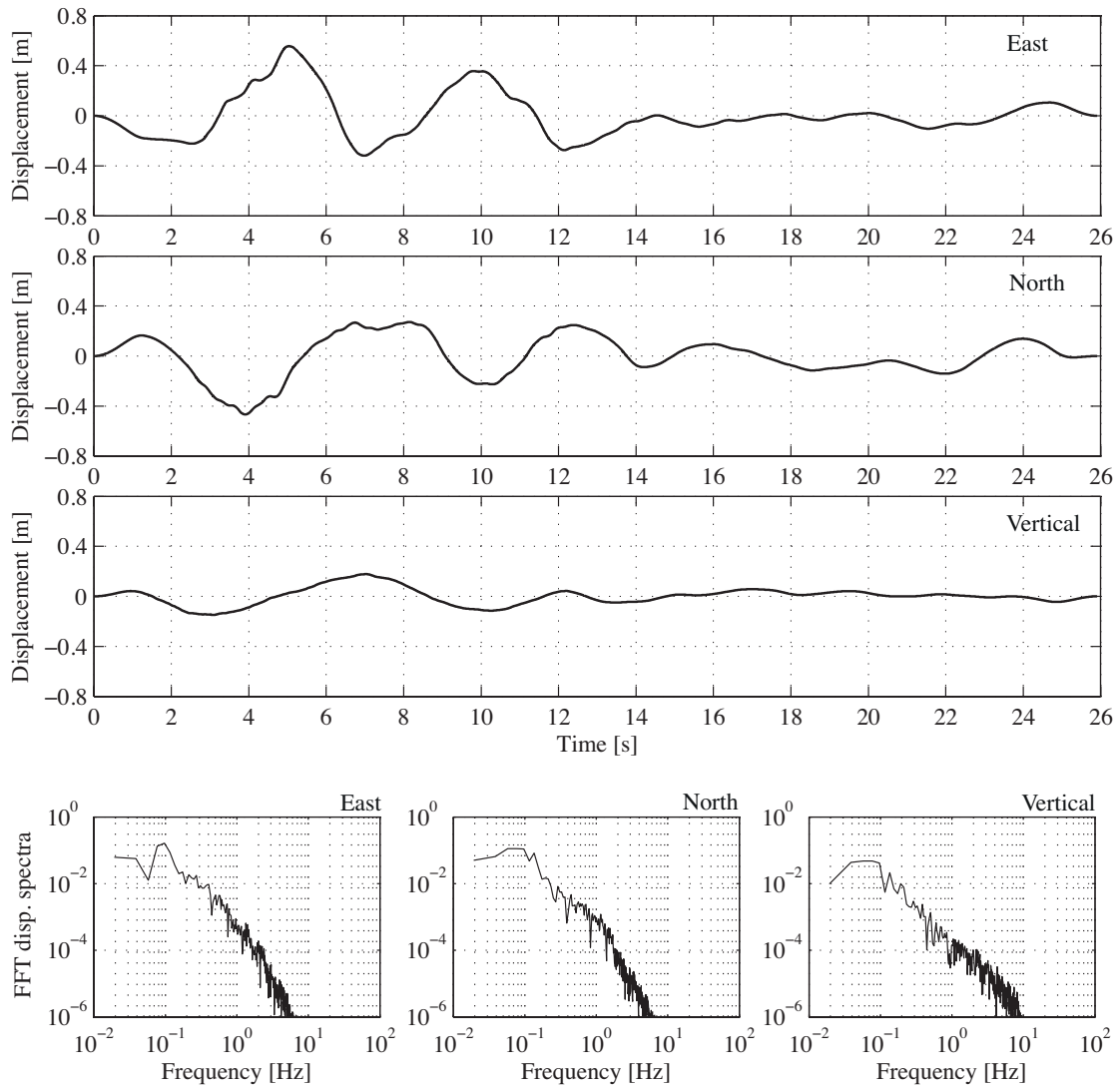
Figure 8.14: The processed displacements of the 1999 Düzce Mw 7.0 aftershock based on the recorded and processed accelerations of Fig. 8.13 at station TK.8101 very close to the epicenter. The displacements are still relatively large at 1 Hz for the East and North components.

also Fig. 7.9). In the frequency range between 3 Hz and 10 Hz with the largest amplitude and phase response of the 25 Hz B_L and above 5 Hz for the 50 Hz B_L, also visible in the comparison of the spectra in Fig. 8.15 (right), the appearing displacements are too small to generate significant displacement errors.
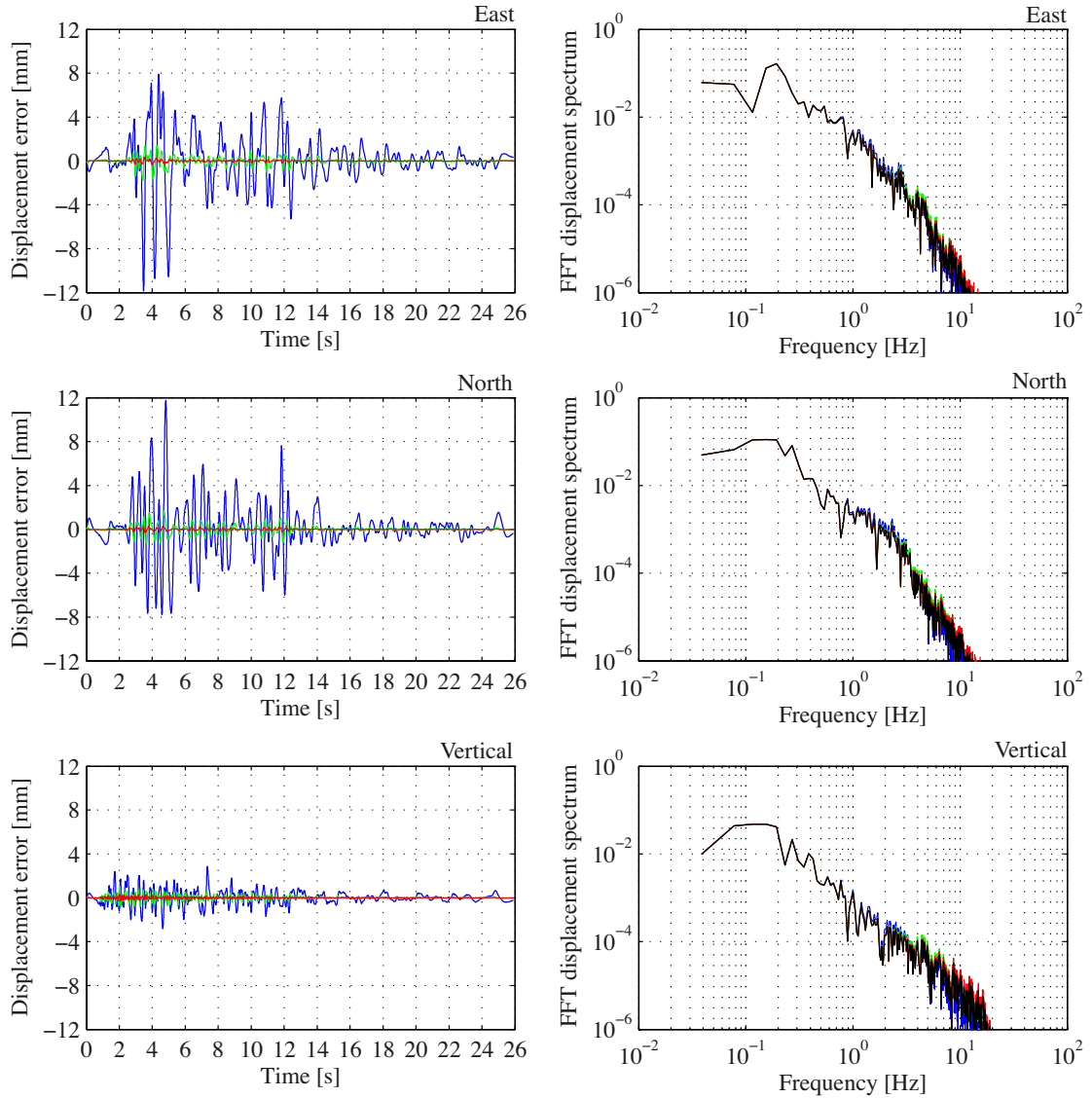
Figure 8.15: The displacement errors (left) and the spectrum comparison (right) to the initial displacements (black) from Fig. 8.14 are calculated for three different GPS receiver PLL bandwidths B_L of 10 Hz (blue), 25 Hz (green) and 50 Hz (red) for the East, North and Up components. Due to the higher displacements around 1 Hz than during the L'Aquila mainshock, the GNSS displacement error is about 2 times larger and greater than 1 cm for a narrow PLL B_L of 10 Hz.

8.2.3 2011 Tohoku-Oki Mw 9.0

On 2011-03-11 at 05:46:23 UTC a huge earthquake occurred on the Japan Trench megath-rust near the East coast of Honshu at a depth of 32 km. The mainshock of the event called Tohoku-Oki had an immense moment magnitude of Mw 9.0. Historically, a lot of events between Mw 7 and Mw 8 occurred at this megathrust, where the Pacific plate subducts below Japan with a speed of 8–8.5 cm/year (*Simons et al.*, 2011). The extreme perma-nent displacements over the NE part of Honshu, measured by a dense GNSS network (about 2000 stations nationwide) of the Geospatial Information Authority of Japan (GSI,
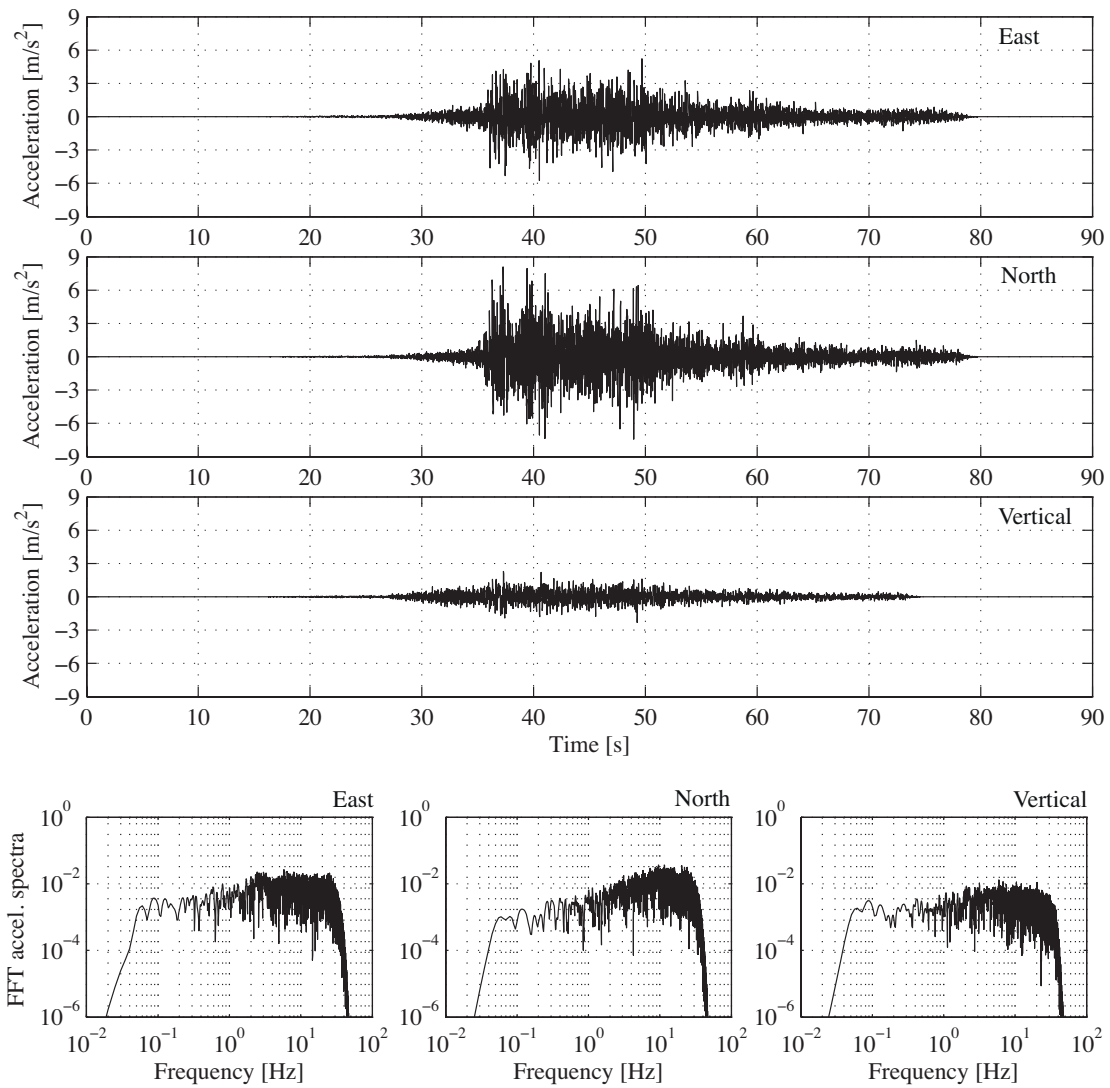
Figure 8.16: The processed accelerations of the 2011 Tohoku-Oki Mw 9.0 mainshock for the East, North and vertical components at station MYG011 with an epicentral distance of 75.7 km. The North component contains large high-frequent accelerations, but they are smaller in the lower frequency spectrum than in the other components.

www.gis.go.jp), reached up to 4.3 m in horizontal direction and a maximum settlement of 0.66 m. In addition to the GNSS network, two main national strong-motion seismograph networks exist in Japan, the K-NET (Kyoshin network) and the KiK-net (Kiban-Kyoshin network). The K-NET contains over 1000 stations distributed at each 20 km over Japan. It is operated by the National Research Institute for Earth Science and Disaster Prevention (NIED). Each station consists of a strong-motion seismograph on the ground surface. The approximately 700 nationwide stations of the KiK-net have a pair of seismographs on the ground surface as well as in a borehole combined with high-sensitivity seismometers (Hi-net). For the following analysis the station with the shortest epicentral distance has been chosen in order to guarantee large high-frequency displacements. The station MYG011 of the K-NET is ruptured 75.7 km from the epicenter of the 2011 Tokoku-Oki mainshock,
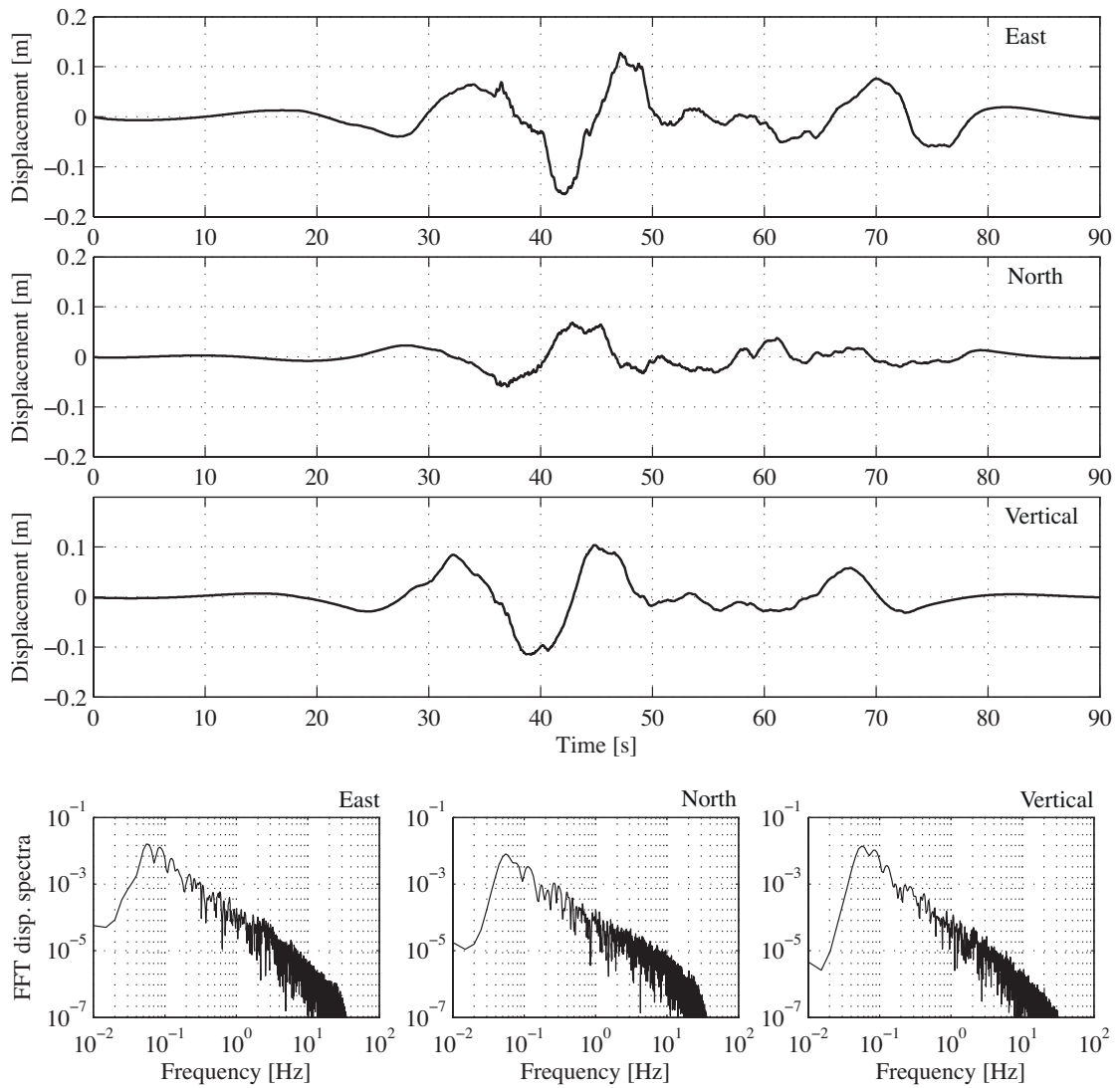
Figure 8.17: The processed displacements of the 2011 Tohoku-Oki Mw 9.0 mainshock (neglecting permanent coseismic displacement) based on the recorded and processed accelerations of Fig. 8.16 at station MYG011. The displacements at 1 Hz are similar to those of the L'Aquila mainshock and smaller than during the Düzce event, but the event duration is so different.

and 49.7 km from the subterranean fault. The East, North and vertical components of the accelerations recorded at MYG011 with 100 sps are band-pass filtered within 0.05 Hz and 48 Hz, visible in Fig. 8.16. This filtering additionally eliminates the permanent coseismic displacements. The North component shows the largest accelerations which are mainly distributed above 10 Hz. The East and vertical components consist of smaller PGA, but larger accelerations at lower frequencies (see spectra in Fig. 8.16). This is the reason of a smaller PGD in the North component compared to East and vertical as shown in Fig. 8.17. The peak displacements are about two times smaller than the Düzce record, but the shaking duration is much longer which indicates the much higher energy and, finally, higher moment magnitude. The displacements recorded at MYG011 are similarly distributed in the frequency range above 0.3 Hz as observed for the smaller L'Aquila event that was
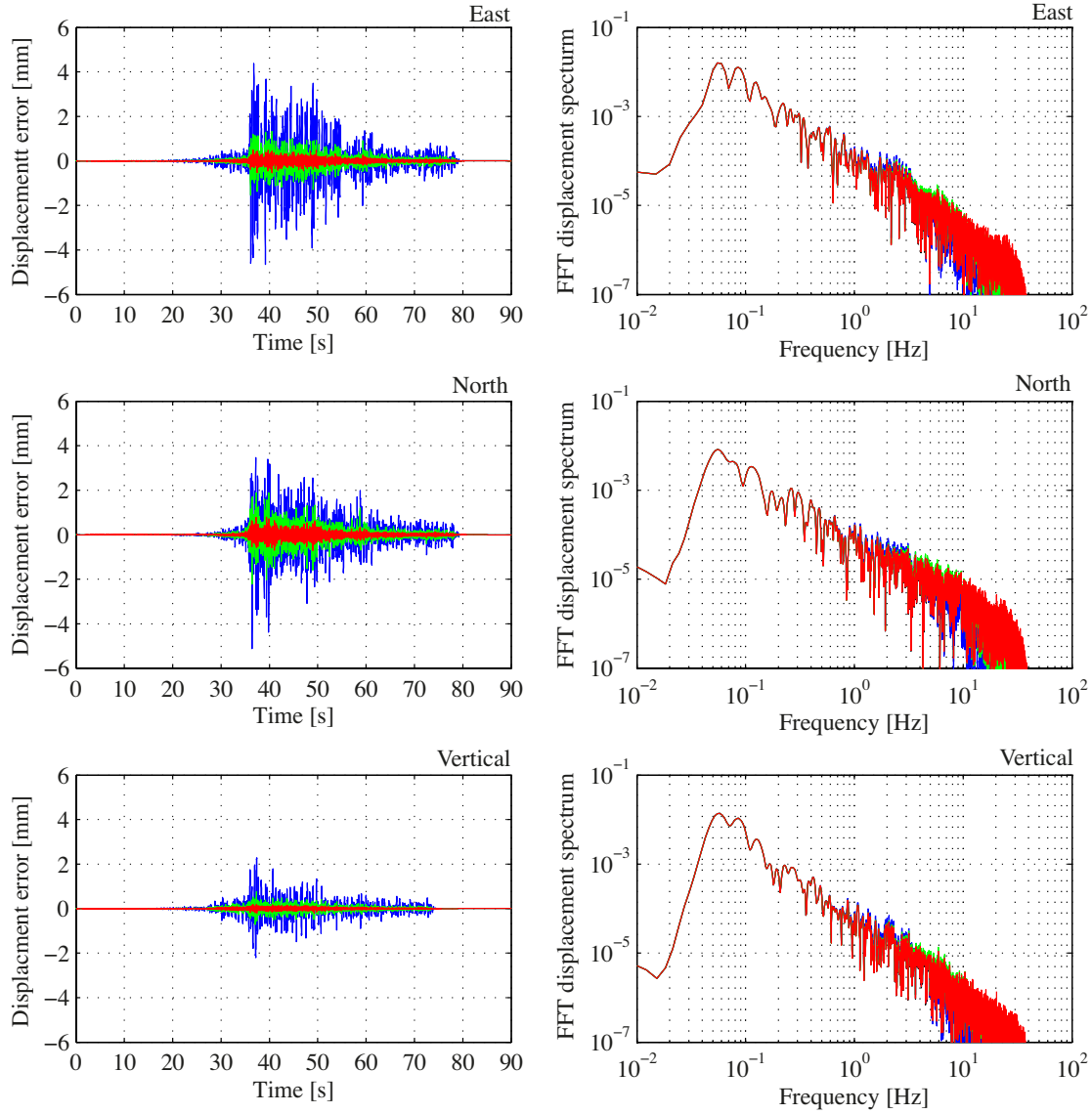
Figure 8.18: The displacement errors (left) and the spectrum comparisons (right) to the initial displacements (black) from Fig. 8.17 are calculated for three different GPS receiver PLL bandwidths B_L of 10 Hz (blue), 25 Hz (green) and 50 Hz (red) for the East, North and vertical components. The magnitude of the responses are similar to those measured during the L'Aquila event much closer to the epicenter.

recorded much closer to the epicenter. Therefore, the GNSS displacement error for both events is in the same order, compare Figs. 8.18 and 8.12.

Assuming the same L_c noise level obtained from the shake table experiments in Sec. 8.1.3, the GNSS receiver frequency response is not in all cases a limiting factor for the high-rate GNSS measurements of such seismic events. However, the analysis was only done with one PLL implementation and filter parameter set. A geodetic network generally consists of many different receiver types, each with its own response which potentially affects different frequency ranges.

8.3 Limitations and Contribution of High-Rate GNSS to Seismology

The high-rate GNSS receiver responses induced by high-frequency motions as shown in Sec. 7.2 made it necessary to demonstrate the impact on seismic events. The first part of this chapter was dedicated to the shake table experiments generating an expected earthquake for Switzerland with a moment magnitude of 5.0. It could be shown that the measurements, made by a 100 sps GNSS receiver based on a standard double-difference processing of the ionosphere-free linear combination, is able to retrieve the ground-motions between 0.1 and 2 Hz. However, displacements at 2 Hz of such a moderate earthquake are at the limit of the accuracy of the processed L_c coordinates, even very close to the epicenter. For all three receiver configurations (changed strong loop B_L), the L_c noise above 0.1 Hz, is about 3 mm that leads to a chosen 95% detection level of 6 mm. The noise level is for the most part independent from the loop bandwidth because on the one hand the analyzed frequency range does not only include thermal noise, but also external perturbations such as multipath and atmosphere below 1 Hz, which are not affected by the receiver frequency response. On the other hand the L_c thermal noise is mainly determined by the limited bandwidth of the weak P2/L2 signal, which was identical for all receiver configurations. Additionally, the measured noise level was not only independent of the loop bandwidth, but also of the baseline length (> 0 m). This is in good agreement with Fig. 5.28 that shows no significant differences between a baseline of 10 m and 110 km for the frequency spectrum above 0.1 Hz (even from 0.01 Hz). This is a very positive aspect for the GNSS network design for seismological purposes. A baseline of 100 km guarantees a sufficient separation of two receivers for differentially detecting the ground motions induced by an earthquake.

In addition to the noise level, the response of a GNSS receiver might be a limiting factor. However, due to the fact, that no high-frequency displacements can significantly be detected in case of the simulated M 5.0 earthquake, the displacement errors caused by the receiver response reach the significance level (95%) only with a narrow B_L of 10 Hz (almost 15 mm) mainly caused by the phase shift. But if the GNSS receiver response is known, it can be removed by applying an inverse filter. In general, high-frequency energy attenuates faster than low frequency. With an increased epicentral distance, the observed ground-motions are more and more shifted to lower frequencies and the displacement errors caused by the GNSS receiver response are strongly reduced for all applicable loop bandwidths. The receiver response analyses were expanded to real events with moment magnitudes of 6.3, 7.0 and 9.0. The largest displacement errors caused by the receiver response during the Düzce earthquake reach a similar level as shown for the moderate M 5.0 synthetic earthquake (using a narrow B_L of 10 Hz). These are good news that the receiver response of a GNSS receiver is not in all cases a critical issue concerning the measurements of earthquake-induced ground motions.

The measurements of the M 5.0 synthetic earthquake showed that high-rate GPS is able to retrieve signals up to 1 Hz and slightly above (see the spectra in Sec. 8.1.3). This requires a sampling rate higher than 1 sps, at least 10 sps to 20 sps for a sufficient oversampling. The contribution of GNSS measurements to seismology at these high frequencies is not concludingly checked. On the one hand the magnitudes of the displacements (at around

1 Hz) generated by an earthquake are close to the detection level of the GPS L_c coordinates with the legacy GPS signals. On the other hand the inversion algorithms do not include GNSS signals above 1 Hz nowadays. However, a high-rate GNSS receiver co-located with seismic instruments would assure the fidelity from DC to 100 Hz.

8.4 Additional Applications

The monitoring of infrastructure, such as buildings and bridges, are a very suitable field for high-rate GNSS. The movements are periodic oscillations for the most part and the main interest is often in accurately determined frequencies for risk and stability studies. The periodicity of the motions, e. g. self-oscillations, has the huge advantage that extremely small amplitudes can be detected by high-rate GNSS. It has been shown in Sec. 7 that the recorded frequency of an oscillation in the high-frequency spectrum perfectly corresponds to the true motion frequency.

In the following an example of a small pedestrian bridge is given, for which the resonance frequencies had to be determined. The responsible civil engineers wanted to know, if the final construction behaves as modeled. This bridge, called Auen bridge, was built over the Aare river between Rupperswil and Auenstein in the Canton Aargau and was opened in September 2010. The main resonance frequencies are close to the range where they could potentially be activated by pedestrians. For this purpose, measurements have to be performed regularly in order to assure that the characteristics did not change.

Figure 8.19: The Auen bridge over the Aare river (left). The pedestrian bridge is constructed as a suspension bridge with two longitudinal beams (right).

The high-rate GPS measurements were performed with two Javad Sigma-G3TAJ receivers with 100 sps, one connected to the GNSS antenna GrAnt-G3T mounted on the bridge and the second one as a reference with a baseline length of about 30 m. Due to this short baseline, only CA/L1 observations were processed. The receiver configuration was set to a 3rd order PLL with a B_L of 25 Hz. The processed 100 sps kinematic coordinates are visible in Fig.8.20 (blue) for one manual excitation of the bridge. The oscillations were recorded with additional measurement equipments, e. g. a theodolite-based imaging system, called QDaedalus (*Bürki et al.*, 2010). The measurements of two such systems are
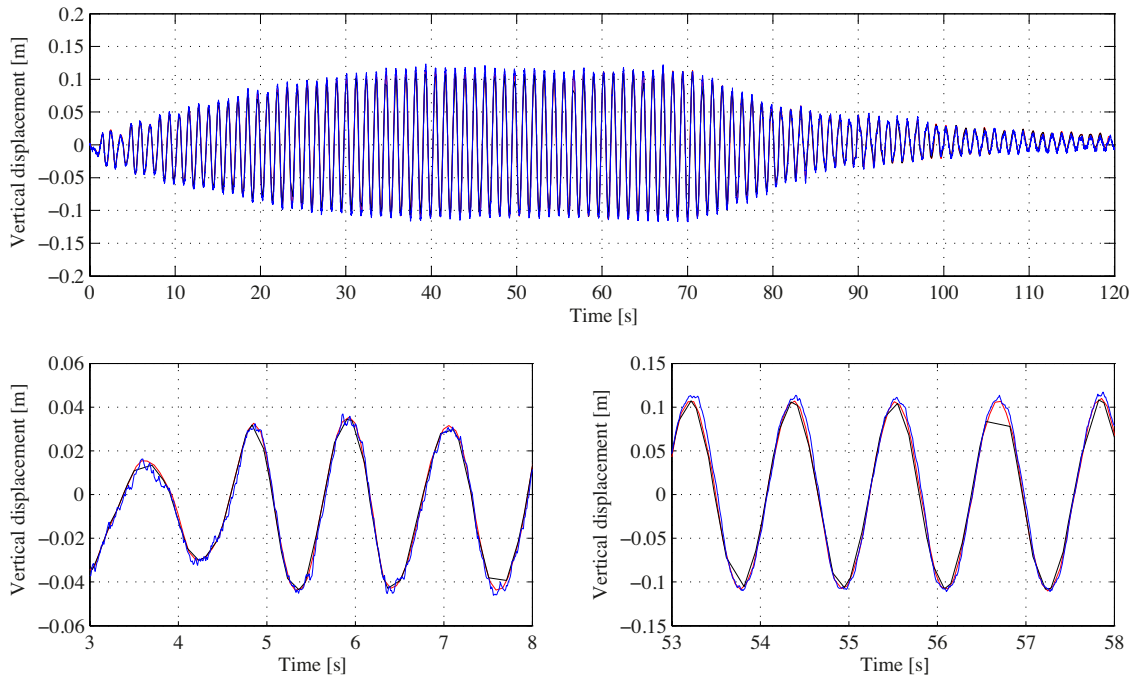
Figure 8.20: 100 sps GPS CA/L1 kinematic coordinates (blue) of the oscillating Auen bridge recorded by a Javad Sigma-G3TAJ receiver with a Javd GrAnt-G3T GNSS antenna mounted on the bridge. The GPS observations are compared with two Q-Daedalus theodolite-based imaging systems (black and red) with a lower and not always constant sampling-rate of 18 sps. For the main resonance frequency of 0.9 Hz the measurements of all systems are in very good agreement.

shown in Fig. 8.20 as red and black lines. The sampling-rate of the QDaedalus system was theoretically 18 sps, but not constant over the whole experiment period. However, the GNSS records perfectly match the vertical natural oscillation of 1st order (V1) derived from QDaedalus. The frequency of V1 is about 0.9 Hz (see Fig. 8.21 left) and no amplitude and phase response, causing displacement errors, are expected at this frequency for this receiver configuration. Due to the large number of oscillation cycles, extremely small amplitudes can be detected shown in Fig. 8.21 (right). All these frequencies can be assigned to one of the modeled vertical (V) or torsional (T) resonance frequencies in Tab. 8.2. In order to cover all the modeled frequencies, the bridge had to be differently excited. Finally, all resonance frequencies (excluding T6) could be derived from the 100 sps GPS records. For T5 two frequencies are close to the expected value, but could not definitively be allocated. The deviation for V1 is assessed by independent measurement techniques and measured in different years. The modeled value is confirmed to be slightly too high. The high-rate GPS records additionally allow the derivation of resonance frequencies up to 7 Hz, but no model is existing in order to allow an approval and an assignment of these high-order resonance frequencies. High-rate GNSS was the only technique which successfully detected the oscillation frequencies above 3 Hz, therefore no amplitude and phase comparison is possible. Looking at the frequency response in Figs. 7.9 and 7.10 for a Javad receiver operating with a B_L of 25 Hz (green), signals at 3 Hz as detected and shown in Fig. 8.21 are overestimated by about 20%.
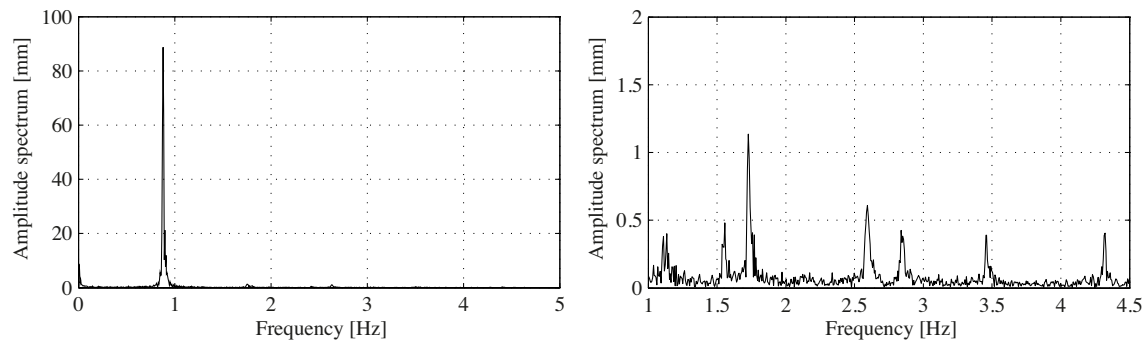
Figure 8.21: The amplitude spectra of the 100 sps GPS records of the oscillation shown in Fig. 8.20. The left spectrum shows the 1st order vertical resonance frequency. On the right a zoom into the spectrum showing resonance frequencies up to order 7, see also Tab. 8.2.

Table 8.2: The comparison between the modeled resonance frequencies by the responsible civil engineers and the frequencies retrieved from the 100 sps GPS data. V stands for vertical, T for torsion with the number of the corresponding order.

Resonance type	Model [Hz]	100 sps GPS [Hz]
V1	0.95	0.88
T1	1.11	1.12
V2	1.14	1.16
T2	1.50	1.55
V3	1.75	1.75
T3	2.11	2.17
V4	2.33	2.40
T4	2.68	2.61
V5	2.94	2.84
T5	3.31	3.34/3,46
V6	3.56	3.50
T6	3.86	-
V7	4.20	4.32
T7	4.47	4.43

9 Conclusions and Outlook

The main goal of this thesis was the thorough investigation and quantification of errors affecting high-rate GNSS observations in the frequency spectrum above 1 Hz, where the potential benefit of high-rate GNSS with sampling rates up to 100 sps is expected. Two main errors could be identified, 1) the carrier phase jitter induced by thermal noise and 2) the GNSS receiver frequency response due to highly dynamic motions. The magnitude of these errors and their distribution over the frequency spectrum are dependent on the received signal strength at baseband, on the characteristics of the observed signals, and on the design of the tracking loops with their parameters, such as filter coefficients and bandwidth.

One of the crucial indicators for the tracking quality is the received signal strength at baseband described by the carrier-to-noise density ratio C/N_0. This value additionally limits the applicable range of the baseband parameters, especially the bandwidth of the code and carrier tracking loops. The loop bandwidth in combination with C/N_0 determines the amount of the carrier phase jitter induced by thermal noise and the frequency range affected by the receiver response.

The encryption of modulated codes has been identified as a critical issue especially for the quality of GPS carrier observations beyond 1 Hz. Decryption algorithms lead to significantly lower C/N_0 and consequently higher carrier jitter, which is at least 2.5 times higher for encrypted signals like P2/L2 and P1/L1 than for non-encrypted signals. The consequences are significant with respect to GNSS networks mainly using the ionosphere-free linear combination. However, it is a positive aspect that from 0.01 Hz to 50 Hz no significant differences in the noise level between a 10 m and a 100 km baseline exist. Additionally, the modernization of the GNSS signal schemes has the potential to significantly reduce the noise level on linear combinations due to much more open service signals and would result in a better sensitivity to high-frequency signals. In general, a user has to pay attention to the selected tracking components of a specific carrier in the receiver. E. g. GPS L1 carrier tracking of the P1 component instead of C/A leads to totally different characteristics and quality.

The experimental setup with a single-axis shake table and a very well-known ground-truth allowed a precise determination of the receiver frequency response between 1 and 20 Hz. The detected relative amplitude errors can reach about 50% and the phase shifts increase up to 90 deg independent of the loop bandwidth. These large errors demonstrate that a GNSS receiver is not an "all can be done tool" and the errors can only be reduced by an inverse-filter with a known transfer function. For this purpose, in order to reduce the amount of work which is necessary for a calibration with a shake table, the users have to get access to the tracking loop parameters as in the case of Javad.

During the shake table experiments generating periodic signals with high dynamics a loss of lock or a strong non-linear behavior could not be observed. The linearity is a positive

aspect with respect to the applicability of inverse filters and for the error-free recovery of the frequency of a periodic signal. This is important for structural monitoring, where an accurate frequency detection is a primary goal. However, in this thesis only geodetic receivers of highest quality were used. It has to be tested, if low-cost receivers with typically lower oscillator quality reach an unstable tracking state during highly dynamic motions.

In addition to the shake table setup, the zero-baseline configuration allowed not only the determination of the carrier phase jitter, but also delivered insights into the tracking characteristics of a receiver. It was even possible to detect wrongly implemented baseband functions in the firmware. The methodologies and equipments used in this thesis for the investigation of the errors in the high-frequency spectrum would be strongly supported by a software receiver. The measurements in a specific configuration have only to be performed once because the IF samples can be stored and used for an extensive investigation and comparison of the influence of different receiver parameters.

The two main errors (carrier phase jitter and dynamic stress) investigated in this thesis are relevant for all applications using high-rate GNSS. For capturing seismic ground motions the carrier phase jitter is the dominant factor. The impact of the receiver response is small because the sensitivity of GNSS to ground motions in the near-field ends slightly beyond 1 Hz. Only extremely narrow bandwidths would produce significant displacement errors due to the receiver response. However, with the modernization of the GNSS signals and accordingly lowered carrier jitter the detectable range is potentially enlarged to signals with higher frequencies and would require a careful analysis of the dominance of the receiver response compared to the noise level. Additionally, a lot of GNSS networks include old receivers which are optimized for static applications using extremely narrow bandwidths. They are a potential risk with respect to the tracking stability and loss of lock.

Further applications, such as structural health monitoring, navigation, aero-gravimetry, machine guidance, sport applications, and ionospheric scintillation studies would profit from highly sampled GNSS observations. However, the ionospheric scintillations themselves are a potential error source in the high-frequency spectrum beyond 1 Hz, especially in regions with an extremely high ionosphere activity. Also applications under strong dynamics, such as rocket launches, could make use of the newest technologies of high-rate GNSS receivers in combination with an external guiding, e. g. by an INS. Future GNSS signals and improved satellite hardware (especially satellite clocks) could have an additional positive impact on the applicability of high-rate GNSS.

Bibliography

Ahmed, I. (2010), *Pipelined ADC Design and Enhancement Techniques*, Analog Circuits and Signal Processing, 200 pp., Springer Netherlands, ISBN 978-90-481-8652-5.

Alegre Pérez, J. P., B. C. López, and S. C. Pueyo (2011), *Automatic Gain Control: Techniques and Architectures for RF Receivers*, Analog Circuits and Signal Processing, 133 pp., Springer, ISBN 978-1-4614-0166-7.

Ameri, G., F. Gallovic, and F. Pacor (2012), Complexity of the Mw 6.3 2009 L'Aquila (central Italy) earthquake: 2. Broadband strong motion modeling, *Journal of Geophysical Research*, *117*(B4), doi:10.1029/2011JB008729.

Ashby, N. (2003), Relativity in the Global Positioning System, *Living Reviews in Relativity*, *6*(1), 42, doi:10.12942/lrr-2003-1.

Avallone, A., M. Marzario, A. Cirella, A. Piatanesi, A. Rovelli, C. Di Alessandro, E. D'Anastasio, N. D'Agostino, R. Giuliani, and M. Mattone (2011), 10 Hz GPS seismology for moderate magnitude earthquakes: the case of the Mw 6.3 L'Aquila (Central Italy) event, *Journal of Geophysical Research*, *116*, B02305, doi:10.1029/2010JB007834.

Barker, B. C., J. W. Betz, J. E. Clark, J. T. Correia, J. T. Gillis, S. Lazar, K. A. Rehborn, and J. R. Straton (2006), Overview of the GPS M code signal, *Unclassified Documentation Rev. 8-98*, MITRE Corporation, Bedford, MA.

Bayrak, Y., and S. Öztürk (2004), Spatial and temporal variations of the aftershocks sequences of the 1999 Izmit and Düzce earthquakes, *Earth, Planets and Space*, *56*, 933–944, doi:10.1186/BF03351791.

Best, R. E. (2003), *Phase-Locked Loops – Design, Simulation, and Applications*, 5th ed., 421 pp., McGraw-Hill, ISBN 0-07-141201-8.

Betz, J. W. (2001), Binary offset carrier modulations for radionavigation, *Navigation*, *48*(4), 227–246.

Bilich, A. L., J. F. Cassidy, and K. M. Larson (2008), GPS seismology: application to the 2002 Mw 7.9 Denali fault earthquake, *Bulletin of the Seismological Society of America*, *98*(2), 593–606, doi:10.1785/0120070096.

Birgören, G., H. Sekiguchi, and K. Irikura (2004), Rupture model of the 1999 Düzce, Turkey, earthquake deduced from high and low frequency strong motion data, *Geophysical Research Letters*, *31*, doi:10.1029/2003GL019194.

Bock, Y., L. Prawirodirdjo, and T. I. Melbourne (2004), Detection of arbitrarily large dynamic ground motions with a dense high-rate GPS network, *Geophysical Research Letters*, *31*, L06604, doi:10.1029/2003GL019150.

Böhm, J., A. E. Niell, P. Tregoning, and H. Schuh (2006), Global Mapping Function (GMF): A new empirical mapping function based on numerical weather model data, *Geophysical Research Letters*, *33*, L07304,, doi:10.1029/2005GL025546.

Bürki, B., S. Guillaume, P. Sorber, and H.-P. Oesch (2010), DAEDALUS - A versatile usable digital clip-on measuring system for Total Stations, in *Proceedings of the 2010 International Conference on Indoor Positioning and Indoor Navigation (IPIN 2010)*, edited by R. Mautz, H. Ingensand, and M. Kunz, IEEE, Zurich, Switzerland.

Chiou, T.-Y. (2005), GPS receiver performance using inertial-aided carrier tracking loop, in *Proceedings of the 18th International Technical Meeting of the Satellite Division*, pp. 2895–2910, Long Beach, CA.

Clinton, J. F. (2004), Modern digital seismology: instrumentation, and small amplitude studies in the engineering world, Ph.D. thesis, California Institute of Technology, Pasadena, CA.

Clinton, J. F., K. M. Larson, and A. Bilich (2007), High-rate GPS data - when are they useful?, *Eos Transactions AGU*, *88*(52), Fall Meet. Suppl., Abstract G13B-1235.

Conley, R., R. Cosentino, C. J. Hegarty, E. D. Kaplan, L. Leva, M. Uijt de Haag, and K. Van Dyke (2006), Performance of Stand-Alone GPS, in *Understanding GPS: Principles and Applications*, edited by E. D. Kaplan and C. J. Hegarty, 2nd ed., chap. 7, pp. 301–378, Artech House, Norwood, MA, ISBN 978-1-58053-894-7.

Couch II, L. W. (2013), *Digital and analog communication systems*, 8th ed., 784 pp., Pearson Education Limited, Harlow, England, ISBN 978-0-273-77421-1.

Dach, R., U. Hugentobler, P. Fridez, and M. Meindl (2007), *Bernese GPS Software Version 5.0*, Astronomical Institute, University of Berne, Switzerland.

Elósegui, P., J. L. Davis, D. Oberlander, R. Baena, and G. Ekström (2006), Accuracy of high-rate GPS for seismology, *Geophysical Research Letters*, *33*, L11308, doi: 10.1029/2006GL026065.

Emore, G. L., J. S. Haase, K. Choi, K. M. Larson, and A. Yamagiwa (2007), Recovering seismic displacements through combined use of 1-Hz GPS and strong-motion accelerometers, *Bulletin of the Seismological Society of America*, *97*(2), 357–378, doi: 10.1785/0120060153.

Encinas, J. B. (1993), *Phase Locked Loops*, no. 6 in Microwave Technology Series, 1st ed., 193 pp., Chapman & Hall, ISBN 978-1-4613-6337-8.

Fäh, D., J. R. Moore, J. Burjanek, I. Iosifescu, L. A. Dalguer, F. Dupray, C. Michel, J. Woessner, A. Villiger, J. Laue, I. Marschall, V. Gischig, S. Loew, S. Alvarez, W. Balderer, P. Kästli, D. Giardini, C. Iosifescu, L. Hurni, P. Lestuzzi, A. Karbassi, C. Baumann, A. Geiger, A. Ferrari, L. Lalou, J. F. Clinton, and N. Deichmann (2012), Coupled seismogenic geohazards in alpine regions, *Bolletino di Geofisica Teorica ed Applicata*, *53*(4), 485–508, doi:10.4430/bgta0048.

Feairheller, S., and R. Clark (2006), The Russian GLONASS System, in *Understanding GPS: Principles and applications*, edited by E. D. Kaplan and C. J. Hegarty, 2nd ed., chap. 11.1, pp. 595–615, Artech House, Norwood, MA, ISBN 978-1-58053-894-7.

Floc'H, J., and J. J. Soellner (2007), Comparison between BOC, CBOC and TMBOC tracking, in *Proceedings of the 2007 Technical Meeting of The Insitute of Navigation*, pp. 964–973, San Diego, CA.

Friis, H. T. (1944), Noise figures in radio receivers, in *Proceedings of the IRE*, vol. 32, pp. 419–422, IEEE, doi:10.1109/JRPROC.1944.232049.

Fuchser, T. D. (1976), Oscillator stability for carrier phase lock, *Internal Memorandum G(S)-60233*, Texas Instruments Incorporated.

Gallovic, F., and J. Zahradnik (2012), Complexity of the Mw 6.3 2009 L'Aquila (central Italy) earthquake: 1. Multiple finite-extent source inversion, *Journal of Geophysical Research*, *117*(B4), doi:10.1029/2011JB008709.

Gardner, F. M. (2005), *Phaselock Techniques*, 3rd ed., 450 pp., John Wiley & Sons, Inc., ISBN 978-0-471-43063-6.

Giardini, D., S. Wemer, D. Fäh, and N. Deichmann (2004), *Seismic Hazard Assessment of Switzerland, 2004*, vol. 1.1, 95 pp., Swiss Seismological Service.

GLONASS ICD (2008), *Global Navigation Satellite System (GLONASS) Interface Control Document, Navigation Signals in Bands L1, L2*, 5.1 ed., Russian Institute of Space Device Engineering.

Gold, R. (1967), Optimal binary sequences for spread spectrum multiplexing, *IEEE Transactions on Information Theory*, *33*(3), 619–621.

Häberling, S. (2009), GPS als Rotationssensor - Bestimmung von 3D-Antennenrotationen mittels Phase Wind-up, Master thesis, ETH Zurich, Zurich, Switzerland.

Häberling, S., M. Rothacher, Y. Zhang, J. F. Clinton, and A. Geiger (2015), Assessment of high-rate GPS using a single-axis shake table, *Journal of Geodesy*, *89*(7), 697–709, doi:10.1007/s00190-015-0808-2.

HBM (2012a), WA inductive standard displacement transducers, *Data Sheet B0553-8.5 en*, HBM GmbH, Darmstadt, Germany.

HBM (2012b), PC measurement electronics Spider8, *Operating Manual B0405-7.0 en*, HBM GmbH, Darmstadt, Germany.

Hegarty, C. J., E. Powers, and B. Fonville (2004), Accounting for timing biases between GPS, modernized GPS, and Galileo signals, in *Proceedings of 36th Annual Precise Time and Time Interval (PTTI) Meeting*, pp. 307–318, Washington, DC.

Hekmat, T., N. Nilass, and M. Maurer (1995), Integrated GPS/GLONASS antenna for high performance applications, in *Proceedings of the 8th International Technical Meeting of the Satellite Division of The Institute of Navigation (ION GPS 1995)*, pp. 845–851, Palm Springs, CA.

Hofmann-Wellenhof, B., H. Lichtenegger, and E. Wasle (2008), *GNSS - Global Navigation Satellite Systems, GPS, GLONASS, Galileo, and more*, 516 pp., Springer-Verlag, Wien, Austria, ISBN 978-3-211-73012-6.

Houlié, N., D. Dreger, and A. Kim (2014), GPS source solution of the 2004 Parkfield earthquake, *Scientific Reports*, *4*, 3646, doi:10.1038/srep03646.

Huber+Suhner (2014), BNC-Resistive Power Divider - Type 4901.01.A, *Product Catalogue 2014/12*, Huber+Suhner AG, Herisau, Switzerland.

Humphreys, T. E., M. L. Psiaki, and P. M. Kintner (2005), GPS carrier tracking loop performance in the presence of ionospheric scintillations, in *Proceedings of the 2005 ION GNSS Conference*, Long Beach, CA.

Hung, H.-K., and R. Ruey-Juin (2013), Surface waves of the 2011 Tohoku earthquake: observations of Taiwan´s dense high-rate GPS network, *Journal of Geophysical Research*, *118*, 332–345, doi:10.1029/2012JB009689.

Hung, P. V., D. N. Chien, and N. V. Khang (2014), A method of side-peak mitigation for binary offset carrier modulated GNSS signals applied in GNSS receivers, *American Journal of Networks and Communications*, *3*(3), 39–48, doi:10.11648/j.ajnc.20140303.12.

IERS (2010), IERS Conventions (2010), *IERS Technical Note 36*, IERS Convention Centre, Frankfurt a. M., Germany.

IGS (2013), Rinex - the receiver independent exchange format, *Format Definition 3.02*, International GNSS Service (IGS), RINEX Working Group and RTCM-SC104.

Imperatori, W., and P. M. Mai (2013), Broad-band near-field ground motion simulations in 3-dimensional scattering media, *Geophysical Journal International*, *192*, 725–744, doi: 10.1093/gji/ggs041.

IS-GPS-200G (2012), *Navstar GPS space segment/navigation user interface, IS-GPS-200G*, 207 pp., Global Positioning Systems Directorate.

IS-GPS-705B (2012), *Navstar GPS space segment/user segment L5 interface*, 90 pp., Global Positioning Systems Directorate.

IS-GPS-800C (2012), *Navstar GPS space segment/user segment L1C interface*, 119 pp., Global Positioning Systems Directorate.

Javad (2013), Javad Sigma-G3TAJ, *Data Sheet 2.4*, Javad GNSS, San Jose, CA.

Javad (2014), Javad GrAnt, *Data Sheet 2.6*, Javad GNSS, San Jose, CA.

Ji, C., K. M. Larson, Y. Tan, K. W. Hudnut, and K. Choi (2004), Slip history of the 2003 San Simeon earthquake constrained by combining 1-Hz GPS, strong motion, and teleseismic data, *Geophysical Research Letters*, *31*, L17608, doi:10.1029/2004GL020448.

Johnson, J. B. (1928), Thermal agitation of electricity in conductors, *Physical Review*, *32*, 97–109, doi:http://dx.doi.org/10.1103/PhysRev.32.97.

Karras, T. J. (1965), Equivalent noise bandwidth analysis form transfer functions, *NASA Technical Note D–2842*, National Aeronautics and Space Administration (NASA), Washington, DC.

Kinemetrics (2005), EpiSensor ES-T - Force Balance Accelerometer, *User Guide, Document 301900, Revision D*, Kinemetrics Inc, Pasadena, CA.

Klepczynski, W., and P. Ward (2000), Freuquency stability requirements for narrow band receivers, in *Proceedings of the 32nd Annual Time and Time Interval (PTTI) Meeting*, Klepczynski, W. and Ward, P., pp. 415–422, Reston, VA.

Kouba, J. (2003), Measuring seismic waves induced by large earthquakes with GPS, *Studia Geophysica et Geodaetica*, *47*(4), 741–755, doi:10.1023/A:1026390618355.

Kouba, J. (2004), Improved relativistic transformations in GPS, *GPS Solutions*, *8*(3), 170–180, doi:10.1007/s10291-004-0102-x.

Kouba, J. (2005), A possible detection of the 26 December 2004 great Sumatra-Andaman Islands earthquake with solution products of the International GNSS service, *Studia Geophysica et Geodaetica*, *49*(4), 463–483, doi:10.1007/s11200-005-0022-4.

Kraus, J. D. (1988), *Antennas*, 2nd ed., 892 pp., McGraw-Hill.

Kreemer, C., G. Blewitt, and F. Maerten (2006), Co- and postseismic deformation of the 28 March 2005 Nias Mw 8.7 earthquake from continuous GPS data, *Geophysical Research Letters*, *33*, L07307, doi:10.1029/2005GL025566.

Kunysz, W. (2003), A three dimensional choke ring ground plane antenna, in *Proceedings of the 16th International Technical Meeting of the Satellite Division of The Institute of Navigation (ION GPS/GNSS 2003)*, pp. 1883–1888, Portland, OR.

Langbein, J., and Y. Bock (2004), High-rate real-time GPS network at Parkfield: utility for detecting fault slip and seismic displacements, *Geophysical Research Letters*, *31*, L15S20, doi:10.1029/2003GL019408.

Langbein, J., J. R. Murray, and H. A. Snyder (2006), Coseismic and initial postseismic deformation from the 2004 Parkfield, California, earthquake, observed by Global Positioning System, electronic distance meter, creepmeters, and borehole strainmeters, *Bulletin of the Seismological Society of America*, *96*(4B), S304–S320, doi:10.1785/0120050823.

Larson, K. M., and S. Miyazaki (2008), Resolving static offsets from high-rate GPS data: the 2003 Tokachi-Oki earthquake, *Earth Planets Space*, *60*(8), 801–808.

Larson, K. M., P. Bodin, and J. Gomberg (2003), Using 1-Hz GPS data to measure deformations caused by the Denali fault earthquake, *Science*, *300*(5624), 1421–1424, doi:10.1126/science.1084531.

Leica (2008), Leica GPS1200+ Series - High Performance GNSS Systems, *Technical Specifications 738812en-XII.08-RDV*, Leica Geosystems AG, Heerbrugg, Switzerland.

Meindl, M. (2011), *Combined Analysis of Observations from Different Global Navigation Satellite Systems*, *Geodätisch-geophysikalische Arbeiten in der Schweiz*, vol. 83, Schweizerische Geodätische Kommission, ISBN 978-3-908440-27-7.

Mirgorodskaya, T. (2013), GLONASS Government Policy, Status and Modernization Plans, in *IGNSS 2013*, Gold Coast, Australia.

Miyazaki, S., K. M. Larson, K. Choi, K. Hikima, K. Koketsu, P. Bodin, J. Haase, G. Emore, and A. Yamagiwa (2004), Modeling the rupture process of the 2003 September 25 Tokachi-Oki (Hokkaido) earthquake using 1-Hz GPS data, *Geophysical Research Letters*, *31*, L21603, doi:10.1029/2004GL021457.

Montenbruck, O., A. Hauschild, S. Häberling, B. Braun, G. Katsigianni, and U. Hugentobler (2015), High-rate clock variations of the Galileo IOV-1/2 satellites and their impact on carrier tracking by geodetic receivers, *GPS Solutions*, pp. 1–10, doi:10.1007/s10291-015-0503-z.

Moschas, F., and S. Stiros (2014), PLL bandwidth and noise in 100 Hz GPS measurements, *GPS Solutions*, *19*, 173–185.

Munekane, H. (2012), Coseismic and early postseismic slips associated with the 2011 off the Pacific coast of Tohoku Earthquake sequence: EOF analysis of GPS kinematic time series, *Earth Planets Space*, *64*(12), 1077–1091.

Nanometrics (2012), Taurus - Portable Seismograph, *User Guide 3.5*, Nanometrics Inc, Kanata, Canada.

Nikolaidis, R. M., Y. Bock, P. J. de Jonge, P. Shearer, D. C. Agnew, and M. Van Domselaar (2001), Seismic wave observations with the Global Positioning System, *Journal of Geophysical Research*, *106*(B10), 21,897–21,916.

Nyquist, H. (1928), Thermal agitation of electric charge in conductors, *Physical Review*, *32*, 110–113, doi:http://dx.doi.org/10.1103/PhysRev.32.110.

OD SIS ICD Galileo (2010), *European GNSS (Galileo) Open Service Signal in Space Interface Control Document*, 1.1 ed., 196 pp., European Union.

Ohta, Y., I. Meiano, T. Sagiya, F. Kimata, and K. Hirahara (2006), Large surface wave of the 2004 Sumatra-Andaman earthquake captured by the very long baseline kinematic analysis of 1-Hz GPS data, *Earth Planets Space*, *58*(2), 153–157.

Olsen, K., S. M. Day, L. A. Dalguer, J. Mayhew, Y. Cui, J. Zhu, V. M. Cruz-Atienza, D. Roten, P. Maechling, T. H. Jordan, D. Okaya, and A. Chourasia (2009), ShakeOut-D: Ground motion estimates using an ensemble of large earthquakes on the southern San Andreas fault with spontaneous rupture propagation, *Geophysical Research Letters*, *36*, L04303, doi:10.1029/2008GL036832.

Petrie, E. J., M. Hernandez-Pajaras, P. Spalla, P. Moore, and M. A. King (2011), A Review of Higher Order Ionospheric Refraction Effects on Dual Frequency GPS, *Surveys of Geophysics*, *32*(3), 197–253, doi:10.1007/s10712-010-9105-z.

Pratt, A. R. (1989), g-Effects on Oscillator performance in GPS receivers, *Navigation*, *36*(1), 63–75.

Psimoulis, P., M. Meindl, N. Houlié, and M. Rothacher (2015), Consistency of GPS and strong-motion records: case study Mw9.0 Tohoku-Oki 2011 earthquake, *Smart Structures and Systems*, *16*(2).

Quanser (2008), Position control and earthquake analysis, *Quanser Shake Table II User Manual 632, Revision 3.50*, Quanser Inc, Markham, Canada.

Rebeyrol, E., C. Macabiau, L. Lestarquit, L. Ries, J.-L. Issler, M.-L. Boucheret, and M. Bousquet (2005), BOC power spectrum densities, in *Proceedings of the 2005 National Technical Meeting of The Institute of Navigation*, pp. 769–778, San Diega, CA.

Rothacher, M., and G. Mader (2003), Receiver and satellite antenna phase center offsets and variations, in *Proceedings of the Network, Data, and Analysis Centre Workshop 2002*, edited by Thétreault et al., pp. 141–152, IGS Central Bureau, Pasadena, CA.

Rothacher, M., W. Gurtner, S. Schaer, R. Weber, S. Schlüter, and H. O. Hase (1996), Azimuth- and Elevation-Dependent Phase Center Corrections for Geodetic GPS Antennas Estimated from GPS Calibration Campaigns, in *GPS Trends in Precise Terrestrial, Airborne, and Spaceborne Applications, International Association of Geodesy Symposia, Boulder, CO*, vol. 115, chap. 5, pp. 338–338, Springer-Verlag, ISBN 978-3-540-60872-1.

Rushanan, J. J. (2006), Weil sequences: A family of binary sequences with good correlation properties, in *Proceedings of International Symposium on Information Theory*, pp. 1948–1652, IEEE, Seattle, WA, doi:10.1109/ISIT.2006.261556.

Salem, D. R. (2010), Approaches for the combined tracking of GPS L1/L5 signals, Ph.D. thesis, University of Calgary, Calgary, Canada.

Schaer, S. (1999), *Mapping and Predicting the Earth's Ionosphere Using the Global Positioning System, Geodätisch-geophysikalische Arbeiten in der Schweiz*, vol. 59, Schweizerische Geodätische Kommission, ISBN 3-908440-01-7.

Schmid, R., and M. Rothacher (2003), Estimation of elevation-dependent satellite antenna phase center variations, *Journal of Geodesy*, *77*(7–8), 440–448, doi:10.1007/s00190-003-0339-0.

Shi, C., Y. Lou, H. Zhang, Y. Zhao, J. Geng, R. Wang, R. Fang, and J. Liu (2010), Seismic deformation of the M 8.0 Wenchuan earthquake from high-rate GPS observations, *Advances in Space Research*, *46*, 228–235.

Shivaramaiah, N. C., and A. G. Dempster (2009), The Galileo E5 AltBOC: Understanding the signal structure, in *Proceedings of the IGNSS Symposium 2009*, Gold Coast, Australia.

Simons, M., S. E. Minson, A. Sladen, F. Ortega, J. Jiang, S. E. Owen, L. Meng, J.-P. Ampuero, S. Wei, R. Chu, D. V. Heimberger, H. Kanamori, E. Hetland, A. W. Moore, and F. H. Webb (2011), The 2011 Magnitude 9.0 Tohoku-Oki Earthquake: Mosaicking the Megathrust from Seconds to Centuries, *Science*, *332*(6036), 1421–1425, doi:10.1126/science.1206731.

Sousa, F. M. G., and F. D. Nunes (2013), New expressions for the auocorrelation function of BOC GNSS signals, *Navigation*, *60*(1), 1–9, doi:10.1002/navi.30.

Spilker, J. J. (1980), GPS signal structure and performance characteristics, in *Navigation*, vol. 1, edited by P. M. Janiczek, pp. 29–54, The Institute of Navigation, Washington, DC, ISBN 0-936406-00-3.

Spilker, J. J. (1996), GPS Signal Structure and Theoretical Performance, in *Global Positioning System: Theory and Applications*, vol. 1, edited by B. W. Parkinson and J. J. Spilker, chap. 3, pp. 57–119, American Institute of Aeronautics and Astronautics, ISBN 156347106X.

Stansell, T. A., K. W. Hudnut, and R. G. Keegan (2011), Future wave - L1C signal performance and receiver design, *GPS World, April 2011*, 30–41.

Stensby, J. L. (1997), *Phase-Locked Loops - Theory and Applications*, 382 pp., CRC Press, Boca Raton, FL, ISBN 0-8493-9471-6.

Tausworthe, R. C. (1971), A Second/Third-Order Hybrid Phase-Locked Receiver for Tracking Doppler Rates, *Technical Report 32–1526 Vol. 1*, JPL, Telecommunications Division.

Ugazio, S., M. Fantino, and L. Lo Presti (2011), Design of second and third order PLLs with adaptive bandwidth in real time, in *Proceedings of the 2011 International Technical Meeting of The Institute of Navigation*, pp. 1281–1292, San Diegao, CA.

Van Dierendonck, A. J. (1996), GPS Receivers, in *Global Positioning System: Theory and Applications*, vol. 1, edited by B. W. Parkinson and J. J. Spilker, chap. 8, pp. 329–407, American Institute of Aeronautics and Astronautics, ISBN 156347106X.

Van Dierendonck, A. J., S. S. Russell, K. E. Kopitzke, and M. Birnbaum (1980), The GPS navigation message, in *Navigation*, vol. 1, edited by P. M. Janiczek, pp. 55–73, Institute of Navigation, Washington, DC, ISBN 0-936406-00-3.

Van Dierendonck, A. J., P. Fenton, and T. Ford (1992), Theory and performance of narrow correlator spacing in a GPS receiver, *Navigation, 39*(3), 265–283.

Villiger, A. (2014), Dense GNSS network for small scale tectonic analysis in the Canton of Valais, in *Imvrovement of the Kinematic Model of Switzerland (Swiss 4D II), Geodätisch-geophysikalische Arbeiten in der Schweiz*, vol. 90, chap. 7, pp. 101–108, Schweizerische Geodätische Kommission, ISBN 978-3-908440-36-9.

Wang, G., F. Blume, C. Meertens, P. Ibanez, and M. Schulze (2012), Performance of high-rate kinematic GPS during strong shaking: observations from shake table tests and the 2010 Chile earthquake, *Geodetic Science, 2*(1), 15–30, doi:10.2478/v10156-011-0020-0.

Wang, G.-Q., D. M. Boore, G. Tang, and X.-Y. Zhou (2007), Comparisons of ground motions from colocated and closely spaced one-sample-per-second Global Positioning System and accelerograph recordings of the 2003 M 6.5 San Simeon, California, earthquake in the Parkfield region, *Bulletin of the Seismological Society of America, 97*(1B), 76–98, doi:10.1785/0120060053.

Ward, P., J. W. Betz, and C. J. Hegarty (2006), Satellite Signal Acquisition, Tracking, and Data Modulation, in *Understanding GPS: Principles and Applications*, edited by E. D. Kaplan and C. J. Hegarty, 2nd ed., chap. 4, pp. 153–241, Artech House, Norwood, MA, ISBN 978-1-58053-894-7.

Whitlow, D. (2003), Design and operation of automatic gain control loops for receivers in modern communications systems, *Microwave Journal*, *46*(5).

Woo, K. T. (2000), Optimum semi-codeless carrier phase tracking of L2, *Navigation*, *47*(2), 82–99.

Wu, J. T., C. Wu, G. A. Hajj, W. I. Bertiger, and S. M. Lichten (1993), Effects of antenna orientation on GPS carrier phase, *Manuscripta Geodatica*, *18*, 91–98.

Yin, S., H. Wdowinski, Y. Liu, W. Gan, G. Huang, B. Xiao, and S. Liang (2013), Strong ground motion recorded by high-rate GPS of the 2008 M 8.0 Wenchuan earthquake, China, *Seismological Research Letters*, *84*(2), 210–218.

Zhou, X., W. Sun, B. Zhao, G. Fu, J. Dong, and Z. Nie (2012), Geodetic observations detecting coseismic displacements and gravity changes caused by the Mw = 9.0 Tohoku-Oki earthquake, *Journal of Geophysical Research*, *117*, doi:10.1029/2011JB008849.

A Figures
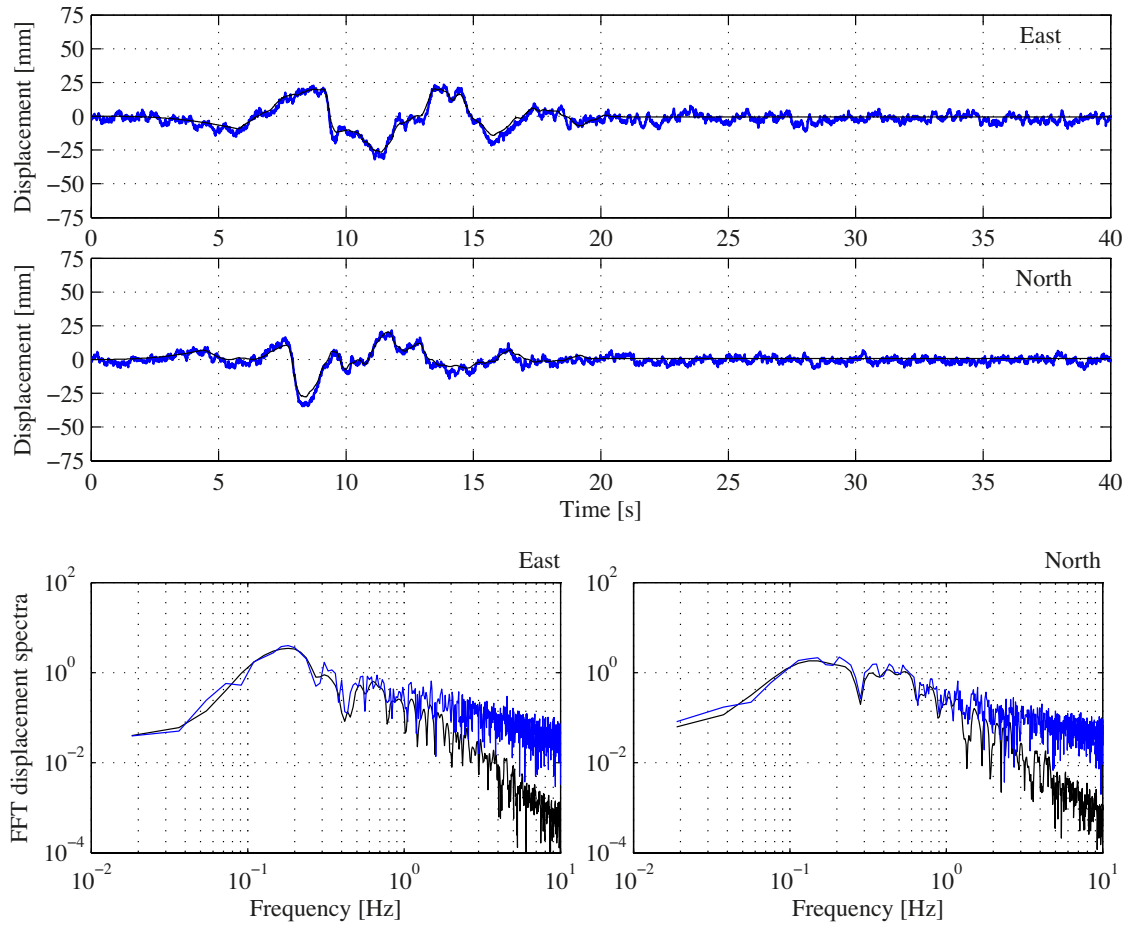
Figure A.1: The East and North components of the simulated M5.0 earthquake from Fig. 8.2 generated by the shake table (black) and measured with 100 sps GPS with a PLL B_l of 10 Hz (blue). The data is high-pass filtered with a low-cut frequency of 0.1 Hz, visible in the spectra below.
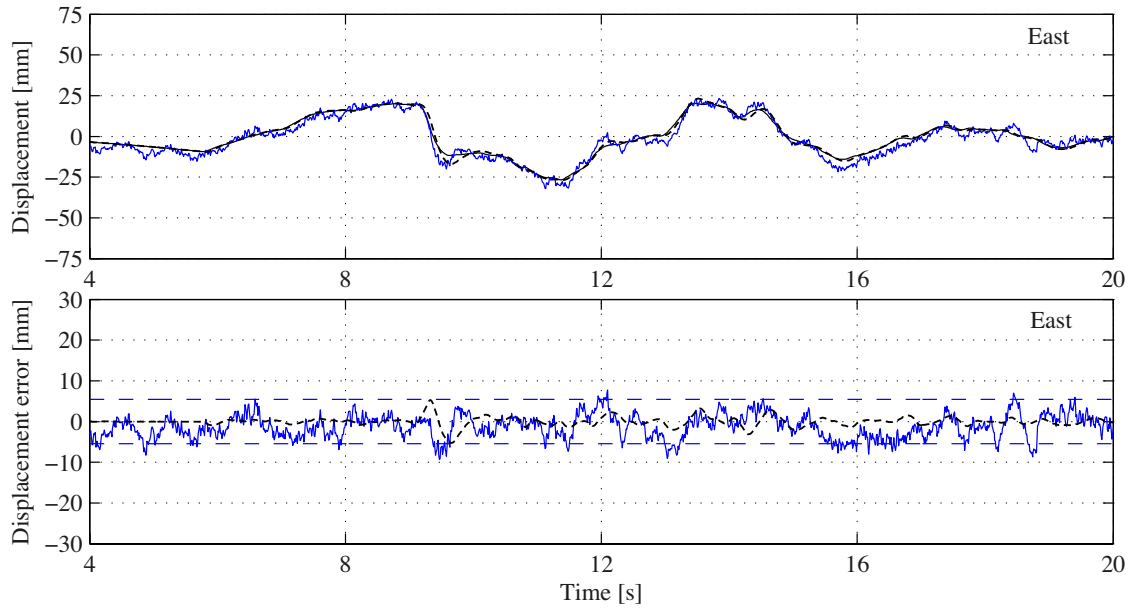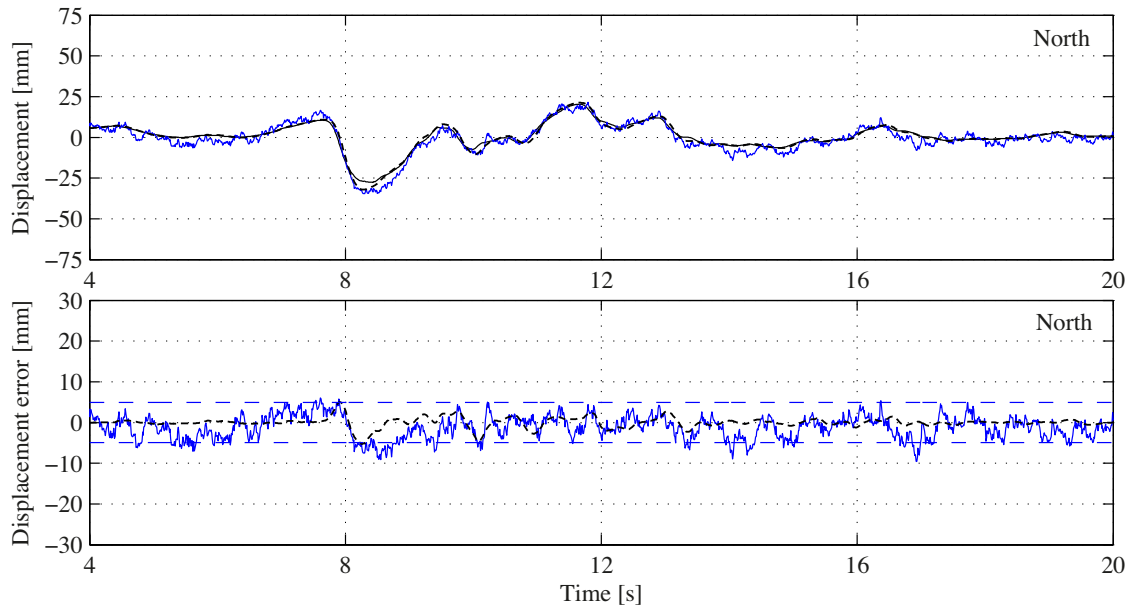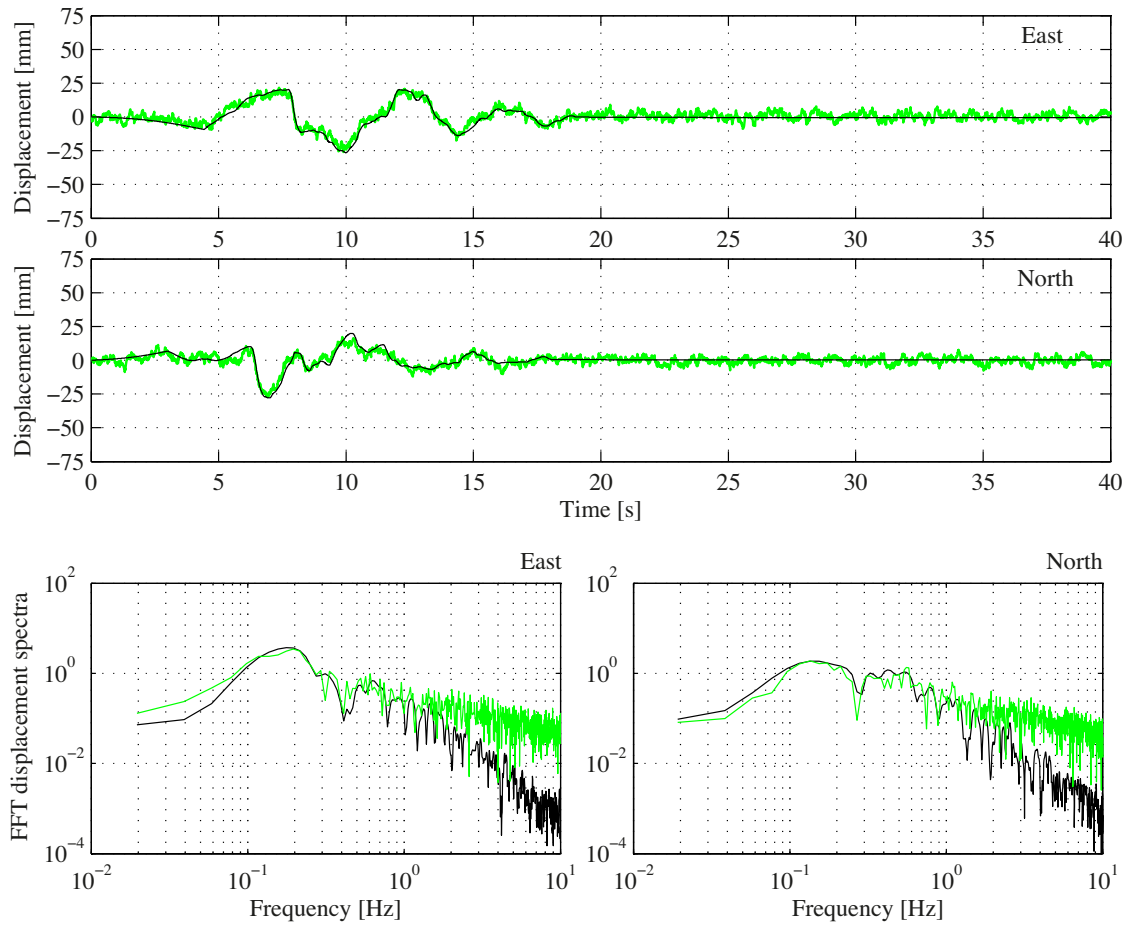
Figure A.2: The East component from second 4 to 20 from Fig. A.1 with the additional black dashed line reprsenting the simulated response according to Eq. (7.9) with a PLL B_L of 10 Hz. At the bottom the receiver responses reduced by the input motion (black line on top). The horizontal dashed blue line marks the 95% threshold (2σ) of the GPS measurements estimated over the 40 s of the event.

Figure A.3: The North component from second 4 to 20 from Fig. A.4 with the additional black dashed line reprsenting the simulated response according to Eq. (7.9) with a PLL B_L of 10 Hz. At the bottom the receiver responses reduced by the input motion (black line on top). The horizontal dashed blue line marks the 95% threshold (2σ) of the GPS measurements estimated over the 40 s of the event.

Figure A.4: The East and North components of the simulated M5.0 earthquake from Fig. 8.2 generated by the shake table (black) and measured with 100 sps GPS with a PLL B_l of 25 Hz (green). The data is high-pass filtered with a low-cut frequency of 0.1 Hz, visible in the spectra below.
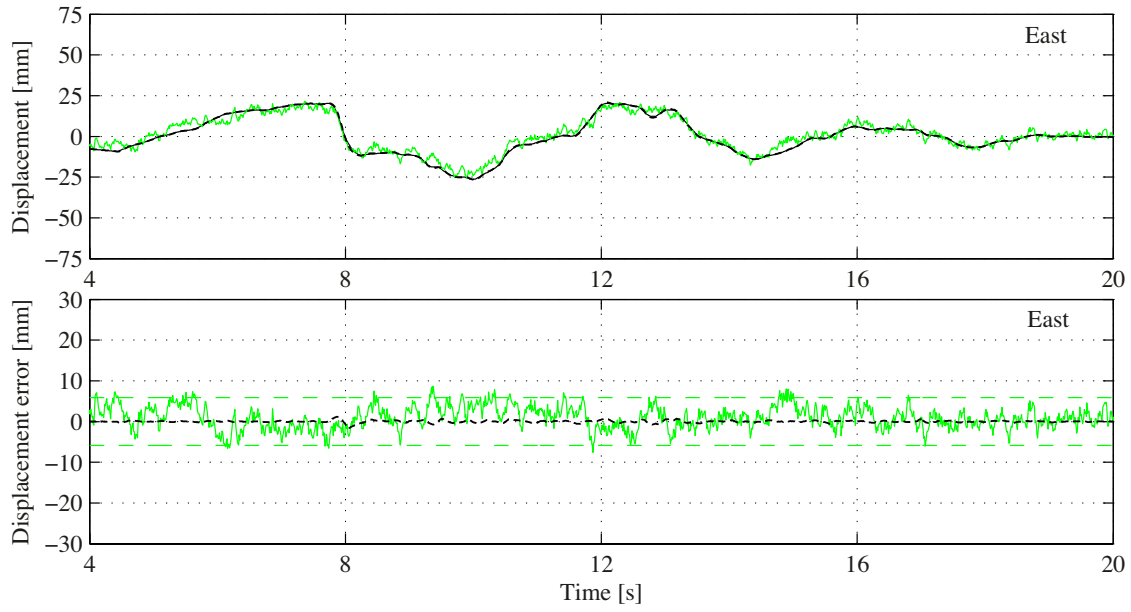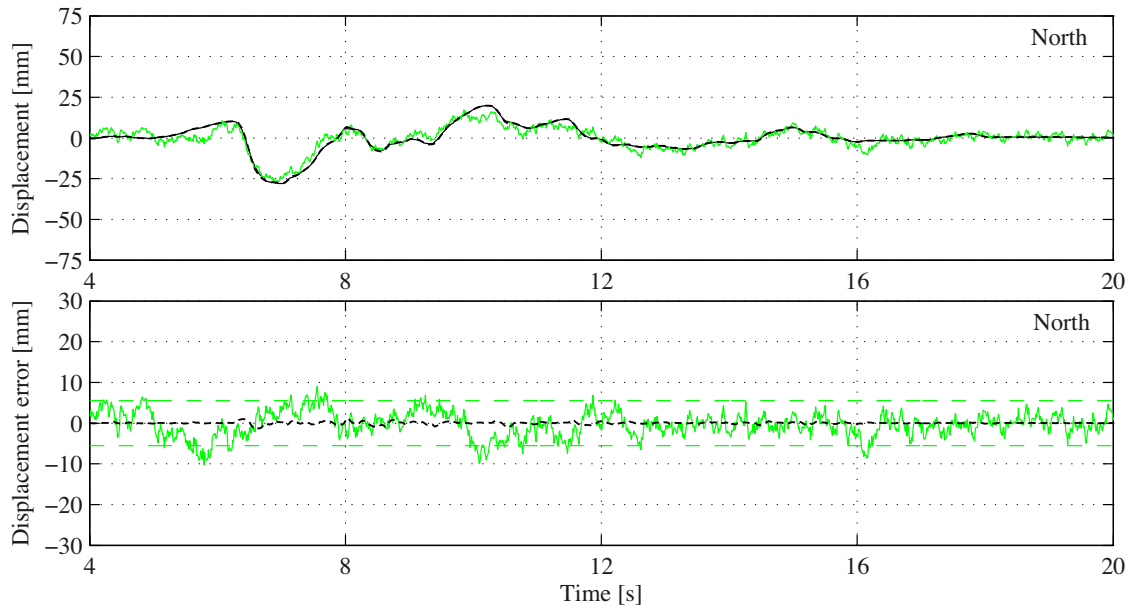
Figure A.5: The East component from second 4 to 20 from Fig. A.4 with the additional black dashed line reprsenting the simulated response according to Eq. (7.9) with a PLL B_L of 25 Hz. At the bottom the receiver responses reduced by the input motion (black line on top). The horizontal dashed green line marks the 95% threshold (2σ) of the GPS measurements estimated over the 40 s of the event.

Figure A.6: The North component from second 4 to 20 from Fig. A.4 with the additional black dashed line reprsenting the simulated response according to Eq. (7.9) with a PLL B_L of 25 Hz. At the bottom the receiver responses reduced by the input motion (black line on top). The horizontal dashed green line marks the 95% threshold (2σ) of the GPS measurements estimated over the 40 s of the event.
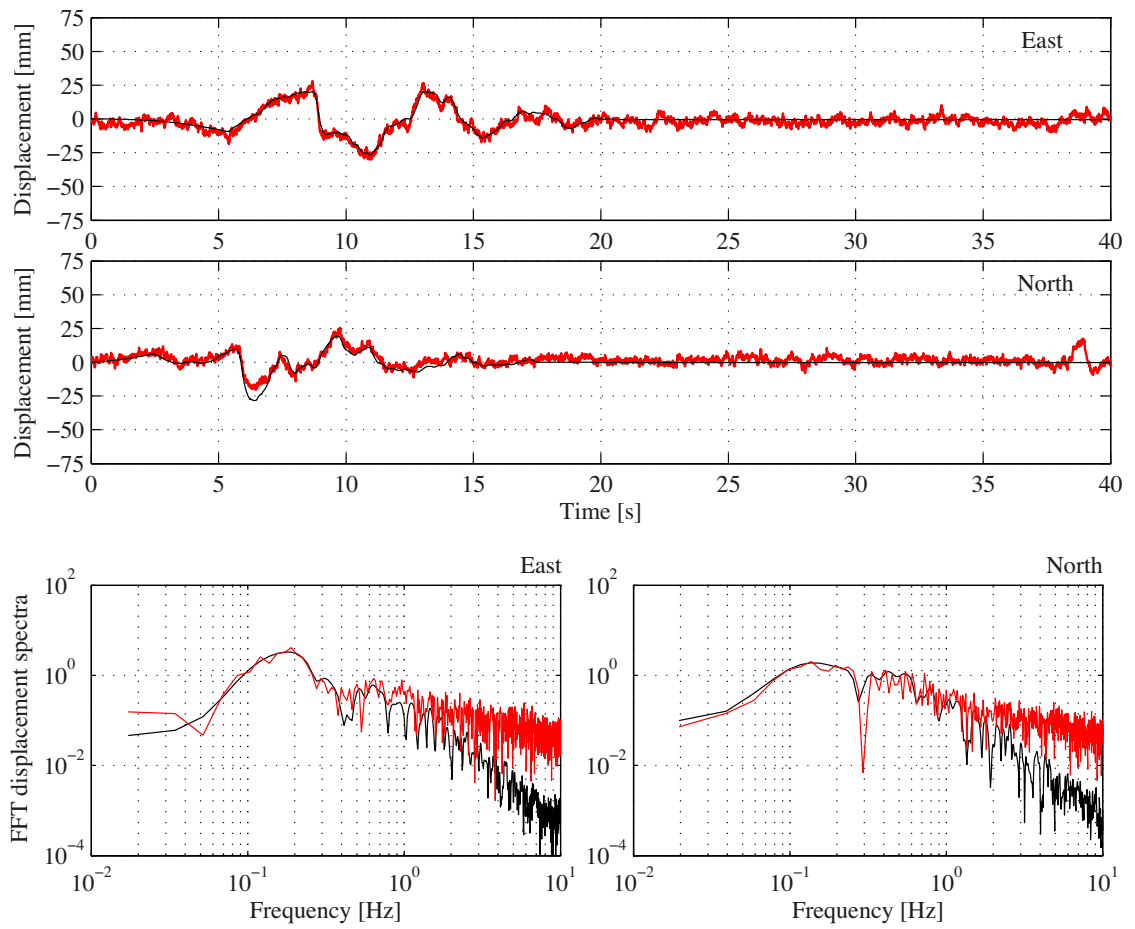
Figure A.7: The East and North components of the simulated M5.0 earthquake from Fig. 8.2 generated by the shake table (black) and measured with 100 sps GPS with a PLL B_l of 50 Hz (red. The data is high-pass filtered with a low-cut frequency of 0.1 Hz, visible in the spectra below.
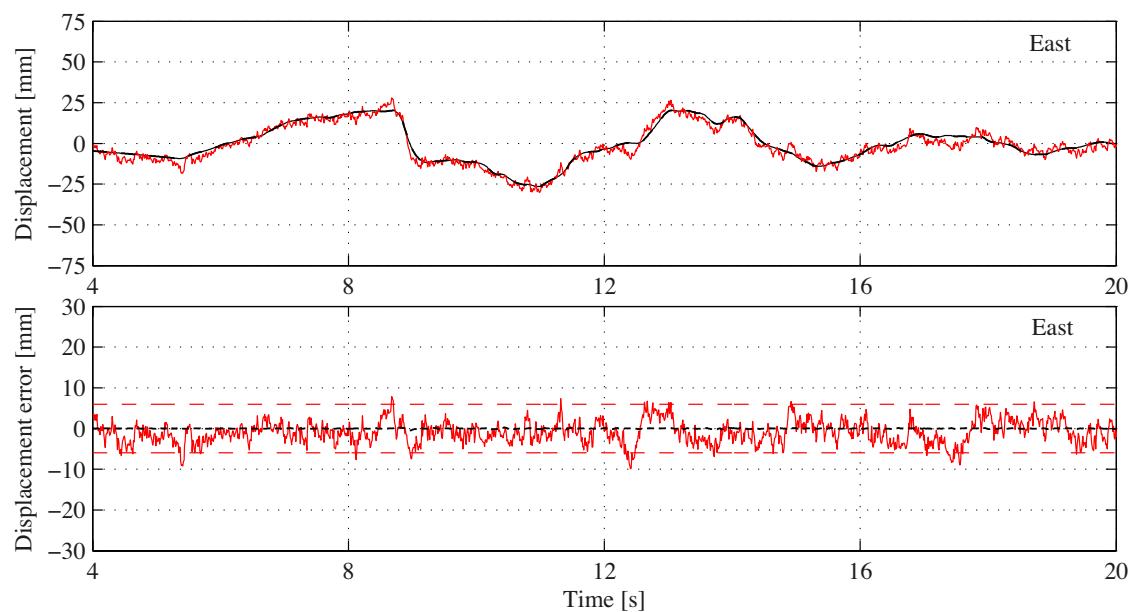
Figure A.8: The East component from second 4 to 20 from Fig. A.7 with the additional black dashed line reprsenting the simulated response according to Eq. (7.9) with a PLL B_{L} of 50 Hz. At the bottom the receiver responses reduced by the input motion (black line on top). The horizontal dashed red line marks the 95% threshold (2σ) of the GPS measurements estimated over the 40 s of the event.
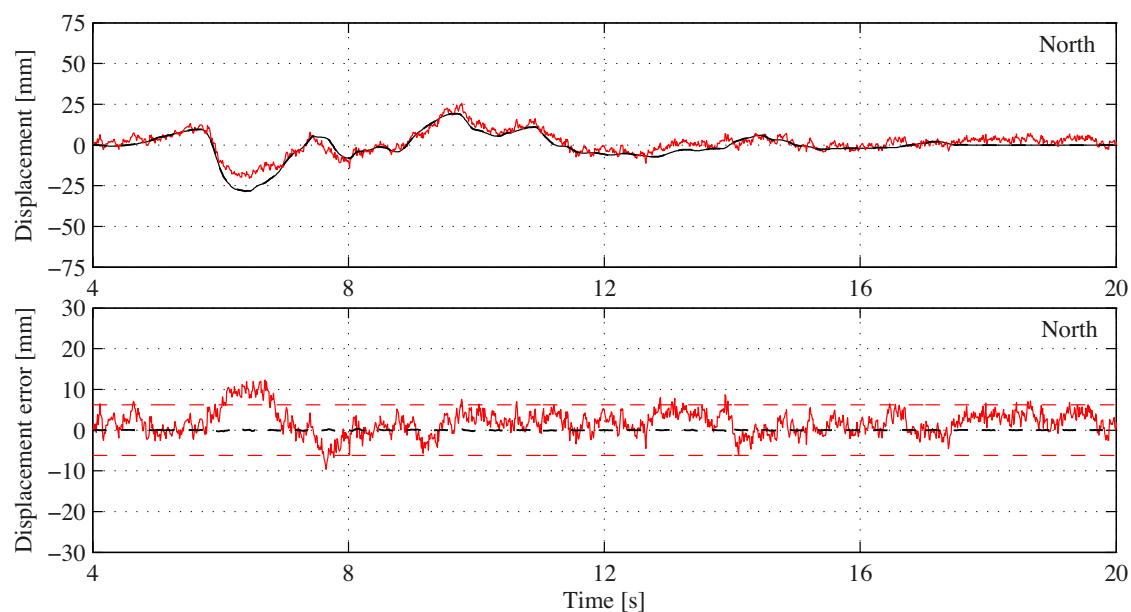

Figure A.9: The North component from second 4 to 20 from Fig. A.7 with the additional black dashed line reprsenting the simulated response according to Eq. (7.9) with a PLL B_{L} of 50 Hz. At the bottom the receiver responses reduced by the input motion (black line on top). The horizontal dashed red line marks the 95% threshold (2σ) of the GPS measurements estimated over the 40 s of the event.